Soil-Structure Interaction Analysis of Monopile Foundations Supporting Offshore Wind Turbines

by

Bipin Kumar Gupta

A thesis

presented to the University of Waterloo

in fulfillment of the

thesis requirement for the degree of

Doctor of Philosophy

in

Civil Engineering

Waterloo, Ontario, Canada, 2018

Examining Committee Membership

The following served on the Examining Committee for this thesis. The decision of the Examining Committee is by majority vote.

External Examiner	Dr. Bipul Chandra Hawlader Professor & Research Chair in Seafloor Mechanics Department of Civil Engineering, Faculty of Engineering and Applied Science, Memorial University of Newfoundland
Supervisor	Dr. Dipanjan Basu Associate Professor, Department of Civil and Environmental Engineering, University of Waterloo
Internal Member	Dr. Giovanni Cascante Professor, Department of Civil and Environmental Engineering, University of Waterloo
Internal Member	Dr. Wei-Chau Xie Professor, Department of Civil and Environmental Engineering, University of Waterloo
Internal-external Member	Dr. Clifford Butcher Assistant Professor, Department of Mechanical and Mechatronics Engineering, University of Waterloo

I hereby declare that I am the sole author of this thesis. This is a true copy of the thesis, including any required final revisions, as accepted by my examiners.

I understand that my thesis may be made electronically available to the public.

Abstract

Monopile foundations supporting offshore wind turbines are hollow circular steel piles of diameter 4-6 m and a slenderness ratio (length/radius) of 10-12 driven into the seabed in an average water depth of 35 m. They are subjected to large lateral forces and overturning moments at the seabed level from wind, waves, and water currents acting on the wind turbine structure. Currently, they are designed using the *p-y* analysis method (*p* is the soil reaction force per unit length at any point along the pile shaft and *y* is the corresponding pile displacement at that point) which has a number of shortcomings. The *p-y* analysis was originally developed from a few full-scale field pile-load tests on small-diameter piles (less than 2 m in diameter) and their applicability to large-diameter monopiles is questionable. Besides, it is empirical, site-specific, and does not account for the three-dimensional pile-soil interaction important for large-diameter monopiles, thereby, resulting in a conservative design and an increase in the cost of the project. Three-dimensional finite element analysis can be used for the analysis and design of monopiles, but such analyses require significantly large computational time and effort besides, the specific expertise of finite element software that further limits its use in practice.

The primary objective of this thesis is to develop a computationally efficient continuum-based mathematical model that takes the three-dimensional monopile-soil interaction into account. In the thesis, three tasks are performed towards the development of the mathematical model. First, a mathematical framework is developed to analyze laterally loaded monopiles following the Timoshenko beam theory in a multilayered elastic soil deposit subjected to static lateral loading. In the analysis, it is shown that successive simplification of the analysis can lead to monopiles modeled as a Euler-Bernoulli and rigid beam. The analysis is verified with finite element solutions and the suitability of the application each of the beam theories to obtain monopile response (head-displacement and rotation) is also investigated besides, a comparison of the computational time between the present analysis and finite element analysis is also shown. In the second task, the aforementioned framework is extended to analyze monopiles embedded in a multilayered linear viscoelastic soil deposit with frequency-independent hysteretic material damping subjected to harmonic dynamic lateral loading. It is shown that the analysis can be reduced to model monopiles following the

Rayleigh, Euler-Bernoulli, and rigid beam theory. The analysis is verified with well-established solution techniques reported in the literature. Further, the results and the computational time obtained from this analysis are compared with those of the analysis in the first task for four different monopiles with varying slenderness ratio currently installed in the field. The purpose of the comparison is to investigate the applicability of the dynamic analysis for obtaining monopile response which is subjected to cyclic loadings of frequency less than 1.0 Hz. It is found that the static analysis following the Euler-Bernoulli beam theory is sufficient for obtaining monopile response.

In the third task, the mathematical framework developed in the first task is extended to analyze laterally loaded monopiles modeled as a Euler-Bernoulli beam in a multilayered nonlinear elastic soil deposit and subjected to static loading. In the analysis, the nonlinear elastic relationships describing the variation of shear modulus with shear strain reported in the literature either applicable to undrained clays or sandy soil deposits are utilized. The mathematical accuracy of the analysis is verified by comparing results obtained from the analysis with the results of finite element analysis. A comparison of the computational time between the present and finite element analysis is also shown to demonstrate the computational efficiency of the present analysis. The results of the analysis are further validated with the results of several full-scale field pile-load tests and the *p-y* analysis procedure available in the literature. The accuracy of the results from this nonlinear elastic approach is further ensured by comparing monopile response with those of finite element simulations where the soil is modeled using an elastic-plastic constitutive model. A comparison of the monopile response is also shown in the *p-y* analysis to investigate the appropriateness of the currently used *p-y* curves to analyze and design monopiles. Finally, a preliminary step-by-step design procedure for monopile foundations embedded in nonlinear elastic soil deposit is developed following the recommendations outlined in current codes of practice for offshore wind turbines.

Acknowledgments

First and foremost, I would like to express my sincere gratitude to my advisor Professor Dipanjan Basu for giving me the opportunity to pursue my Doctoral studies at the University of Waterloo, introducing me to this methodology of solving laterally loaded pile problems, for his continuous support, patience, motivation, and prompt feedback to my queries during the course of this research work. I am also very thankful to him for helping me improve my writing, presentation, and tutoring skills besides, I gratefully acknowledge the financial support he provided me during my Doctoral studies.

I am extremely thankful to Dr. Giovanni Cascante, Dr. Wei-Chau Xie, Dr. Dr. Hamidreza Jahed Motlagh, Clifford Butcher, and Dr. Bipul Chandra Hawlader for agreeing to serve as my committee members, their valuable feedbacks, and the time to review my work. I would also like to acknowledge the faculty members at the University of Waterloo whose courses benefited me in my research work.

I would like to recognize the financial support (Graduate Research Studentship, International Doctoral Student Award, University of Waterloo Graduate Scholarship, and others) that I received from the University of Waterloo.

I would also like to thank my friends and colleagues (Wei Zhang, Faraz Goodarzi, Mahdi Fazeli, Mina Lee, Dr. M.J. Rodriguez, M. Irfan, F. Alonso Diaz, Sabah Hassan, Cristobal Lara, and Dr. Hassan Ali) in the geotechnical engineering group.

My time in Waterloo was enjoyable largely because of the few friends that I made in Waterloo. I am particularly thankful to Idhayachandhiran Ilampooranan (a.k.a. ANNA) for all his help and support when I traveled to Canada, Rahul Deshpande for introducing me to those therapeutic sessions of ping pong and others, Abhishek Singhi for his unconditional help and support during my not so good days in Waterloo, and Vadiraj AM for the food he occasionally cooked for us. I greatly appreciate your presence in my life and would cherish the memories and conversations that we have had during our food sessions.

Finally, I thank my parents, brothers, sisters-in-law, and nieces. I know and understand the sacrifices you have made to bring me to this position; I earnestly acknowledge the love, support, and encouragement that you have provided me during these four years. I would also like to thank my friends Sayantan Chakraborty for keeping in touch (mostly all Saturday's during these four years) and always being there to listen when I needed an ear and Dr. Tanmoy Mukhopadhyay for the help and support you always provided when I needed.

Dedication

To my family

Table of Contents

List of Figures

List of Tables

CHAPTER 1

Introduction

1.1 General

Of the various sources of renewable energy, wind energy is a popular choice in many developed and developing countries. Wind turbines are installed onshore and offshore almost everywhere across the world. While onshore wind turbines are an option in most countries, the Western European countries have moved offshore to meet their high energy demands. There have been rapid installations of offshore wind turbines (OWTs) in Europe with a total installed capacity of 11,027 MW, with UK and Germany being the leading producers (Ho et al. 2016). While Europe covers almost 84% of the offshore wind market, countries like China, Japan, South Korea, Taiwan, and the USA have also set up ambitious targets for offshore wind power generation (GWEC 2017). The advantages of OWTs are that a continuous and steady supply of wind over a large area is available and that large-sized wind turbines capable of generating significantly high energy can be constructed.

Although OWTs are becoming popular, it is a relatively new technology with different engineering challenges. OWTs are subjected to large environmental and mechanical loads which are transferred to the foundations at the sea level. This makes it necessary to adopt a foundation system which can effectively resist these loads. Various types of OWT foundation systems have been used so far depending on the depth of installation – the gravity base and monopiles at shallow to moderate water depths, and the suction buckets, jacket, tripod at larger water depths. Monopiles are the most common type of OWT foundation (about 80% (Ho et al. 2016)) because of their simple design, fabrication and installation processes (IRENA 2012). Currently, monopiles are typically 4-6 m in diameter, installed in water depths of around 35 m supporting OWTs with a rated power output of up to 5 MW. Monopiles are designed using the *p-y* method which was developed to design piles of diameter less than 2 m. Therefore, their use to design monopiles is questionable. Besides, monopile foundations are also expected to support even larger sized OWTs with a power output of more than 6 MW in deeper water depths of up to 60 m which would require larger sized monopiles of diameter 7.5-10 m (Kallehave et al. 2015) commonly termed as XL monopiles. The use of the *p-y* method to design such large diameter piles might lead to an uneconomical and conservative design.

Therefore, further research studies on different aspects of monopiles supporting OWTs are necessary to produce safe and economical designs.

1.2 Literature Review

This section provides a brief overview of the existing OWT monopile systems with respect to their typical dimensions, loading conditions, current design considerations, and past research studies.

1.2.1 OWT structure monopile system

Figure 1.1 shows a three-bladed OWT structure which typically has a rated power output of 2-5 MW. The turbine system is a heavy rotating mass comprising the blade, nacelle, rotor, and hub assembly resting on a tall slender steel tubular column (which is the tower). For example, a 3.6 MW Siemens OWT has a tower height of 90 m and a blade diameter of 120 m (Siemens AG 2016). The tower and turbine system is connected to the substructure via a transition piece. The substructure is a monopile which essentially is a hollow circular steel pile of diameter typically ranging over 4-6 m, driven hydraulically into the seabed in water depths of approximately 35 m (Doherty and Gavin 2012) and a slenderness ratio (length/radius) of 10-12 (Klinkvort and Hededal 2013).

The OWT structure is subjected to various static and dynamic loads of cyclic nature. The axial static loads from the self-weight of the tower, turbine, and the substructure assembly. The dynamic lateral loads are from the wind load on the tower and turbine assembly with a predominant frequency of 0.01 Hz (Bhattacharya et al. 2011**)**, and the waves and water current loads on the tower and substructure with a frequency typically in the range of 0.1-0.3 Hz (Kallehave et al. 2015). There are additional dynamic lateral loads from the vibrations of the rotor at the hub level, typically in the range of 0.14-0.31 Hz (often termed as 1P) and vibrations arising from blade shadowing effects in the range of 0.42-0.93 Hz (termed as the 3P frequency, i.e., thrice the rotor frequency) for a standard 3 MW wind turbine (Bhattacharya et al. 2011). These loads on the OWT system have to be resisted by the monopile, and therefore, the geotechnical design of monopile is important to ensure satisfactory performance of the OWT during its typical service life of 20 years (DNV 2014).

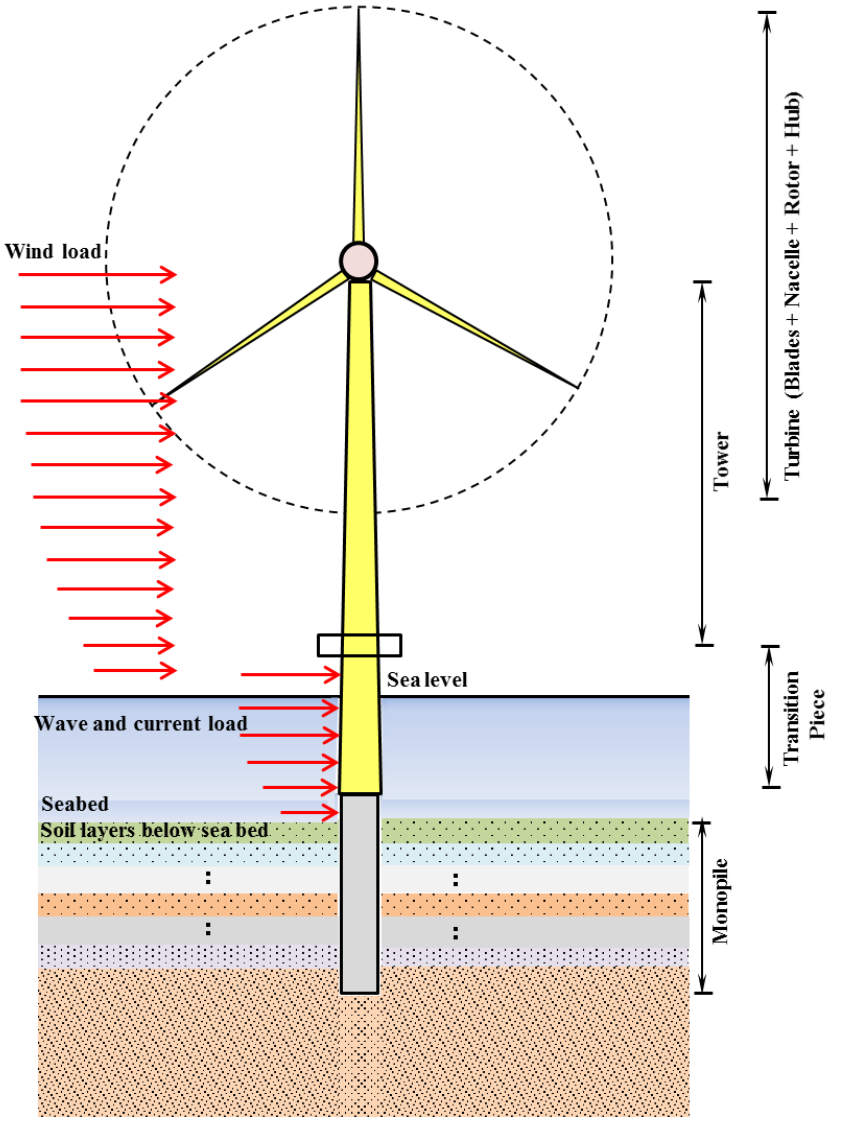

Figure 1.1: Schematic diagram of an OWT-monopile system with imposed environmental loads

1.2.2 Design requirements of OWT monopile

Both the ultimate and serviceability limit state criteria should be considered for the geotechnical design of monopiles (DNV 2014). The typical serviceability limit state criteria set for monopiles are in terms of maximum rotation of the monopile head at the seabed level, while the typical ultimate limit state criteria set for monopiles are in terms of their collapse load. Another important design consideration is that the natural frequency of the OWT

structure should not be close to the forcing frequency of the imposed dynamic loads. The details of the design requirements are mentioned below:

- Ultimate limit state (ULS) criterion: Sufficient monopile capacity should be ensured under axial and lateral loading such that the applied loads do not cause the collapse of the monopile under axial and lateral loads during an extreme loading event.
- Serviceability limit state (SLS) criterion: Displacement tolerances at the monopile head are required for satisfactory performance of the OWT under instantaneous and long-term cyclic loads. The maximum allowable rotation for monopile at the seabed is 0.5° under extreme loading conditions, of which 0.25° is from installation tolerances. Therefore, the usual allowable limit for monopile head rotation is 0.25°.
- Resonance avoidance criterion: Current OWTs are designed as "soft–stiff" which means that the first natural frequency of the global OWT structure-monopile system should be ±10% away from the excitation frequency bands – 1P (rotor frequency) and 3P (blade passing frequency) typically ranging over 0.3–1.0 Hz (see Figure 1.2) (DNV 2002).

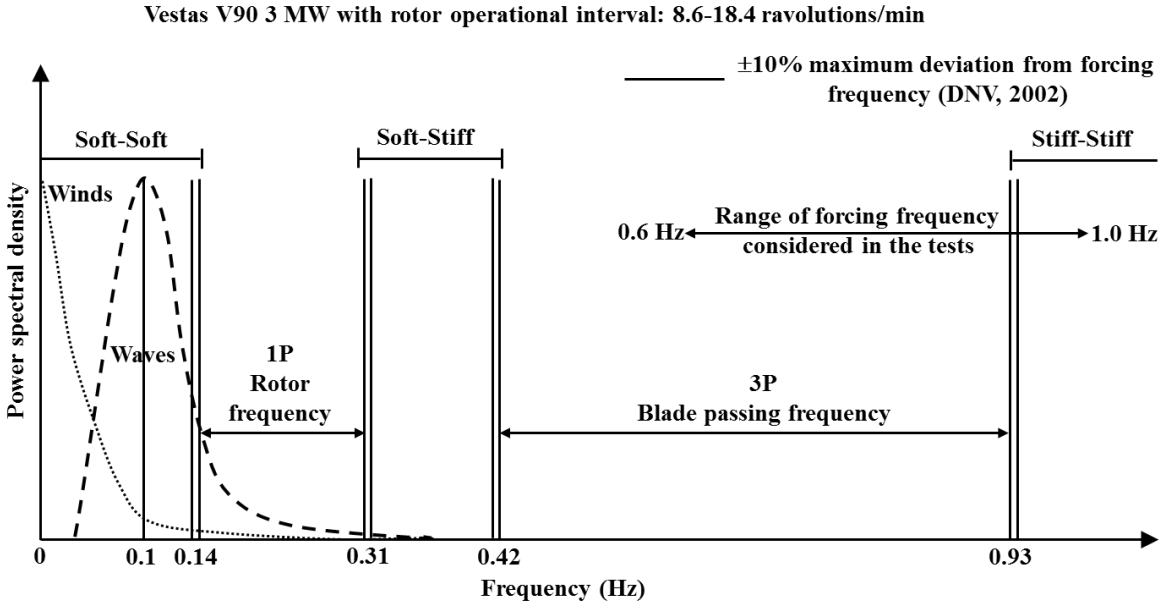

Figure 1.2: Forcing frequencies of a Vestas V90 3 MW OWT (Regenerated from Bhattacharya et al. 2011)

1.2.3 Research studies and developments

Several research studies on various aspects of OWT structure monopile system have been conducted by researchers across the world. These studies can be primarily grouped into two categories: (i) load-deformation studies on monopiles and (ii) studies on the natural frequency of the OWT-monopile system.

Load-deformation studies on monopiles

Monopiles are laterally loaded piles that should satisfy both the ULS and SLS criteria for adequate performance. For offshore applications, the design of such laterally loaded piles is currently based on the *p-y* method (GL 2005, API 2011, DNV 2014). In the *p-y* method, the soil is modeled as a series of uncoupled (Winkler) nonlinear springs attached to the pile shaft along its entire length, and the pile is modeled as a Euler-Bernoulli beam. The soil springs are characterized by nonlinear force-displacement (*p-y*) relationships (commonly termed as *p-y* curves) for static and cyclic loading (see Figure 1.3). The *p-y* curves depend on soil properties and depth at which the spring is attached to the pile.

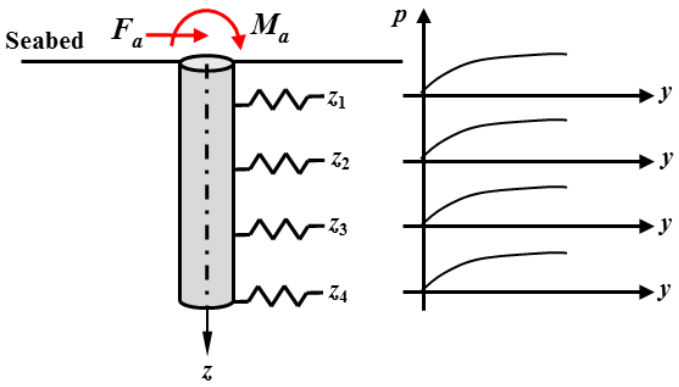

Figure 1.3: Nonlinear *p-y* curves for laterally loaded monopile

However, the widely-used *p-y* method recommended by the American Petroleum Institute (API 2011) was originally developed for long, slender piles (Matlock 1970, Reese 1975) because of which its applicability to large-diameter monopiles is questionable. This is particularly true because the *p-y* curves were developed by back-analyzing the results of a few full-scale field load tests on slender piles with 21 m length and 61 cm diameter, and the method does not explicitly take into account the mechanics of three-dimensional (3-D) pile-soil

interaction important for large-diameter monopiles. The *p-y* curve for cyclic load was developed for less than 100 load cycles while the monopiles are subjected to billions of load cycles ($> 10^7$) over the service life of the OWT (Achmus et al. 2011).

This drawback prompted researchers across the world to examine the applicability of the existing *p-y* method to large diameter monopiles under static and cyclic loads and explore other aspects of monopile behavior important for design. An exhaustive literature survey based on the different aspects of monopile behavior highlighting the major contributions is summarised next. The literature is categorized based on the loading conditions adopted in the studies.

- Static loading

Three dimensional (3-D) finite element (FE) analyses (Weimann et al. 2004, Lesny and Weimann 2005, 2006, Abdel-Rahman and Achmus 2005, Bekken 2009, Hearn and Edgers 2010, Moller and Christiansen 2011, Haiderali et al. 2013), geotechnical centrifuge tests (Alderlieste 2011), 1-*g* model laboratory tests (Moller and Christiansen 2011, Zhu et al. 2015), and field tests on reduced-scale (Li et al. 2017) monopiles in sandy and clayey soils showed that the existing *p-y* curves are not suitable for design of monopiles because they overestimate the soil stiffness, and thus underestimate monopile displacement. Therefore, efforts were made to modify the existing API recommended *p-y* curves for sandy (Weimann et al. 2004, Sorensen et al. 2010, Achmus et al. 2011, Zhu et al. 2015, Li et al. 2017) and clayey (Pradhan 2012) soils. A method similar to the *p-y* analysis was also proposed to design monopiles based on 3-D FE modeling in conjunction with site-specific field tests (Byrne et al. 2015 a, b, Zdravkovic et al. 2015, Murphy et al. 2018). Additional monopile-soil response curves i.e., m-θ curves describing the relationship between the distributed moment m along monopile shaft and rotation θ of the monopile cross-section, S-y curves describing the relationship between the shear force S at the pile base and pile base displacement y, and M-θ curves describing the relationship between the moment at the monopile base and monopile base rotation were developed. The design curves were implemented in a 1-D FE framework in which the pile was modeled as a Timoshenko beam and the soil adjacent to the pile was represented by translational and rotational springs characterized by the p-y, m-θ, S-y, and M-θ curves.

- Cyclic loading

Centrifuge tests (Alderlieste 2011, Grajales et al. 2015), 1-*g* model or small-scale laboratory tests (Leblanc et al. 2010a, Alderlieste 2011, Moller and Christiansen 2011, Hansen et al. 2011, Abadie and Byrne 2014, Abadie 2015, Nicolai and Ibsen 2015, Liao et al. 2018), and numerical modeling (Grajales et al. 2015, Depina et al. 2015, Carswell et al. 2016, Page et al. 2017, Chong and Pasten 2017, Barari et al. 2017, Aasen et al. 2017, Yang et al. 2017) on monopiles in sandy and clayey soils subjected to short- and long-term cyclic loads reported an increase in monopile displacement and changes in the stiffness of the monopile-soil system with the number of load cycles. A theoretical model to obtain the monopile response in sandy soil was suggested in which the modulus degradation of sand with load cycles was determined from cyclic triaxial tests and given as input to a FE (Lesny and Hinz 2007, Achmus et al. 2009, Depina et al. 2015) or a finite difference (Yang et al. 2017) model to subsequently develop design charts (Achmus et al. 2009, Yang et al. 2017). Design charts to determine accumulated monopile rotation because of random two-way cyclic loading from a limited amount of empirical data on small-scale tests were also developed (Leblanc et al. 2010b). A design procedure for monopiles in sandy soil from the results of a series of centrifuge tests for any loading amplitude, characteristics, and a number of load cycles was also suggested (Klinkvort and Hededal 2013, 2014).

Studies on the natural frequency of the OWT-monopile system

For estimating the natural frequency of an OWT structure, the stiffness of the monopile-soil system at seabed level can be characterized by a static lateral translational stiffness K_{rr}, cross-coupling stiffness $K_{r\psi}$, and rotational stiffness $K_{\psi\psi}$ represented as springs (see Figure 1.4). A research study (Zaaijer 2006) was conducted to evaluate these spring constants K_{rr}, $K_{r\psi}$, and $K_{\psi\psi}$ using three different approaches: (i) effective fixity length in which a rigid clamping of the pile was used beyond an effective depth of 3.3-3.7 times the pile diameter, (ii) FE simulation and continuum model proposed by previous studies on laterally loaded piles, and (iii) simplified uncoupled springs from both force and displacement based method of a FE model. The range of applicability of each of the methods in the calculation of natural frequency was investigated, and it was suggested that the continuum and FE models gave a reasonable estimation of natural frequency. Further research studies led to the development of

approximate (Adhikari and Bhattacharya 2011) and exact (Adhikari and Bhattacharya 2012) equations using which an assessment of the natural frequency of an OWT-foundation system can be made. In these studies, the foundation was initially modeled with static springs K_{rr} and $K_{\psi\psi}$ (see Figure 1.4) while the tower and turbine were modeled as a Euler-Bernoulli beam with a mass at the end. A reasonable match was obtained between the results of the developed equations and those of small-scale experiments and measured values of real wind farm sites (Bhattacharya and Adhikari 2011). The method was further improved by including the cross-coupling spring $K_{r\psi}$ (see Figure 1.4) and modeling the tower both as a Timoshenko and Euler-Bernoulli beam. Comparison of results with those of wind farm sites gave a reasonably accurate initial estimate of the natural frequency of wind turbines. A higher-order beam theory for the tower did not improve the natural frequency prediction much (Arany et al. 2015).

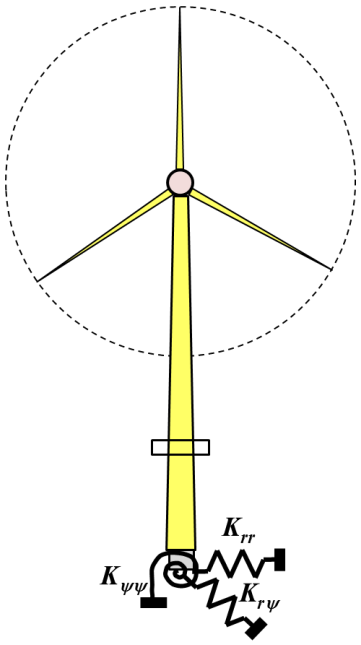

Figure 1.4: A simplified model for calculation of natural frequency

Beside the development of static spring constants for estimating the natural frequency of OWTs, a few studies were also conducted to observe the effect of long-term cyclic loads on the natural frequency of OWTs. Small-scale tests (Bhattacharya et al. 2013, Lombardi et al. 2013) on OWT in homogeneous, isotropic soft clay under long-term cyclic loads at three sets of forcing frequency and amplitude showed a degradation of soil stiffness with a decrease in the natural frequency of the OWT. A greater decrease in natural frequency at higher strain

levels was also observed. Further, the damping of the system was high at higher strain level and loads. The tests were also repeated for monopiles in sandy soils, and it was reported that there was an increase in stiffness of the soil that led to an increase in natural frequency (Arany et al. 2015).

1.3 Limitations of existing studies

The previous section provides information on the current state-of-art of the OWT-monopile system, their design considerations, and a brief discussion on the applicability of the existing analysis methods to monopiles. At the same time, the behavior and design of monopiles under static, short- and long-term cyclic loads, and methods to predict the natural frequency of the OWT structure are also discussed. Research studies on monopiles are limited in number, and there are a variety of aspects on which further work is required, as described below:

- The API recommended *p-y* method is still used in practice for analyzing and designing monopiles (e.g., Bisoi and Haldar 2014, 2015). Although there are improved *p-y* analysis methods for monopiles, these methods are very site-specific. Similarly, the design methodologies developed from experimental and numerical studies are from a limited number of tests or analysis either on idealized soil profiles or for site-specific conditions. Therefore, there is clearly a need of an analytical, semi-analytical or a numerical model that can account for 3-D monopile-soil interaction, consider the soil variabilities actually encountered in the field and can be used in routine design projects without resorting to sophisticated and computationally expensive FE tools.
- To predict the natural frequency of the OWT structure the spring constants (as shown in Figure 1.4) should be known. The exact or approximate method developed for calculating the natural frequency of OWT utilize equations available in the literature from previous studies on laterally loaded piles to quantify these spring constants. However, the equations are oversimplified, developed for idealized soil profiles, and are based on considerations of static stiffness of the pile-soil system. Moreover, their application to the monopile-soil system is also questionable because monopiles are subjected to cyclic/dynamic loads during their lifetime and dynamic stiffness might be necessary for accurate predictions of the natural frequency of the OWT. FE tools can be used for individual projects; however,

an analytical, semi-analytical or a numerical tool would be very useful because a large number of analyses for varied soil profiles can be done to develop the static and dynamic spring constants (commonly referred to as static and dynamic impedance functions in the geotechnical foundation engineering literature) quite easily and economically.

- Conventionally, laterally loaded piles have always been modeled as a Euler-Bernoulli beam in any analytical, semi-analytical or numerical procedures (for example the *p-y* method) for analysis and design of laterally loaded piles. However, for monopiles, most of the literature classifies the monopile as a perfectly rigid body while some numerical studies use the Timoshenko beam theory. Thus, there is clearly a lack of consensus in the literature as to which beam theory is really suitable for modeling monopiles. Therefore, an investigation of the suitability of the application of different beam theories (Timoshenko, Euler-Bernoulli, Rayleigh and rigid beam theory) to monopiles is necessary.

1.4 Objectives of the present research

Based on the limitations identified in the literature, the specific objectives of the present research reported in this thesis are:

- Develop a mathematically rigorous but a computationally efficient model for analysis of laterally loaded monopiles in a multilayered soil deposit that
  i. accounts for 3-D monopile-soil interaction and eliminates the requirement of developing a new or modifying the existing *p-y* curves for application to monopiles,
  ii. can be used to quickly predict the monopile head displacement and rotation under different loading conditions (static, dynamic or cyclic) through use of appropriate soil properties and constitutive relationships, and
  iii. can be used to quickly perform an exhaustive parametric study for monopiles embedded in various soil profiles to obtain the spring constants K_{rr}, $K_{r\psi}$, and $K_{\psi\psi}$ required for estimation of the natural frequency of OWTs, without resorting to expensive and time-consuming FE analysis.
- Investigate the application of various beam theories to model monopiles.

1.5 Organization of the thesis

The thesis contains six chapters and is organized as follows:

- **Chapter 1** provides a brief introduction of the current state-of-art on the OWT-monopile system and a summary of the research objectives.
- **Chapter 2** provides the development of a continuum-based framework for analyzing laterally loaded monopiles in a multilayered elastic soil, subjected to static loading using the Timoshenko beam theory. It is shown that the framework can be progressively reduced to obtain monopile response following the Euler-Bernoulli and rigid beam theory. The results obtained from the present analysis following various beam theories are compared with 3-D FE analysis and appropriate recommendations on the use of different beam theories for modeling monopiles in a linear elastic soil deposit are also made. A comparison of the computational time required to obtain monopile response between the present and 3-D FE analysis is also shown.
- **Chapter 3** provides the development of a continuum-based mathematical framework for analyzing laterally loaded monopiles in multilayered linear viscoelastic soil with hysteretic material damping, subjected to steady-state cyclic/dynamic loading using the Timoshenko beam theory. It is shown that the framework can be progressively reduced to obtain monopile response following the Rayleigh, Euler-Bernoulli, and rigid beam theory. The results obtained from the present analysis following different beam theories are verified with the results of existing solutions available in the literature. Further, the applicability of the dynamic analysis to estimate monopile response at a cyclic/dynamic loading frequency of less than 1.0 Hz is also investigated.
- **Chapter 4** provides the development of a continuum-based framework for analyzing laterally loaded monopiles in a multilayered nonlinear elastic soil, subjected to static loading using the Euler-Bernoulli beam theory. The mathematical accuracy and computational efficiency of this analysis are compared with 3-D FE analysis. Further, the accuracy of the present analysis is validated with predicted results obtained from the *p-y* analysis and measured response from full-scale field pile-load tests for a few case studies in clayey and sandy soil deposit, available in the literature. To assess the applicability of the present nonlinear elastic approach in predicting monopile response, the results obtained from the present analysis are also compared with the results of equivalent 3-D FE simulations using a linear elastic-perfectly plastic constitutive model and the *p-y*

analysis. A comparison of the computational time from the present nonlinear elastic approach, linear elastic-perfectly plastic FE analysis, and the *p-y* analysis is also shown.

- **Chapter 5** demonstrates a preliminary step-by-step design procedure for laterally loaded monopiles using the nonlinear elastic analysis developed in **Chapter 4**.
- **Chapter 6** provides the conclusions resulting from the present work along with recommendations for future research.

CHAPTER 2

Static Analysis of Laterally Loaded Monopiles in Multilayered Elastic Soil

2.1 Introduction

In this chapter, the mathematical framework for the static analysis of laterally loaded monopiles embedded in a multilayered soil deposit is presented. In the analysis, the soil is modeled as a 3-D elastic continuum and the monopile is modeled following the Timoshenko beam theory. Rational soil displacement functions are assumed and the principle of minimum potential energy is applied to obtain the differential equations describing the monopile and soil displacements. The differential equations governing monopile and soil displacements are solved analytically and numerically, respectively, following an iterative algorithm. Further, it is shown that the framework can be simplified to obtain monopile response following the Euler-Bernoulli and rigid beam theories.

The results (pile displacement and rotation) obtained from the present analysis following different beam theories are compared with the results of equivalent 3-D FE analysis for several cases of small-diameter piles and large-diameter monopiles. The difference in the prediction of pile and monopile response following different beam theories from the present analysis with that of equivalent 3-D FE analysis is quantified. Besides, recommendations on the use of different beam theories for modeling monopiles following different beam theories are also made. Further, a comparison of the computational time required to obtain pile and monopile response between different beam theories and equivalent 3-D FE analysis is also shown.

2.2 Overview of existing formulations for static analysis of laterally loaded piles in elastic soil

There are several computational algorithms with varying degree of sophistication available in the literature, for estimating pile response embedded in homogeneous, heterogeneous, and multilayered elastic soil deposit and subjected to static lateral loading. These methods can be categorized into three major groups: (i) Winkler type subgrade-reaction based analytical formulation (Reese and Matlock 1956, Matlock and Reese 1960, Vesic 1961,

Davisson and Gill 1963, Gill 1968, Alizadeh and Davisson 1970, Carter 1984, Bowles 1996, Ashford and Juirnarongrit 2003, Salgado 2008), (ii) continuum-based 3-D semi-analytical boundary element (BE) (Poulos 1971, Banerjee and Davies 1978, Ai et al. 2017) formulation based on Mindlin's fundamental solution (Mindlin 1936) and the numerical FE (Desai and Appel 1976, Kuhlemeyer 1979, Randolph 1981, Chow 1987, Carter and Kulhawy 1992, Higgins et al. 2013) formulation, and (iii) approximate continuum-based analytical and semi-analytical formulation using variational calculus (Sun 1994, Guo and Lee 2001, Shen and Teh 2004, Yang and Liang 2006, Basu et al. 2009).

Of the various formulations available, the Winkler type subgrade-reaction based formulations for laterally loaded piles (derived from beams on an elastic foundation (BEF)) are the most popular and widely used by geotechnical engineers because these approaches are easy to understand and use, mathematically convenient, and computationally inexpensive. In this formulation, the soil is represented by a series of independent, 1-D, linear elastic springs characterized by the coefficient of subgrade-reaction k (unit is F/L^2; F is force and L is length) at distinct locations along the pile length where the soil reaction force per unit length p (unit is F/L) at any point is proportional to the pile displacement y (unit is L) at that point; the relationship between p and y is mathematically expressed as $p = k \times y$. Majority of the research in this formulation has been devoted towards developing simple correlations to quantify k (representing the compressional resistance of soil) as a function of the pile radius and the Young's modulus and Poisson's ratio of soil (e.g., Vesic 1961, Carter 1984, Ashford and Juirnarongrit 2003, Salgado 2008), such that an analytical solution of the fourth-order linear differential equation governing pile displacement can be obtained. This requires parameter calibration from laboratory or full-scale experiments (e.g., Gill 1960, Alizadeh and Davisson 1970, Salgado 2008) on laterally loaded piles such that the pile response can be predicted accurately; however, these correlations are not rigorous enough to be used in the routine geotechnical design. Besides, in this formulation the soil is characterized by k i.e., a one-parameter foundation model and it neglects the shear interaction (characterized by the soil parameter t) between adjacent Winkler springs which are referred to as the two-parameter foundation model in the BEF literature (Filonenko-Borodich 1946, Pasternak 1954, Vlasov and Leont'ev 1966, Vallabhan and Das 1991).

The numerical (BE and FE) formulations where the soil is modeled as a continuum are conceptually superior to the Winkler-based formulations because they account for the true interaction (both the soil parameters *k* and *t*) between the pile and soil, however, in these formulations the mathematics involved is often too complex which perhaps makes the formulations unattractive, the algorithm computationally expensive, and not quite useful for routine geotechnical practice. The advantage of the approximate continuum-based formulations is that these formulations have the ability to capture the important aspect of the mechanics of the problem and predict pile response without significant loss of accuracy, being mathematically too complex, and computationally too intensive.

In most of the aforementioned formulations, the pile is modeled as an elastic Euler-Bernoulli beam; the Euler-Bernoulli beam theory does not account for the effect of shear deformation within the beam/pile cross-section. The Euler–Bernoulli beam theory used in the formulations is applicable for modeling the bending behavior of beams (piles) with slenderness ratios (length/radius) typically greater than 20. For piles that are stubby – for example, large-diameter monopiles – the use of the Euler–Bernoulli theory is questionable, and perhaps the Timoshenko beam theory is more appropriate. The shear deformation that is likely to be non-negligible in large-diameter monopiles is not taken into account by the Euler–Bernoulli beam theory but can be captured by the Timoshenko beam theory (Shames & Dym 1985). The use of the Timoshenko beam theory may be particularly necessary for monopiles supporting offshore wind turbines because these piles have low slenderness ratio of 10 – 12 (Klinkvort & Hededal 2014) and very large diameters in the range of 4 – 6 m, with future installations planned with diameters as large as 7·5 – 10 m (Byrne et al. 2015). In fact, the rigid beam theory may also be applicable for monopiles subjected to lateral loads because, sometimes, the monopiles undergo rigid body rotation (Abdel-Rahman & Achmus 2005, Klinkvort & Hededal 2013). Rigid body motion is also possible for large-diameter stubby drilled shafts and bored piles as well if the stiffness of the surrounding soil is much less compared with the stiffness of the pile (Yang & Liang 2006).

In this chapter, an approximate continuum-based formulation for the static analysis of laterally loaded monopiles following the Timoshenko beam theory in multilayered elastic soil is presented. This formulation is an extension of an existing analysis framework on static analysis of laterally loaded piles following the Euler–Bernoulli beam theory (Basu et al. 2009).

In the present analysis, it is shown that the new formulation offers a generalized framework which under simplified assumptions, leads to monopiles/piles modeled as Euler–Bernoulli and rigid beams. Closed-form solutions for monopile displacement, rotation, bending moment, shear force, and soil reaction are obtained considering all the three beam theories. The advantages of this formulation are (i) unlike the Winkler type subgrade-reaction based formulation, this formulation leads to a Pasternak (1954) type two-parameter subgrade-reaction based representation of the soil in which the Winkler soil springs are coupled through shear interaction between them, (ii) the values of the soil spring constant k and shear parameter t of the two-parameter model are not assigned *a priori* but are rather an outcome of the analysis, (iii) the mathematics involved in this formulation is comparatively simpler in comparison to the BE and FE formulations which makes the solution process tractable and computationally inexpensive, and (iv) this formulation can be extended to obtain response of piles/monopiles embedded in a viscoelastic soil subjected to dynamic loading (discussed in Chapter 3) and to account for soil nonlinearity (discussed in Chapter 4).

2.3 Mathematical Formulation

2.3.1 Problem definition

Figure 2.1 shows a hollow circular monopile modeled as Timoshenko beam embedded in a multilayered elastic soil deposit. The monopile has a length L_p, radius r_p, wall thickness t_p {= 6.35 + (2 × r_p)/100 mm (API 2011)}, area of cross-section A_p, and second moment of inertia I_p. The monopile is characterized by its shear modulus G_p [= E_p/{2 × (1 + ν_p)}] where E_p is Young's modulus and ν_p is the Poisson's ratio of the monopile. The soil layers are characterized by the Lame's constants λ_{si} [= $E_{si}\nu_{si}$/{(1 + ν_{si})(1 − 2ν_{si})}] and G_{si} [= E_{si}/{2 × (1 + ν_{si})}] where E_{si} is Young's modulus and ν_{si} is the Poisson's ratio of the i^{th} layer. The thickness of any i^{th} layer is given by $H_i - H_{i-1}$ (with $H_0 = 0$). Each layer has an infinite radial extent and the bottom n^{th} layer has an infinite vertical extent in the downward direction.

No slippage or separation between the monopile and the surrounding soil or between the soil layers is allowed in the analysis. A cylindrical r-θ-z coordinate system is chosen for analysis (shown in Figure 2.1). The monopile head is flush with the ground surface and the loading on the wind turbine structure (shown in Figure 1.1) is modeled as a concentrated

horizontal force F_a and/or moment M_a at the monopile head. The goal of the analysis is to obtain monopile response – displacement w, rotation dw/dz, bending moment M, and soil reaction p – as a function of depth z, under the action of the applied loading.

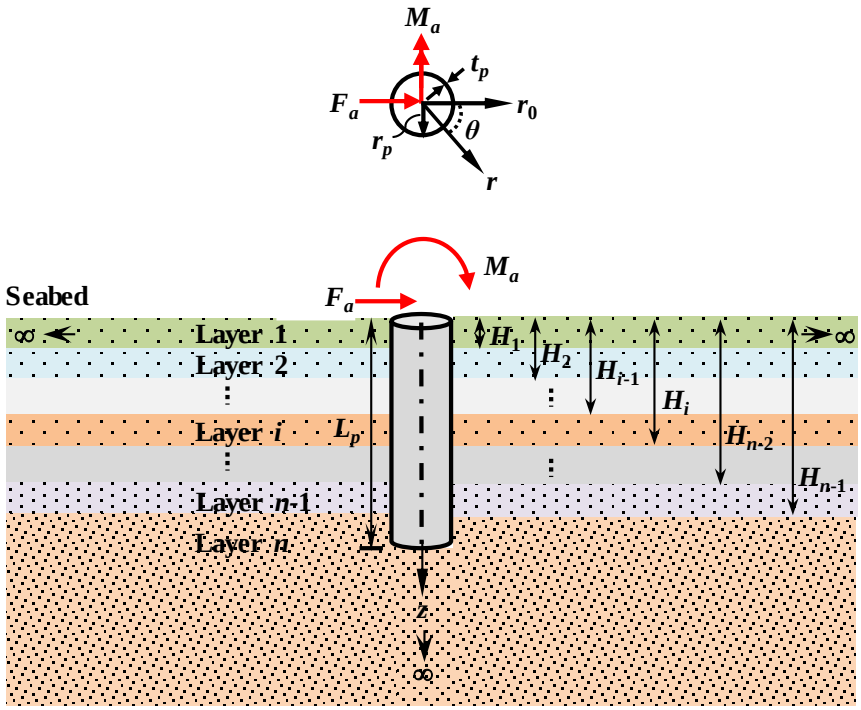

Figure 2.1: A monopile embedded in a multilayered elastic soil deposit and subjected to static lateral loads

2.3.2 Displacements, strain, and strain energy density in soil

The horizontal soil displacements generated by the monopile displacement $w(z)$ is described as a product of three separable functions each of which varies with one of the three dimensions. The vertical soil displacement u_z is assumed to be negligible because the effect of vertical displacement on the horizontal response of piles has been found to be negligible by several researchers like Tajimi (1969), Nogami and Novak (1977), Novak and Nogami (1977), and Mylonakis (2001). Mathematically, the horizontal soil displacements u_r and u_θ are expressed as (Basu et al. 2009)

$$u_r(r,\theta,z) = w(z)\phi_r(r)\cos\theta \tag{2.1}$$

$$u_\theta(r,\theta,z) = -w(z)\phi_\theta(r)\sin\theta \tag{2.2}$$

where ϕ_r and ϕ_θ are dimensionless functions in the radial and tangential directions and are functions of the radial coordinate that are both assumed to be equal to 1.0 at $r = r_p$ (ensures perfect contact between monopile and soil) and are both assumed to be equal to zero at $r = \infty$ (ensures that the soil displacements because of monopile movement decreases with increase in radial distance from the monopile and eventually become zero). The sine and cosine functions ensure that the variation of the soil displacements in the tangential direction is compatible with the horizontal monopile displacement.

Using the soil displacement field, the infinitesimal soil strains (with contractive strains assumed positive) is expressed as

$$\begin{bmatrix} \varepsilon_{rr} \\ \varepsilon_{\theta\theta} \\ \varepsilon_{zz} \\ \varepsilon_{r\theta} \\ \varepsilon_{rz} \\ \varepsilon_{\theta z} \end{bmatrix} = \begin{bmatrix} -\dfrac{\partial u_r}{\partial r} \\ -\dfrac{u_r}{r} - \dfrac{1}{r}\dfrac{\partial u_\theta}{\partial \theta} \\ -\dfrac{\partial u_z}{\partial z} \\ -\dfrac{1}{2}\left(\dfrac{1}{r}\dfrac{\partial u_r}{\partial \theta} + \dfrac{\partial u_\theta}{\partial r} - \dfrac{u_\theta}{r}\right) \\ -\dfrac{1}{2}\left(\dfrac{\partial u_z}{\partial r} + \dfrac{\partial u_r}{\partial z}\right) \\ -\dfrac{1}{2}\left(\dfrac{1}{r}\dfrac{\partial u_z}{\partial \theta} + \dfrac{\partial u_\theta}{\partial z}\right) \end{bmatrix} = \begin{bmatrix} -w(z)\dfrac{d\phi_r(r)}{dr}\cos\theta \\ -w(z)\dfrac{\phi_r(r) - \phi_\theta(r)}{r}\cos\theta \\ 0 \\ \dfrac{1}{2}w(z)\left\{\dfrac{\phi_r(r) - \phi_\theta(r)}{r} + \dfrac{d\phi_\theta(r)}{dr}\right\}\sin\theta \\ -\dfrac{1}{2}\dfrac{dw(z)}{dz}\phi_r(r)\cos\theta \\ \dfrac{1}{2}\dfrac{dw(z)}{dz}\phi_\theta(r)\sin\theta \end{bmatrix} \tag{2.3}$$

Further, using the stress-strain relationship, the strain energy density $\sigma_{pq}\varepsilon_{pq}/2$ (σ_{pq} and ε_{pq} are soil stress and strain tensors and the summation is implied by the repetition of the indices p and q) of soil is given by

$$\begin{aligned} U_D = \frac{1}{2}\Bigg[& \left(\lambda_s + 2G_s\right) w^2 \left(\frac{d\phi_r}{dr}\right)^2 + 2\lambda_s w^2 \frac{d\phi_r}{dr}\frac{\left(\phi_r - \phi_\theta\right)}{r} + \left(\lambda_s + 3G_s\right) w^2 \frac{\left(\phi_r - \phi_\theta\right)^2}{r^2} \\ & + G_s w^2 \left(\frac{d\phi_\theta}{dr}\right)^2 + 2G_s w^2 \frac{\left(\phi_r - \phi_\theta\right)}{r}\frac{d\phi_\theta}{dr} + G_s \left(\frac{dw}{dz}\right)^2 \phi_r^2 + G_s \left(\frac{dw}{dz}\right)^2 \phi_\theta^2 \Bigg] \end{aligned} \tag{2.4}$$

2.3.3 Minimization of potential energy of the monopile - soil system

The potential energy of the monopile-soil system with the monopile modeled as Timoshenko beam subjected to a force F_a and/or moment M_a at the head (Figure 2.1), is given as

$$\Pi = \int_0^{L_p} \frac{1}{2} E_p I_p \left(\frac{d\psi}{dz} \right)^2 dz + \int_0^{L_p} \frac{1}{2} G_p A_p \beta^2 dz + \int_{\Omega_0} U_D d\Omega - F_a \, w\big|_{z=0} + M_a \, \psi\big|_{z=0} \tag{2.5}$$

where the first integral in the right hand side of equation (2.5) is the strain energy of the monopile arising from the bending deformation such that ψ is the bending slope of monopile axis, the second integral is the strain energy of the monopile arising from the shearing deformation such that β is the slope of monopile axis because of shear deformation, and the third integral represents the total strain energy of the soil domain; Ω_0 being the appropriate soil domain that participates in the monopile-soil interaction (Ω_0 encompasses a volume theoretically extending to infinite distances in all radial directions from the monopile axis and in the downward vertical direction from the monopile base, except the cylindrical volume occupied by the monopile). The external work done by the applied force F_a and moment M_a at the monopile head is given by the other two terms.

According to the Timoshenko beam theory $\psi(z)$ is the slope due to bending deformation and $\beta(z)$ is the slope due to shear deformation, therefore the total slope $dw/dz = \psi(z) + \beta(z)$ (Shames and Dym 1985). The theory assumes that the shear strain is constant at all points over a cross-section of the beam which is not true and incurs an error. Therefore, a correction factor κ was introduced by Cowper (1966) based on the theory of elasticity to account for the non-uniform shear strain distribution along a cross-section of the beam and still retain the simple theory of Timoshenko beam. According to Cowper, for a hollow circular cross-section, the shear correction factor is given by $\kappa [= 6 \times \{(1 + \nu_p)(1 + r_a^2)\}/\{(7 + 6\nu_p) \times (1 + r_a^2)^2 + (20 + 6\nu_p) \times r_a^2\}]$, where r_a is the ratio of inner radius to outer radius of the circular hollow cross-section.

Substituting $\beta(z) = dw/dz - \psi(z)$ and including the correction factor κ, equation (2.5) is rewritten as

$$\Pi = \int_0^{L_p} \frac{1}{2} E_p I_p \left(\frac{d\psi}{dz} \right)^2 dz + \int_0^{L_p} \frac{1}{2} \kappa G_p A_p \left(\frac{dw}{dz} - \psi \right)^2 dz + \int_{\Omega_0} U_D d\Omega - F_a \, w\big|_{z=0} + M_a \, \psi\big|_{z=0} \tag{2.6}$$

A mechanical system in equilibrium has minimum potential energy. Therefore, minimizing the total potential energy of the monopile-soil system (i.e., setting the first variation of the potential energy $\delta\Pi$ equal to 0) leads to the required differential equations governing the equilibrium of the monopile-soil system. Considering a layered system, setting $\delta\Pi = 0$ in equation (2.6) after substituting U_D from equation (2.4) results in

$$
\begin{aligned}
\delta\Pi = &\sum_{i=1}^{n}\int_{H_{i-1}}^{H_i}\left[E_pI_p\frac{d\psi_i}{dz}\delta\left(\frac{d\psi_i}{dz}\right)+\kappa G_pA_p\left(\frac{dw_i}{dz}-\psi_i\right)\delta\left(\frac{dw_i}{dz}-\psi_i\right)\right]dz\\
&+\pi\sum_{i=1}^{n}\int_{H_{i-1}}^{H_i}\int_{r_p}^{\infty}\left[\left\{\left(\lambda_{si}+2G_{si}\right)\left(\frac{d\phi_r}{dr}\right)^2+2\lambda_{si}\frac{1}{r}\frac{d\phi_r}{dr}+\left(\lambda_{si}+3G_{si}\right)\left(\phi_r-\phi_\theta\right)^2\frac{1}{r^2}\right.\right.\\
&\left.\left.+G_{si}\left(\frac{d\phi_\theta}{dr}\right)^2+2G_{si}\left(\phi_r-\phi_\theta\right)\frac{1}{r}\frac{d\phi_\theta}{dr}\right\}w_i\delta w_i+G_{si}\left\{\phi_r^2+\phi_\theta^2\right\}\frac{dw_i}{dz}\delta\left(\frac{dw_i}{dz}\right)\right]rdrdz\\
&+\pi r_p^2\int_{L_p}^{\infty}G_{sn}\frac{dw_{n+1}}{dz}\delta\left(\frac{dw_{n+1}}{dz}\right)dz-F_a\delta w_1\big|_{z=0}+M_a\delta\psi_1\big|_{z=0}\\
&+\left\{\pi\sum_{i=1}^{n+1}\int_{H_{i-1}}^{H_i}\int_{r_p}^{\infty}\left[\left\{\lambda_{si}w_i^2\frac{1}{r}\frac{d\phi_r}{dr}+\left(\lambda_{si}+3G_{si}\right)w_i^2\frac{\phi_r}{r^2}-\left(\lambda_{si}+3G_{si}\right)w_i^2\frac{\phi_\theta}{r^2}\right.\right.\right.\\
&\left.\left.+G_{si}w_i^2\frac{1}{r}\frac{d\phi_\theta}{dr}+G_{si}\left(\frac{dw_i}{dz}\right)^2\phi_r\right\}\delta\phi_r+\left\{\left(\lambda_{si}+2G_{si}\right)w_i^2\left(\frac{d\phi_r}{dr}\right)\right.\\
&\left.\left.\left.+\lambda_{si}w_i^2\frac{\phi_r}{r}-\lambda_{si}w_i^2\frac{\phi_\theta}{r}\right\}\delta\left(\frac{d\phi_r}{dr}\right)\right]rdrdz\right\}\\
&+\pi\sum_{i=1}^{n+1}\int_{H_{i-1}}^{H_i}\int_{r_p}^{\infty}\left\{-\lambda_{si}w_i^2\frac{1}{r}\frac{d\phi_r}{dr}+\left(\lambda_{si}+3G_{si}\right)w_i^2\frac{\phi_\theta}{r^2}-\left(\lambda_{si}+3G_{si}\right)w_i^2\frac{\phi_r}{r^2}\right.\\
&-G_{si}w_i^2\frac{1}{r}\frac{d\phi_\theta}{dr}+G_{si}\left(\frac{dw_i}{dz}\right)^2\phi_\theta\Big\}\delta\phi_\theta+\left\{G_{si}w_i^2\frac{d\phi_\theta}{dr}+G_{si}w_i^2\frac{\phi_r}{r}\right.\\
&\left.\left.-G_{si}w_i^2\frac{\phi_\theta}{r}\right\}\delta\left(\frac{d\phi_\theta}{dr}\right)\right]rdrdz=0
\end{aligned}
\tag{2.7}
$$

Note, that the n^{th} layer in equation (2.7) is artificially split into n and $n + 1$ layers. The variations of w, ψ, ϕ_r, and ϕ_θ in equation (2.7) are independent, therefore the terms associated with δw, $\delta\psi$, $\delta\phi_r$, and $\delta\phi_\theta$ must individually be equal to zero in order to satisfy equation (2.7).

2.3.4 Analytical solution of differential equations describing monopile displacement

Integrating by parts the terms associated $\delta(dw/dz)$ and $\delta(d\psi/dz)$ in equation (2.7), then collecting all the terms associated with δw and $\delta\psi$ and equating them to zero results in the differential equations of $w(z)$ and $\psi(z)$. A set of coupled differential equations of $w(z)$ and $\psi(z)$ for the i^{th} layer is obtained for the domain $0 \le z \le L_p$ as

$$E_p I_p \frac{d^2\psi_i}{dz^2} + \kappa G_p A_p \left(\frac{dw_i}{dz} - \psi_i \right) = 0 \tag{2.8}$$

$$\kappa G_p A_p \left(\frac{d\psi_i}{dz} - \frac{d^2 w_i}{dz^2} \right) + k_i w_i - 2t_i \frac{d^2 w_i}{dz^2} = 0 \tag{2.9}$$

where $w_i = w(z)$ and $\psi_i = \psi(z)$ within the i^{th} soil layer and the soil parameters k_i and t_i are given by

$$\begin{aligned} k_i = \pi \Bigg[& \left(\lambda_{si} + 2G_{si}\right) \int_{r_p}^{\infty} r \left(\frac{d\phi_r}{dr} \right)^2 dr + G_{si} \int_{r_p}^{\infty} r \left(\frac{d\phi_\theta}{dr} \right)^2 dr + 2\lambda_{si} \int_{r_p}^{\infty} \left(\phi_r - \phi_\theta\right) \frac{d\phi_r}{dr} dr \\ & + 2G_{si} \int_{r_p}^{\infty} \left(\phi_r - \phi_\theta\right) \frac{d\phi_\theta}{dr} dr + \left(\lambda_{si} + 3G_{si}\right) \int_{r_p}^{\infty} \frac{1}{r} \left(\phi_r - \phi_\theta\right)^2 dr \Bigg] \end{aligned} \tag{2.10}$$

$$t_i = \begin{cases} \dfrac{\pi}{2} G_{si} \left[\displaystyle\int_{r_p}^{\infty} \left(\phi_r^2 + \phi_\theta^2\right) r dr \right]; & i = 1, 2, \ldots, n \\ \dfrac{\pi}{2} G_{sn} \left[\displaystyle\int_{r_p}^{\infty} \left(\phi_r^2 + \phi_\theta^2\right) r dr + r_p^2 \right]; & i = n+1 \end{cases} \tag{2.11}$$

The constant k_i is analogous to the Winkler spring constant and represents the compressive resistance of soil in the i^{th} layer. The constant t_i represents the shear force between the adjacent soil springs that arise because of the differential lateral movement of the soil springs caused by the monopile displacement.

A mathematical transformation is made in terms of an auxiliary function F such that

$$w_i = \frac{F_i}{E_p I_p} - \frac{1}{\kappa G_p A_p} \frac{d^2 F_i}{dz^2} \tag{2.12}$$

$$\psi_i = \frac{1}{E_p I_p} \frac{dF_i}{dz} \tag{2.13}$$

and this results in a single differential equation by combining equations (2.8) and (2.9) as

$$\left(1+\frac{2t_i}{\kappa G_p A_p}\right)\frac{d^4F_i}{dz^4}-\left(\frac{k_i}{\kappa G_p A_p}+\frac{2t_i}{E_p I_p}\right)\frac{d^2F_i}{dz^2}+\frac{k_i}{E_p I_p}F_i=0 \tag{2.14}$$

with the corresponding relevant boundary conditions

$$\left[\left\{1+\frac{2t_1}{\kappa G_p A_p}\right\}\frac{d^3F_1}{dz^3}-\frac{2t_1}{E_p I_p}\frac{dF_1}{dz}\right]=F_a \tag{2.15a}$$

$$\frac{d^2F_1}{dz^2}=-M_a \tag{2.15b}$$

$$\left\{\frac{F_i}{E_p I_p}-\frac{1}{\kappa G_p A_p}\frac{d^2F_i}{dz^2}\right\}=\left\{\frac{F_{i+1}}{E_p I_p}-\frac{1}{\kappa G_p A_p}\frac{d^2F_{i+1}}{dz^2}\right\} \tag{2.16a}$$

$$\frac{dF_i}{dz}=\frac{dF_{i+1}}{dz} \tag{2.16b}$$

$$\left[\left\{1+\frac{2t_i}{\kappa G_p A_p}\right\}\frac{d^3F_i}{dz^3}-\frac{2t_i}{E_p I_p}\frac{dF_i}{dz}\right]=\left[\left\{1+\frac{2t_{i+1}}{\kappa G_p A_p}\right\}\frac{d^3F_{i+1}}{dz^3}-\frac{2t_{i+1}}{E_p I_p}\frac{dF_{i+1}}{dz}\right] \tag{2.16c}$$

$$\frac{d^2F_i}{dz^2}=\frac{d^2F_{i+1}}{dz^2} \tag{2.16d}$$

$$\left[\left\{1+\frac{2t_n}{\kappa G_p A_p}\right\}\frac{d^3F_n}{dz^3}-\frac{2t_n}{E_p I_p}\frac{dF_n}{dz}\right]=\sqrt{2k_n t_{n+1}}\left\{\frac{F_n}{E_p I_p}-\frac{1}{\kappa G_p A_p}\frac{d^2F_n}{dz^2}\right\} \tag{2.17a}$$

$$\frac{d^2F_n}{dz^2}=0 \tag{2.17b}$$

Equations (2.15a)-(2.15b) are applicable at the monopile head (z = 0), equations (2.16a)-(2.16d) are applicable at the interface between the i^{th} and the $(i + 1)^{\text{th}}$ layers ($z = H_i$), and equations (2.17a)-(2.17b) are applicable at the monopile base ($z = L_p$).

Closed-form solution of the differential equation representing monopile displacement (equation (2.14)) is obtained by substituting $F(z) = e^{vz}$ into the equation and obtaining a characteristic equation in terms of v. Introducing layering and evaluating the roots $v^{(i)}$ of the characteristic equation, the solution is obtained as

$$F_i(z)=C_1^{(i)}e^{v_1^{(i)}z}+C_2^{(i)}e^{-v_1^{(i)}z}+C_3^{(i)}e^{v_2^{(i)}z}+C_4^{(i)}e^{-v_2^{(i)}z} \tag{2.18}$$

where the associated exponential terms are the solutions of the differential equations, $C_1^{(i)}$, $C_2^{(i)}$, $C_3^{(i)}$, and $C_4^{(i)}$ are the integration constants for the i^{th} layer, and $v^{(i)}$ in equation (2.18) is given as

$$v_{1,2}^{(i)} = \sqrt{\frac{\left(\frac{2t_i}{E_pI_p} + \frac{k_i}{\kappa G_pA_p}\right) \pm \sqrt{\left(\frac{2t_i}{E_pI_p} + \frac{k_i}{\kappa G_pA_p}\right)^2 - \frac{4k_i}{E_pI_p}\left(1 + \frac{2t_i}{\kappa G_pA_p}\right)}}{2\left(1 + \frac{2t_i}{\kappa G_pA_p}\right)}} \tag{2.19}$$

The integrations constants for each layer are determined using the boundary conditions from equations (2.15)-(2.17). The function F is expressed in terms of the integration constants following equation (2.18) which is then used to obtain the monopile displacement w and the bending slope ψ by substituting F in equations (2.12) and (2.13), respectively.

For the domain below the monopile ($L_p \leq z \leq \infty$) the terms associated with δw_{n+1} in equation (2.7) are equated to zero. As w_{n+1} is not known *a priori* within $L_p < z < \infty$, $\delta w_{n+1} \neq 0$ because of which the integrand in the integral between $z = L_p$ and $z = \infty$ must be equal to zero. This gives the differential equation of w_{n+1}

$$2t_{n+1}\frac{d^2w_{n+1}}{dz^2} - k_n w_{n+1} = 0 \tag{2.20}$$

At infinite vertical distance down from the monopile (i.e., at $z = \infty$) $w_{n+1} = 0$ (this makes the term associated with δw_{n+1} at $z = \infty$ equal to zero) and at the monopile base (i.e., at $z = L_p$) $w_{n+1} = w_n$. Using these boundary conditions, the solution of equation (2.20) is obtained as

$$w_{n+1} = w_n\big|_{z=L_p} e^{-\sqrt{\frac{k_n}{2t_{n+1}}}(z-L_p)} \tag{2.21}$$

2.3.5 Numerical solution of differential equations describing soil displacement

Referring back to equation (2.7), collecting the terms associated with $\delta\phi_r$ and $\delta\phi_\theta$, setting the terms associated with $\delta\phi_r$ and $\delta\phi_\theta$ at $r = r_p$ and $r = \infty$ equal to zero (since the variations of ϕ_r and ϕ_θ are known at $r = r_p$ and $r = \infty$), and within the interval $r_p < r < \infty$ (since $\delta\phi_r \neq 0$ and $\delta\phi_\theta \neq 0$ as ϕ_r and ϕ_θ is not known *a priori* within $r_p < r < \infty$) gives the following set of coupled differential equations for ϕ_r and ϕ_θ.

$$\frac{d^2\phi_r}{dr^2} + \frac{1}{r}\frac{d\phi_r}{dr} - \left[\left(\frac{\gamma_1}{r}\right)^2 + \left(\frac{\gamma_2}{r_p}\right)^2\right]\phi_r = \frac{\gamma_3^2}{r}\frac{d\phi_\theta}{dr} - \left(\frac{\gamma_1}{r}\right)^2\phi_\theta \tag{2.22a}$$

$$\frac{d^2\phi_\theta}{dr^2}+\frac{1}{r}\frac{d\phi_\theta}{dr}-\left[\left(\frac{\gamma_4}{r}\right)^2+\left(\frac{\gamma_5}{r_p}\right)^2\right]\phi_\theta=-\frac{\gamma_6^2}{r}\frac{d\phi_r}{dr}-\left(\frac{\gamma_4}{r}\right)^2\phi_r \tag{2.22b}$$

where γ_1-γ_6 are dimensionless constants given by

$$\gamma_x=\sqrt{\frac{\sum_{i=1}^{n}A_i\int_{H_{i-1}}^{H_i}w_i^2dz+A_n\sqrt{\frac{t_{n+1}}{2k_{n+1}}}w_n^2\Big|_{z=L_p}}{\sum_{i=1}^{n}B_i\int_{H_{i-1}}^{H_i}w_i^2dz+B_n\sqrt{\frac{t_{n+1}}{2k_{n+1}}}w_n^2\Big|_{z=L_p}}} \qquad (x=1,3,4,6) \tag{2.23a}$$

$$\gamma_x=\sqrt{\frac{\sum_{i=1}^{n}A_i\int_{H_{i-1}}^{H_i}\left(\frac{dw_i}{dz}\right)^2dz+A_n\sqrt{\frac{k_n}{8t_{n+1}}}w_n^2\Big|_{z=L_p}}{\sum_{i=1}^{n}B_i\int_{H_{i-1}}^{H_i}w_i^2dz+B_n\sqrt{\frac{t_{n+1}}{2k_n}}w_n^2\Big|_{z=L_p}}} \qquad (x=2,5) \tag{2.23b}$$

in which $A_i = (\lambda_{si} + 3G_{si})$ for x = 1 and 4, $A_i = G_{si}$ for x = 2 and 5, and $A_i = (\lambda_{si} + G_{si})$ for x = 3 and 6; while $B_i = (\lambda_{si} + 2G_{si})$ for x = 1, 2, and 3, and $B_i = G_{si}$ for x = 4, 5, and 6.

The differential equations of ϕ_r and ϕ_θ (equations (2.22a) and (2.22b)) are interdependent and solved simultaneously using a 1-D FD scheme. The discretized forms of the differential equations are given as

$$\frac{\phi_r^{l+1}-2\phi_r^l+\phi_r^{l-1}}{\Delta r^2}+\frac{1}{r_l}\frac{\phi_r^{l+1}-\phi_r^{l-1}}{2\Delta r}-\left[\left(\frac{\gamma_1}{r_l}\right)^2+\left(\frac{\gamma_2}{r_p}\right)^2\right]\phi_r^l=\frac{\gamma_3^2}{r_l}\frac{\phi_\theta^{l+1}-\phi_\theta^{l-1}}{2\Delta r}-\left(\frac{\gamma_1}{r_l}\right)^2\phi_\theta^l \tag{2.24a}$$

$$\frac{\phi_\theta^{l+1}-2\phi_\theta^l+\phi_\theta^{l-1}}{\Delta r^2}+\frac{1}{r_l}\frac{\phi_\theta^{l+1}-\phi_\theta^{l-1}}{2\Delta r}-\left[\left(\frac{\gamma_4}{r_l}\right)^2+\left(\frac{\gamma_5}{r_p}\right)^2\right]\phi_\theta^l=-\frac{\gamma_6^2}{r_l}\frac{\phi_r^{l+1}-\phi_r^{l-1}}{2\Delta r}-\left(\frac{\gamma_4}{r_l}\right)^2\phi_r^l \tag{2.24b}$$

where the superscript l represents the node number at a radial distance r_l from the monopile edge and Δr is the discretization length (i.e., the distance between two consecutive nodes) (see Figure 2.2). The 1-D FD grid has its first node at the monopile-soil boundary (i.e., at $r = r_p$) and is chosen sufficiently long and dense so as to allow proper attenuation of the displacement functions for accurate results (i.e., Δr is chosen sufficiently small, and the total number of finite difference nodes m is taken sufficiently large so that $m\Delta r \to \infty$).

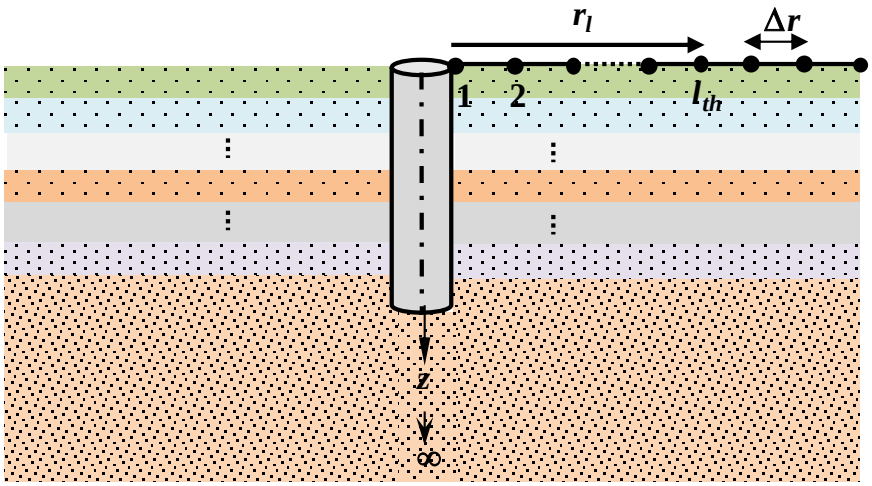

Figure 2.2: Finite difference discretization along the radial direction for calculation of soil displacement functions

Equations (2.24a) and (2.24b) when rewritten for nodes 2 through (m – 1) (i.e., excluding the 1st and the m^{th} nodes at which the values of ϕ_r and ϕ_θ are known) generate two sets of simultaneous equations with each set containing m – 2 equations. These sets of equations can be represented in the matrix form as

$$\left[X^{\phi_r}\right]\{\phi_r\} = \left\{Y^{\phi_\theta}\right\} \tag{2.25a}$$

$$\left[X^{\phi_\theta}\right]\{\phi_\theta\} = \left\{Y^{\phi_r}\right\} \tag{2.25b}$$

where $[X^{\phi r}]_{(m-2)\times(m-2)}$ and $[X^{\phi\theta}]_{(m-2)\times(m-2)}$ are the tri-diagonal matrices with FD coefficients of the unknown vectors $\{\phi r\}_{(m-2)\times 1}$ and $\{\phi\theta\}_{(m-2)\times 1}$, respectively, and $\{Y^{\phi r}\}_{(m-2)\times 1}$ and $\{Y^{\phi\theta}\}_{(m-2)\times 1}$ are the corresponding right-hand side vectors containing terms with unknowns ϕ_θ and ϕ_r, respectively.

The nonzero elements of the left-hand-side matrix $[X^{\phi r}]$ in equation (2.25a) are given by

$$\left[X^{\phi_r}\right]_{y,y-1} = \frac{1}{\Delta r^2} - \frac{1}{2r_l\Delta r} \tag{2.26a}$$

$$\left[X^{\phi_r}\right]_{y,y} = -\frac{2}{\Delta r^2} - \left[\left(\frac{\gamma_1}{r_l}\right)^2 + \left(\frac{\gamma_2}{r_p}\right)^2\right] \tag{2.26b}$$

$$\left[X^{\phi_r}\right]_{y,y+1} = \frac{1}{\Delta r^2} + \frac{1}{2r_l \Delta r} \tag{2.26c}$$

where $y = l - 1$. The y^{th} row of the corresponding $\{Y^{\phi_\theta}\}$ vector in equation (2.25a) is given by

$$\left\{Y^{\phi_\theta}\right\}_y = \frac{\gamma_3^2}{r_l}\frac{\phi_\theta^{l+1} - \phi_\theta^{l-1}}{2\Delta r} - \left(\frac{\gamma_1}{r_l}\right)^2 \phi_\theta^l \tag{2.27a}$$

The boundary conditions ($\phi_r = 1$ at node 1 and $\phi_r = 0$ at node m) modifies the 1st and $(m-2)^{\text{th}}$ rows of $\{Y^{\phi_\theta}\}$, which is given by

$$\left\{Y^{\phi_\theta}\right\}_1 = -\frac{1}{\Delta r^2} + \frac{1}{2r_2 \Delta r} + \frac{\gamma_3^2}{r_2}\frac{\phi_\theta^{(3)} - 1}{2\Delta r} - \left(\frac{\gamma_1}{r_2}\right)^2 \phi_\theta^{(2)} \tag{2.27b}$$

$$\left\{Y^{\phi_\theta}\right\}_{m-2} = \frac{\gamma_3^2}{r_{m-1}}\frac{-\phi_\theta^{m-2}}{2\Delta r} - \left(\frac{\gamma_1}{r_{m-1}}\right)^2 \phi_\theta^{m-1} \tag{2.27c}$$

The non-zero elements of the left-hand-side matrix $[X^{\phi_\theta}]$ in equation (2.25b) are given by

$$\left[X^{\phi_\theta}\right]_{y,y-1} = \frac{1}{\Delta r^2} - \frac{1}{2r_l \Delta r} \tag{2.28a}$$

$$\left[X^{\phi_\theta}\right]_{y,y} = -\frac{2}{\Delta r^2} - \left[\left(\frac{\gamma_4}{r_l}\right)^2 + \left(\frac{\gamma_5}{r_p}\right)^2\right] \tag{2.28b}$$

$$\left[X^{\phi_\theta}\right]_{y,y+1} = \frac{1}{\Delta r^2} + \frac{1}{2r_l \Delta r} \tag{2.28c}$$

The y^{th}, 1st and $(m-2)^{\text{th}}$ rows of the vector $\{Y^{\phi_r}\}$ in equation (2.25b) are given by

$$\left\{Y^{\phi_r}\right\}_y = -\frac{\gamma_6^2}{r_l}\frac{\phi_r^{l+1} - \phi_r^{l-1}}{2\Delta r} - \left(\frac{\gamma_4}{r_l}\right)^2 \phi_r^l \tag{2.29a}$$

$$\left\{Y^{\phi_r}\right\}_1 = -\frac{1}{\Delta r^2} + \frac{1}{2r_2 \Delta r} - \frac{\gamma_6^2}{r_2}\frac{\phi_r^{(3)} - 1}{2\Delta r} - \left(\frac{\gamma_4}{r_2}\right)^2 \phi_r^{(2)} \tag{2.29b}$$

$$\left\{Y^{\phi_r}\right\}_{m-2} = -\frac{\gamma_3^2}{r_{m-1}}\frac{-\phi_r^{m-2}}{2\Delta r} - \left(\frac{\gamma_4}{r_{m-1}}\right)^2 \phi_r^{m-1} \tag{2.29c}$$

As the right-hand vectors in equations (2.25a) and (2.25b) contain the unknowns ϕ_r and ϕ_θ, iterations are necessary to obtain their values. An initial estimate of ϕ_r is made and given as input to $\{Y^{\phi_r}\}$, and ϕ_θ is determined by solving equation (2.25b). The calculated ϕ_θ values are then given as input to $\{Y^{\phi_\theta}\}$ to obtain ϕ_r from equation (2.25b). The newly obtained values

of ϕ_r are again used to obtain new values of ϕ_θ, and these iterations are continued until convergence is reached. The criteria set for convergence are $\frac{1}{m}\sum_{l=1}^{m}\left|\phi_r^{\,l\,\text{previous}}-\phi_r^{\,l\,\text{current}}\right|\le 10^{-6}$ and $\frac{1}{m}\sum_{l=1}^{m}\left|\phi_r^{\,l\,\text{previous}}-\phi_r^{\,l\,\text{current}}\right|\le 10^{-6}$ where $\phi^{\,l\,\text{previous}}$ and $\phi^{\,l\,\text{current}}$ are the values of the ϕ functions (i.e., ϕ_r and ϕ_θ) at the l^{th} node for the previous and current iterations, respectively.

2.3.6 Solution algorithm

Monopile displacement and slope can be calculated from equations (2.12) and (2.13), respectively. However, the soil parameters k_i and t_i must be known to obtain the monopile displacement and slope. The parameters k_i and t_i depend on the functions ϕ_r and ϕ_θ which in turn depend on w through the six dimensionless constants γ_1-γ_6. Therefore, an iterative algorithm is followed to obtain the solutions.

An initial guess of 1.0 is made for γ_1-γ_6 using which ϕ_r and ϕ_θ are determined, which are then substituted in equations of k_i and t_i to obtain their values. Using the calculated values of k_i and t_i, monopile displacements and slopes are calculated. The calculated monopile displacements and slopes are then used to calculate γ_1-γ_6 which are compared with the assumed initial values. If the differences are more than the prescribed tolerable limit of 0.001, the calculations described so far are repeated with the calculated values of γ_1-γ_6 as the new initial guesses. Iterations are continued until the values of γ_1-γ_6 between successive iterations fall below the prescribed limit. Figure 2.3 illustrates the solution algorithm to obtain the solution which is implemented in a MATLAB script on a computer with Intel® Core™ i5-3210M CPU @ 2.50 GHz and 8 GB RAM.

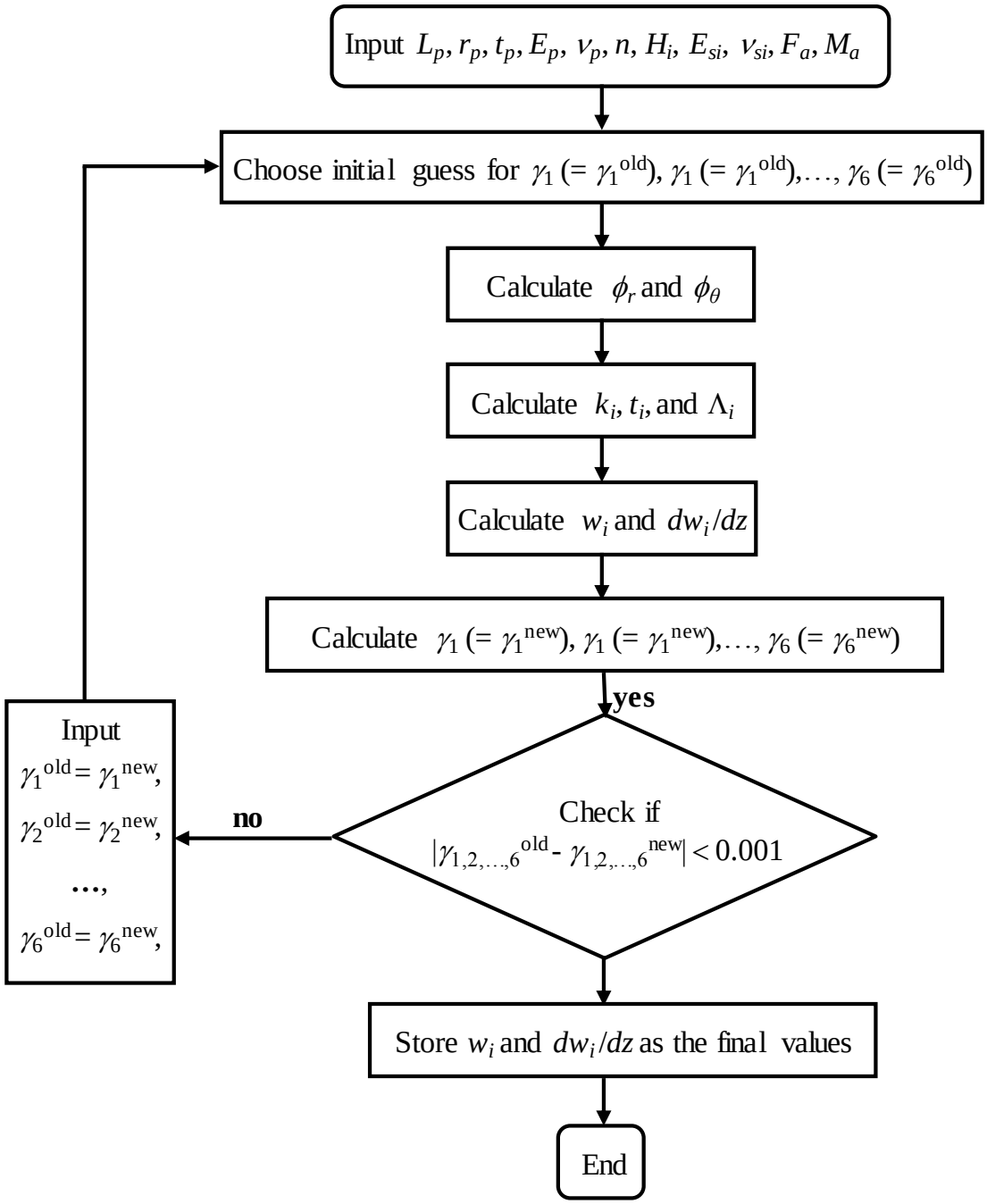

Figure 2.3: Solution algorithm

2.4 Simplification of analysis to Euler-Bernoulli beam theory

The Euler-Bernoulli beam theory neglects shear deformation which can be mathematically implemented by assuming infinite shear stiffness in the monopile. Indeed, if it is assumed that $G_p \rightarrow \infty$, then the second term on the right hand side of equation (2.12) becomes zero so that the relationships $F(z) = E_p I_p w(z)$ and $\psi(z) = dw(z)/dz$ are obtained from

equations (2.12) and (2.13), respectively. Further, equation (2.14) simplifies to the differential equation governing the monopile displacement *w* that follows the Euler-Bernoulli beam theory (the terms containing G_p in the denominator becomes equal to zero). Similarly, the associated boundary conditions that are given by equations (2.15a)-(2.17b) simplify to the boundary conditions applicable to a monopile following the Euler-Bernoulli beam theory.

The corresponding differential equation for monopile displacement following the Euler-Bernoulli beam theory

$$E_p I_p \frac{d^4 w_i}{dz^4} - 2t_i \frac{d^2 w_i}{dz^2} + k_i w_i = 0 \tag{2.30}$$

with the relevant boundary conditions at different layer interface given by

$$E_p I_p \frac{d^3 w_1}{dz^3} - 2t_1 \frac{dw_1}{dz} = F_a \tag{2.31a}$$

$$E_p I_p \frac{d^2 w_1}{dz^2} = -M_a \tag{2.31b}$$

$$w_i = w_{i+1} \tag{2.32a}$$

$$\frac{dw_i}{dz} = \frac{dw_{i+1}}{dz} \tag{2.32b}$$

$$\left[E_p I_p \frac{d^3 w_i}{dz^3} - 2t_i \frac{dw_i}{dz} \right] = \left[E_p I_p \frac{d^3 w_{i+1}}{dz^3} - 2t_{i+1} \frac{dw_{i+1}}{dz} \right] \tag{2.32c}$$

$$\frac{d^2 w_i}{dz^2} = \frac{d^2 w_{i+1}}{dz^2} \tag{2.32d}$$

$$\left[E_p I_p \frac{d^3 w_n}{dz^3} - 2t_n \frac{dw_n}{dz} \right] = \sqrt{2k_n t_{n+1}} w_n \tag{2.33a}$$

$$\frac{d^2 w_n}{dz^2} = 0 \tag{2.33b}$$

Closed-form solution of the differential equation representing monopile displacement (equation (2.30)) is obtained by substituting $w(z) = e^{sz}$ into the equation and obtaining a characteristic equation in terms of *s*. Introducing layering and evaluating the roots $s^{(i)}$ of the characteristic equation, the solution is obtained as

$$w_i(z) = D_1^{(i)} e^{s_1^{(i)} z} + D_2^{(i)} e^{-s_1^{(i)} z} + D_3^{(i)} e^{s_2^{(i)} z} + D_4^{(i)} e^{-s_2^{(i)} z} \tag{2.34}$$

where the associated exponential terms are the solutions of the differential equations, $D_1^{(i)}$, $D_2^{(i)}$, $D_3^{(i)}$, and $D_4^{(i)}$ are the integration constants for the i^{th} layer and $s^{(i)}$ in equation (2.34) is given as

$$s^{(i)} = \sqrt{\frac{\frac{2t_i}{E_p I_p} \pm \sqrt{\left(\frac{2t_i}{E_p I_p}\right)^2 - \frac{4k_i}{E_p I_p}}}{2}} \tag{2.35}$$

The integration constants are determined and the function $w(z)$ is expressed in terms of the integration constants at different layer boundaries to obtain the monopile displacement, slope, bending moment, shear force, and soil reaction.

2.5 Simplification of analysis to rigid beam theory

For rigid monopiles, the displacement profile is linear (as there is no deformation present in the monopile) so that the monopile displacement can be given by

$$w(z) = w_h - \psi_h z \tag{2.36}$$

where ψ_h is the clockwise rotation of the monopile axis that remains constant with depth. Although equation (2.36) is assumed *a priori*, it does not violate the analysis framework developed in this study following the variational principles of mechanics (by minimizing the total potential energy) because, if a function is known *a priori*, it can be substituted in the framework without developing its governing differential equations. Equations (2.22)-(2.29) are also valid for rigid piles.

Because of the assumed linear monopile displacement profile, direct algebraic equations for monopile head displacement w_h and rotation ψ_h can be developed following the rigid beam theory as shown below

$$\begin{Bmatrix} w_h \\ \psi_h \end{Bmatrix} = \begin{bmatrix} \sum_{i=1}^{n} \int_{H_{i-1}}^{H_i} k_i dz + \sqrt{2k_n t_{n+1}} & -\sum_{i=1}^{n} \int_{H_{i-1}}^{H_i} k_i z dz - 2t_n - \sqrt{2k_n t_{n+1}} L_p \\ -\sum_{i=1}^{n} \int_{H_{i-1}}^{H_i} k_i z dz - \sqrt{2k_n t_{n+1}} L_p & \sum_{i=1}^{n} \int_{H_{i-1}}^{H_i} k_i z^2 dz + 2t_n L_p + \sqrt{2k_n t_{n+1}} L_p^2 \end{bmatrix}^{-1} \begin{Bmatrix} F_a \\ M_a \end{Bmatrix} \tag{2.37}$$

2.6 Calculation of secondary variables

In addition to monopile displacement, its bending moment *M*, shear force *V*, and the soil reaction *p* at the monopile-soil interface are of interest. These quantities are given by (also expressed in terms of *F*)

$$M(z) = -E_p I_p \frac{d\psi}{dz} = -\frac{d^2F}{dz^2} \tag{2.38a}$$

$$V(z) = -\kappa G_p A_p \left(\frac{dw}{dz} - \psi \right) = \frac{d^3F}{dz^3} \tag{2.38b}$$

$$p(z) = -2t\frac{d^2w}{dz^2} + kw = \frac{2t}{\kappa G_p A_p}\frac{d^4F}{dz^4} - \left(\frac{2t}{E_p I_p} - \frac{1}{\kappa G_p A_p} \right)\frac{d^2F}{dz^2} + \frac{k}{E_p I_p}F \tag{2.38c}$$

The foregoing equations are valid for Euler-Bernoulli theory as well after the required simplifications are made (by setting the terms with G_p in the denominator equal to zero and substituting $F = E_p I_p w$ and $\psi = dw/dz$). For rigid theory, bending moment, and shear force do not have much meaning, but the soil reaction is important and can be obtained from equation (2.38c) by setting d^2w/dz^2 equal to zero (because ψ is constant with depth).

For the Timoshenko theory, the shear angle β can be calculated using

$$\beta(z) = \frac{V}{\kappa G_p A_p} \tag{2.39}$$

2.7 Results

In order to verify the accuracy of the present analysis a comparison of results (pile response – displacement and rotation) obtained from the present analysis is done with the results of equivalent 3-D FE analysis for the case of small-diameter reinforced concrete piles with solid circular cross-section and large-diameter steel monopiles with a hollow circular cross-section. The percentage difference in the prediction of response between the results from the present analysis (following the Timoshenko, Euler-Bernoulli, and rigid beam theory) and those of 3-D FE analysis is quantified. A comparison of the computational time required to obtain results between the present and equivalent 3-D FE analysis is also shown. Further, a parametric study is performed for monopiles for various cases of relative monopile-soil

stiffness ratio and monopile slenderness ratio in the homogeneous soil to investigate the applicability of different beam theories for obtaining monopile response.

2.7.1 Comparison of results from present analysis with FE analysis for small-diameter reinforced concrete piles with a solid circular cross-section

In this subsection, the accuracy of the results obtained from the present analysis (following the Timoshenko and Euler-Bernoulli beam theory) is verified with the results of equivalent 3-D FE analysis (performed using Abaqus) for the case of small-diameter solid circular reinforced concrete piles with E_p = 28 GPa and ν_p = 0.2. In Abaqus, the pile and the soil are modeled as a single cylindrical part with appropriate partitioning to represent the pile and soil separately. This also ensures that there is no slippage or separation between the soil and the pile. The top soil surface is flush with the pile head and the bottom soil surface extends to a finite depth of 20 m below the pile base for the cases analyzed. The horizontal radial extent of the soil domain (i.e., the vertical curved boundary of the FE domain) for each case is considered at a distance of 20 m from the pile axis. Different boundary conditions are prescribed at the boundaries of the model – all components of displacements are assumed to be zero along the bottom (horizontal) surface and two horizontal components are assumed to be zero along the outer, curved (vertical) surface of the soil domain. Eight-node continuum reduced integration (C3D8R) elements are used, with an approximate global seed size of 0.8. The optimal domains and meshes described are obtained by performing convergence checks ensuring that there are no boundary effects. Concentrated force and moment are applied in a single increment to a reference point at the centroid of the pile head, to which all the nodes at the pile top are connected using a rigid body constraint.

Figures 2.4 and 2.5 show the comparison of the displacement and rotation profiles from the present analysis with those of equivalent 3-D FE analysis for piles in a homogeneous and three-layer soil, respectively. The details of the inputs of the pile and soil properties for both the problems analyzed are shown in the figures. The shear correction factor $\kappa = 6 \times (1 + \nu_p)/(7 + 6\nu_p)$ (Cowper 1966) (applicable to solid circular cross-section) is utilized to obtain the results from the present analysis following the Timoshenko beam theory. The comparison of results following the rigid beam theory does not make much sense for such long piles with slenderness ratio $L_p/r_p > 20$ because they do not undergo rigid body rotation. From the comparison, it is

evident that the present analysis produces accurate results in comparison to 3-D FE analysis, besides, the Timoshenko and Euler-Bernoulli beam theory in the present analysis produce nearly identical results; this indicates that the effect of shear deformation for such long piles with a solid circular cross-section is not significant. This observation is found to be true for several other analyses on solid reinforced concrete piles. For the problems shown (Figures 2.4 and 2.5) the difference in the pile head response between the present and FE analysis is approximately less than 0.5%.

A comparison of the computational (CPU processing) time required to obtain the results is also shown in Table 2.1. It can be seen from the table that the FE analysis requires a lesser computational effort to generate pile response in comparison to the present analysis; however, it is important to note that the reported time for the FE analysis does not include the time required to model the pile-soil geometry, input of the pile-soil properties, and generation of the mesh which is a tedious and time-consuming process and depends on the expertise of the user on a particular FE software. Therefore, it can be inferred that the present analysis is computationally efficient in comparison to FE analysis, since, it requires simple inputs of pile-soil data within the MATLAB script to obtain results. Further, it can also be seen from Table 2.1, that the difference in computational time between the Timoshenko and Euler-Bernoulli beam theory is also negligible; therefore, the response of small-diameter solid reinforced concrete piles can be obtained following the Euler-Bernoulli beam theory instead of the Timoshenko beam theory.

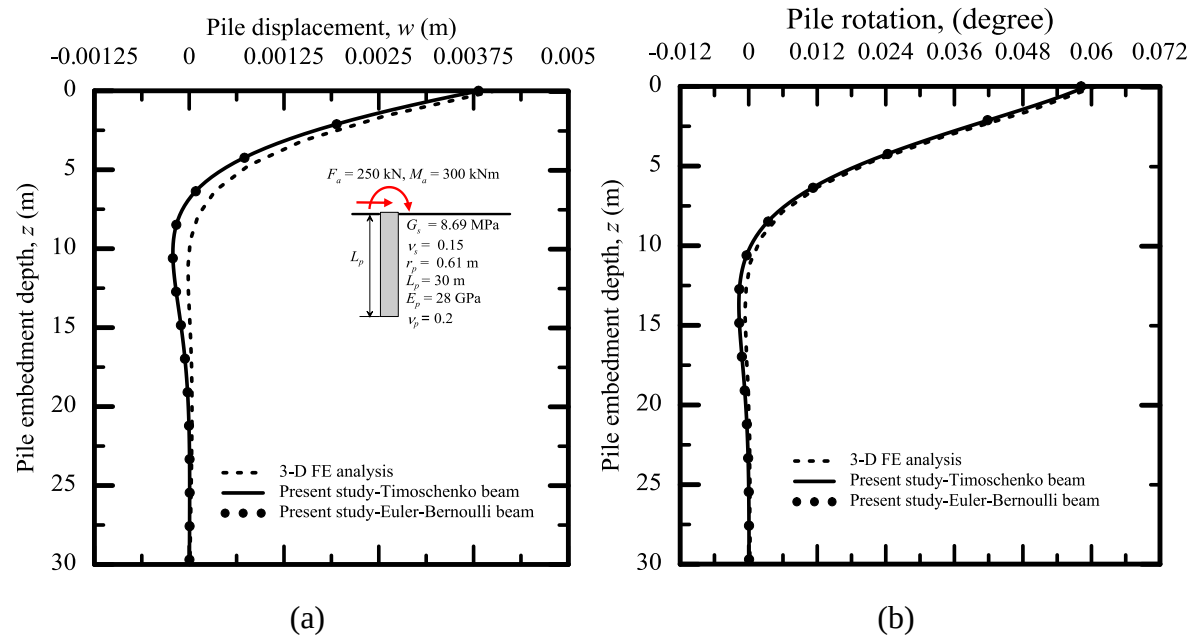

Figure 2.4: Comparison of present analysis with 3-D FE analysis for a pile with a solid cross-section of 0.61 m radius in a homogeneous soil deposit (a) displacement and (b) rotation

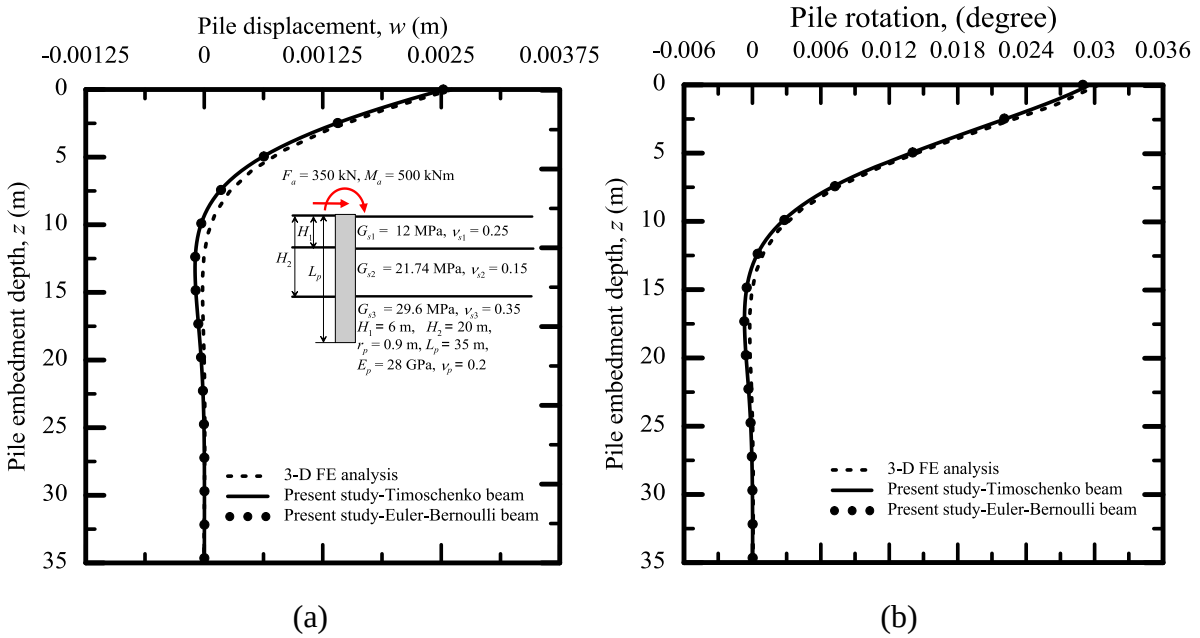

Figure 2.5: Comparison of present analysis with 3-D FE analysis for a circular pile with a solid cross-section of 0.9 m radius in a three-layered soil deposit (a) displacement and (b) rotation

Table 2.1: Computational time required for 3-D FE analysis and present analysis for small-diameter piles with a solid circular cross-section

Solved problems	FE analysis, (secs)	Present analysis, (secs)		
		Timoshenko	Euler-Bernoulli	Rigid
Figures 2.4(a)-(b)	224	244	237	-
Figures 2.5(a)-(b)	236	251	248	-

2.7.2 Comparison of results from present analysis with FE analysis for large-diameter steel monopiles with a hollow circular cross-section

The response of hollow circular steel monopiles (E_p = 210 GPa and ν_p = 0.3) obtained using the present analysis is shown in this subsection through three example problems. For each problem, the response of monopile is compared with the results of equivalent 3-D FE analysis (performed using Abaqus) in which the same inputs of monopile and soil geometry, properties, and loads are given. In Abaqus, the monopile and soil are modeled as a single cylindrical part with appropriate partitioning to represent the monopile and soil separately which ensures no slippage or separation between the soil and monopile. The top soil surface is flush with the monopile head and the bottom soil surface extends to a finite depth of 20 m below the monopile base for the cases analyzed. The horizontal radial extent of the soil domain is selected to be 80 m from the monopile axis. Different boundary conditions are prescribed at the boundaries of the model – all components of displacements are assumed to be zero along the bottom (horizontal) surface and two horizontal components are assumed to be zero along the outer curved (vertical) surface of the soil domain. Eight-noded reduced integration (C3D8R) brick elements are used to model both the soil and monopile domain. A global approximate seed size of 2.4 is chosen to develop the mesh for all the three problems, based on convergence checks. Concentrated force and moment are applied in a single load increment to a reference point at the monopile head, to which all the nodes of the monopile are connected.

Figures 2.6, 2.7, and 2.8 show the comparison of monopile response (displacement and rotation profiles) from the present analysis with those of FE analysis in a homogeneous, two-layer, and three-layer soil deposit, respectively, for three different monopile radius 2.5, 4, and, 5 m of different slenderness ratio. The details of inputs for these problems are shown in the figures. From the comparison of the results presented in Figures 2.6-2.8, it is evident that a fairly good match is obtained between the present and FE analysis for all the three example

problems solved. Four additional example problems are also analyzed in which the monopile length ranges over 20-30 m, the slenderness ratio ranges over 6-12, and one-, two-, and three-layer soil deposits are considered. Table 2.2 gives the percentage difference obtained in monopile head displacement and rotation for all the problems solved. In all these examples, it is observed that the Timoshenko beam theory produces monopile head displacement and rotation closest to the corresponding FE solutions (as evident in Figures 2.6-2.8 and Table 2.2); however, the difference between the results from Timoshenko and Euler-Bernoulli theory are not significantly different. The rigid theory is found to produce the maximum error (> 10 %) in comparison with the FE solutions.

The comparison of the computational time between the present and FE analysis is also shown in Table 2.3; it can be inferred from the comparison that the present analysis is computationally efficient than FE analysis (for similar reasons discussed for the case of solid reinforced concrete piles). The rigid beam theory generates faster results than the Timoshenko and Euler-Bernoulli beam theory, although the difference with FE analysis is greater in comparison to the Timoshenko and Euler-Bernoulli beam theory.

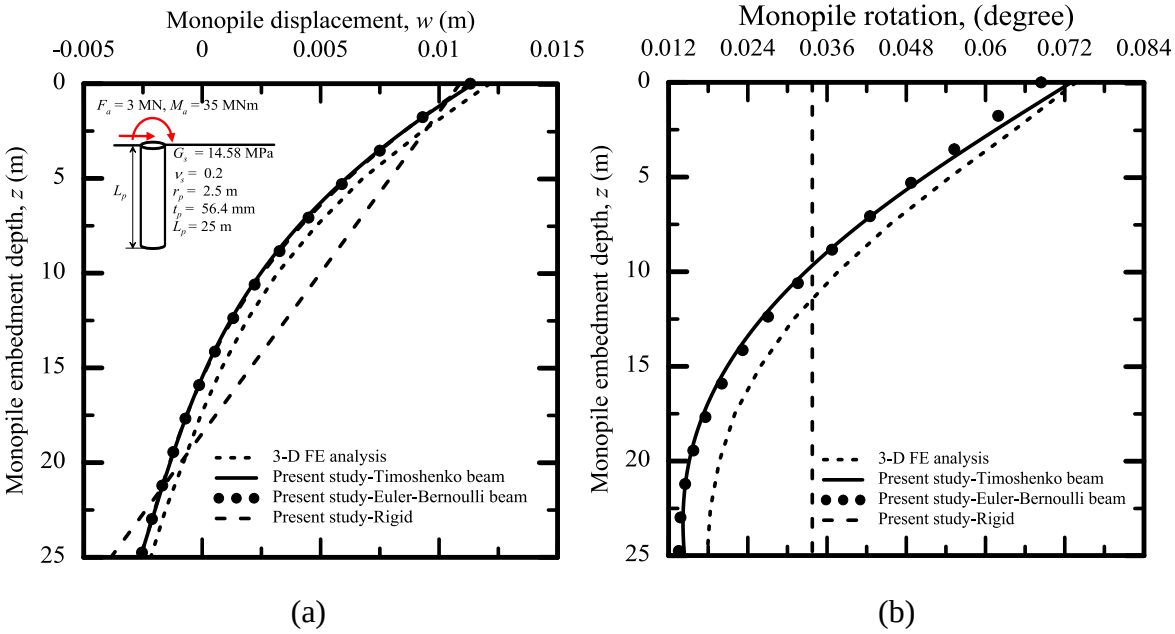

Figure 2.6: Comparison of present analysis with 3-D FE analysis for a circular monopile with a hollow cross-section of 2.5 m radius in a homogeneous soil deposit (a) displacement and (b) rotation

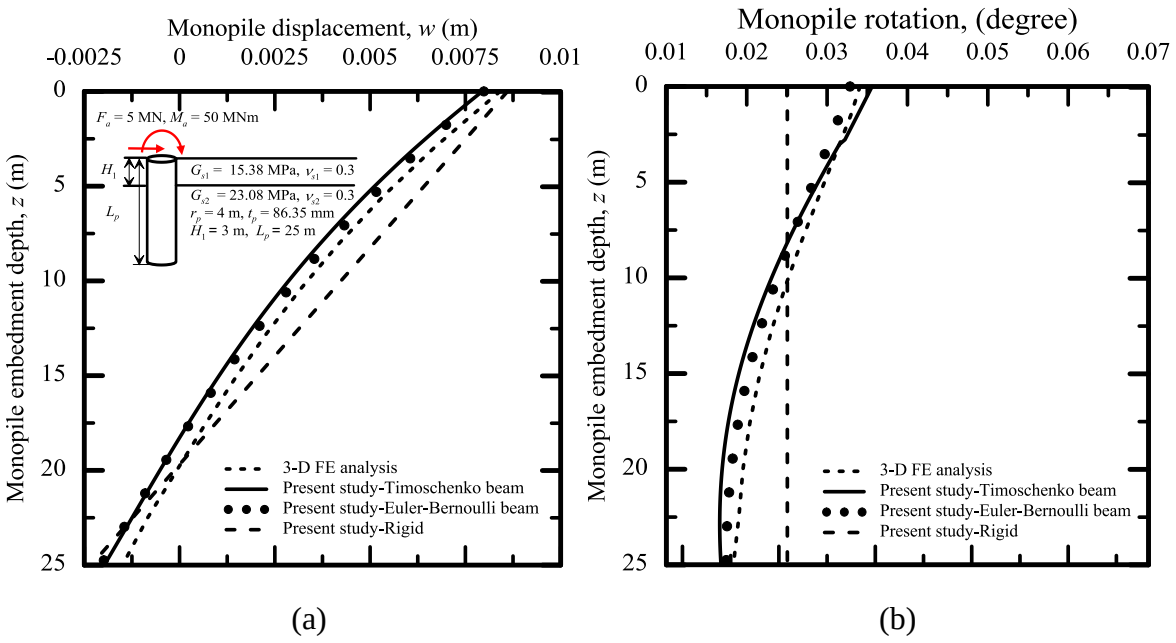

Figure 2.7: Comparison of present analysis with 3-D FE analysis for a circular monopile with a hollow cross-section of 4 m radius in a two-layer soil deposit (a) displacement and (b) rotation

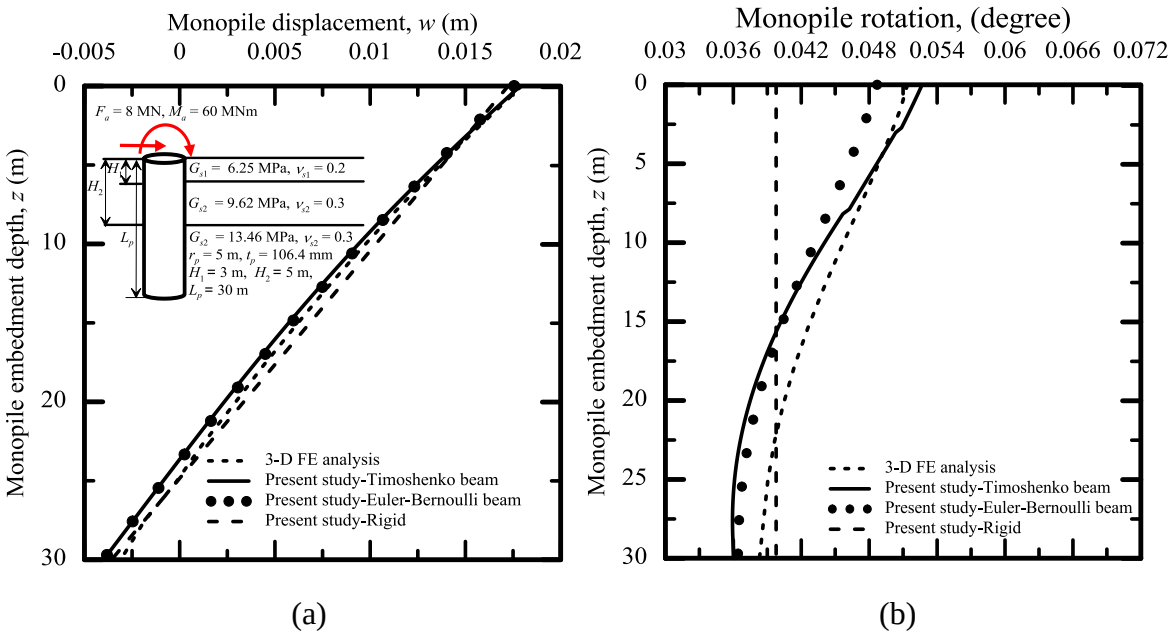

Figure 2.8: Comparison of present analysis with 3-D FE analysis for a circular monopile with a hollow cross-section of 5 m radius in a three-layer soil deposit (a) displacement and (b) rotation

Table 2.2: Percentage difference in estimation of monopile head displacement and rotation using the different beam theories with finite element analysis

Beam theory	% difference in head displacement	% difference in head rotation
Timoshenko	0.4 – 3.4	1.3 – 2.5
Euler-Bernoulli	1.9 – 5.1	4.6 – 8.1
Rigid	4.1 – 7.8	12 – 54.1

Table 2.3: Computational time required for 3-D FE analysis and present analysis for large-diameter monopiles with a hollow circular cross-section

Solved problems	FE analysis, (secs)	Present analysis, (secs)		
		Timoshenko	Euler-Bernoulli	Rigid
Figures 2.6(a)-(b)	402	483	480	339
Figures 2.7(a)-(b)	403	491	488	346
Figures 2.8(a)-(b)	409	498	494	357

2.7.3 Applicability of different beam theories to monopiles

To further investigate the applicability of the different beam theories to model monopile behaviour, monopile displacements and slopes (often the design criterion) are systematically calculated for different monopile-soil stiffness ratios E_p/G_s^* (according to Randolph (1981), ν_s has a negligible contribution to lateral soil resistance of piles and the effect of ν_s can be taken into account by defining an equivalent shear modulus $G_s^* = G_s \times (1+0.75\,\nu_s)$; the advantage of G_s^* is that the monopile response can be investigated in terms of a single soil parameter that integrates the effect of both the elastic constants) and monopile slenderness ratios L_p/r_p, for monopiles embedded in homogeneous soil.

Figures 2.9(a)-(d) shows the dimensionless monopile head displacements $w_h G_s^* r_p/F_a$ and $w_h G_s^* r_p^2/M_a$, and the total head rotations $\psi_h G_s^* r_p^2/F_a$ and $\psi_h G_s^* r_p^3/M_a$ for applied forces and moments, respectively, as functions of relative monopile-soil stiffness ratio E_p/G_s^* for varying cases of pile slenderness ratio for the Timoshenko and Euler-Bernoulli theory only. According to the Timoshenko beam theory the shear correction factor κ for different monopile radius produces different values of the shear correction factor. However, it is observed in the analysis that the different κ values produced negligible differences in the dimensionless

monopile response; therefore the plots corresponding to the Timoshenko beam theory in Figures 2.9(a)-(d) are respectively, applicable to all the steel monopiles.

Figures 2.9(a)-(d) show that for monopiles, the two beam theories produce different head responses when $E_p/G_s^* \leq 10^4$ for all the cases of monopile slenderness ratio analyzed. For the case of an applied force at the monopile head, the Euler-Bernoulli beam theory is found to underestimate the dimensionless head displacement and rotation for $E_p/G_s^* \leq 10^4$. For the case of an applied moment at the monopile head, the Euler-Bernoulli beam theory overestimates the dimensionless head displacement although the head rotation is found to be nearly equal for both the beam theories. The difference in response obtained from Timoshenko and Euler-Bernoulli beam theories for the case of monopiles for $E_p/G_s^* \leq 10^4$ arise most likely because of the effect of warping in the monopile cross-section. Thus, for monopiles in an elastic soil deposit different beam theories should be used to estimate accurate monopile head response, especially for low values of relative monopile-soil stiffness ratio (i.e., for $E_p/G_s^* \leq 10^4$).

Further, Figures 2.10(a)-(d) show the dimensionless monopile head displacements $w_h G_s^* r_p/F_a$ and $w_h G_s^* r_p^2/M_a$, and head rotations $\psi_h G_s^* r_p^2/F_a$ and $\psi_h G_s^* r_p^3/M_a$ for applied forces and moments, respectively, as functions of pile slenderness ratio L_p/r_p. For these figures, the effect of the shear correction factor κ in the Timoshenko beam is found to be negligible as well. It is evident from these figures that the rigid beam theory can be used with reasonable accuracy for cases with $E_p/G_s^* \geq 10^5$ (see also Table 2.4). Table 2.4 gives a summary of the range of applicability of different beam theories for monopiles.

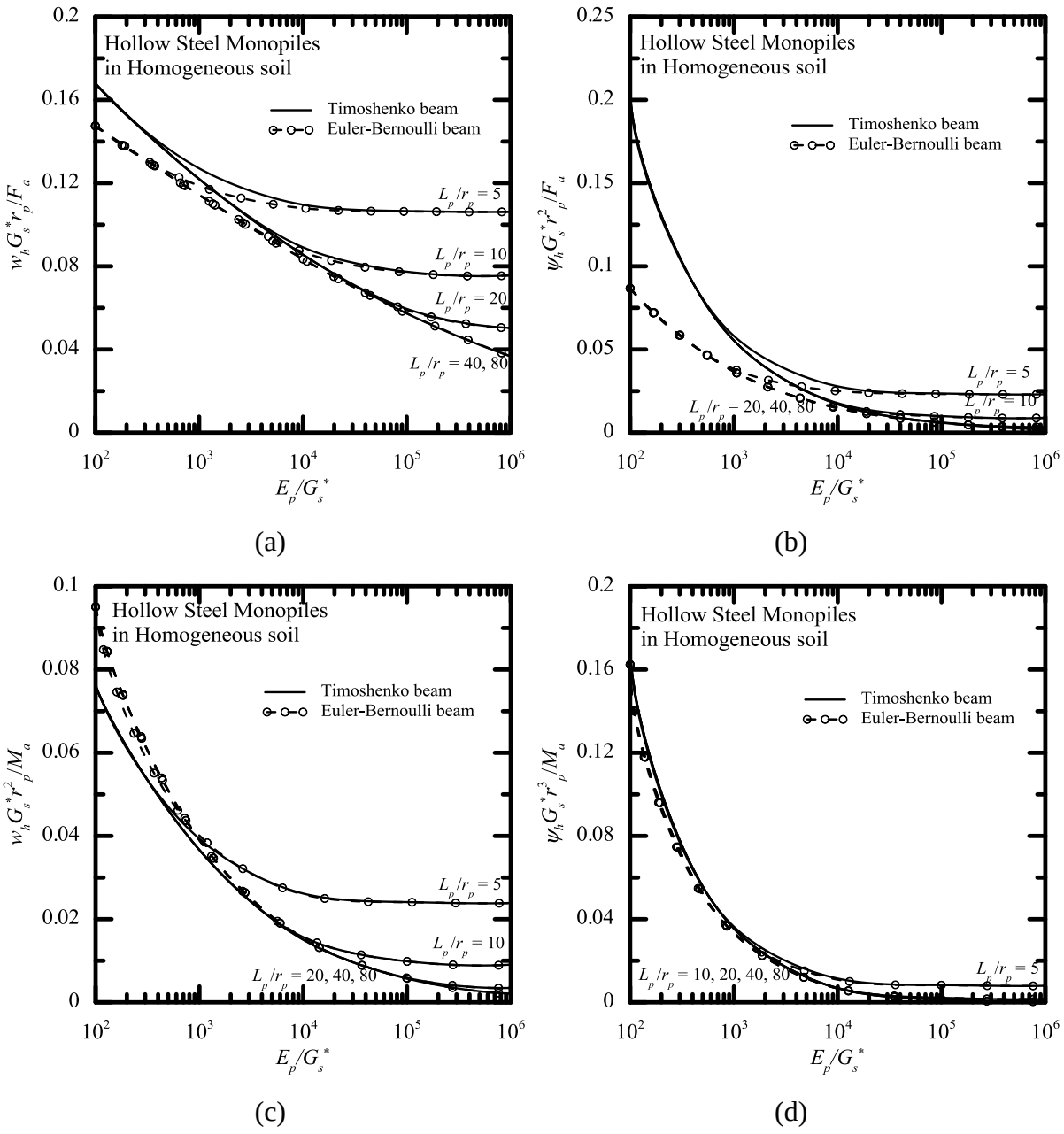

Figure 2.9: (a) Dimensionless displacement caused by applied force, (b) dimensionless head rotation caused by applied force, (c) dimensionless head displacement caused by applied moment, and (d) dimensionless head rotation caused applied moment for monopiles with hollow circular cross-sections as functions of monopile-soil stiffness ratio obtained using Timoshenko and Euler-Bernoulli beam theories

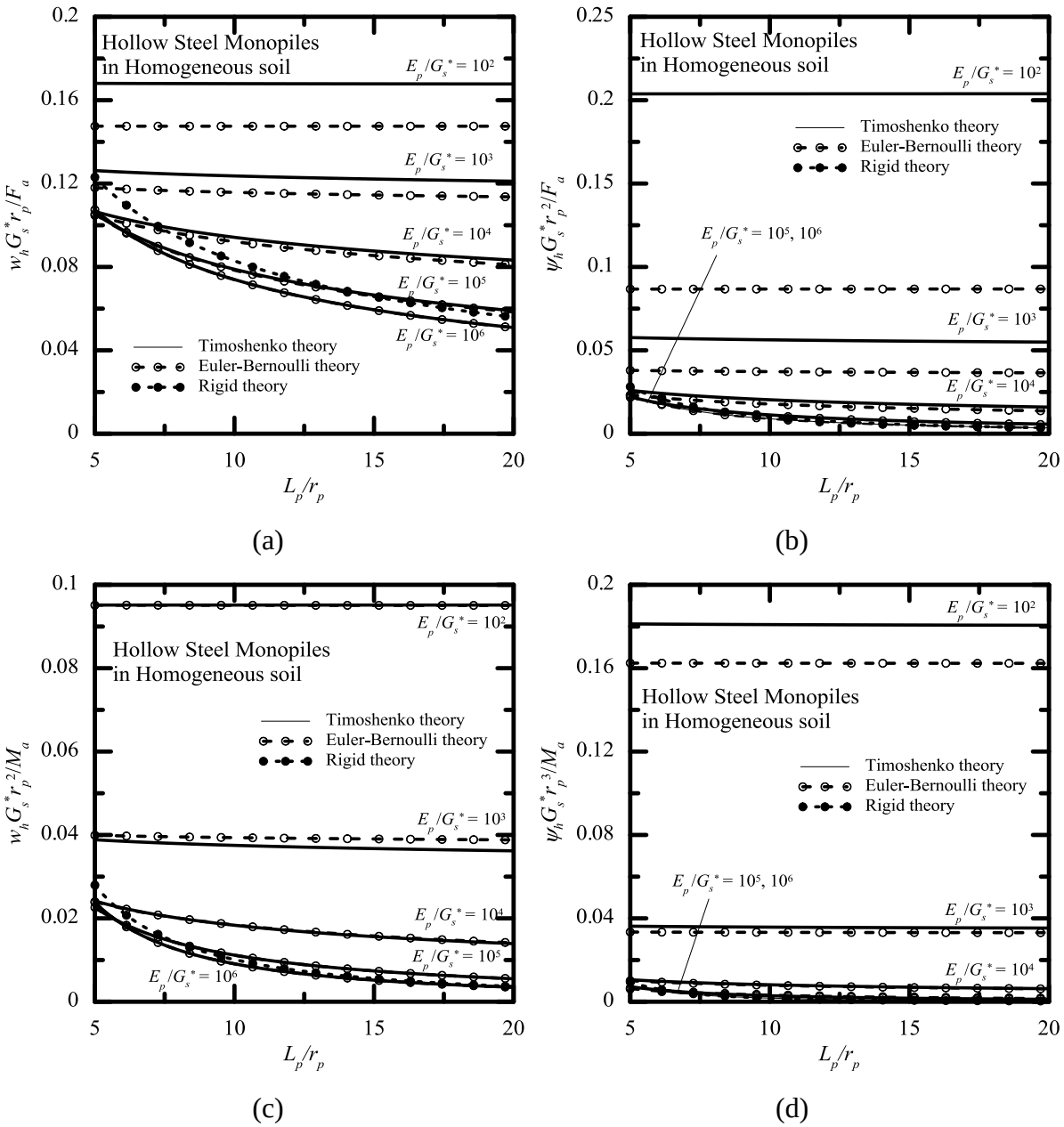

Figure 2.10: (a) Dimensionless displacement caused by applied force, (b) dimensionless head rotation caused by applied force, (c) dimensionless head displacement caused by applied moment, and (d) dimensionless head rotation caused applied moment for monopiles with hollow circular cross-sections as functions of monopile slenderness ratio obtained using Timoshenko, Euler-Bernoulli, and rigid beam theories

Thus, for monopiles in an elastic soil deposit, the monopile should be modeled either as a Timoshenko or Euler Bernoulli beam. Modeling the monopile as a Timoshenko beam is preferable for $E_p/G_s^* \leq 10^4$, as it gives the best prediction of head rotation. The rigid beam theory can be used to make a first-hand estimate of the monopile head displacement and

rotation and it may also find its application in the design of drilled piers or caissons supporting bridges and transmission towers.

Table 2.4: Applicability of different beam theories for monopiles with different slenderness ratio (L_p/r_p) and relative monopile-soil stiffness ratio (E_p/G_s^*)

L_p/r_p	E_p/G_s^*	Beam theory to predict pile head response
5-80	$> 10^4$	Timoshenko or Euler-Bernoulli
	$\leq 10^4$	Timoshenko
5-20	$\geq 10^5$	Rigid*

*Rigid theory should only be used for a quick initial estimate of monopile head displacement and Timoshenko or Euler-Bernoulli beam theories should be used for accurate prediction of monopile head response

2.8 Summary

A mathematical framework for the static analysis of laterally loaded monopiles is presented in which the Timoshenko beam theory is used to model the monopile and elastic continuum theory is used to model the soil. A rational displacement field is assumed for the soil and the equilibrium of the monopile-soil system is obtained by applying the principle of minimum potential energy. The differential equations describing the monopile and soil displacements obtained using the variational principle of mechanics are solved analytically and numerically, respectively, following an iterative algorithm. It is shown mathematically that the Timoshenko beam theory leads to the most generalized form of the differential equations, and successive simplifications to these equations result in the equations for the Euler-Bernoulli and rigid beam theories, respectively.

Several example problems for the case of small-diameter reinforced concrete piles with solid circular cross-section and large-diameter steel monopiles with hollow circular cross-section are solved using the analysis and compared with the response obtained from 3-D FE analysis. The percentage difference in the prediction of pile response from the present analysis following different beam theories with those of 3-D FE analysis is quantified. A comparison of the computational time required to obtain a response from the present analysis with those of 3-D FE analysis is also shown. Further, a systematic parametric study based on normalized monopile head displacement and rotation is performed to investigate the range of applicability of different beam theories for obtaining monopile response.

CHAPTER 3

Dynamic Analysis of Laterally Loaded Monopiles in Multilayered Viscoelastic Soil

3.1 Introduction

In this chapter, the mathematical framework developed in Chapter 1 is extended to include the effect of dynamic loading on monopiles. In the analysis, the soil is modeled as a 3-D multilayered viscoelastic continuum with frequency independent hysteretic material damping and the monopile is modeled following the Timoshenko beam theory. Rational soil displacement functions are assumed and the Extended Hamilton's Principle in conjunction with the calculus of variation is applied to obtain the differential equations describing monopile and soil displacements. The differential equations governing monopile and soil displacements are solved analytically and numerically, respectively, following an iterative algorithm. Further, it is shown that the framework can be progressively reduced to obtain monopile response following the Rayleigh, Euler-Bernoulli, and rigid beam theories.

The results (complex dynamic impedance functions, displacement, and rotation) obtained from the present analysis following different beam theories are verified with the results of existing solutions, available in the literature. Example problems are solved to investigate the applicability of different beam theories for reinforced concrete piles with solid circular cross-section and steel piles with a hollow circular cross-section. Further, the applicability of the dynamic analysis versus the static analysis (Chapter 2) to estimate the response of large-diameter monopiles (typically subjected to a cyclic/dynamic loading of frequency less than 1.0 Hz (see Figure 1.2)), is investigated. For the investigation, a comparison of the dynamic and static response (monopile-head displacement and rotation) following different beam theories (Timoshenko, Euler-Bernoulli, and rigid) of four different monopiles currently installed at wind farm sites in Europe is done. A comparison of the computational time to obtain the dynamic and static response of monopile is also shown and the appropriateness of the applicability of dynamic analysis to obtain monopile response is discussed.

3.2 Overview of existing formulations for dynamic analysis of laterally loaded piles in viscoelastic soil

In the literature, several formulations are available for the dynamic analysis of laterally loaded piles which can be broadly categorized into four major groups: (i) Winkler spring model (associated with dashpots to represent the hysteretic and radiation damping) based analytical and numerical (Novak 1974, Novak et al. 1978, Roesset 1980, Gazetas and Dobry 1984, Makris and Gazetas 1992, Mylonakis 2001, Gerolymos and Gazetas 2006, Varun et al. 2009, Zhong and Huang 2013) formulations for piles embedded in homogeneous or layered soils either floating in a half-space or overlying rigid bases, (ii) 3-D continuum-based semi-analytical BE (Kaynia and Kausel 1982, Sen et al. 1985, Kaynia and Kausel 1991, Padron et al. 2008, Ai and Li 2015) and FE (Blaney et al. 1976, Kuhlemeyer 1979, Roesset and Angelides 1980, El-Marsarfawi et al. 1992, Wu and Finn 1997, Thammarak 2009) formulations for piles embedded in homogeneous and layered half-spaces, (iii) rigorous continuum-based analytical or semi-analytical (Nozoe et al. 1985, Pak and Jennings 1987, Rajapakse and Shah 1987, 1989) formulations for piles embedded in homogeneous half-spaces or overlying rigid bases, and (iv) approximate analytical studies for piles embedded in homogeneous soil overlying rigid bases (Nogami and Novak 1977, Novak and Nogami 1977, Sun and Pires 1993, 1995, Zheng et al., 2013, Shadlou and Bhattacharya 2014, Liu et al. 2016, Anoyatis et al. 2016).

Of the different analysis methods available, the Winkler based formulations are the most popular and widely used by geotechnical engineers because these approaches (commonly known as the Beam on Dynamic Winkler Foundation (BDWF)) are mathematically convenient, computationally inexpensive, and can be easily extended to include the effect of soil nonlinearity. However, the methods based on Winkler approach require parameter calibration (e.g., Winkler spring constants and damping coefficients for the dashpots) for accurate prediction of pile and superstructure response and either neglect the coupled vibration between the pile-soil or between the soil layers, besides, leading to unrealistic pile behavior at low frequencies of vibration. The rigorous continuum-based numerical solutions (e.g., FE formulations) have an advantage over the Winkler type formulations as these methods consider the coupled vibration of the pile and soil. However, these methods are computationally intensive and expensive, and may also require the modeling of non-reflecting viscous boundary conditions to include the effect of radiation damping which can affect the accuracy of the

solution. The rigorous analytical or semi-analytical continuum-based studies have the advantage of taking into account the effect of material and radiation damping within the formulation and solution process without recourse to artificial dashpots (as required in Winkler-type and continuum-based FE methods); however, the mathematics involved are often complex, computationally expensive, and not quite useful for routine geotechnical practice. The advantage of the approximate analytical continuum-based methods is that these methods have the ability to capture the important physics of the problem without being mathematically too complex and computationally too intensive.

In most of the aforementioned analytical, semi-analytical, and numerical dynamic analysis of laterally loaded piles, the pile is modeled as an elastic Euler-Bernoulli beam that does not account for the effect of shear deformation and rotatory inertia of the pile cross-section. For large-diameter drilled shafts and monopiles, the use of Euler-Bernoulli beam theory is questionable, and perhaps the Timoshenko beam theory is more appropriate (as discussed in Chapter 2). The effect of shear deformation (included in the mathematical framework developed in Chapter 2) and rotatory inertia which are likely to be non-negligible in piles and monopiles, are not taken into account by the Euler-Bernoulli beam theory but can be captured by the Timoshenko beam theory (Shames and Dym 1985).

In this chapter, an approximate continuum-based formulation for analysis of laterally loaded monopiles (modeled as a Timoshenko beam) in multilayered viscoelastic soil and subjected to harmonic force and/or moment at the monopile head, is presented. It is shown in the analysis that the formulation offers a unified framework which under simplified assumptions leads to monopiles/piles modeled as Rayleigh (which takes into account only the rotatory inertia but not the shear deformation (Strutt 1877)), Euler–Bernoulli (which does not take into account both the rotatory inertia and the shear deformation), and rigid beams. A significant advantage of the present formulation is that the values of soil spring constant k, shear parameter t, inertial resistance Λ, and the radiation damping coefficient ξ_r of the soil are not assigned *a priori* but are rather obtained as part of the solution; therefore, no ad hoc inputs based on empirical equations or parameter calibration are necessary unlike the Winkler or FE formulations.

3.3 Mathematical formulation

3.3.1 Problem definition

Figure 3.1 shows a hollow circular monopile modeled as a Timoshenko beam in a soil deposit with n layers. The monopile has a length L_p, radius r_p, wall thickness t_p, area of cross-section A_p, and second moment of inertia I_p and is characterized by its shear modulus G_p and density ρ_p. Each soil layer is modeled as a homogeneous, isotropic, and linear viscoelastic 3-D continuum with frequency independent hysteretic material damping (Kramer 1996) characterized by density ρ_{si}, complex Lame's constant $\overline{\lambda_{si}} = \lambda_{si}\left(1+2j\xi_{si}\right)$ and $\overline{G_{si}} = G_{si}\left(1+2j\xi_{si}\right)$ where $\lambda_{si} = E_{si}\nu_{si}/\{(1+\nu_{si})(1-2\nu_{si})\}$, $G_{si} = E_{si}/\{2(1+\nu_{si})\}$, E_{si} is Young's modulus, ν_{si} is the Poisson's ratio, ξ_{si} is the frequency independent material damping ratio of the soil (the subscript i denotes the i^{th} layer), and $j = \sqrt{-1}$. The thickness of any i^{th} layer is given by $H_i - H_{i-1}$ (with $H_0 = 0$). The monopile head is flush with the ground surface and subjected to a time-harmonic horizontal force $F_a(t) = F_0 e^{j\Omega t}$ and/or moment $M_a(t) = M_0 e^{j\Omega t}$ where Ω = circular forcing frequency, F_0 = applied force amplitude, M_0 = applied moment amplitude, and t = time.

The goal of the analysis is to obtain the steady-state monopile head displacement and rotation caused by the applied force and/or moment and subsequently evaluate the dynamic monopile head impedances for the swaying, coupled swaying-rocking, and rocking mode of monopile vibration. In the analysis, no slippage or separation between the monopile and the surrounding soil or between the soil layers is considered. A right-handed cylindrical (r-θ-z) coordinate system is chosen such that its origin lies at the centre of the monopile head, the z-axis coincides with the monopile axis and points downward, the reference radial direction r_0 coincides with the direction of the applied force F_a, and the tangential distance θ measured from r_0 is clockwise positive when looked down from the top of the monopile.

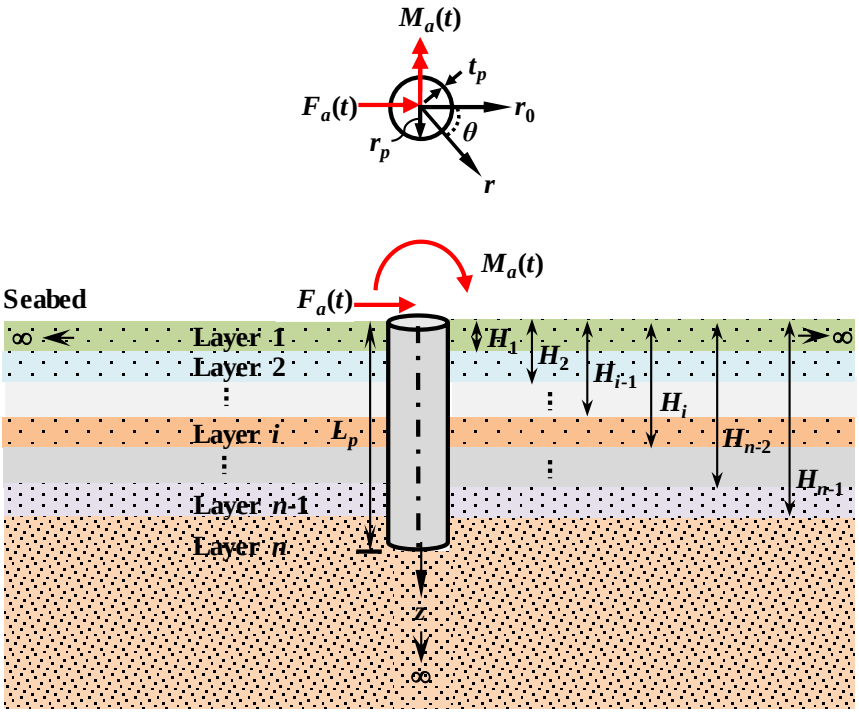

Figure 3.1: A monopile embedded in a multilayered viscoelastic soil deposit and subjected to time-harmonic lateral loads

3.3.2 Displacements, strain, and strain energy density in soil

The horizontal soil displacement field, generated by the monopile displacement, is described as a product of separable functions, each of which varies with one of the three spatial dimensions and time. The vertical soil displacement u_z is neglected in the analysis, as discussed in Chapter 2. The soil displacement field in the radial and tangential direction is expressed as

$$u_r(r,\theta,z,t) = w(z,t)\phi_r(r)\cos\theta \tag{3.1}$$

$$u_\theta(r,\theta,z,t) = -w(z,t)\phi_\theta(r)\sin\theta \tag{3.2}$$

where $w(z,t) = w(z)e^{j\Omega t}$ in which $w(z)$ is the steady-state monopile displacement, $\phi_r(r)$ and $\phi_\theta(r)$ are the dimensionless functions in the radial and tangential directions, respectively, that are both assumed to be equal to one at $r = r_p$, and equal to zero at $r = \infty$. The sine and cosine functions ensure that the variation of the soil displacements in the tangential direction is compatible with the horizontal monopile displacement.

Using the soil displacement field, the infinitesimal soil strains (with contractive strains assumed positive) is expressed as

$$\begin{bmatrix}\varepsilon_{rr}\\ \varepsilon_{\theta\theta}\\ \varepsilon_{zz}\\ \varepsilon_{r\theta}\\ \varepsilon_{rz}\\ \varepsilon_{\theta z}\end{bmatrix}=\begin{bmatrix}-\dfrac{\partial u_r}{\partial r}\\ -\dfrac{u_r}{r}-\dfrac{1}{r}\dfrac{\partial u_\theta}{\partial\theta}\\ -\dfrac{\partial u_z}{\partial z}\\ -\dfrac{1}{2}\left(\dfrac{1}{r}\dfrac{\partial u_r}{\partial\theta}+\dfrac{\partial u_\theta}{\partial r}-\dfrac{u_\theta}{r}\right)\\ -\dfrac{1}{2}\left(\dfrac{\partial u_z}{\partial r}+\dfrac{\partial u_r}{\partial z}\right)\\ -\dfrac{1}{2}\left(\dfrac{1}{r}\dfrac{\partial u_z}{\partial\theta}+\dfrac{\partial u_\theta}{\partial z}\right)\end{bmatrix}=\begin{bmatrix}-w(z,t)\dfrac{\partial\phi_r(r)}{\partial r}\cos\theta\\ -w(z,t)\dfrac{\phi_r(r)-\phi_\theta(r)}{r}\cos\theta\\ 0\\ \dfrac{1}{2}w(z,t)\left\{\dfrac{\phi_r(r)-\phi_\theta(r)}{r}+\dfrac{\partial\phi_\theta(r)}{\partial r}\right\}\sin\theta\\ -\dfrac{1}{2}\dfrac{\partial w(z,t)}{\partial z}\phi_r(r)\cos\theta\\ \dfrac{1}{2}\dfrac{\partial w(z,t)}{\partial z}\phi_\theta(r)\sin\theta\end{bmatrix} \tag{3.3}$$

Further, using the elastic stress-strain relationship, the strain energy density $\sigma_{pq}\varepsilon_{pq}/2$ of the viscoelastic soil with frequency independent material damping is given by

$$\begin{aligned}U_D=\frac{1}{2}\Bigg[&\left(\overline{\lambda_{si}}+2\overline{G_{si}}\right)w^2\left(\frac{\partial\phi_r}{\partial r}\right)^2+2\overline{\lambda_{si}}w^2\frac{\partial\phi_r}{\partial r}\frac{(\phi_r-\phi_\theta)}{r}+\left(\overline{\lambda_{si}}+3\overline{G_{si}}\right)w^2\frac{(\phi_r-\phi_\theta)^2}{r^2}\\&+\overline{G_{si}}w^2\left(\frac{\partial\phi_\theta}{\partial r}\right)^2+2\overline{G_{si}}w^2\frac{(\phi_r-\phi_\theta)}{r}\frac{\partial\phi_\theta}{\partial r}+\overline{G_{si}}\left(\frac{\partial w}{\partial z}\right)^2\phi_r^2+\overline{G_{si}}\left(\frac{\partial w}{\partial z}\right)^2\phi_\theta^2\Bigg]\end{aligned} \tag{3.4}$$

3.3.3 Application of Extended Hamilton Principle to monopile-soil system

The total potential energy ($\prod$) of the monopile-soil system using the Timoshenko beam theory (Shames and Dym 1985) is given by

$$\Pi=\int_0^{L_p}\frac{1}{2}E_pI_p\left(\frac{\partial\psi}{\partial z}\right)^2dz+\int_0^{L_p}\frac{1}{2}\kappa G_pA_p\left(\frac{\partial w}{\partial z}-\psi\right)^2dz+\int_{\Omega_0}U_D\,rdrd\theta dz \tag{3.5}$$

where the first integral in the right hand side of equation (3.5) is the strain energy of the monopile arising from the bending deformation such that ψ is the bending slope of monopile axis, the second integral is the strain energy of the monopile arising from the shearing deformation such that dw/dz is the total slope (i.e., slope caused by both bending and shearing) of the monopile axis, the third integral represents the total strain energy of the soil domain Ω_0 that participates in the monopile-soil interaction, κ (same a Chapter 1) is a correction factor to account for the non-uniform shear strain distribution within the monopile cross-section.

The total kinetic energy (T) of the monopile-soil system using the Timoshenko beam theory is given by

$$\mathrm{T} = \frac{1}{2}\int_0^{L_p} \rho_p A_p \left(\frac{\partial w}{\partial t}\right)^2 dz + \frac{1}{2}\int_0^{L_p} \rho_p I_p \left(\frac{\partial \psi}{\partial t}\right)^2 dz + \frac{1}{2}\int_{L_p}^{\infty}\int_0^{2\pi}\int_0^{r_p} \rho_s \left\{\left(\frac{\partial u_r}{\partial t}\right)^2 + \left(\frac{\partial u_\theta}{\partial t}\right)^2\right\} r dr d\theta dz + \frac{1}{2}\int_0^{\infty}\int_0^{2\pi}\int_{r_p}^{\infty} \rho_s \left\{\left(\frac{\partial u_r}{\partial t}\right)^2 + \left(\frac{\partial u_\theta}{\partial t}\right)^2\right\} r dr d\theta dz \tag{3.6}$$

where the first and the second integrals on the right-hand side of equation (3.6) represent the kinetic energy from the translational and rotatory inertias of the monopile, respectively, the third integral represents the kinetic energy of the cylindrical soil domain below the monopile, and the fourth integral represents the kinetic energy of the remaining soil domain that participates in the monopile-soil interaction.

The work done W_{nc} by the external force $F_a(t)$ and moment $M_a(t)$ is given by

$$W_{nc} = F_a\, w\big|_{z=0} - M_a \left.\frac{\partial \psi}{\partial z}\right|_{z=0} \tag{3.7}$$

where the first and the second term on the right-hand side of equation (3.7) represents the work done by the applied force and moment to undergo the shearing and bending deformation at the monopile head, respectively.

According to the Extended Hamilton's Principle, the motion of a given system from time t_1 to t_2 under equilibrium satisfies the following (Craig and Kurdila 2006, Humar 2012)

$$\int_{t_1}^{t_2} \delta\left(\mathrm{T} - \Pi\right) dt + \int_{t_1}^{t_2} \delta W_{nc}\, dt = 0 \tag{3.8}$$

where $\delta(\cdot)$ is the variational operator, and t_1 and t_2 are the times at which the configuration of the system are assumed to be known. Substituting equations (3.1), (3.2), (3.5), (3.6), and (3.7) in equation (3.8) and considering explicit soil layering as described in Figure 3.1 results in

$$\int_{t_1}^{t_2}\Bigg[\sum_{i=1}^{n}\int_{H_{i-1}}^{H_i}\rho_p A_p\frac{\partial w_i}{\partial t}\delta\left(\frac{\partial w_i}{\partial t}\right)dz+\sum_{i=1}^{n}\int_{H_{i-1}}^{H_i}\rho_p A_p\frac{\partial \psi_i}{\partial t}\delta\left(\frac{\partial \psi_i}{\partial t}\right)dz$$

$$+\sum_{i=1}^{n}\int_{H_{i-1}}^{H_i}\int_{r_p}^{\infty}\rho_{si}\frac{\partial w_i}{\partial t}\delta\left(\frac{\partial w_i}{\partial t}\right)\left(\phi_r^2+\phi_\theta^2\right)rdrdz+\int_{L_p}^{\infty}\int_{r_p}^{\infty}\rho_{sn}\frac{\partial w_i}{\partial t}\delta\left(\frac{\partial w_i}{\partial t}\right)\left(\phi_r^2+\phi_\theta^2\right)rdrdz$$

$$+\int_{L_p}^{\infty}\rho_{sn}A_p\frac{\partial w_i}{\partial t}\delta\left(\frac{\partial w_i}{\partial t}\right)dz-\sum_{i=1}^{n}\int_{H_{i-1}}^{H_i}E_pI_p\frac{\partial \psi_i}{\partial z}\delta\left(\frac{\partial \psi_i}{\partial z}\right)dz$$

$$-\sum_{i=1}^{n}\int_{H_{i-1}}^{H_i}\kappa G_pA_p\left(\frac{\partial w_i}{\partial z}-\psi_i\right)\delta\left(\frac{\partial w_i}{\partial z}-\psi_i\right)dz-\pi\sum_{i=1}^{n}\int_{H_{i-1}}^{H_i}\int_{r_p}^{\infty}\Bigg\{\left(\overline{\lambda_{si}}+2\overline{G_{si}}\right)\left(\frac{\partial \phi_r}{\partial r}\right)^2+2\overline{\lambda_{si}}\frac{\phi_r}{r}\frac{\partial \phi_r}{\partial r}$$

$$-2\overline{\lambda_{si}}\frac{\phi_\theta}{r}\frac{\partial \phi_r}{\partial r}+\left(\overline{\lambda_{si}}+3\overline{G_{si}}\right)\frac{\phi_r^2}{r^2}+\left(\overline{\lambda_{si}}+3\overline{G_{si}}\right)\frac{\phi_\theta^2}{r^2}-2\left(\overline{\lambda_{si}}+3\overline{G_{si}}\right)\frac{\phi_r\phi_\theta}{r^2}+\overline{G_{si}}\left(\frac{\partial \phi_\theta}{\partial r}\right)^2$$

$$+2\overline{G_{si}}\frac{\phi_r}{r}\frac{\partial \phi_\theta}{\partial r}-2\overline{G_{si}}\frac{\phi_\theta}{r}\frac{\partial \phi_\theta}{\partial r}\Bigg\}w_i\delta w_i rdrdz-\pi\sum_{i=1}^{n}\int_{H_{i-1}}^{H_i}\int_{r_p}^{\infty}\left\{\overline{G_{si}}\phi_r^2+\overline{G_{si}}\phi_\theta^2\right\}\frac{\partial w_i}{\partial z}\delta\left(\frac{\partial w_i}{\partial z}\right)rdrdz$$

$$-\pi r_p^2\int_{L_p}^{\infty}\overline{G_{sn}}\frac{\partial w_{n+1}}{\partial z}\delta\left(\frac{\partial w_{n+1}}{\partial z}\right)dz+F_a\delta w_1\big|_{z=0}-M_a\delta\left(\frac{\partial \psi_1}{\partial z}\right)\Bigg|_{z=0}$$

$$-\pi\sum_{i=1}^{n+1}\int_{H_{i-1}}^{H_i}\int_{r_p}^{\infty}\Bigg\{\overline{\lambda_{si}}w_i^{\,2}\frac{1}{r}\frac{\partial \phi_r}{\partial r}+\left(\overline{\lambda_{si}}+3\overline{G_{si}}\right)w_i^{\,2}\frac{\phi_r}{r^2}-\left(\overline{\lambda_{si}}+3\overline{G_{si}}\right)w_i^{\,2}\frac{\phi_\theta}{r^2}$$

$$+\overline{G_{si}}w_i^{\,2}\frac{1}{r}\frac{\partial \phi_\theta}{\partial r}+\overline{G_{si}}\left(\frac{\partial w_i}{\partial z}\right)^2\phi_r+\rho_{si}\left(\frac{\partial w_i}{\partial t}\right)^2\phi_r\Bigg\}\delta\phi_r rdrdz$$

$$-\pi\sum_{i=1}^{n+1}\int_{H_{i-1}}^{H_i}\int_{r_p}^{\infty}\left\{\left(\overline{\lambda_{si}}+2\overline{G_{si}}\right)w_i^{\,2}\left(\frac{\partial \phi_r}{\partial r}\right)+\overline{\lambda_{si}}w_i^{\,2}\frac{\phi_r}{r}-\overline{\lambda_{si}}w_i^{\,2}\frac{\phi_\theta}{r}\right\}\delta\left(\frac{\partial \phi_r}{\partial r}\right)rdrdz$$

$$-\pi\sum_{i=1}^{n+1}\int_{H_{i-1}}^{H_i}\int_{r_p}^{\infty}\Bigg\{-\overline{\lambda_{si}}w_i^{\,2}\frac{1}{r}\frac{\partial \phi_r}{\partial r}-\left(\overline{\lambda_{si}}+3\overline{G_{si}}\right)w_i^{\,2}\frac{\phi_r}{r^2}+\left(\overline{\lambda_{si}}+3\overline{G_{si}}\right)w_i^{\,2}\frac{\phi_\theta}{r^2}$$

$$-\overline{G_{si}}w_i^{\,2}\frac{1}{r}\frac{\partial \phi_\theta}{\partial r}+\overline{G_{si}}\left(\frac{\partial w_i}{\partial z}\right)^2\phi_\theta+\rho_{si}\left(\frac{\partial w_i}{\partial t}\right)^2\phi_\theta\Bigg\}\delta\phi_\theta rdrdz$$

$$-\pi\sum_{i=1}^{n+1}\int_{H_{i-1}}^{H_i}\int_{r_p}^{\infty}\left\{\overline{G_{si}}w_i^{\,2}\left(\frac{\partial \phi_\theta}{\partial r}\right)+\overline{G_{si}}w_i^{\,2}\frac{\phi_r}{r}-\overline{G_{si}}w_i^{\,2}\frac{\phi_\theta}{r}\right\}\delta\left(\frac{\partial \phi_\theta}{\partial r}\right)rdrdz\Bigg]dt=0 \tag{3.9}$$

Performing integration by parts on the terms associated with $\delta(\partial w/\partial z)$, $\delta(\partial w/\partial t)$, $\delta(\partial \psi/\partial z)$, $\delta(\partial \psi/\partial t)$, $\delta(\partial \phi_r/\partial r)$, and $\delta(\partial \phi_\theta/\partial r)$ in equation (3.9) leads to an equation of the form

$$\int A(w)\delta w\,dz+\int B(\psi)\delta\psi\,dz+\int C(\phi_r)\delta\phi_r\,dr+\int D(\phi_\theta)\delta\phi_\theta\,dr=0 \tag{3.10}$$

where δw, $\delta\psi$, $\delta\phi_r$, and $\delta\phi_\theta$ are the first variations of the functions w, ψ, ϕ_r, and ϕ_θ, respectively, and $A(\cdot)$, $B(\cdot)$, $C(\cdot)$, and $D(\cdot)$ are the differential operators. Considering the variations of w, ψ, ϕ_r, and ϕ_θ separately and equating the terms associated with δw, $\delta\psi$, $\delta\phi_r$, and $\delta\phi_\theta$ individually to zero produce the governing differential equations $A(w) = 0$, $B(\psi) = 0$, $C(\phi_r) = 0$, and, $D(\phi_\theta) = 0$, for w, ψ, ϕ_r, and ϕ_θ, respectively, along with the appropriate boundary conditions.

3.3.4 Analytical solution of differential equations describing monopile displacement

Considering the terms associated with δw and $\delta\psi$ for $0 \le z \le L_p$, the governing differential equations of w and ψ are obtained. A set of coupled differential equations of $w(z)$ and $\psi(z)$ for the i^{th} layer is obtained for the domain $0 \le z \le L_p$ as

$$E_p I_p \frac{\partial^2 \psi_i}{\partial z^2} + \kappa G_p A_p \left(\frac{\partial w_i}{\partial z} - \psi_i \right) = \rho_p I_p \frac{\partial^2 \psi_i}{\partial t^2} \tag{3.11}$$

$$\kappa G_p A_p \left(\frac{\partial \psi_i}{\partial z} - \frac{\partial^2 w_i}{\partial z^2} \right) + k_i w_i - 2t_i \frac{\partial^2 w_i}{\partial z^2} = -\left(\rho_p A_p + \Lambda_i \right) \frac{\partial^2 w_i}{\partial t^2} \tag{3.12}$$

where the soil parameters k_i, t_i, and Λ_i are given by

$$\begin{aligned} k_i = \pi \Bigg[& \left(\overline{\lambda_{si}} + 2\overline{G_{si}} \right) \int_{r_p}^{\infty} r \left(\frac{\partial \phi_r}{\partial r} \right)^2 dr + \overline{G_{si}} \int_{r_p}^{\infty} r \left(\frac{\partial \phi_\theta}{\partial r} \right)^2 dr + 2\overline{\lambda_{si}} \int_{r_p}^{\infty} \left(\phi_r - \phi_\theta \right) \frac{\partial \phi_r}{\partial r} dr \\ & + 2\overline{G_{si}} \int_{r_p}^{\infty} \left(\phi_r - \phi_\theta \right) \frac{\partial \phi_\theta}{\partial r} dr + \left(\overline{\lambda_{si}} + 3\overline{G_{si}} \right) \int_{r_p}^{\infty} \frac{1}{r} \left(\phi_r - \phi_\theta \right)^2 dr \Bigg] \end{aligned} \tag{3.13}$$

$$t_i = \begin{cases} \dfrac{\pi}{2} \overline{G_{si}} \left[\displaystyle\int_{r_p}^{\infty} \left(\phi_r^2 + \phi_\theta^2 \right) r dr \right]; & i = 1, 2, \ldots, n \\ \dfrac{\pi}{2} \overline{G_{sn}} \left[\displaystyle\int_{r_p}^{\infty} \left(\phi_r^2 + \phi_\theta^2 \right) r dr + r_p^2 \right]; & i = n+1 \end{cases} \tag{3.14}$$

$$\Lambda_i = \begin{cases} \pi \rho_{si} \left[\displaystyle\int_{r_p}^{\infty} \left(\phi_r^2 + \phi_\theta^2 \right) r dr \right]; & i = 1, 2, \ldots, n \\ \pi \rho_{sn} \left[\displaystyle\int_{r_p}^{\infty} \left(\phi_r^2 + \phi_\theta^2 \right) r dr + r_p^2 \right]; & i = n+1 \end{cases} \tag{3.15}$$

The constant k_i, t_i, and Λ_i represents the compressive, shear, and inertial resistance of soil in the i^{th} layer, respectively.

A mathematical transformation is made in terms of an auxiliary function F as shown below

$$w_i = \frac{F_i}{E_p I_p} - \frac{1}{\kappa G_p A_p}\frac{\partial^2 F_i}{\partial z^2} + \frac{\rho_p}{\kappa G_p E_p A_p}\frac{\partial^2 F_i}{\partial t^2} \tag{3.16}$$

$$\psi_i = \frac{1}{E_p I_p}\frac{\partial F_i}{\partial z} \tag{3.17}$$

and this results in a single differential equation of F by combining equations (3.11) and (3.12) as

$$\begin{aligned}&\left(1+\frac{2t_i}{\kappa G_p A_p}\right)\frac{d^4 F_i}{dz^4} - \left\{\left(\frac{k_i}{\kappa G_p A_p}+\frac{2t_i}{E_p I_p}\right) - \left(\frac{\rho_p}{E_p}+\frac{2t_i\rho_p}{\kappa G_p E_p A_p}+\frac{\rho_p A_p+\Lambda_i}{\kappa G_p A_p}\right)\Omega^2\right\}\frac{d^2 F_i}{dz^2} \\ &+\left\{\frac{k_i}{E_p I_p} - \left(\frac{k_i\rho_p}{\kappa G_p E_p A_p}+\frac{\rho_p A_p+\Lambda_i}{E_p I_p}\right)\Omega^2 + \left(\frac{\rho_p A_p+\Lambda_i}{\kappa G_p E_p A_p}\right)\rho_p\Omega^4\right\}F_i = 0\end{aligned} \tag{3.18}$$

with the corresponding boundary conditions also expressed in terms of the auxiliary function F.

$$\left[\left\{1+\frac{2t_1}{\kappa G_p A_p}\right\}\frac{d^3 F_1}{dz^3} - \left\{\frac{2t_1}{E_p I_p} - \rho_p\Omega^2\left(\frac{2t_1}{\kappa G_p E_p A_p}+\frac{1}{E_p}\right)\right\}\frac{dF_1}{dz}\right]\Bigg|_{z=0} = F_0 \tag{3.19a}$$

$$\left.\frac{d^2 F_1}{dz^2}\right|_{z=0} = -M_0 \tag{3.19b}$$

$$\begin{aligned}&\left\{\left(\frac{1}{E_p I_p} - \frac{\rho_p\Omega^2}{\kappa G_p E_p A_p}\right)F_i - \frac{1}{\kappa G_p A_p}\frac{d^2 F_i}{dz^2}\right\}\Bigg|_{z=H_i} \\ &= \left\{\left(\frac{1}{E_p I_p} - \frac{\rho_p\Omega^2}{\kappa G_p E_p A_p}\right)F_{i+1} - \frac{1}{\kappa G_p A_p}\frac{d^2 F_{i+1}}{dz^2}\right\}\Bigg|_{z=H_{i+1}}\end{aligned} \tag{3.20a}$$

$$\left.\frac{dF_i}{dz}\right|_{z=H_i} = \left.\frac{dF_{i+1}}{dz}\right|_{z=H_{i+1}} \tag{3.20b}$$

$$\left[\left\{1+\frac{2t_i}{\kappa G_p A_p}\right\}\frac{d^3F_i}{dz^3}-\left\{\frac{2t_i}{E_pI_p}-\rho_p\Omega^2\left(\frac{2t_i}{\kappa G_p E_p A_p}+\frac{1}{E_p}\right)\right\}\frac{dF_i}{dz}\right]_{z=H_i}$$
$$=\left[\left\{1+\frac{2t_{i+1}}{\kappa G_p A_p}\right\}\frac{d^3F_{i+1}}{dz^3}-\left\{\frac{2t_{i+1}}{E_pI_p}-\rho_p\Omega^2\left(\frac{2t_{i+1}}{\kappa G_p E_p A_p}+\frac{1}{E_p}\right)\right\}\frac{dF_{i+1}}{dz}\right]_{z=H_{i+1}} \tag{3.20c}$$

$$\frac{d^2F_i}{dz^2}=\frac{d^2F_{i+1}}{dz^2} \tag{3.20d}$$

$$\left[\left\{1+\frac{2t_n}{\kappa G_p A_p}\right\}\frac{d^3F_n}{dz^3}-\left\{\frac{2t_n}{E_pI_p}-\rho_p\Omega^2\left(\frac{2t_n}{\kappa G_p E_p A_p}+\frac{1}{E_p}\right)\right\}\frac{dF_n}{dz}\right]_{z=L_p}$$
$$=-2t_{n+1}\left.\frac{dw_{n+1}}{dz}\right|_{z=L_p} \tag{3.21a}$$

$$\frac{d^2F_n}{dz^2}=0 \tag{3.21b}$$

Equations (3.19a)-(3.19b) are applicable at the monopile head (z = 0), equations (3.20a)-(3.20d) are applicable at the interface between the i^{th} and the $(i+1)^{\text{th}}$ layers ($z = H_i$), and equations (3.21a)-(3.21b) are applicable at the monopile base ($z = L_p$).

Closed-form solution of the function F is obtained for the differential equation (3.18) as

$$F_i(z)=C_1^{(i)}e^{v_1^{(i)}z}+C_2^{(i)}e^{-v_1^{(i)}z}+C_3^{(i)}e^{v_2^{(i)}z}+C_4^{(i)}e^{-v_2^{(i)}z} \tag{3.22a}$$

where

$$v_{1,2}^{(i)}=\pm\sqrt{\frac{\alpha_i\pm\sqrt{\alpha_i^{\,2}-4\eta_i}}{2}} \tag{3.22b}$$

in which

$$\alpha_i=\frac{\left(\frac{2t_i}{E_pI_p}+\frac{k_i}{\kappa G_p A_p}\right)-\left\{\frac{\rho_p}{E_p}+\frac{2t_i\rho_p}{\kappa G_p E_p A_p}+\left(\frac{\rho_p A_p+\Lambda_i}{\kappa G_p A_p}\right)\right\}\Omega^2}{\left(1+\frac{2t_i}{\kappa G_p A_p}\right)} \tag{3.22c}$$

$$\eta_i = \frac{\dfrac{k_i}{\kappa G_p A_p} - \left(\dfrac{\rho_p A_p + \Lambda_i}{E_p I_p} + \dfrac{k_i \rho_p}{\kappa G_p E_p A} \right) \Omega^2 + \left(\dfrac{\rho_p A_p + \Lambda_i}{\kappa G_p E_p A} \right) \rho_p \Omega^4}{\left(1 + \dfrac{2t_i}{\kappa G_p A_p} \right)} \tag{3.22d}$$

The integration constants $C_1^{(i)}$, $C_2^{(i)}$, $C_3^{(i)}$, and $C_4^{(i)}$ in equation (3.22a) for the i^{th} layer can be determined using appropriate boundary conditions given in equations (3.19)-(3.21). After obtaining $F(z)$, $w(z)$, and $\psi(z)$ are calculated from equations (3.16) and (3.17), respectively.

Considering the terms associated with δw_{n+1} for $L_p < z < \infty$ leads to the differential equation of $w(z)$ below the monopile

$$2t_{n+1} \frac{\partial^2 w_{n+1}}{\partial z^2} - k_{n+1} w_{n+1} - \Lambda_{n+1} \frac{\partial^2 w_{n+1}}{\partial t^2} = 0 \tag{3.23}$$

where the soil parameters k_{n+1}, t_{n+1}, and Λ_{n+1} are defined in equations (3.13)-(3.15). The boundary condition for equation (3.23) at the monopile base (i.e., at $z = L_p$) is $w_n = w_{n+1}$, which ensures the continuity of displacement. For the case of $z \to \infty$, the solution of equation (3.23) satisfying the boundary conditions is given by

$$w_{n+1}(z) = -w_n(z)\big|_{z=L_p} \left(\sqrt{\frac{k_n - \Lambda_{n+1}\Omega^2}{2t_{n+1}}} \right) e^{-\sqrt{\frac{k_n - \Lambda_{n+1}\Omega^2}{2t_{n+1}}}(z - L_p)} \tag{3.24}$$

3.3.5 Numerical solution of differential equations describing soil displacement

Considering the terms associated with $\phi_r(r)$ and $\phi_\theta(r)$ in equation (3.10), the corresponding differential equations are obtained as

$$\frac{d^2\phi_r}{dr^2} + \frac{1}{r}\frac{d\phi_r}{dr} - \left[\left(\frac{\gamma_1}{r} \right)^2 + \left(\frac{\gamma_2}{r_p} \right)^2 \right] \phi_r = \frac{\gamma_3^2}{r}\frac{d\phi_\theta}{dr} - \left(\frac{\gamma_1}{r} \right)^2 \phi_\theta \tag{3.25a}$$

$$\frac{d^2\phi_\theta}{dr^2} + \frac{1}{r}\frac{d\phi_\theta}{dr} - \left[\left(\frac{\gamma_4}{r} \right)^2 + \left(\frac{\gamma_5}{r_p} \right)^2 \right] \phi_\theta = -\frac{\gamma_6^2}{r}\frac{d\phi_r}{dr} - \left(\frac{\gamma_4}{r} \right)^2 \phi_r \tag{3.25b}$$

with the corresponding boundary conditions $\phi_r(r_p) = \phi_\theta(r_p) = 1$ and $\phi_r(\infty) = \phi_\theta(\infty) = 0$. The dimensionless constants γ_1-γ_6 in equations (3.25a) and (3.25b) are given by

$$\gamma_x = \sqrt{\frac{\sum_{i=1}^{n+1} A_i \int_{H_{i-1}}^{H_i} w_i^2 dz}{\sum_{i=1}^{n+1} B_i \int_{H_{i-1}}^{H_i} w_i^2 dz}} \qquad (x = 1, 3, 4, 6) \tag{3.26a}$$

$$\gamma_x = r_p \sqrt{\frac{\sum_{i=1}^{n+1} A_i \int_{H_{i-1}}^{H_i} \left(\frac{dw_i}{dz}\right)^2 dz - \sum_{i=1}^{n+1} \rho_{si} \Omega^2 \int_{H_{i-1}}^{H_i} w_i^2 dz}{\sum_{i=1}^{n+1} B_i \int_{H_{i-1}}^{H_i} w_i^2 dz}} \qquad (x = 2, 5) \tag{3.26b}$$

in which $A_i = \left(\overline{\lambda_{si}} + 2\overline{G_{si}}\right)$ for x = 1 and 4, $A_i = \overline{G_{si}}$ for x = 2 and 5, and $A_i = \left(\overline{\lambda_{si}} + \overline{G_{si}}\right)$ for j = 3 and 6; while $B_i = \left(\overline{\lambda_{si}} + 2\overline{G_{si}}\right)$ for x = 1, 2 and 3, and $B_i = \overline{G_{si}}$ for x = 4, 5, and 6. Solutions for equations (3.25a) and (3.25b) are obtained simultaneously (as these equations are coupled) using the 1-D FD method described in Chapter 2.

3.3.6 Solution algorithm

Monopile displacement and slope can be calculated from Equation (3.16) and (3.17) respectively. However, the soil parameters k_i, t_i, and Λ_i must be known to obtain monopile displacement and slope. The parameters k_i, t_i, and Λ_i depend on the functions ϕ_r and ϕ_θ which, in turn; depend on w through the six dimensionless constants γ_1-γ_6. Therefore, an iterative algorithm is followed to obtain solutions.

An initial guess of 1.0 is made for γ_1-γ_6 using which ϕ_r and ϕ_θ are determined, which are then substituted in equations of k_i, t_i, and Λ_i to obtain their values. Using the calculated values of k_i, t_i, and Λ_i monopile displacements and slopes are calculated. The calculated monopile displacements and slopes are then used to calculate γ_1-γ_6 which are compared with the assumed initial values. If the differences are more than the prescribed tolerable limit of 0.001, the calculations described so far are repeated with the calculated values of γ_1-γ_6 as the new initial guesses. Iterations are continued until the values of γ_1-γ_6 between successive iterations fall below the prescribed limit. Figure 3.2 illustrates the solution algorithm which is implemented

in a MATLAB script on a computer with Intel® Core™ i5-3210M CPU @ 2.50 GHz and 8 GB RAM.

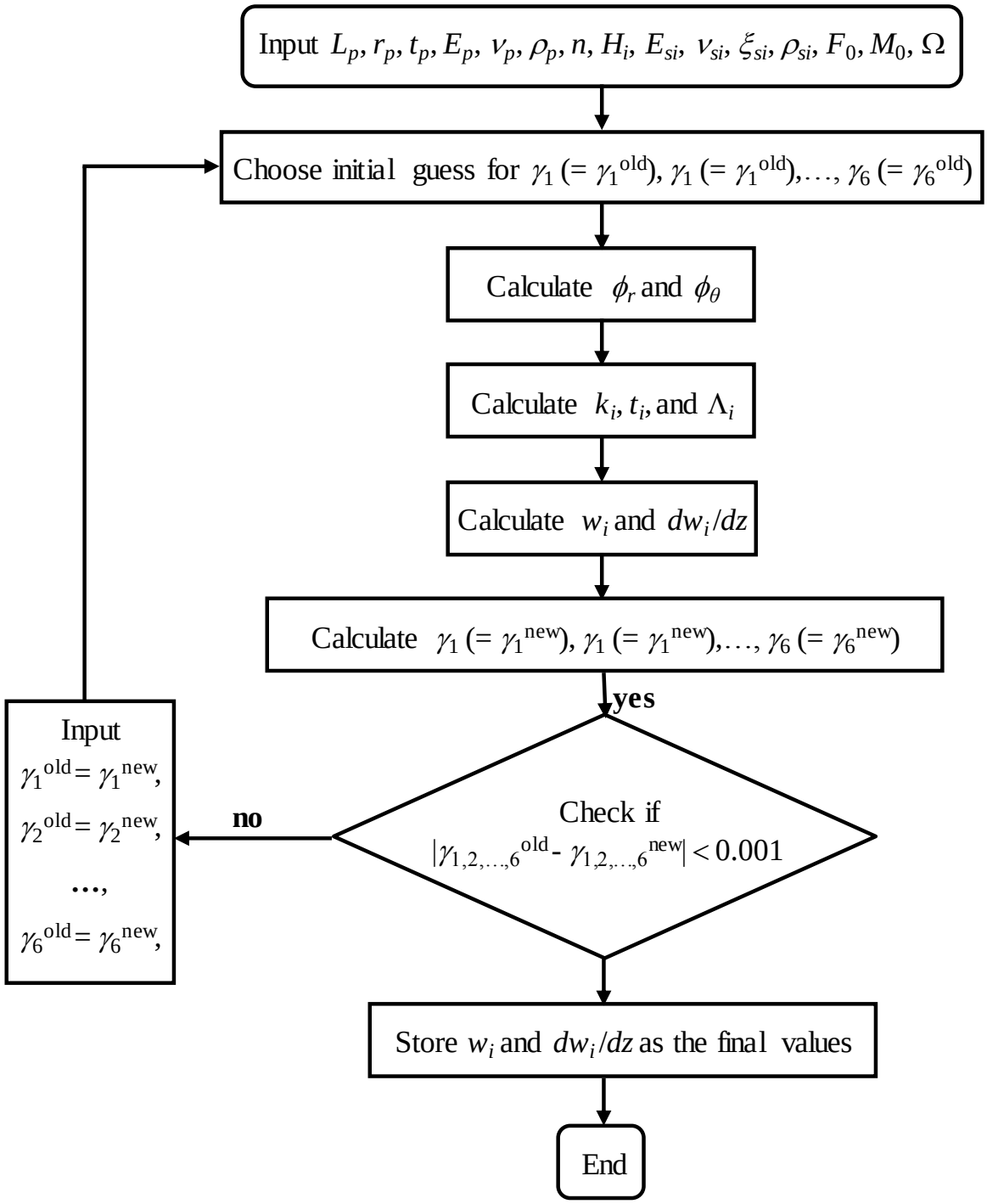

Figure 3.2: Solution algorithm

3.4 Simplification of analysis to Rayleigh and Euler-Bernoulli beam theory

The Rayleigh beam theory neglects the shear deformation which can be mathematically implemented by assuming infinite shear stiffness in the monopile. Setting $G_p \to \infty$ in equation (3.16) results in $F_i(z) = E_p I_p w_i(z)$ which simplifies the differential equation (3.18) as

$$E_p I_p \frac{d^4 w_i}{dz^4} - \left(2t_i - \rho_p I_p \Omega^2\right) \frac{d^2 w_i}{dz^2} + \left\{k_i - \left(\rho_p A_p + \Lambda_i\right)\Omega^2\right\} w_i = 0 \tag{3.28a}$$

with the relevant boundary conditions at different layer interfaces given

$$E_p I_p \frac{d^3 w_1}{dz^3} - \left(2t_1 - \rho_p I_p \Omega^2\right) \frac{dw_1}{dz} = F_0 \tag{3.28a}$$

$$E_p I_p \frac{d^2 w_1}{dz^2} = -M_0 \tag{3.28b}$$

$$w_i = w_{i+1} \tag{3.29a}$$

$$\frac{dw_i}{dz} = \frac{dw_{i+1}}{dz} \tag{3.29b}$$

$$E_p I_p \frac{d^3 w_i}{dz^3} - \left(2t_i - \rho_p I_p \Omega^2\right) \frac{dw_i}{dz} = E_p I_p \frac{d^3 w_{i+1}}{dz^3} - \left(2t_{i+1} - \rho_p I_p \Omega^2\right) \frac{dw_{i+1}}{dz} \tag{3.29c}$$

$$\frac{d^2 w_i}{dz^2} = \frac{d^2 w_{i+1}}{dz^2} \tag{3.29d}$$

$$E_p I_p \frac{d^3 w_n}{dz^3} - \left(2t_n - \rho_p I_p \Omega^2\right) \frac{dw_n}{dz} = -2t_{n+1} \frac{dw_{n+1}}{dz} \tag{3.30a}$$

$$\frac{d^2 w_n}{dz^2} = 0 \tag{3.30b}$$

Equation (3.27) along with the boundary conditions given by equation (3.28)-(3.30) gives monopile displacement w following the Rayleigh beam theory (Strutt 1877). Closed-form solution of w in equation (3.27) can be written in a similar way as given by equations (3.22a) and (3.22b) with w_i replacing F_i in equation (3.22a) with the coefficients α_i and η_i in equation (3.22b) being replaced for the case of Rayleigh beam theory by the following

$$\alpha_i = \frac{2t_i - \rho_p I_p \Omega^2}{E_p I_p} \tag{3.31b}$$

$$\eta_i = \frac{k_i - \left(\rho_p A_p + \Lambda_i\right)\Omega^2}{E_p I_p} \tag{3.31b}$$

The Euler-Bernoulli beam theory neglects both the shear deformation and rotatory inertia of beam cross-section. This can be mathematically obtained by setting $\rho_p I_p = 0$ in the differential equation and boundary conditions for the case of the Rayleigh beam theory (i.e., equations (3.27)-(3.30)).

3.5 Simplification of analysis to rigid beam theory

For rigid monopiles, the displacement profile is linear (similar to Chapter 2) and the monopile displacement is expressed as

$$w(z,t) = w_h(t) - \psi_h(t) z \tag{3.32}$$

where ψ_h is the clockwise rotation of the monopile axis at any time t. Equations (3.25)-(3.26) along with the solution procedure described in Chapter 2 are also valid for rigid piles.

The algebraic equations for monopile head displacement w_h and rotation ψ_h including the effect of translational and rotatory inertia of the monopile following the rigid beam theory are given by

$$\begin{Bmatrix} w_h \\ \psi_h \end{Bmatrix} = \begin{bmatrix} \overline{K_{rr}} & \overline{K_{r\psi}} \\ \overline{K_{\psi r}} & \overline{K_{\psi\psi}} \end{bmatrix}^{-1} \begin{Bmatrix} F_0 \\ M_0 \end{Bmatrix} \tag{3.33}$$

where

$$\overline{K_{rr}} = \sum_{i=1}^{n} \int_{H_{i-1}}^{H_i} \left(k_i - \Lambda_i \Omega^2\right) dz + \sqrt{2t_{n+1}\left(k_n - \Lambda_{n+1}\Omega^2\right)} - m_p \Omega^2 \tag{3.34a}$$

$$\overline{K_{r\psi}} = -\left[\sum_{i=1}^{n} \int_{H_{i-1}}^{H_i} \left(k_i - \Lambda_i \Omega^2\right) z dz + \left\{ 2t_n + \sqrt{2t_{n+1}\left(k_n - \Lambda_{n+1}\Omega^2\right)} L_p \right\} - m_p \Omega^2 \frac{L_p}{2} \right] \tag{3.34b}$$

$$\overline{K_{\psi r}} = -\left[\sum_{i=1}^{n} \int_{H_{i-1}}^{H_i} \left(k_i - \Lambda_i \Omega^2\right) z dz + \sqrt{2t_{n+1}\left(k_n - \Lambda_{n+1}\Omega^2\right)} L_p - m_p \Omega^2 \frac{L_p}{2} \right] \tag{3.34c}$$

$$\overline{K_{\psi\psi}} = \sum_{i=1}^{n} \int_{H_{i-1}}^{H_i} \left(k_i - \Lambda_i \Omega^2\right) z^2 dz + \left\{ 2t_n L_p + \sqrt{2t_{n+1}\left(k_n - \Lambda_{n+1}\Omega^2\right)} L_p^2 \right\} - m_p \Omega^2 \frac{L_p^2}{4} - m_p \left\{ \frac{r_p^2 - \left(r_p - t_p\right)^2}{4} + \frac{L_p^2}{12} \right\} \Omega^2 \tag{3.34d}$$

such that

$$m_p = \rho_p \pi \left\{ r_p^2 - \left(r_p - t_p \right)^2 \right\} L_p \tag{3.35}$$

3.6 Calculation of secondary variables

In addition to monopile displacement, the quantities of interest are the monopile bending moment *M*, shear force *V*, and the soil reaction force *p* per unit pile length at the monopile-soil interface. These quantities are also expressed in terms of *F* as

$$M(z) = E_p I_p \frac{d\psi}{dz} = \frac{d^2 F}{dz^2} \tag{3.36a}$$

$$V(z) = -\kappa G_p A_p \left(\frac{dw}{dz} - \psi \right) = \frac{d^3 F}{dz^3} + \frac{\rho_p \Omega^2}{E_p} \frac{dF}{dz} \tag{3.36b}$$

$$\begin{aligned} p(z) &= 2t \frac{d^2 w}{dz^2} - \left\{ k - \left(\rho_p A_p + \Lambda \right) \Omega^2 \right\} w \\ &= \frac{2t}{\kappa G_p A_p} \frac{d^4 F}{dz^4} + \left\{ \left(\frac{k}{\kappa G_p A_p} + \frac{2t}{E_p I_p} \right) - \left(\frac{\rho_p}{E_p} + \frac{2t \rho_p}{\kappa G_p E_p A_p} + \frac{\rho_p A_p + \Lambda}{\kappa G_p A_p} \right) \right\} \frac{d^2 F}{dz^2} \\ &\quad - \left\{ \frac{k}{E_p I_p} - \left(\frac{k \rho_p}{\kappa G_p E_p A_p} + \frac{\rho_p A_p + \Lambda}{E_p I_p} \right) \Omega^2 + \left(\frac{\rho_p A_p + \Lambda}{\kappa G_p E_p A_p} \right) \rho_p \Omega^4 \right\} F \end{aligned} \tag{3.36c}$$

The foregoing equations are valid for Rayleigh and Euler-Bernoulli theories as well after the required simplifications are made (by setting the terms with G_p in the denominator equal to zero for Rayleigh beam theory and additionally setting $\rho_p I_p = 0$ for Euler-Bernoulli beam theory, and substituting $F = E_p I_p w$ and $\psi = dw/dz$). For the Timoshenko beam theory, the shear rotation β can be calculated using

$$\beta(z) = \frac{V}{\kappa G_p A_p} \tag{3.37}$$

3.7 Results

To demonstrate the accuracy of the present analysis the results (complex dynamic pile-head impedances and pile response – displacement and rotation) from this analysis following the Timoshenko and Euler-Bernoulli beam theories are compared with the results of different

solution techniques (approximate continuum based formulation, rigorous continuum based formulation, and Winkler based formulation) available in the literature, for the case of solid reinforced concrete piles. The accuracy of the results (pile response – displacement and rotation) obtained from the present analysis following the rigid beam theory is verified with the results of 3-D FE analysis and Winkler based formulation, available in the literature. Two example problems are analyzed using the present analysis following the Timoshenko, Rayleigh, and Euler-Bernoulli beam theories for piles with solid and hollow cross-sections in a two-layer soil deposit overlying a rigid layer to investigate the effect of shear deformation and rotatory inertia on the dynamic response of laterally loaded piles, for a wide range of dimensionless frequency. Further, the appropriateness of the applicability of the dynamic analysis developed in this chapter versus the static analysis developed in Chapter 2 is investigated for the case of large-diameter monopiles which are typically subjected to a cyclic/dynamic loading of frequency less than 1.0 Hz.

3.7.1 Comparison of results from present analysis with an approximate 3-D analytical solution for small-diameter solid reinforced concrete piles

A comparison of the complex dynamic pile head impedance obtained from the present analysis is done with those by Novak and Nogami (1977) for the case of a free-head pile with pile base encased in a rigid layer (fixed pile base with zero displacements and rotation). Novak and Nogami (1977) based on the work of Tajimi (1969) developed a continuum-based model for analysis of laterally loaded piles (modeled as a Euler-Bernoulli beam) in a linear viscoelastic soil layer with frequency independent hysteretic material damping and embedded in a rigid stratum. In the analysis, zero vertical soil displacement was assumed (similar to the present analysis), appropriate potential functions were introduced to decouple the governing equations of motion for the soil, and the eigenvalue expansion over the vertical coordinate was utilized to obtain the pile response in terms of an infinite trigonometric series. The results from the present analysis are obtained for a solid reinforced concrete pile using the Timoshenko (shear correction factor κ for solid circular cross-section is the same as discussed in Chapter 2) and Euler-Bernoulli beam theories with $L_p/r_p = 20$, $E_p = 28$ GPa, $\nu_p = 0.2$, relative pile-soil stiffness ratio $E_p/G_s = 3 \times 10^3$, $\nu_s = 0.25$, $\lambda_s = 1.5G_s$, pile-soil density ratio $\rho_p/\rho_s = 1.25$, and $\xi_s = 0.025$. Figures 3.3(a)-(c) show the complex dimensionless pile head impedances for

swaying, coupled swaying-rocking, and rocking motions as functions of the applied dimensionless frequency $a_0 = \Omega r_p/V_s$ where $V_s = \sqrt{G_s/\rho_s}$ is the shear wave velocity of soil. The real part of the pile head impedances represents the pile stiffness and the imaginary part denotes the damping present in the system. Clearly, the present analysis captures the essential features of the mechanics of the problem and predicts the cut-off frequency (i.e., the natural frequency of the pile-soil system) very well. Below the cut-off frequency, no waves propagate and no radiation damping is generated in the system which can be seen from the plots. There is a sudden increase in the imaginary part of the complex dynamic impedance beyond the cut-off frequency which indicates that there is the propagation of waves within the pile-soil system and an initiation of the radiation damping (the plot shows the total damping ξ from the frequency dependent radiation damping ξ_r and the frequency independent hysteretic material damping ξ_s). The constant value of the imaginary part below the cut-off frequency is primarily an effect of the presence of only the material damping within the system. Figure 3.3(a) shows the impedance K_{rr} for swaying motion in a normalized form ($K_{rr}L_p^3/(E_pI_p)$), Figure 3.3(b) shows the impedance $K_{r\psi}$ for coupled swaying-rocking motion in a normalized form ($-K_{r\psi}L_p^2/(E_pI_p)$) (note that the impedances $K_{r\psi}$ and $K_{\psi r}$ are nearly equal), while Figure 3.3(c) shows the impedance $K_{\psi\psi}$ for rocking motion in a normalized form ($K_{\psi\psi}L_p/(E_pI_p)$). The match between the results obtained from the present analysis with those by Novak and Nogami (1977) is reasonably well, particularly for the swaying and coupled swaying-rocking modes although the cut-off frequency is overestimated by the present analysis for the rocking mode. This difference in the results is most likely a result of the difference in solution approaches in the two methods. In the present analysis, the impedances obtained using the Timoshenko beam theory is nearly identical to those obtained using the Euler-Bernoulli beam theory for the range of dimensionless frequency investigated.

.

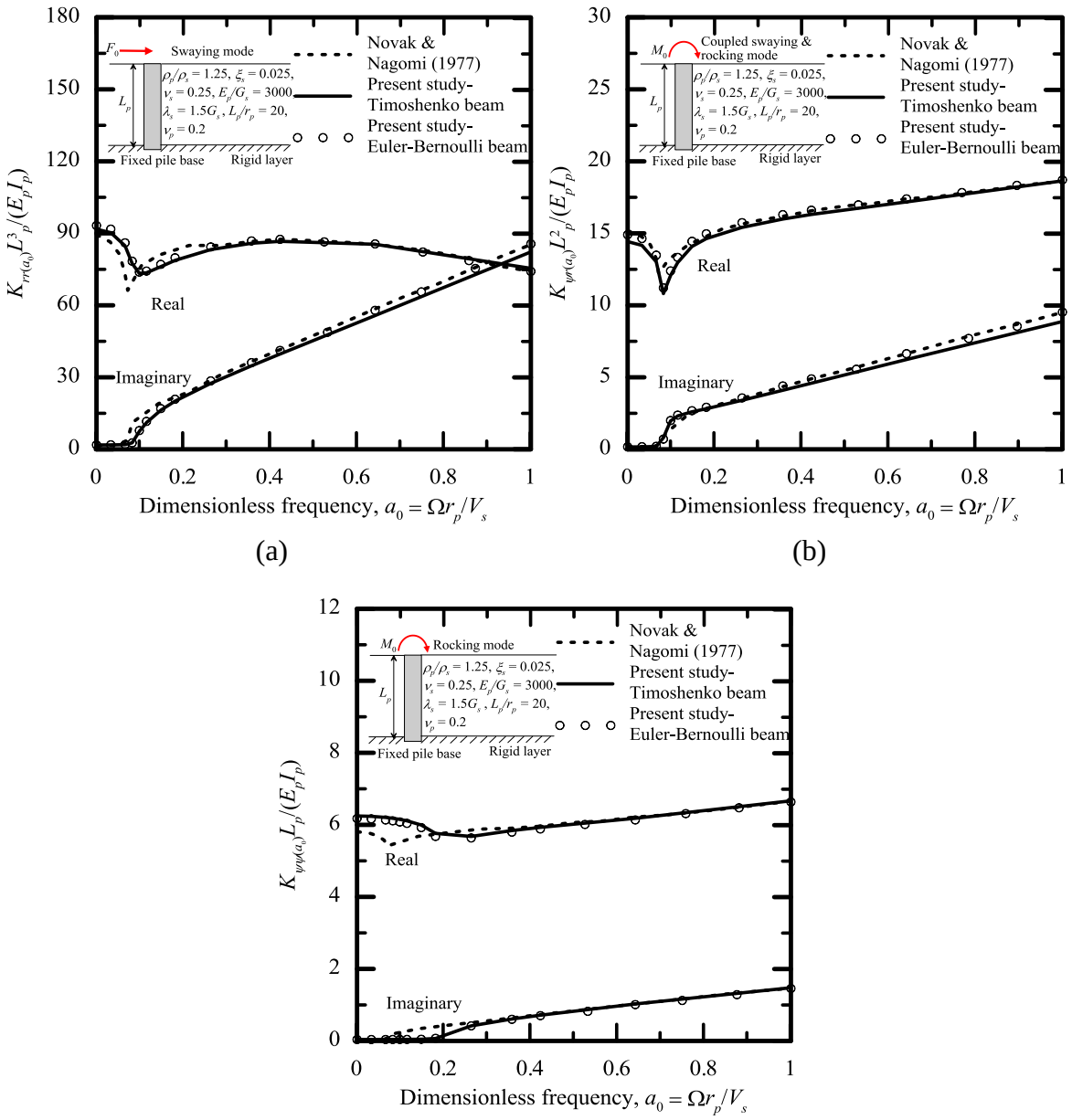

Figure 3.3: Dimensionless complex dynamic pile head impedance for (a) swaying, (b) coupled swaying-rocking, and (c) rocking motions of a free-head solid reinforced concrete piles embedded in a homogeneous soil layer with the pile base encased in a rigid layer

3.7.2 Comparison of results from present analysis with a 3-D elastodynamic solution for small-diameter solid reinforced concrete piles

A comparison of the results obtained from the present analysis is made with those by Pak and Jennings (1987), who developed a rigorous 3-D elastodynamic solution for laterally loaded free-head slender piles floating in homogeneous half-spaces. Pak and Jennings (1987) modeled the soil as a continuum with zero viscous hysteretic material damping and the pile as

a Euler-Bernoulli beam, formulated the pile-soil interaction using a Fredholm integral equation of the second kind and solved the equation using an appropriate numerical method. Dimensionless pile displacement w/r_p and slope dw/dz, caused by an applied force and a moment, as obtained by Pak and Jennings (1987), are compared with the corresponding results of the present analysis performed using the Timoshenko (shear correction factor κ for the pile with solid circular cross-section is the same as that discussed in Chapter 2) and Euler-Bernoulli beam theories, as shown in Figures 3.4(a)-(b). The results are obtained for a solid reinforced concrete pile with $L_p/r_p = 50$, $E_p = 28$ GPa, $\nu_p = 0.2$, relative pile-soil stiffness ratio $E_p/G_s = 1.25 \times 10^4$, $\nu_s = 0.25$, pile-soil density ratio $\rho_p/\rho_s = 1.7$, and $\xi_s = 0$, and an applied dimensionless frequency $a_0 = 0.2$. The match between the results obtained from the present analysis with those by Pak and Jennings (1987) is reasonably well. The results of the present analysis obtained using the Timoshenko beam theory are not appreciably different from the results obtained using the Euler-Bernoulli beam theory. Comparisons are made for three more problems analyzed by Pak and Jennings (1987) and the dimensionless pile displacement and slope are shown in Figures 3.5-3.7 (the input data used for the analysis are given in the figures). As before, the match between the results obtained from the present analysis with those by Pak and Jennings (1987) is well. Although the pile responses matched well in Figures 3.5-3.7, the dynamic pile head impedances were not found to be smooth functions of the forcing frequency, which is in contrast with what Pak and Jennings (1987) obtained. This happened because the present analysis does not truly model a half-space (Sun and Pires 1993, 1995, Gazetas 1995) and is appropriate for modeling pile-soil systems in which the bottom-most soil layer is considered rigid (this condition is more applicable in real fields) (Anoyatis and Lemnitzer 2017).

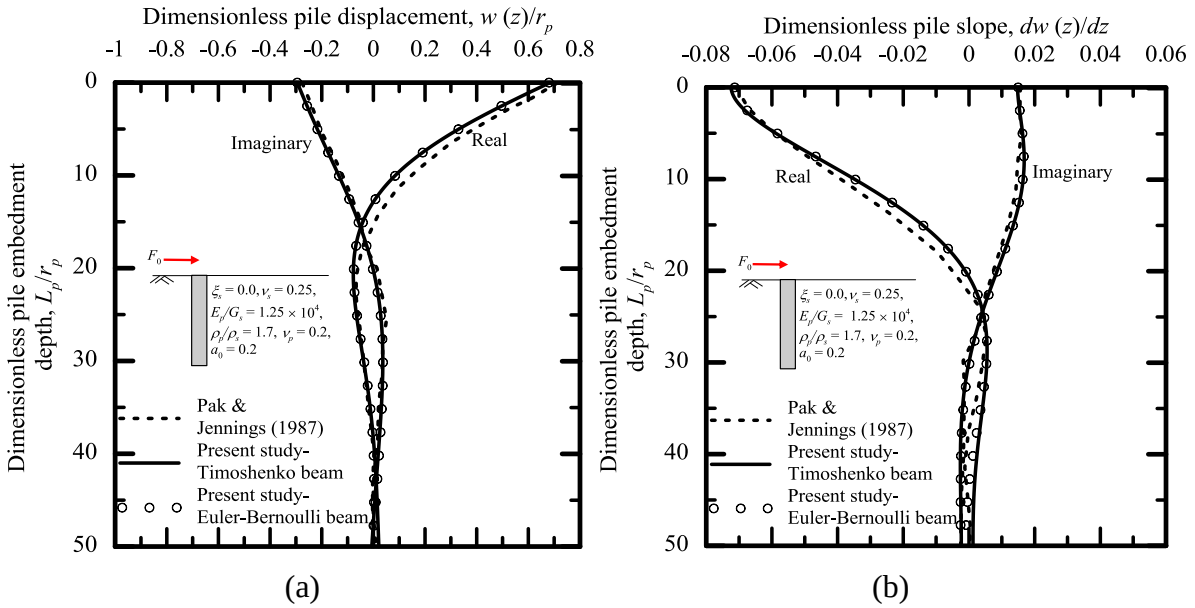

Figure 3.4: Dimensionless pile (a) displacement and (b) slope of a free-head solid reinforced pile with a relative pile-soil stiffness ratio of 1.25×10^4 and subjected to an applied force at the head

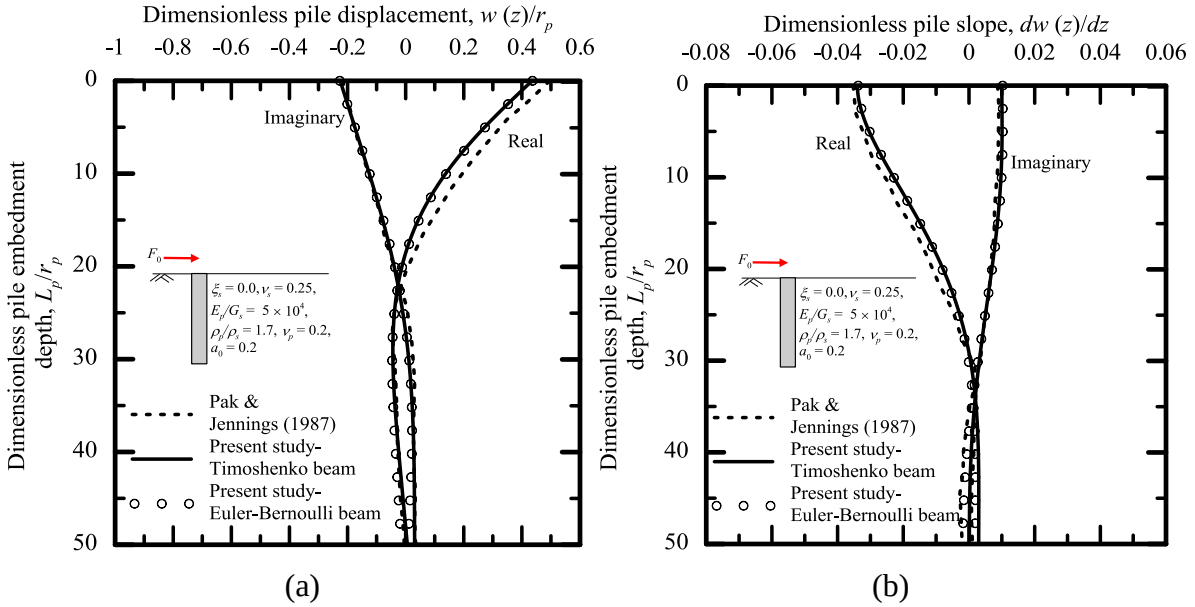

Figure 3.5: Dimensionless pile (a) displacement and (b) slope of a free-head solid reinforced pile with a relative pile-soil stiffness ratio of 5×10^4 and subjected to an applied force at the head

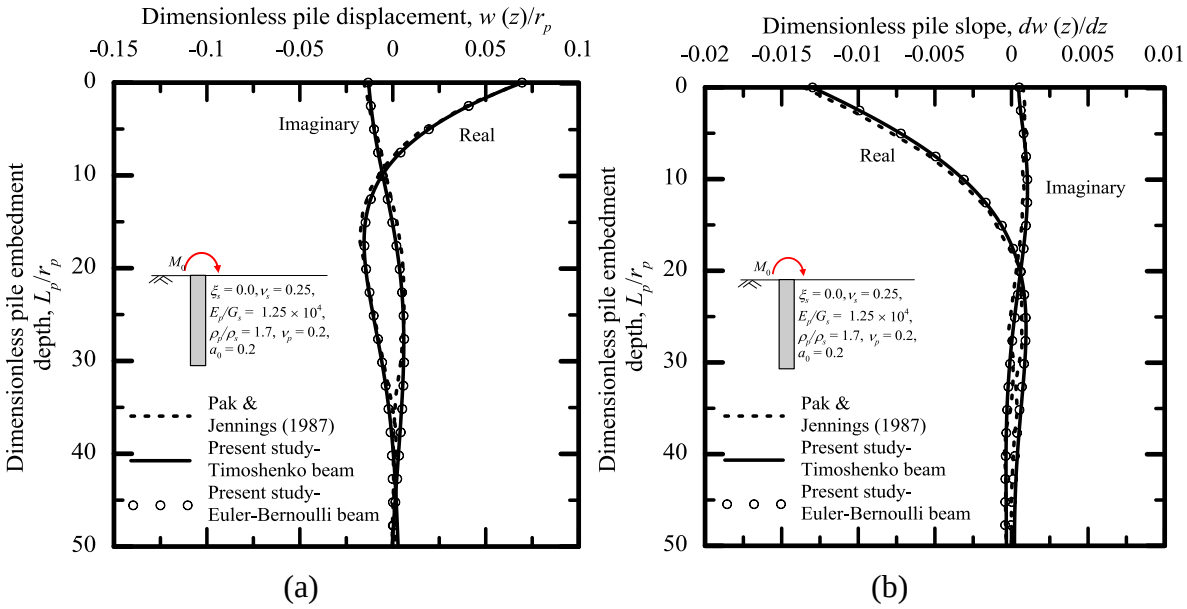

Figure 3.6: Dimensionless pile (a) displacement and (b) slope of a free-head solid reinforced pile with a relative pile-soil stiffness ratio of 1.25×10^4 and subjected to an applied moment at the head

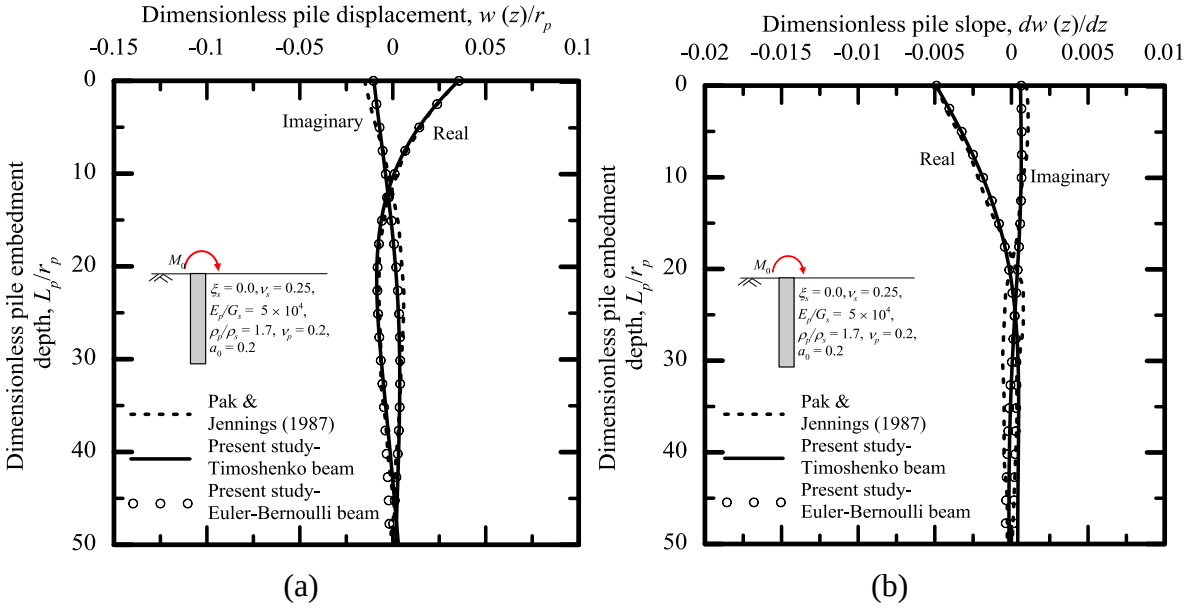

Figure 3.7: Dimensionless pile (a) displacement and (b) slope of a free-head solid reinforced pile with a relative pile-soil stiffness ratio of 5×10^4 subjected to an applied moment at the head

3.7.3 Comparison of results from present analysis with a Winkler based analytical solution for large-diameter solid reinforced concrete piles

A comparison of the present analysis is also made with the analysis developed by Mylonakis (2001) (this analysis was verified with the rigorous numerical FE solution developed by Kaynia and Kausel (1982)) for estimating the lateral dynamic pile head stiffness of fixed-head large diameter shafts embedded in homogeneous, linear viscoelastic soil with the pile bases resting on top of rigid layers (i.e., hinged pile base condition with zero displacement and bending moment at the pile base). Figure 3.8 shows the dynamic swaying pile-head impedance $K_{rr(a_0)}\left[=K_{rr(a_0=0)}(k_{(a_0)}+2j\xi_{(a_0)})\right]$ (the imaginary part ξ is a summation of the frequency-dependent radiation damping ξ_r and frequency independent material damping ξ_s) normalized with respect to the corresponding static swaying impedance, as obtained from the present analysis and Mylonakis (2001). A very good match is obtained between the results of the present and the developed analysis by Mylonakis (2001). Further, the Timoshenko beam theory does not produce a significantly different result in comparison to the Euler-Bernoulli beam theory for the range of dimensionless frequency investigated.

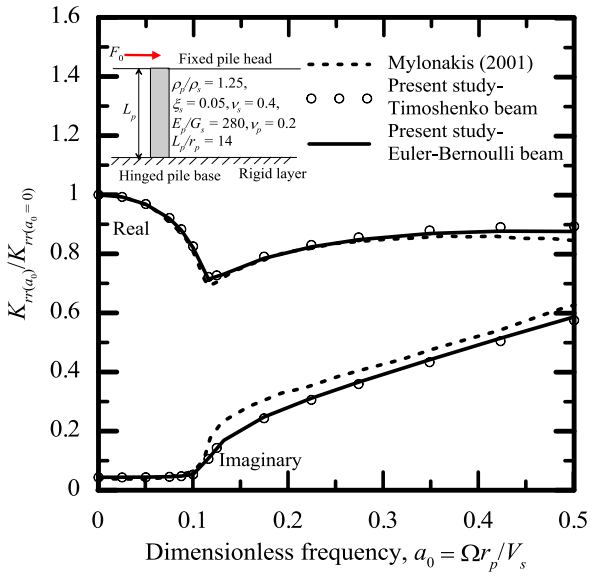

Figure 3.8: Dimensionless dynamic swaying head impedance of a fixed-head solid reinforced concrete pile in a homogeneous soil profile with the pile base resting on top of a rigid stratum

3.7.4 Comparison of results from present analysis with 3-D FE solution and Winkler based solution for the case of large-diameter solid rigid piles

A comparison of the results obtained from the present analysis following the rigid beam theory is made with that of a Winkler-based analysis developed by Varun et al. (2009) for estimating the dynamic response of rigid piles embedded in a multilayered soil deposit. Varun et al. (2009) verified their analytical technique with the results of rigorous 3-D FE solution (performed using Abaqus). Figures 3.9(a)-(b) show the comparisons of the maximum pile head displacement and rotation, respectively, as functions of the applied a_0 (= $\Omega r_p/V_{s1}$ where V_{s1} is the shear wave velocity of the topsoil layer) for a massless rigid pile (i.e. ρ_p = 0) embedded into a three-layer soil profile with ξ_{si} = 0. The other details of the pile and the soil properties are provided in the Figures 3.9(a)-(b). The results obtained from the present analysis is also compared with the results of a Winkler based model developed by Zhong and Huang (2013) for estimating the dynamic response of rigid caissons. Figures 3.9(a)-(b) show that a reasonable match is obtained between the results of the present analysis and the results obtained from the Winkler-based analysis and finite element analysis. Results obtained from the present analysis are in good agreement with that of the finite element analysis whereas there is some difference with the results of the Winkler-based analysis.

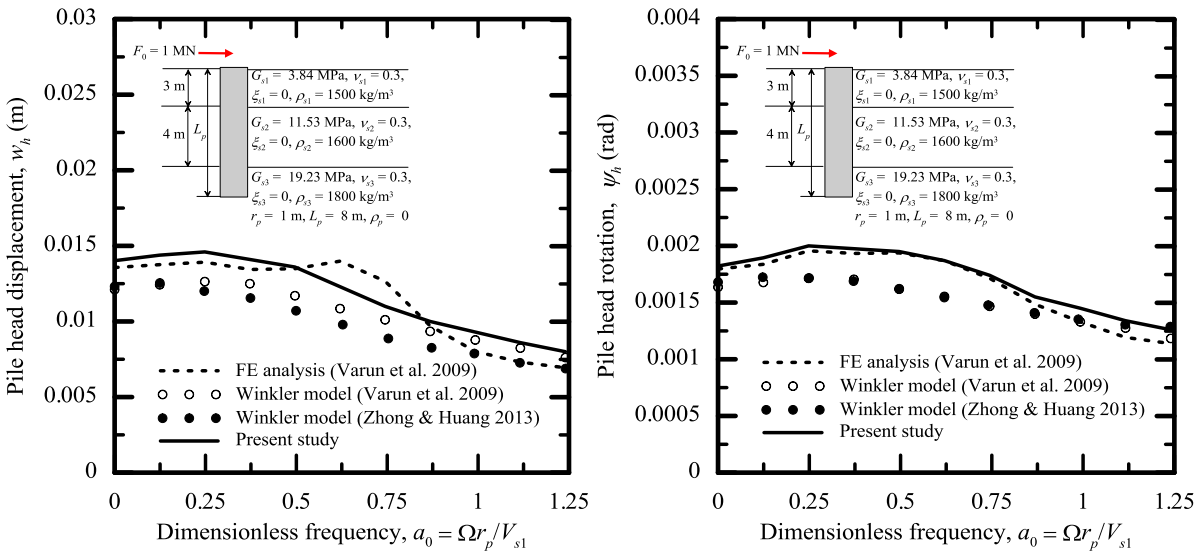

Figure 3.9: Maximum pile head (a) displacement and (b) rotation of a rigid pile embedded in a three-layer soil deposit subjected to a lateral force at the head

3.7.5 Example problems for reinforced concrete solid pile and steel hollow pile in a two-layer soil

Two example problems are analyzed, one with a reinforced concrete pile with a solid cross-section and the other with a steel pipe pile with the hollow cross-section, both embedded in two-layer soil with the pile bases encased in rigid layer (i.e., fixed base condition with zero rotation and displacement). The normalized dynamic pile-head impedances for swaying ($K_{rr}L^3_p/(E_pI_p)$), coupled swaying-rocking ($-K_{r\psi}L^2_p/E_pI_p$), and rocking ($K_{rr}L_p/E_pI_p$)) are plotted in Figures 3.10-3.11 for these two piles as functions of dimensionless frequency a_0 (= $\Omega r_p/V_{s1}$) which is normalized with respect to the shear wave velocity $V_{s1}\left(=\sqrt{G_{s1}/\rho_{s1}}\right)$ of the first soil layer. Results are obtained for all the three beam theories to investigate the effect of shear deformation and rotatory inertia of the pile cross-section on the pile response. The details of the pile and soil properties used as inputs in these examples are shown in the figures.

The variation of the pile head impedances with frequency for these two examples with layered soil profile are similar to those obtained earlier for the problems with a single soil layer. For the case of the reinforced concrete pile (Figure 3.10), the impedances for the swaying and coupled swaying-rocking modes predicted following the Euler-Bernoulli beam theory is slightly greater than that predicted using the Timoshenko beam theory. For the rocking mode, the impedance from the Euler-Bernoulli beam theory is less than that obtained using the Timoshenko beam theory. Further, the Euler-Bernoulli and Rayleigh beam theories produce nearly identical results, which show that the rotatory inertia of the pile cross-section has little effect on the estimation of the pile head impedance for the range of dimensionless frequency investigated. For the case of hollow steel pile (Figure 3.11), the difference in response using the Euler-Bernoulli and Timoshenko beam theories is more but not significantly different. As before, the impedances for the swaying and coupled swaying-rocking modes are greater and that for the rocking mode is less as obtained using the Euler-Bernoulli beam theory when compared with the Timoshenko beam theory; however, the difference is not significant. Again, the Euler-Bernoulli and Rayleigh beam theories produced nearly identical impedances for the range of dimensionless frequency investigated.

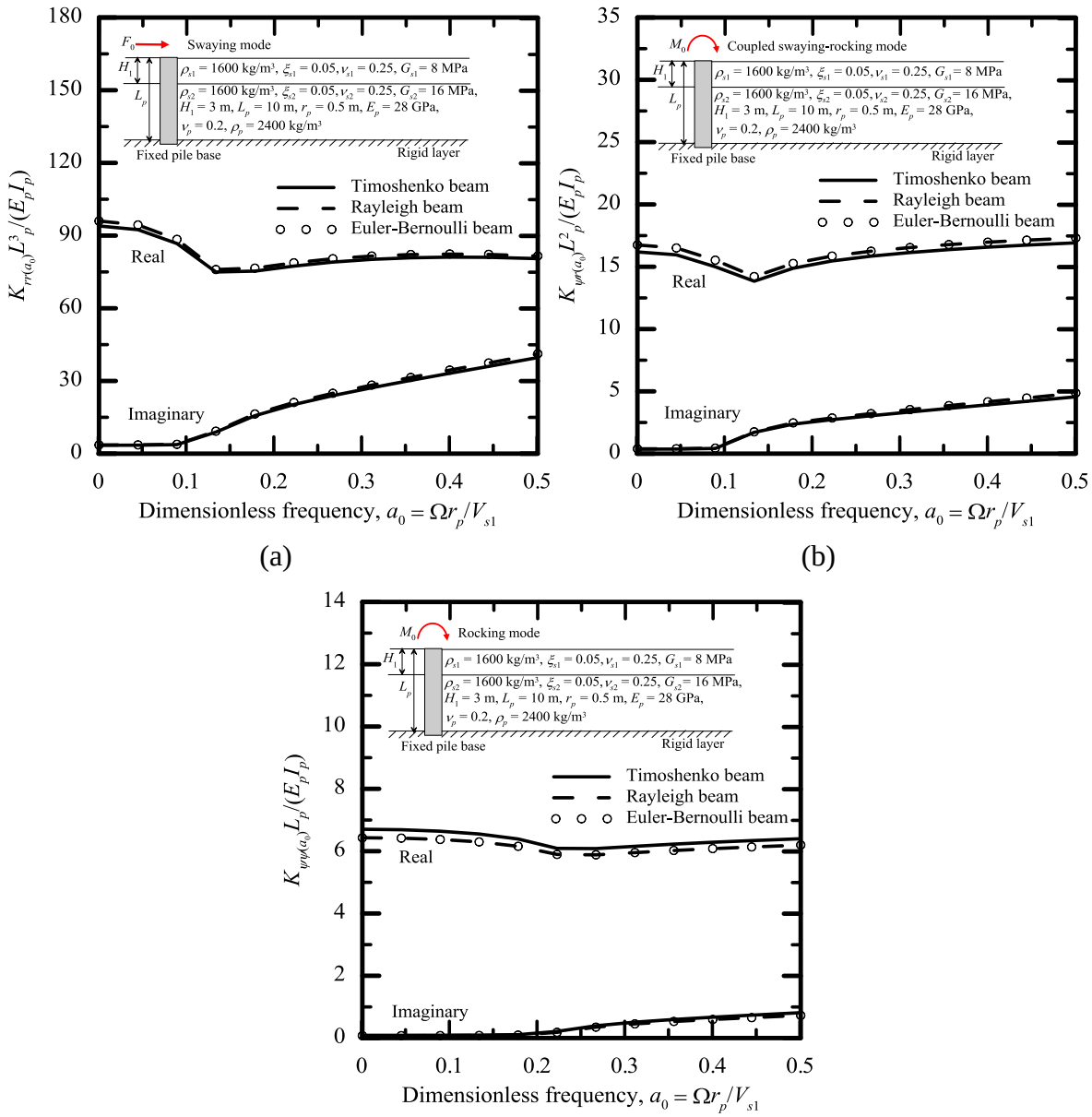

Figure 3.10: Dimensionless pile head impedances for (a) swaying, (b) coupled swaying-rocking, and (c) rocking motions of a free-head solid reinforced concrete pile embedded in a two-layer soil overlying a rigid layer with the pile base encased in the rigid layer

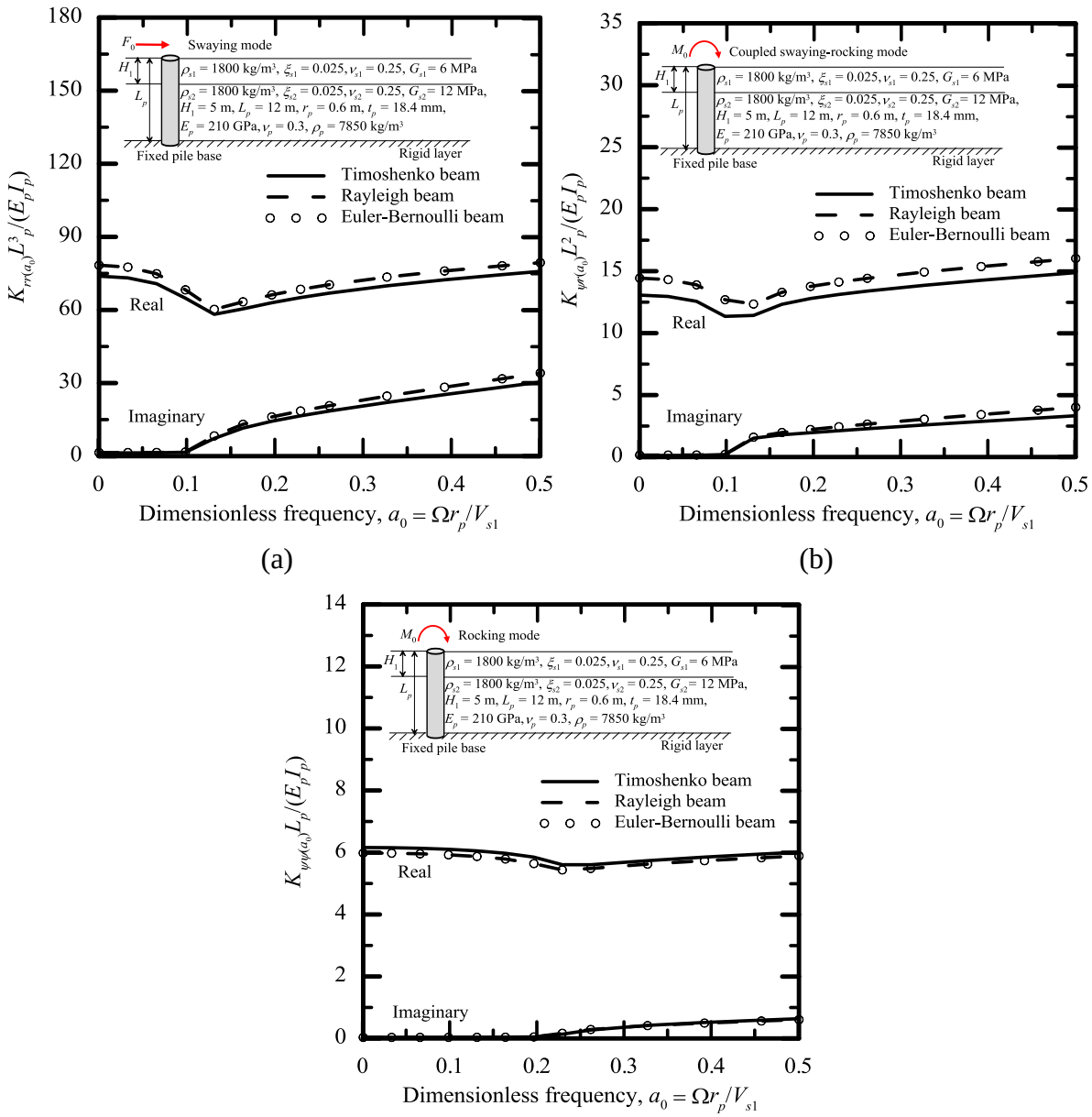

Figure 3.11: Dimensionless pile head impedances for (a) swaying, (b) coupled swaying-rocking, and (c) rocking motions of a free-head hollow steel pile embedded in a two-layer soil overlying a rigid layer with the pile base encased in the rigid layer

3.8 Investigation of the applicability of dynamic analysis to obtain monopile response

In the foregoing section, the accuracy of the present analysis following different beam theory is shown for the case of small-diameter solid reinforced concrete piles with $L_p/r_p \geq 20$ (Figures 3.3-3.7) and large-diameter solid reinforced concrete piles with $L_p/r_p < 20$ (Figures 3.8-3.9) for a wide range of dimensionless frequency encountered in practice. Example

problems are also solved to investigate the difference in results obtained from various beam theories (Timoshenko, Rayleigh, and Euler-Bernoulli) for the case of small-diameter solid reinforced concrete (Figure 3.10) and hollow steel (Figure 3.11) piles with $L_p/r_p \geq 20$. From the comparisons and example problems, it is found that the effect of rotatory inertia is insignificant and the difference in results between the Timoshenko and Euler-Bernoulli beam theory is primarily an effect of shear deformation within the pile cross-section, although the difference is small for the cases studied.

The objective of this section is to investigate and determine the applicability of the dynamic analysis developed in this chapter for estimating the response of large-diameter monopiles versus the static analysis developed in Chapter 2. This investigation is necessary because monopiles are typically subjected to cyclic/dynamic loads of frequency $f < 1$ Hz and in that case the inertial effect of the monopile and soil, the hysteretic material damping ratio, and the radiation damping because of wave propagation within the soil (which are included in this dynamic analysis) might not be significant and the static analysis might be itself sufficient for estimating monopile response. For the investigation, four different monopiles currently supporting offshore wind turbines in Europe (see Table 3.1) are chosen; the monopile properties (L_p, r_p, t_p, E_p = 210 GPa, ν_p = 0.3, and ρ_p = 7850 kg/m^3) and average Young's modulus E_s (obtained from shear wave velocity measurements) of the soil at different wind farm sites are selected following Adhikary and Bhattacharya (2012) and Shadlou and Bhattacharya (2016), respectively, and typical values of ν_s = 0.25, ρ_s = 1700 kg/m^3, and ξ_s = 0.05 (Mylonakis 2001) is assumed. The applied loading F_0 and M_0 are assumed and the maximum dimensionless frequency a_0 for each of the wind farm site reported by Adhikary and Bhattacharya (2012) (see Table 3.1) is used.

Table 3.1 shows the maximum monopile head response (displacement w_h and rotation ψ_h) obtained from the dynamic analysis developed in this chapter and the static analysis developed in Chapter 2 following the Timoshenko, Euler-Bernoulli, and rigid beam theory. It can be seen from Table 3.1 that the difference in the dynamic response of monopiles in a homogeneous viscoelastic soil and the static response of monopiles in a homogeneous elastic soil, is not significantly different. The dynamic response following different beam theories is always greater than the static response for the range of dimensionless frequency investigated. A maximum difference of 4.4%, 4.7%, and 3.7% in the monopile head displacement and 4.4%,

4.8%, and 1.0 % in the monopile head rotation for the Timoshenko, Euler-Bernoulli, and rigid beam theory, respectively, is obtained between the dynamic and static response, for the Walney wind farm site. For all the other wind farm sites (Lely-A2, North Hoyle, Irena Vorrink), the difference between the dynamic and static response of monopiles following different beam theories is either identical or less than 3%. A comparison of the computational time required to obtain monopile response between the present dynamic and static analysis following different beam theories for all the wind farm sites is also depicted in Table 3.2. It is evident from Table 3.2 that the computational time required for the dynamic analysis is approximately three times more than that of the static analysis; this is a result of calculations involving complex numbers within the dynamic analysis. Therefore, from the foregoing discussion, it is evident that performing a dynamic analysis to obtain monopile response which is typically subjected to loading frequency less than 1 Hz is not necessary since the static analysis can produce relatively accurate results, besides, it is computational efficient than the dynamic analysis.

A comparison of the percentage difference in static response obtained from Euler-Bernoulli and rigid beam theory with respect to Timoshenko beam theory for the four wind farm sites is also depicted in Table 3.3. It can be seen that the percentage error in the response obtained from rigid theory is the greatest; this is because the rigid theory is applicable to monopiles when $E_p/G_s^* \geq 10^5$ and L_p/r_p is in the range of 5-20 (Table 2.4). Therefore, a careful consideration of E_p/G_s^* and L_p/r_p is required to use the rigid theory for monopiles. Further, for all the cases studied, the percentage difference in response between the Timoshenko and Euler-Bernoulli beam theory is approximately < 3% for w_h and 9% for ψ_h. Although the Timoshenko beam theory gives a better prediction of monopile head rotation – the difference is typically < 10% for the case of combined loading (F_a and M_a) at the monopile head (also shown in Figures 2.6-2.8). Therefore, the Euler-Bernoulli beam theory can be used to obtain monopile response without significant loss of accuracy instead of the Timoshenko beam theory. Further, the Euler-Bernoulli beam theory, unlike the rigid theory, accounts for both bending and rigid body rotation irrespective of E_p/G_s^* and L_p/r_p for monopiles available in the practice.

Table 3.1: Dynamic and static response of monopiles from the present analysis for wind farm sites in Europe

Wind farm site	**Soil property**	**Monopile properties**	**Applied loading**	**Dynamic response of monopiles in homogeneous viscoelastic soil**			**Static response of monopiles in homogeneous elastic soil**		
				Timoshenko	**Euler-Bernoulli**	**Rigid**	**Timoshenko**	**Euler-Bernoulli**	**Rigid**
Lely-A2, Netherlands	E_s = 42.5 MPa	L_p = 20.9 m r_p = 1.85 m t_p = 35 mm	F_0 = 3 MN M_0 = 30 MN f = 0.94 Hz a_0 = 0.11	w_h = 14.7 mm ψ_h = 0.147°	w_h = 14.5 mm ψ_h = 0.138°	w_h = 11.3 mm ψ_h = 0.043°	w_h = 14.4 mm ψ_h = 0.147°	w_h = 14.3 mm ψ_h = 0.138°	w_h = 11.2 mm ψ_h = 0.042°
North Hoyle, Wales, UK	E_s = 382.5 MPa	L_p = 33 m r_p = 2 m t_p = 46.4 mm	F_0 = 5 MN M_0 = 60 MN f = 0.717 Hz a_0 = 0.03	w_h = 4.6 mm ψ_h = 0.094°	w_h = 4.6 mm ψ_h = 0.086°	w_h = 1.3 mm ψ_h = 0.003°	w_h = 4.6 mm ψ_h = 0.094°	w_h = 4.5 mm ψ_h = 0.086°	w_h = 1.3 mm ψ_h =0.003 °
Irena Vorrink, Netherlands	E_s = 42.5 MPa	L_p = 19 m r_p = 1.75 m t_p = 28 mm	F_0 = 2.5 MN M_0 = 20 MN f = 0.91 Hz a_0 = 0.1	w_h = 12.4 mm ψ_h = 0.136°	w_h = 12.3 mm ψ_h = 0.126°	w_h = 9.8 mm ψ_h = 0.042°	w_h = 12.3 mm ψ_h = 0.136°	w_h = 12.1 mm ψ_h = 0.126°	w_h = 9.5 mm ψ_h = 0.04°
Walney, England, UK	E_s = 30 MPa	L_p = 23.5 m r_p = 3 m t_p = 80 mm	F_0 = 8 MN M_0 = 100 MN f = 0.90 Hz a_0 = 0.2	w_h = 34.1 mm ψ_h = 0.152°	w_h = 33.9 mm ψ_h = 0.145°	w_h = 34.8 mm ψ_h = 0.108°	w_h = 32.6 mm ψ_h = 0.148°	w_h = 32.3 mm ψ_h = 0.138°	w_h = 33.5 mm ψ_h = 0.107°

Table 3.2: Computational time required to obtain the dynamic and static response of monopiles from the present analysis for wind farm sites in Europe

Wind farm site	**Dynamic analysis, (secs)**			**Static analysis, (secs)**		
	Timoshenko	**Euler-Bernoulli**	**Rigid**	**Timoshenko**	**Euler-Bernoulli**	**Rigid**
Lely-A2, Netherlands	1349	1033	534	381	371	297
North Hoyle, Wales, UK	935	748	624	279	268	213
Irena Vorrink, Netherlands	1123	825	535	383	367	281
Walney, England, UK	1559	1202	504	591	563	452

Table 3.3: Percentage difference in static response obtained from Euler-Bernoulli and rigid beam theory with respect to Timoshenko beam theory for wind farm sites in Europe

Wind farm site	L_p/r_p	E_p/G_s^*	**% difference in the static head displacement w_h between Timoshenko (T), Euler-Bernoulli (EB), and Rigid (R) beam theory**		**% difference in the static head rotation ψ_h between Timoshenko (T), Euler-Bernoulli (EB), and Rigid (R) beam theory**	
			(T-EB)/TB×100 %	**(T-R)/T×100 %**	**(T-EB)/T×100 %**	**(T-R)/T×100 %**
Lely-A2, Netherlands	11.3	$> 10^4$	0.7	22.2	6.1	71.4
North Hoyle, Wales, UK	16.5	$< 10^4$	2.1	71.7	8.5	96.8
Irena Vorrink, Netherlands	10.9	$> 10^4$	1.6	22.7	7.3	70.5
Walney, England, UK	7.9	$> 10^4$	0.9	2.7	6.8	27.7

3.9 Summary

A mathematical framework for the dynamic analysis of laterally loaded monopiles embedded in a multilayered soil is presented in which the Timoshenko beam theory is used to model the monopile and viscoelastic continuum theory is used to model the soil. Rational displacement field, maintaining the 3-D nature of the problem, is assumed for the soil and the equilibrium of the pile-soil system is obtained by applying the extended Hamilton's principle. Two sets of coupled differential equations describing the pile and soil displacements are obtained using the variational principles of mechanics, which are solved analytically and numerically, respectively, following an iterative algorithm. It is shown mathematically that the Timoshenko beam theory leads to the most generalized form of differential equations, and successive simplifications of these equations result in the differential equations for the Rayleigh and Euler-Bernoulli beam theories, respectively.

The accuracy of the proposed method is ensured by comparing the dynamic pile head impedances, pile displacement, and rotation obtained from this analysis with those obtained from three different types of formulations of varying degree of sophistication — approximate continuum-based analytical solution, rigorous continuum-based analytical solution, and approximate Winkler-type analytical solution. Two example problems are analyzed that demonstrate the use of the analysis in layered soil deposit. Further, the applicability of the dynamic analysis developed in this chapter versus the static analysis developed in Chapter 2 is investigated for the case of large diameter monopiles. In the investigation, the dynamic and static response obtained following various beam theories are compared, besides a comparison of the computational time required to obtain monopile response between the dynamic and static analysis is also shown.

CHAPTER 4

Static Analysis of Laterally Loaded Monopiles in Multilayered Nonlinear Elastic Soil

4.1 Introduction

In this chapter, the mathematical framework developed in Chapter 2 is extended to include the effect of nonlinear soil behavior. In the analysis, the monopile is assumed to be an elastic Euler-Bernoulli beam (since the Euler-Bernoulli beam theory produces reasonably accurate pile/monopile response in comparison to the Timoshenko beam theory and accounts for both bending and rigid body rotation, unlike, the rigid beam theory) and each soil layer is considered to be a continuum characterized by nonlinear elastic constitutive relationships which describe the variation of shear modulus with strain. The displacement within the soil mass in different directions because of monopile movement is considered to be a product of separable functions and the principle of virtual work is applied to obtain the governing differential equations describing the monopile and soil displacements that are solved numerically using the 1-D FD method, in an iterative scheme.

The mathematical accuracy of the present analysis is verified by comparing the nonlinear pile response (head displacement and rotation) obtained from the present analysis with those of the response obtained from equivalent 3-D nonlinear elastic FE analysis. A comparison of the time required to obtain results between the present and FE analysis is also shown to demonstrate the computational efficiency of the present analysis. In order to validate the accuracy of the present analysis, the predicted results obtained from the present analysis using nonlinear elastic constitutive relationships are compared with the results of the *p-y* analysis and full-scale field pile-load tests for a few case studies in clayey and sandy soil deposit, available in the literature. Further, to assess the applicability of the present nonlinear elastic approach in predicting monopile response, the results obtained from the present analysis are also compared with the results of elastic-plastic 3-D FE simulations (unlike, the present analysis, the soil behaviour in the FE analysis is described using a linear elastic-perfectly plastic constitutive model following the Tresca yield criterion) and the *p-y* analysis. A comparison of the computational time from the present nonlinear elastic approach, linear

elastic-perfectly plastic FE analysis, and the *p-y* analysis shows that the present analysis predicts accurate and faster results.

4.2 Overview of existing formulations for analysis of laterally loaded piles in nonlinear soil

In the last few decades, several computational methods have been developed to predict the nonlinear response of laterally loaded pile foundations. These methods can be broadly classified into three categories: (i) *p-y* method (McClelland and Focht 1958, Matlock 1970, Reese et al. 1975, Reese and Welch 1975, Georgiadis 1983, O'Neill and Murchinson 1983, O'Neill et al. 1990, Yan and Byrne 1992, Reese 1997, Anderson et al. 2003, Kim et al. 2004, Zhang and Ahmari 2013), (ii) strain wedge model (SWM) (Norris 1986, Gowda 1991, Ashour et al. 1998, Ashour and Norris 2000, Ashour et al. 2002, Xu et al. 2013, Yang et al. 2017), and (iii) continuum-based methods based on FE and FD solution techniques (Desai and Appel 1976, Faruque and Desai 1982, Pressley and Poulos 1986, Kooijman 1989, Trochanis et al. 1991, Bhowmik 1992, Wakai et al. 1999, Yang and Jeremic 2005, Kim and Jeong 2011, Ahmed and Hawlader 2016).

Of the different methods discussed above, the *p-y* method is widely used by geotechnical engineers and also included in several design codes of practice (API 2011, DNV 2014). In the *p-y* method, the pile is considered to be an elastic Euler-Bernoulli beam while the soil is modeled as a series of independent, nonlinear, 1-D springs at distinct locations along the pile length which are characterized by nonlinear force-displacement relationships (commonly termed as *p-y* curves). This kind of modeling is often referred to as a beam on nonlinear Winkler foundation (BNWF) in the geotechnical foundation engineering literature. These *p-y* curves depend on the soil properties and depth at which the spring is attached to the pile (*p* is the soil reaction force per unit pile length at a given depth and *y* is the corresponding lateral pile displacement at that depth). However, there are a few limitations associated with the *p-y* method: (i) the *p-y* curves are modeled as independent springs along the pile-shaft which are characterized by the spring constant *k* along the pile-shaft and they do not account for the shear transfer *t* between adjacent soil layers; thus, neglecting the continuum nature of the pile-soil interaction problem, (ii) the *p-y* curves reported in several design codes (e.g., API 2011 and DNV 2014) are developed from a few full-scale field pile-load tests on slender piles

and their applicability to larger-diameter piles (e.g., monopiles) is questionable, besides, the curves developed are site-specific and considerable judgment is required for using these *p-y* curves to predict pile response at a different site; in fact, standard *p-y* curves have often failed to predict the actual pile response (Yan and Byrne 1992, Kim et al. 2004), and (iii) parameters such as the ε_{50} (strain corresponding to one half of the maximum deviatoric stress) used for soft clay (Matlock 1970) and stiff clay (Reese et al. 1975) criterion for the development of *p-y* curves (also available in commercial software's such as LPILE (Reese and Wang 1997)) is semi-empirical.

The SWM eliminates some of the limitations of the *p-y* method by estimating the *p-y* curves for the 1-D BNWF from the soil strain in the 3-D passive wedge mobilized in front of the pile because of pile movement, thus, providing a theoretical link between the more sophisticated 3-D pile-soil interaction and the simpler 1-D BNWF characterization. However, both the *p-y* method and the SWM depend on parameters (e.g., ε_{50}) that are based on the user's experience rather than fundamental considerations, hence, these methods are semi-empirical. Besides, it is shown in the literature that both the *p-y* method and SWM are unsuitable to analyze and design monopiles (Lesny et al. 2007).

The continuum-based method with FE or FD solution techniques using commercially available software packages (e.g., Abaqus) or self-developed research codes can handle various geometry, boundary conditions, and elastic-plastic constitutive soil models which can be used to predict the nonlinear response of laterally loaded piles accurately and realistically. Despite the versatility associated with these methods, their use in routine geotechnical engineering design is limited because of (i) the modeling knowledge and expertise required to develop such solution techniques or the use of a particular software package and (ii) such solution techniques require considerably large computational effort to obtain solutions. The FE software packages (e.g., Abaqus) facilitate the use of sophisticated constitutive relationships based on elasticity and plasticity theory (soil yielding and strain/work hardening or softening) to model the nonlinear soil behaviour; however, such models based on plasticity theory are useful when the design interest is the estimation of ultimate load capacity (Osman et al. 2007). For most laterally loaded pile problems, the primary interest in design is the estimation of head response under working load conditions (e.g., head rotation $\psi_h = 0.5°$ is the design criterion for laterally loaded monopiles under extreme loading conditions); thus, the use

of such sophisticated constitutive models based on plasticity theory might not be necessary and nonlinear elastic soil models may be sufficient to predict reasonably accurate pile response with lesser computational effort.

In this chapter, an approximate continuum-based method is developed to estimate the nonlinear response of monopile foundations. In this analysis, the monopile is modeled following the Euler-Bernoulli beam theory and each soil layer is characterized by nonlinear elastic constitutive relationships, available in the literature. The nonlinear pile response obtained from this analysis is verified and validated with the results of equivalent 3-D FE analysis (both using nonlinear elastic and elastic-plastic constitutive models), full-scale field pile-load tests, and the *p-y* analysis for piles embedded in clayey and sandy soil deposit. There are several advantages of the present analysis: (i) the solution algorithm is faster compared to an equivalent 3-D FE analysis because in the present analysis the solution of the differential equations describing soil displacements are 1-D in nature although the actual problem is 3-D, (ii) reasonable accurate and computationally faster prediction of monopile response can be made using nonlinear elastic constitutive relationships for soil in comparison to an equivalent 3-D FE analysis with sophisticated elastic-plastic constitutive models.

4.3 Soil nonlinearity

The stress-strain behavior of soil is highly nonlinear i.e., the soil stiffness (e.g., secant shear modulus or Young's modulus) decays with strain (e.g., shear strain), except for very small strains (typically less than 10^{-6} (Atkinson 2000) or 10^{-5} (Osman et al. 2007)). This degradation of soil modulus with strain is often expressed as a ratio of G_s/G_{s0} where G_s is the secant shear modulus at any strain and G_{s0} is the initial (small-strain or elastic) shear modulus. Figure 4.1 depicts a typical modulus degradation curve with the induced shear strain (γ) for soil. There are several such modulus degradation curves available in the literature for clayey and sandy soil deposit (Kondner 1963, Duncan and Chang 1970, Seed and Idriss 1970, Hardin and Drnevich 1972, Fahey and Carter 1993, Ishibashi and Zhang 1993, Lee and Salgado 2000, Darendali 2001, Menq 2003, Zhang et al. 2005, Osman et al. 2007, Vardanega and Bolton 2013, Oztoprak and Bolton 2013); these modulus degradation curves are often expressed in the form of a power law or a hyperbolic expression and can be used to obtain the response of

monopiles. In this chapter, three such nonlinear elastic constitutive relationships are used; a brief description of the relationships is given in the subsequent subsections of this section.

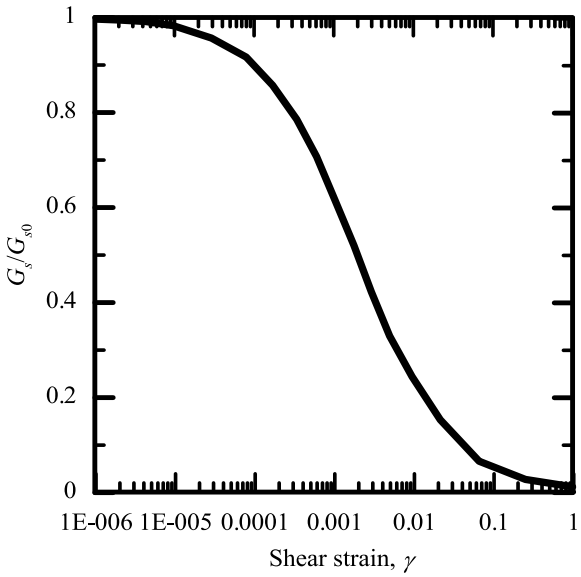

Figure 4.1: Normalized secant shear modulus versus shear strain curve

4.3.1 Nonlinear elastic soil models for undrained clay

Osman et al. (2007) proposed a power law expression (equation (4.1a)) based on the results of a few triaxial compression test performed on three different types of clay (Gault clay, London clay, and Kaolin clay with overconsolidation ratio (*OCR*) 35, 30 and 1, respectively) sheared at an effective confining stress of about 100 kPa (performed by Dasari 1996) which is given by

$$G_s = G_{s0}\left(\frac{\varepsilon_q}{\varepsilon_{q0}}\right)^b \tag{4.1a}$$

where

$$\varepsilon_q = \sqrt{\frac{2}{9}\left[\left(\varepsilon_{rr}-\varepsilon_{\theta\theta}\right)^2+\left(\varepsilon_{\theta\theta}-\varepsilon_{zz}\right)^2+\left(\varepsilon_{zz}-\varepsilon_{rr}\right)^2\right]+\frac{4}{3}\left(\varepsilon_{r\theta}^2+\varepsilon_{\theta z}^2+\varepsilon_{zr}^2\right)} \tag{4.1b}$$

ε_q is the deviatoric strain for a 3-D strain state in the soil, ε_{rr}, $\varepsilon_{\theta\theta}$, ε_{zz}, $\varepsilon_{r\theta}$, $\varepsilon_{\theta z}$, and ε_{zr} are the strain components for a 3-D strain state in soil for a r-θ-z coordinate system, ε_{q0} is the maximum deviatoric strain of linear elastic (initial or small-strain) behavior at ~ 10^{-5}, and b (= – 0.5) is a curve fitted parameter describing the nonlinear variation of soil with deviatoric strain.

In a recent study, Vardanega and Bolton (2013) formulated a modified hyperbolic expression (equation (4.2a)) from their statistical study on a database of 67 tests on 21 clays and plastic silts on the undrained shear stress-strain data of fine-grained soils reported in the literature for use in the foundation engineering practice. The compiled tests data included fine-grained soil from various countries, under a variety of conditions, from normally consolidated to heavily consolidated, and performed in a variety of shear testing devices over a period of 30 years. The hyperbolic expression is given by

$$G_s = \frac{G_{s0}}{1+\left(\frac{\gamma}{\gamma_{ref}}\right)^{\alpha}} \tag{4.2a}$$

where for a 3-D strain state in soil γ is considered to be the octahedral engineering shear strain γ_{oct}, which is given by

$$\gamma_{oct} = \frac{2}{3}\sqrt{\left(\varepsilon_{rr}-\varepsilon_{\theta\theta}\right)^2+\left(\varepsilon_{\theta\theta}-\varepsilon_{zz}\right)^2+\left(\varepsilon_{zz}-\varepsilon_{rr}\right)^2+6\left(\varepsilon_{r\theta}^2+\varepsilon_{\theta z}^2+\varepsilon_{zr}^2\right)} \tag{4.2b}$$

α (= 0.736) is the curvature parameter describing the nonlinear variation of soil with strain, and γ_{ref} {= $J \times (PI/1000)$} is the octahedral reference shear strain at which the initial shear modulus is halved where J = 2.2 and PI is plasticity index of clay, which is expressed numerically.

The initial shear modulus G_{s0} described in equations (4.1a) and (4.2a) can be obtained from shear wave velocity measurements either in the laboratory (using the resonant column or the bender element tests) or in the field (using the plate-load tests, seismic cone penetration tests, cross-hole tests). There are several such relationships proposed in the literature for the estimation G_{s0} where it is correlated to various elementary soil parameters such as void ratio, plasticity index, initial mean effective stress, overconsolidation ratio, and the shear strength of soil (Hardin and Black 1968, Hara et al. 1974, Duncan and Buchignani 1976, Viggiani and Atkinson 1995, Shibuya et al. 1996, Atkinson 2000). In this study, the G_{s0} for an undrained clayey soil deposit is obtained following the correlation proposed by Duncan and Buchignani (1976) (also included in USACE 1990) which describes the variation of the initial (small-strain or elastic) Young's modulus E_{s0} of the undrained clay soil as a function of three basic soil parameters – undrained shear strength s_u, plasticity index PI, and the overconsolidation ratio

OCR (these parameters can be easily obtained from a geotechnical site investigation report). The correlation proposed by Duncan and Buchignani (1976) is given by

$$E_{s0} = K_c s_u \tag{4.3}$$

where

K_c is a correlation factor and is a function of the *PI* and *OCR* which was obtained from field measurements and can be estimated from Figure 4.2. The small-strain shear modulus for the undrained clay can be evaluated following G_{s0} [= E_{s0}/{2 × (1 + ν_s)}] for a Poisson's ratio ν_s = 0.49.

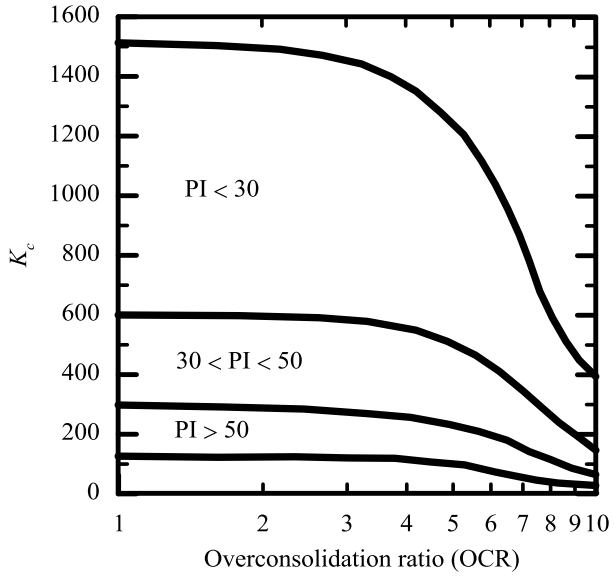

Figure 4.2: Relationship between K_c, *PI*, and *OCR* for clays (Regenerated from USACE (1990))

4.3.2 Nonlinear elastic soil model for sand

Oztoprak and Bolton (2013) formulated a modified hyperbolic expression (equation (4.4)) from the shear stress-strain data of sandy soils performed on a database of 454 tests, available in the literature for obtaining the nonlinear response of geotechnical engineering structures, subjected to static loading. The database consisted of sandy soils with various grain size and gradation (e.g., clean sands, gravels, sands with fines and/or gravels, and gravels with sands and fines), types (e.g., reconstituted and/or undisturbed Toyura, Ottawa, Ishikari sand), under a variety of state (e.g., saturation, void ratio, relative density, confining stress, and drainage conditions), and tested under static and dynamic conditions. The best-fit functional

relationship from the secant shear modulus degradation data demonstrated in Figure 4.3 is given by

$$G_s = \frac{G_{s0}}{1+\left(\frac{\gamma-\gamma_e}{\gamma_{ref}}\right)^{\alpha}} \tag{4.4}$$

where γ (note that for $\gamma < \gamma_e$, $G_s/G_{s0} = 1$) for a 3-D strain state in soil is considered to be the octahedral shear strain (see equation (4.2b)), γ_e is the elastic threshold strain beyond which the shear modulus falls below its maximum, γ_{ref} is the characteristic reference strain at which the initial elastic shear modulus is halved, and α is the curvature parameter. The numerical values of γ_e, γ_{ref}, and α are reported in Table 4.1.

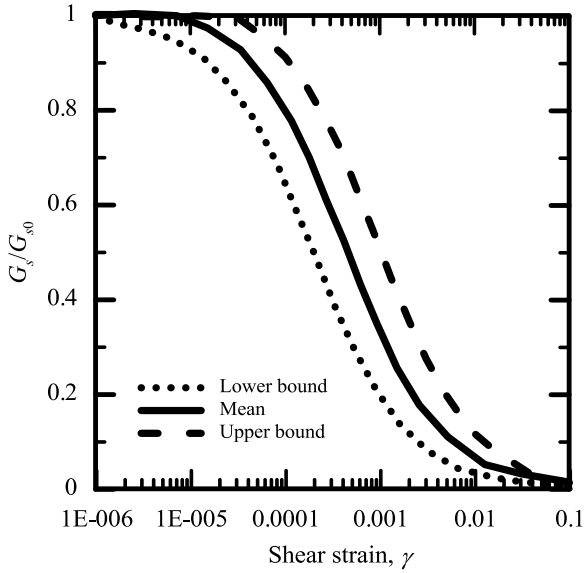

Figure 4.3: Normalized secant shear modulus versus shear strain curve for sandy soil (Regenerated from Oztoprak and Bolton (2013))

Table 4.1: Fitted parameters for lower bound, mean, and upper bound curves in Figure 4.3

Parameters	**Lower bound**	**Mean**	**Upper bound**
γ_{ref}	0.0002	0.00044	0.001
γ_e	0	0.000007	0.00003
α	0.88	0.88	0.88

Several researchers (Hardin and Black 1966, Darendali 2001, Menq 2003, Salgado 2008) in the past have proposed relationships to obtain the initial shear modulus G_{s0} of sandy soils. In this study, the G_{s0} for a sandy soil deposit is obtained following the relationship (equation (4.5)) proposed by Hardin and Black (1966)

$$\frac{G_{s0}}{p_a} = C_g \frac{e_g - e_0}{1 + e_0} \left(\frac{\sigma'_{m0}}{p_a} \right)^{n_g} \tag{4.5}$$

where C_g, e_g, and n_g are intrinsic soil properties (C_g = 612.0, e_g = 2.17, and n_g = 0.44 corresponding to Ottawa sand); σ'_{m0} is the initial mean effective stress, p_a is the reference stress (= 100 kPa), and e_0 is the initial void ratio.

4.4 Mathematical formulation

4.4.1 Problem definition

Figure (4.4) shows a hollow circular steel monopile modeled as a Euler-Bernoulli beam, embedded in a multilayered nonlinear elastic soil deposit. The monopile has a length L_p, radius r_p, wall thickness t_p, area of cross-section A_p, second moment of inertia I_p, and characterized by Young's modulus E_p. The soil layers are characterized by a modulus degradation relationship described by the equations (4.1), (4.2), or (4.3). The soil layers extend to an infinite distance along the radial direction and the n^{th} soil layer extends to infinity in the vertical direction. A cylindrical r-θ-z coordinate system is chosen for the purpose of analysis where the origin of the coordinate system lies at the center of the monopile head. Further, in the analysis, no slippage or separation between the monopile and the surrounding soil is assumed. The objective of the analysis is to predict the nonlinear monopile response – head displacement w_h and rotation ψ_h because of the application of the static horizontal force F_a and/or moment M_a.

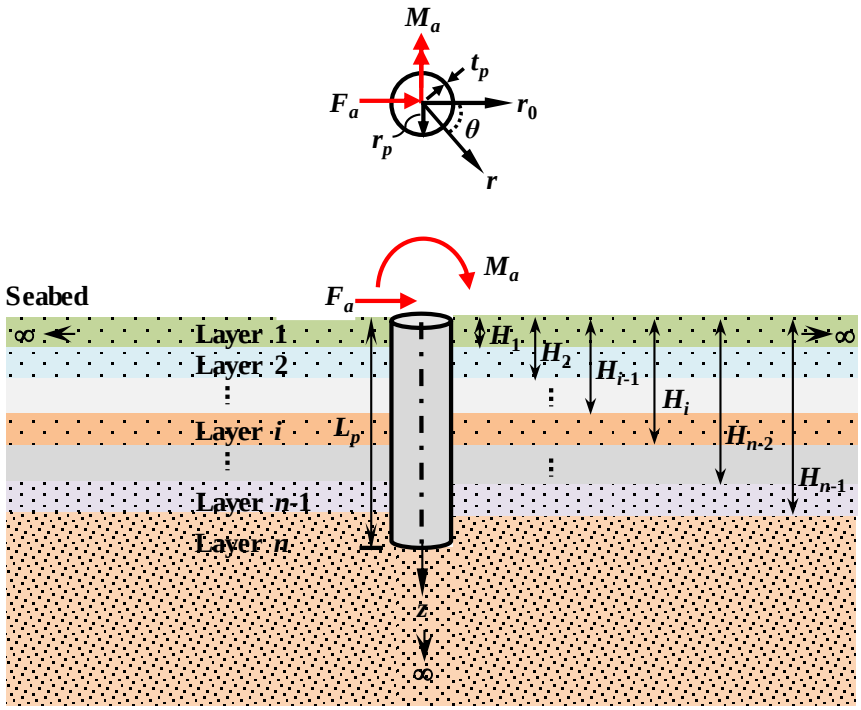

Figure 4.4: A monopile embedded in a multilayered nonlinear elastic soil and subjected to static lateral loads

4.4.2 Displacements, strains, and stress in soil

The soil displacement field in the radial and tangential direction generated by the monopile displacement $w(z)$ is expressed as a product of separable functions and given by

$$u_r(r,\theta,z) = w(z)\phi_r(r)\cos\theta \tag{4.6}$$

$$u_\theta(r,\theta,z) = -w(z)\phi_\theta(r)\sin\theta \tag{4.7}$$

where $\phi_r(r)$ and $\phi_\theta(r)$ are both assumed to be equal to one at $r = r_p$ and equal to zero at $r = \infty$.

Using the soil displacement field, the infinitesimal soil strains (with contractive strains assumed positive) is expressed as

$$\begin{bmatrix}\varepsilon_{rr}\\ \varepsilon_{\theta\theta}\\ \varepsilon_{zz}\\ \varepsilon_{r\theta}\\ \varepsilon_{rz}\\ \varepsilon_{\theta z}\end{bmatrix}=\begin{bmatrix}-\dfrac{du_r}{dr}\\ -\dfrac{u_r}{r}-\dfrac{1}{r}\dfrac{du_\theta}{d\theta}\\ -\dfrac{du_z}{dz}\\ -\dfrac{1}{2}\left(\dfrac{1}{r}\dfrac{du_r}{d\theta}+\dfrac{du_\theta}{dr}-\dfrac{u_\theta}{r}\right)\\ -\dfrac{1}{2}\left(\dfrac{du_z}{dr}+\dfrac{du_r}{dz}\right)\\ -\dfrac{1}{2}\left(\dfrac{1}{r}\dfrac{du_z}{d\theta}+\dfrac{du_\theta}{\partial z}\right)\end{bmatrix}=\begin{bmatrix}-w(z)\dfrac{d\phi_r(r)}{dr}\cos\theta\\ -w(z)\dfrac{\phi_r(r)-\phi_\theta(r)}{r}\cos\theta\\ 0\\ \dfrac{1}{2}w(z)\left\{\dfrac{\phi_r(r)-\phi_\theta(r)}{r}+\dfrac{d\phi_\theta(r)}{dr}\right\}\sin\theta\\ -\dfrac{1}{2}\dfrac{dw(z)}{dz}\phi_r(r)\cos\theta\\ \dfrac{1}{2}\dfrac{dw(z)}{dz}\phi_\theta(r)\sin\theta\end{bmatrix} \tag{4.8}$$

Further, using the stress-strain relationship, the stress state at any point within the soil mass is given by

$$\sigma_{pq}=\lambda_s\delta_{pq}\varepsilon_{ll}+2G_s\varepsilon_{pq} \tag{4.9}$$

where σ_{pq} and ε_{pq} are soil stress and strain tensors and the summation is implied by the repetition of the indices p and q and δ_{pq} is the Kronecker's delta.

4.4.3 Principle of virtual work

Applying the principle of virtual work to the monopile-soil system (Figure 4.4) the following equation is obtained

$$\begin{aligned}&E_pI_p\int_0^{L_p}\left(\frac{d^2w}{dz^2}\right)\delta\left(\frac{d^2w}{dz^2}\right)dz+\int_0^{\infty}\int_0^{2\pi}\int_{r_p}^{\infty}\sigma_{pq}\delta\varepsilon_{pq}rdrd\theta+\int_{L_p}^{\infty}\int_0^{2\pi}\int_0^{r_p}\sigma_{pq}\delta\varepsilon_{pq}rdrd\theta\\&-F_a\,\delta w\big|_{z=0}+M_a\delta\left(\frac{dw}{dz}\right)\Big|_{z=0}=0\end{aligned} \tag{4.10}$$

where the first, second, and third integral on the left-hand side of equation (4.10) denotes the internal virtual work done by the monopile, the soil except the cylindrical soil domain below the monopile base, and the cylindrical soil domain of radius r_p below the monopile base, respectively. The fourth and the fifth term on the left-hand side of equation (4.10) denotes the external virtual work done by the applied force and moment, respectively.

Substituting equations (4.8) and (4.9) in equation (4.10) and introducing layering, the following equation is obtained

$$\sum_{i=1}^{n}\int_{H_{i-1}}^{H_i} E_p I_p \left(\frac{d^2 w_i}{dz^2}\right)\delta\left(\frac{d^2 w_i}{dz^2}\right)dz + \int_{L_p}^{\infty} \pi r_p^2 G_{sn0}\left(\frac{dw_{n+1}}{dz}\right)\delta\left(\frac{dw_{n+1}}{dz}\right)dz$$

$$+\sum_{i=1}^{n}\int_{H_{i-1}}^{H_i}\int_{0}^{2\pi}\int_{r_p}^{\infty}\left\{\left(\lambda_{si}+2G_{si}\right)\left(\frac{d\phi_r}{dr}\right)^2\cos^2\theta + 2\lambda_{si}\frac{d\phi_r}{dr}\left(\frac{\phi_r-\phi_\theta}{r}\right)\cos^2\theta\right.$$

$$+\left(\lambda_{si}+2G_{si}\right)\left(\frac{\phi_r-\phi_\theta}{r}\right)^2\cos^2\theta + G_{si}\left(\frac{\phi_r-\phi_\theta}{r}\right)^2\sin^2\theta + 2G_{si}\frac{d\phi_\theta}{dr}\left(\frac{\phi_r-\phi_\theta}{r}\right)\sin^2\theta$$

$$\left.+G_{si}\left(\frac{d\phi_r}{dr}\right)^2\sin^2\theta\right\} w_i\delta w_i\, r dr d\theta dz$$

$$+\sum_{i=1}^{n}\int_{H_{i-1}}^{H_i}\int_{0}^{2\pi}\int_{r_p}^{\infty}\left\{G_{si}\phi_\theta^2\sin^2\theta + G_{si}\phi_r^2\cos^2\theta\right\}\left(\frac{dw_i}{dz}\right)\delta\left(\frac{dw_i}{dz}\right)r dr d\theta dz$$

$$-F_a\,\delta w_1\big|_{z=0} + M_a\delta\left(\frac{dw_1}{dz}\right)\Bigg|_{z=0}$$

$$+\sum_{i=1}^{n+1}\int_{H_{i-1}}^{H_i}\int_{0}^{2\pi}\int_{r_p}^{\infty}\left\{\lambda_{si}w_i^2\cos^2\theta\left(\frac{\phi_r-\phi_\theta}{r}\right) + \left(\lambda_{si}+2G_{si}\right)w_i^2\cos^2\theta\frac{d\phi_r}{dr}\right\}\delta\left(\frac{d\phi_r}{dz}\right)r dr d\theta dz$$

$$+\sum_{i=1}^{n+1}\int_{H_{i-1}}^{H_i}\int_{0}^{2\pi}\int_{r_p}^{\infty}\left\{\lambda_{si}\frac{w_i^2}{r}\frac{d\phi_r}{dr}\cos^2\theta + \left(\lambda_{si}+2G_{si}\right)\frac{w_i^2}{r^2}\left(\phi_r-\phi_\theta\right)\cos^2\theta + G_{si}\frac{w_i^2}{r^2}\left(\phi_r-\phi_\theta\right)\sin^2\theta\right.$$

$$\left.+G_{si}\frac{w_i^2}{r}\sin^2\theta\frac{d\phi_\theta}{dr} + G_{si}\left(\frac{dw_i}{dz}\right)^2\cos^2\theta\,\phi_r\right\}\delta\phi_r\, r dr d\theta dz$$

$$+\sum_{i=1}^{n+1}\int_{H_{i-1}}^{H_i}\int_{0}^{2\pi}\int_{r_p}^{\infty}\left\{G_{si}w_i^2\sin^2\theta\left(\frac{\phi_r-\phi_\theta}{r}\right) + G_{si}w_i^2\sin^2\theta\frac{d\phi_\theta}{dr}\right\}\delta\left(\frac{d\phi_\theta}{dz}\right)r dr d\theta dz$$

$$+\sum_{i=1}^{n+1}\int_{H_{i-1}}^{H_i}\int_{0}^{2\pi}\int_{r_p}^{\infty}\left\{-\lambda_{si}\frac{w_i^2}{r}\frac{d\phi_r}{dr}\cos^2\theta - \left(\lambda_{si}+2G_{si}\right)\frac{w_i^2}{r^2}\left(\phi_r-\phi_\theta\right)\cos^2\theta\right.$$

$$\left.-G_{si}\frac{w_i^2}{r^2}\left(\phi_r-\phi_\theta\right)\sin^2\theta - G_{si}\frac{w_i^2}{r}\sin^2\theta\frac{d\phi_\theta}{dr} + G_{si}\left(\frac{dw_i}{dz}\right)^2\sin^2\theta\,\phi_\theta\right\}\delta\phi_\theta\, r dr d\theta dz = 0$$

(4.11)

Note, that the n^{th} layer is artificially split into n^{th} and $(n + 1)^{th}$ layer. Further, in the equation (4.11), G_{si} {$= E_{si}/(2 \times (1 + \nu_{si}))$} and λ_{si} {$= 2G_{si}(1 - \nu_{si})/(1 - 2\nu_{si})$} varies with strain at each point within the soil mass which implies that they are functions of the radial r and tangential θ coordinate (i.e., $G_{si} = G_{si}(r,\theta)$ and $\lambda_{si} = \lambda_{si}(r,\theta)$) and therefore, included within the integrations unlike equation (2.7) in Chapter 2. Further, for the circular soil domain of radius r_p below the monopile base, the soil stiffness is not expected to degrade much and therefore,

the shear modulus in this region is assumed to be equal to the small-strain shear modulus (i.e., $G_{sn} = G_{sn0}$).

4.4.4 Numerical solution of monopile displacement

Performing integration by parts on the terms associated with $\delta(d^2w/dz^2)$ and $\delta(dw/dz)$, in equation (4.11), then collecting all the terms associated with δw and equating them to zero results in the differential equations of $w(z)$. Considering the terms associated with δw within the region $0 \le z \le L_p$, the governing differential equations of w is obtained and given by

$$E_p I_p \frac{d^4 w_i}{dz^4} - 2t_i \frac{d^2 w_i}{dz^2} + k_i w_i = 0 \tag{4.12}$$

with the relevant boundary conditions at different layer interface given by

$$E_p I_p \frac{d^3 w_1}{dz^3} - 2t_1 \frac{dw_1}{dz} = F_a \tag{4.13a}$$

$$E_p I_p \frac{d^2 w_1}{dz^2} = -M_a \tag{4.13b}$$

$$w_i = w_{i+1} \tag{4.14a}$$

$$\frac{dw_i}{dz} = \frac{dw_{i+1}}{dz} \tag{4.14b}$$

$$E_p I_p \frac{d^3 w_i}{dz^3} - 2t_i \frac{dw_i}{dz} = E_p I_p \frac{d^3 w_{i+1}}{dz^3} - 2t_{i+1} \frac{dw_{i+1}}{dz} \tag{4.14c}$$

$$\frac{d^2 w_i}{dz^2} = \frac{d^2 w_{i+1}}{dz^2} \tag{4.14d}$$

$$E_p I_p \frac{d^3 w_n}{dz^3} - 2t_n \frac{dw_n}{dz} = \sqrt{2k_n t_{n+1}}\, w_n \tag{4.15a}$$

$$\frac{d^2 w_n}{dz^2} = 0 \tag{4.15b}$$

where the coefficients k_i and t_i are given by

$$\begin{aligned} k_i = \int_0^{2\pi} \int_{r_p}^{\infty} \Bigg\{ & \left(\lambda_{si} + 2G_{si}\right)\left(\frac{d\phi_r}{dr}\right)^2 \cos^2\theta + 2\lambda_{si}\left(\frac{\phi_r - \phi_\theta}{r}\right)\frac{d\phi_r}{dr}\cos^2\theta + G_{si} r \left(\frac{d\phi_\theta}{dr}\right)^2 \sin^2\theta \\ & + \left(\lambda_{si} + 2G_{si}\right)\left(\frac{\phi_r - \phi_\theta}{r}\right)^2 \cos^2\theta + G_{si}\left(\frac{\phi_r - \phi_\theta}{r}\right)^2 \sin^2\theta + G_{si}\left(\frac{\phi_r - \phi_\theta}{r}\right)\frac{d\phi_\theta}{dr}\sin^2\theta \Bigg\} r\, dr\, d\theta \end{aligned} \tag{4.16}$$

$$t_i = \begin{cases} \frac{1}{2}\int_0^{2\pi}\int_{r_p}^{\infty} G_{sn}\left(\phi_r^2\cos^2\theta + \phi_\theta^2\sin^2\theta\right) r dr d\theta; & i = 1,2,\ldots,n \\ \frac{1}{2}\int_0^{2\pi}\int_{r_p}^{\infty} G_{sn}\left(\phi_r^2\cos^2\theta + \phi_\theta^2\sin^2\theta\right) r dr d\theta + \frac{\pi}{2} r_p^2 G_{sn0}; & i = n+1 \end{cases} \tag{4.17}$$

Note, that the parameters k_i and t_i are functions of the r and θ for a spatially varying G_{si} and λ_{si}, unlike the equations (2.10) and (2.11) in Chapter 2.

For the domain below the monopile base ($L_p \le z \le \infty$) the terms associated with δw_{n+1} in equation (4.11) are equated to zero. As w_{n+1} is not known *a priori* within $L_p < z < \infty$, $\delta w_{n+1} \neq 0$ because of which the integrand in the integral between $z = L_p$ and $z = \infty$ must be equal to zero. This gives the differential equation of w_{n+1}

$$2t_{n+1}\frac{d^2 w_{n+1}}{dz^2} - k_n w_{n+1} = 0 \tag{4.18}$$

At infinite vertical distance down from the monopile (i.e., at $z = \infty$) $w_{n+1} = 0$ (this makes the term associated with δw_{n+1} at $z = \infty$ equal to zero) and at the monopile base (i.e., at $z = L_p$) $w_{n+1} = w_n$. Using these boundary conditions, an analytical solution of equation (4.18) is obtained as

$$w_{n+1} = w_n\big|_{z=L_p} e^{-\sqrt{\frac{k_n}{2t_{n+1}}}(z-L_p)} \tag{4.19}$$

The differential equation governing monopile displacement (equation (4.12)) is solved using the 1-D FD scheme. The FD form of equation (4.12) for various set of nodes (monopile is discretized into a set of uniformly spaced nodes of spacing Δz (see Figure 4.5(b)) with a total number of nodes n (same as the number of soil layers) satisfying the boundary conditions at the monopile head (equations (4.13a)-(4.13b)) and at the monopile base (equations (4.15a)-(4.15b)) are given by

$$\left[\frac{2E_pI_p}{\Delta z^4} + \frac{4t_1}{\Delta z^2} + k_1\right]w_1 + \left[-\frac{4E_pI_p}{\Delta z^4} - \frac{4t_1}{\Delta z^2}\right]w_2 + \left[\frac{2E_pI_p}{\Delta z^4}\right]w_3 = \frac{2F_a}{\Delta z} - \frac{2M_a}{\Delta z^2} \tag{4.20a}$$

$$\left[-\frac{2E_pI_p}{\Delta z^4} - \frac{2t_2}{\Delta z^2}\right]w_1 + \left[\frac{5E_pI_p}{\Delta z^4} + \frac{4t_2}{\Delta z^2} + k_2\right]w_2 + \left[-\frac{4E_pI_p}{\Delta z^4} - \frac{2t_2}{\Delta z^2}\right]w_3 + \left[\frac{E_pI_p}{\Delta z^4}\right]w_4 = \frac{M_a}{\Delta z^2} \tag{4.20b}$$

$$\left[\frac{E_pI_p}{\Delta z^4}\right]w_{i-2}+\left[-\frac{4E_pI_p}{\Delta z^4}-\frac{2t_i}{\Delta z^2}\right]w_{i-1}+\left[\frac{6E_pI_p}{\Delta z^4}+\frac{4t_i}{\Delta z^2}+k_i\right]w_i+\left[-\frac{4E_pI_p}{\Delta z^4}-\frac{2t_i}{\Delta z^2}\right]w_{i+1}+\left[\frac{E_pI_p}{\Delta z^4}\right]w_{i+2}=0 \tag{4.20c}$$

$$\left[\frac{E_pI_p}{\Delta z^4}\right]w_{i-2}+\left[-\frac{4E_pI_p}{\Delta z^4}-\frac{2t_i}{\Delta z^2}\right]w_{i-1}+\left[\frac{5E_pI_p}{\Delta z^4}+\frac{4t_i}{\Delta z^2}+k_i\right]w_i+\left[-\frac{2E_pI_p}{\Delta z^4}-\frac{2t_i}{\Delta z^2}\right]w_{i+1}=0 \tag{4.20d}$$

$$\left[\frac{2E_pI_p}{\Delta z^4}\right]w_{i-2}+\left[-\frac{4E_pI_p}{\Delta z^4}-\frac{4t_i}{\Delta z^2}\right]w_{i-1}+\left[\frac{2E_pI_p}{\Delta z^4}+\frac{4t_i}{\Delta z^2}+\frac{2\sqrt{2k_it_{i+1}}}{\Delta z}+k_i\right]w_i=0 \tag{4.20e}$$

Equations 4.20(a) and 4.20(b) are applicable to nodes 1 and 2 respectively, equations 4.20(c) is applicable to nodes $i = 3 – (n – 2)$, equations 4.20(d) and 4.20(e) are applicable to nodes $i = (n – 1)$ and $i = n$, respectively. These FD equations form a system of linear equations whose solutions results in the monopile displacement w_i at each node along the z-axis. Note, the small-strain shear modulus G_{s0} can be input at each node, which implicitly accounts for layering within the solution process.

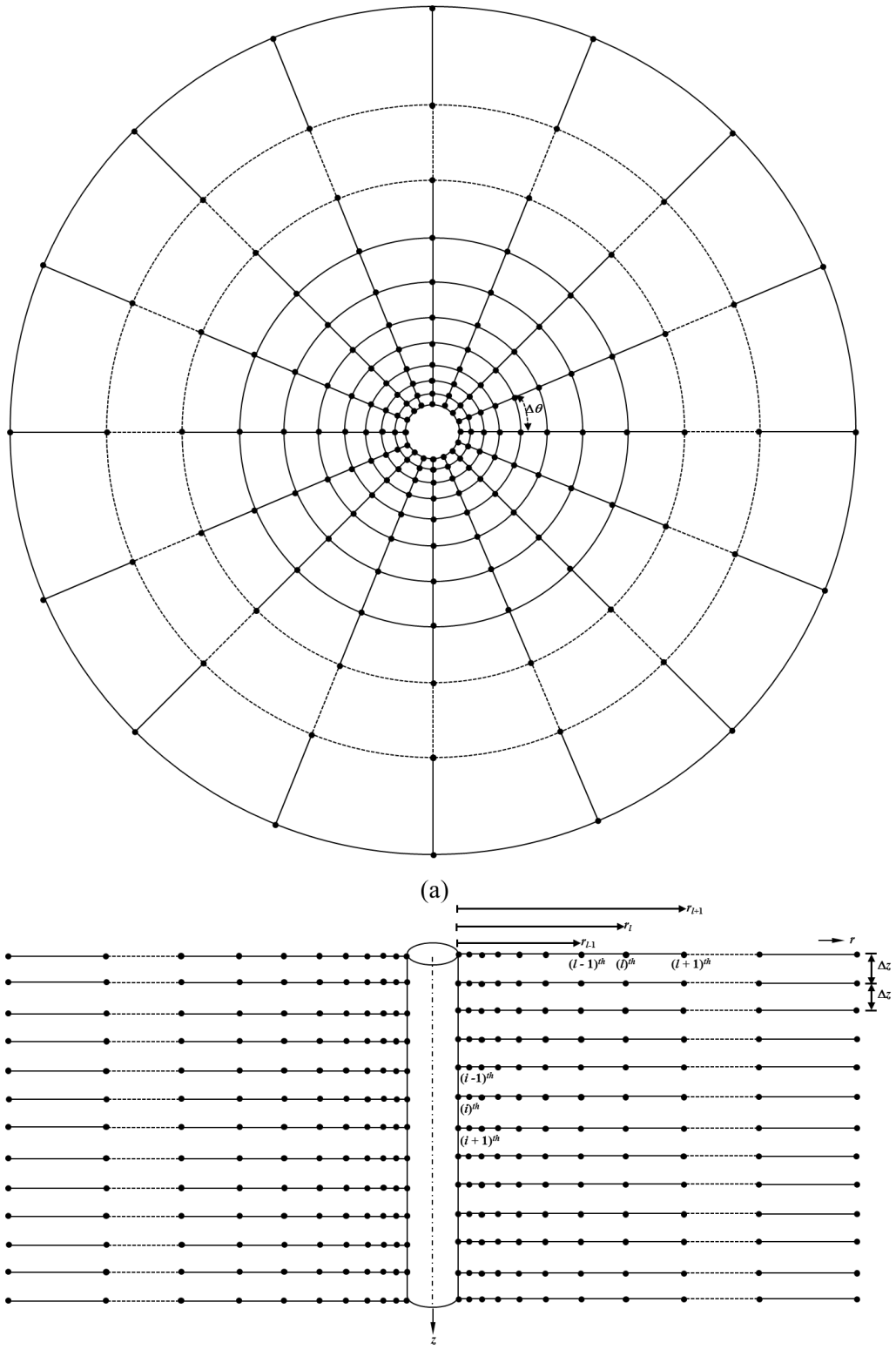

Figure 4.5: Finite difference discretization of the monopile-soil domain

4.4.5 Numerical solution of differential equations describing soil displacement

Referring to equation (4.11), collecting all the terms associated with $\delta\phi_r$, $\delta\phi_\theta$, $\delta(d\phi_r/dr)$, and $\delta(d\phi_\theta/dr)$ and further, performing integration by parts on the terms associated $\delta(d\phi_r/dr)$ and $\delta(d\phi_\theta/dr)$, an equation of the following form is obtained

$$\begin{aligned}
&\int_{r_p}^{\infty}\left\{-m_{s1}\frac{d^2\phi_r}{dr^2}-\frac{dm_{s1}}{dr}\frac{d\phi_r}{dr}-\frac{dm_{s3}}{dr}\left(\frac{\phi_r-\phi_\theta}{r}\right)+m_{s3}\left(\frac{\phi_r-\phi_\theta}{r^2}\right)+\frac{m_{s3}}{r}\frac{d\phi_r}{dr}\right.\\
&\left.-\frac{m_{s3}}{r}\left(\frac{d\phi_r}{dr}-\frac{d\phi_\theta}{dr}\right)+m_{s1}\left(\frac{\phi_r-\phi_\theta}{r^2}\right)+m_{s2}\left(\frac{\phi_r-\phi_\theta}{r^2}\right)+\frac{m_{s2}}{r}\frac{d\phi_\theta}{dr}+n_{s1}\phi_r\right\}\delta\phi_r\,dr\\
&+m_{s1}\frac{d\phi_r}{dr}\delta\phi_r\Big|_{r_p}^{\infty}+m_{s3}\left(\frac{\phi_r-\phi_\theta}{r}\right)\delta\phi_r\Big|_{r_p}^{\infty}\\
&\int_{r_p}^{\infty}\left\{-\frac{dm_{s2}}{dr}\frac{d\phi_\theta}{dr}-m_{s2}\frac{d^2\phi_\theta}{dr^2}-\frac{dm_{s2}}{dr}\left(\frac{\phi_r-\phi_\theta}{r}\right)-\frac{m_{s3}}{r}\frac{d\phi_r}{dr}-m_{s1}\left(\frac{\phi_r-\phi_\theta}{r^2}\right)\right.\\
&\left.-\frac{m_{s2}}{r}\left(\frac{d\phi_r}{dr}-\frac{d\phi_\theta}{dr}\right)+\frac{m_{s2}}{r}\frac{d\phi_\theta}{dr}+n_{s2}\phi_\theta\right\}\delta\phi_\theta\,dr\\
&+m_{s2}\frac{d\phi_\theta}{dr}\delta\phi_\theta\Big|_{r_p}^{\infty}+m_{s2}\left(\frac{\phi_r-\phi_\theta}{r}\right)\delta\phi_\theta\Big|_{r_p}^{\infty}=0
\end{aligned}\tag{4.21}$$

where

$$m_{s1}=\sum_{i=1}^{n+1}\int_{H_{i-1}}^{H_i}\int_0^{2\pi}\left(\lambda_{si}+2G_{si}\right)w_i^2\cos^2\theta\,r\,d\theta\,dz \tag{4.22a}$$

$$m_{s2}=\sum_{i=1}^{n+1}\int_{H_{i-1}}^{H_i}\int_0^{2\pi}G_{si}w_i^2\sin^2\theta\,r\,d\theta\,dz \tag{4.22b}$$

$$m_{s3}=\sum_{i=1}^{n+1}\int_{H_{i-1}}^{H_i}\int_0^{2\pi}\lambda_{si}w_i^2\cos^2\theta\,r\,d\theta\,dz \tag{4.22c}$$

$$n_{s1}=\sum_{i=1}^{n+1}\int_{H_{i-1}}^{H_i}\int_0^{2\pi}G_{si}\left(\frac{dw_i}{dz}\right)^2\cos^2\theta\,r\,d\theta\,dz \tag{4.22d}$$

$$n_{s2}=\sum_{i=1}^{n+1}\int_{H_{i-1}}^{H_i}\int_0^{2\pi}G_{si}\left(\frac{dw_i}{dz}\right)^2\sin^2\theta\,r\,d\theta\,dz \tag{4.22e}$$

Collecting the terms associated with $\delta\phi_r$ and $\delta\phi_\theta$, setting the terms associated with $\delta\phi_r$ and $\delta\phi_\theta$ at $r = r_p$ and $r = \infty$ equal to zero (since the variations of ϕ_r and ϕ_θ are known at $r = r_p$ and $r = \infty$), and within the interval $r_p < r < \infty$ (since $\delta\phi_r \neq 0$ and $\delta\phi_\theta \neq 0$ as ϕ_r and ϕ_θ is not

known *a priori* within $r_p < r < \infty$), a set of coupled differential equations for ϕ_r and ϕ_θ describing soil displacement are obtained.

$$\frac{d^2\phi_r}{dr^2} + \gamma_1 \frac{d\phi_r}{dr} - \gamma_2 \phi_r = \gamma_3 \frac{d\phi_\theta}{dr} - \gamma_4 \phi_\theta \tag{4.23a}$$

$$\frac{d^2\phi_\theta}{dr^2} + \gamma_5 \frac{d\phi_\theta}{dr} - \gamma_6 \phi_\theta = -\gamma_7 \frac{d\phi_r}{dr} - \gamma_8 \phi_r \tag{4.23b}$$

where

$$\gamma_1 = \frac{1}{m_{s1}} \frac{dm_{s1}}{dr} \tag{4.24a}$$

$$\gamma_2 = \frac{1}{r^2}\left(\frac{m_{s1} + m_{s2} + m_{s3}}{m_{s1}}\right) - \frac{1}{r\, m_{s1}} \frac{dm_{s3}}{dr} + \left(\frac{n_{s1}}{m_{s1}}\right) \tag{4.24b}$$

$$\gamma_3 = \frac{1}{r}\left(\frac{m_{s2} + m_{s3}}{m_{s1}}\right) \tag{4.24c}$$

$$\gamma_4 = \frac{1}{r^2}\left(\frac{m_{s1} + m_{s2} + m_{s3}}{m_{s1}}\right) - \frac{1}{r\, m_{s1}} \frac{dm_{s3}}{dr} \tag{4.24d}$$

$$\gamma_5 = \frac{1}{m_{s2}} \frac{dm_{s2}}{dr} \tag{4.24e}$$

$$\gamma_6 = \frac{1}{r^2}\left(\frac{m_{s1}}{m_{s2}}\right) + \frac{1}{r\, m_{s2}} \frac{dm_{s2}}{dr} + \left(\frac{n_{s2}}{m_{s2}}\right) \tag{4.24f}$$

$$\gamma_7 = \frac{1}{r}\left(\frac{m_{s2} + m_{s3}}{m_{s2}}\right) \tag{4.24g}$$

$$\gamma_8 = \frac{1}{r^2} \frac{m_{s1}}{m_{s2}} + \frac{1}{r\, m_{s2}} \frac{dm_{s2}}{dr} \tag{4.24h}$$

The coupled differential equations (equations 4.23(a) and 4.23(b)) are solved simultaneously using a 1-D FD scheme. The discretized forms of the differential equations and the associated coefficients are given as

$$\frac{\phi_r^{l+1} - 2\phi_r^l + \phi_r^{l-1}}{\left(r_{l+1} - r_l\right)\left(r_l - r_{l-1}\right)} + \gamma_1^l \frac{\phi_r^{l+1} - \phi_r^{l-1}}{\left(r_{l+1} - r_{l-1}\right)} - \gamma_2^l \phi_r^l = \gamma_3^l \frac{\phi_\theta^{l+1} - \phi_\theta^{l-1}}{\left(r_{l+1} - r_{l-1}\right)} - \gamma_4^l \phi_\theta^l \tag{4.25a}$$

$$\frac{\phi_\theta^{l+1} - 2\phi_\theta^l + \phi_\theta^{l-1}}{\left(r_{l+1} - r_l\right)\left(r_l - r_{l-1}\right)} + \gamma_5^l \frac{\phi_\theta^{l+1} - \phi_\theta^{l-1}}{\left(r_{l+1} - r_{l-1}\right)} - \gamma_6^l \phi_\theta^l = -\gamma_7^l \frac{\phi_r^{l+1} - \phi_r^{l-1}}{\left(r_{l+1} - r_{l-1}\right)} - \gamma_8^l \phi_r^l \tag{4.25b}$$

where

$$\gamma_1^l = \frac{1}{m_{s1}^l}\frac{m_{s1}^{l+1} - m_{s1}^{l-1}}{r_{l+1} - r_{l-1}} \tag{4.26a}$$

$$\gamma_2^l = \frac{1}{r_l^2}\left(\frac{m_{s1}^l + m_{s2}^l + m_{s3}^l}{m_{s1}^l}\right) - \frac{1}{r_l\, m_{s1}^l}\frac{m_{s3}^{l+1} - m_{s3}^{l-1}}{r_{l+1} - r_{l-1}} + \left(\frac{n_{s1}^l}{m_{s1}^l}\right) \tag{4.26b}$$

$$\gamma_3^l = \frac{1}{r_l}\left(\frac{m_{s2}^l + m_{s3}^l}{m_{s1}^l}\right) \tag{4.26c}$$

$$\gamma_4^l = \frac{1}{r_l^2}\left(\frac{m_{s1}^l + m_{s2}^l + m_{s3}^l}{m_{s1}^l}\right) - \frac{1}{r_l\, m_{s1}^l}\frac{m_{s3}^{l+1} - m_{s3}^{l-1}}{r_{l+1} - r_{l-1}} \tag{4.26d}$$

$$\gamma_5^l = \frac{1}{m_{s2}^{l+1}}\frac{m_{s2}^{l+1} - m_{s2}^{l-1}}{r_{l+1} - r_{l-1}} \tag{4.26e}$$

$$\gamma_6^l = \frac{1}{r_l^2}\left(\frac{m_{s1}^l}{m_{s2}^l}\right) + \frac{1}{r_l\, m_{s2}^l}\frac{m_{s2}^{l+1} - m_{s2}^{l-1}}{r_{l+1} - r_{l-1}} + \left(\frac{n_{s2}^l}{m_{s2}^l}\right) \tag{4.26f}$$

$$\gamma_7^l = \frac{1}{r_l}\left(\frac{m_{s2}^l + m_{s3}^l}{m_{s2}^l}\right) \tag{4.26g}$$

$$\gamma_8^l = \frac{1}{r_l^2}\left(\frac{m_{s1}^l}{m_{s2}^l}\right) + \frac{1}{r_l\, m_{s2}^l}\frac{m_{s2}^{l+1} - m_{s2}^{l-1}}{r_{l+1} - r_{l-1}} \tag{4.26h}$$

where the superscript l represents the node number at a radial distance r_l from the monopile edge and a non-uniform spacing of nodes is assumed with the total number of nodes m such that the discretization length $(r_{l+1} - r_l) \neq (r_l - r_{l-1})$ (see Figure 4.5(b)). The 1-D FD discretization has its first node at the monopile-soil boundary (i.e., at $r = r_p$) and sufficiently long and dense so as to allow proper attenuation of the displacement functions for accurate results.

Equations (4.25a) and (4.25b) when rewritten for nodes 2 through $(m - 1)$ (i.e., excluding the 1st and the last (m^{th}) nodes at which the values of ϕ_r and ϕ_θ are known) generate two sets of simultaneous equations with each set containing $m - 2$ equations. These sets of equations can be represented in the matrix form as

$$\left[X^{\phi_r}\right]\{\phi_r\} = \left\{Y^{\phi_\theta}\right\} \tag{4.27a}$$

$$\left[X^{\phi_\theta}\right]\{\phi_\theta\} = \left\{Y^{\phi_r}\right\} \tag{4.27b}$$

where $[X^{\phi_r}]_{(m-2)\times(m-2)}$ and $[X^{\phi_\theta}]_{(m-2)\times(m-2)}$ are the left-hand-side tridiagonal matrices with finite difference coefficients of the unknown vectors $\{\phi_r\}_{(m-2)\times 1}$ and $\{\phi_\theta\}_{(m-2)\times 1}$, respectively, and $\{Y^{\phi_r}\}_{(m-2)\times 1}$ and $\{Y^{\phi_\theta}\}_{(m-2)\times 1}$ are the corresponding right-hand side vectors containing terms with unknowns ϕ_θ and ϕ_r, respectively.

$[X^{\phi_r}]$ formed from equations (4.27a) (i.e., ϕ_r is unknown) the nonzero elements of the y^{th} row of $[X^{\phi_r}]$ are obtained as

$$\left[X^{\phi_r}\right]_{y,y-1} = \frac{1}{(r_{l+1}-r_l)(r_l-r_{l-1})} - \gamma_1^l \frac{1}{(r_{l+1}-r_{l-1})} \tag{4.28a}$$

$$\left[X^{\phi_r}\right]_{y,y} = -\frac{2}{(r_{l+1}-r_l)(r_l-r_{l-1})} - \gamma_2^l \tag{4.28b}$$

$$\left[X^{\phi_r}\right]_{y,y+1} = \frac{1}{(r_{l+1}-r_l)(r_l-r_{l-1})} + \gamma_1^l \frac{1}{(r_{l+1}-r_{l-1})} \tag{4.28c}$$

where $y = l - 1$. The first, y^{th}, and $(m-2)^{th}$ row of $\{Y^{\phi_\theta}\}$ vector in equation (4.27a) is given by

$$\left\{Y^{\phi_\theta}\right\}_1 = -\frac{1}{(r_3-r_2)(r_2-r_1)} + \gamma_1^2 \frac{1}{(r_3-r_1)} + \gamma_3^2 \frac{\phi_\theta^3 - 1}{(r_3-r_1)} - \gamma_4^2 \phi_\theta^2 \tag{4.29a}$$

$$\left\{Y^{\phi_\theta}\right\}_y = \gamma_3^l \frac{\phi_\theta^{l+1} - \phi_\theta^{l-1}}{(r_{l+1}-r_{l-1})} - \gamma_4^l \phi_\theta^l \tag{4.29b}$$

$$\left\{Y^{\phi_\theta}\right\}_{m-2} = -\gamma_3^{m-1} \frac{\phi_\theta^{m-2}}{r_{m-1}-r_{m-3}} - \gamma_4^{m-1} \phi_\theta^{m-1} \tag{4.29c}$$

$[X^{\phi_\theta}]$ formed from equations (4.27b) (i.e., ϕ_θ is unknown) the nonzero elements of the y^{th} row of $[X^{\phi_\theta}]$ are obtained as

$$\left[X^{\phi_\theta}\right]_{y,y-1} = \frac{1}{(r_{l+1}-r_l)(r_l-r_{l-1})} - \gamma_5^l \frac{1}{(r_{l+1}-r_{l-1})} \tag{4.30a}$$

$$\left[X^{\phi_\theta}\right]_{y,y} = -\frac{2}{(r_{l+1}-r_l)(r_l-r_{l-1})} - \gamma_6^l \tag{4.30b}$$

$$\left[X^{\phi_\theta}\right]_{y,y+1} = \frac{1}{(r_{l+1}-r_l)(r_l-r_{l-1})} + \gamma_5^l \frac{1}{(r_{l+1}-r_{l-1})} \tag{4.30c}$$

where $y = l - 1$. The first, y^{th}, and $(m-2)^{th}$ row of $\{Y^{\phi_r}\}$ vector in equation (4.27b) is given by

$$\left\{Y^{\phi_r}\right\}_1 = -\frac{1}{(r_3 - r_2)(r_2 - r_1)} + \gamma_5^2 \frac{1}{(r_3 - r_1)} - \gamma_7^2 \frac{\phi_r^3 - 1}{(r_3 - r_1)} - \gamma_8^2 \phi_r^2 \tag{4.31a}$$

$$\left\{Y^{\phi_r}\right\}_y = -\gamma_7^l \frac{\phi_r^{l+1} - \phi_r^{l-1}}{(r_{l+1} - r_{l-1})} - \gamma_8^l \phi_r^l \tag{4.31b}$$

$$\left\{Y^{\phi_r}\right\}_{m-2} = \gamma_7^{m-1} \frac{\phi_r^{m-2}}{r_{m-1} - r_{m-3}} - \gamma_8^{m-1} \phi_r^{m-1} \tag{4.31c}$$

The functions ϕ_r and ϕ_θ, are solved using an iterative process for each node within the discretized soil domain (see Figure 4.5(b)). An initial estimate of ϕ_r^l is made and given as input to equations 4.31(a)-4.31(c), and ϕ_θ^l is determined by solving equation 4.27(b) where $[X^{\phi_\theta}]$ is obtained from equations 4.29(a)-4.29(c). The calculated values of ϕ_θ^l are given as input to $\{Y^{\phi_\theta}\}$ (equations 4.29(a)-4.29(c)) and ϕ_r^l is determined from equation 4.27(a) where $[X^{\phi_r}]$ is obtained from equations 4.28(a)-4.28(c). Iterations are performed with the newly obtained ϕ_r^l to calculate ϕ_θ^l until the convergence is reached at each node. The criteria set for convergence to calculate ϕ_r^l and ϕ_θ^l at each node is considered to be $\left|\phi_r^{l\text{previous}} - \phi_r^{l\text{current}}\right| \leq 10^{-6}$ and $\left|\phi_\theta^{l\text{previous}} - \phi_\theta^{l\text{current}}\right| \leq 10^{-6}$, respectively, at the l^{th} node for the previous and current iterations, respectively.

4.4.6 Solution algorithm

The soil parameters *k* and *t* which are functions of ϕ_r and ϕ_θ must be known to obtain *w* from the differential equation (equation (4.12)) describing the monopile displacement. Moreover, the parameters γ_1-γ_8 (equations (4.24a)-(4.24h)) must be known to obtain ϕ_r and ϕ_θ from equations (4.23a) and (4.23b) and these parameters depend on *w* through m_{s1}, m_{s2}, m_{s3}, n_{s1}, and n_{s2} (equations (4.22a)-(4.22e)). Therefore, the differential equation describing monopile displacement w_i and soil displacement ϕ_r and ϕ_θ are coupled and an iterative algorithm is required to obtain a solution.

An initial guess of 1.0 is made for γ_1-γ_8 (equations (4.26a)-(4.26h)) at each grid point (see Figure 4.5(a)) along *r* using which ϕ_r and ϕ_θ are determined using an iterative algorithm

that satisfy the boundary conditions ϕ_r and $\phi_\theta = 1$ at $r = r_p$ and ϕ_r and $\phi_\theta = 0$ at $r = \infty$. After obtaining ϕ_r and ϕ_θ at each grid point, the strain components are calculated (using equation (4.8)) with which the secant shear modulus $G_s(r,\theta)$ are evaluated (using equation (4.1), (4.2) or (4.3)), at each grid point in the soil domain along r and θ and at each node along the z-axis (see Figure 4.5(b)). It is important to note that the induced displacement and strain varies at each point in the monopile-soil domain because of which the secant shear modulus also varies at each point (because of the nonlinear stress-strain behaviour of soil), which implies that the deformation induced in the soil mass because of monopile movement renders the soil heterogeneous.

Using the calculated values of $G_s(r,\theta)$, ϕ_r and ϕ_θ, the values of k_i and t_i (described by equations (4.16) and (4.17)) are obtained at each node along the monopile length using the trapezoidal rule of integration where the integration is first performed along the r-direction with step length $(r_{l+1} - r_l)$ or $(r_l - r_{l-1})$ at any tangential distance θ, followed by a subsequent integration over θ with step length $\Delta\theta$ (see Figure 4.5(a)). With the calculated values of k_i and t_i the monopile displacement w_i and rotation dw_i/dz is evaluated (using equation (4.20a)-(4.20e)) at different node points along the monopile length with which the parameters m_{s1}, m_{s2}, m_{s3}, n_{s1}, and n_{s2} (equations (4.22a)-(4.22e)) are evaluated numerically following the trapezoidal rule of integration along the θ and z-direction. First, the integration is performed along θ at any radial distance r_l with a step length $r_l\Delta\theta$; the value of the integration obtained is further integrated along the z-direction with a step length Δz. After obtaining m_{s1}, m_{s2}, m_{s3}, n_{s1}, and n_{s2}, new values of γ_1-γ_8 are evaluated at each grid point and compared to the assumed initial values. If the differences are more than the prescribed tolerable limit of 0.001 at each grid point, the calculations described so far are repeated with the calculated values of γ_1-γ_8 as the new initial guesses. Iterations are continued until the values of γ_1-γ_8 between successive iterations fall below the prescribed limit at each grid point. Figure (4.6) illustrates the solution algorithm which is implemented in a MATLAB script on a computer with Intel® Core™ i5-3210M CPU @ 2.50 GHz and 8 GB RAM.

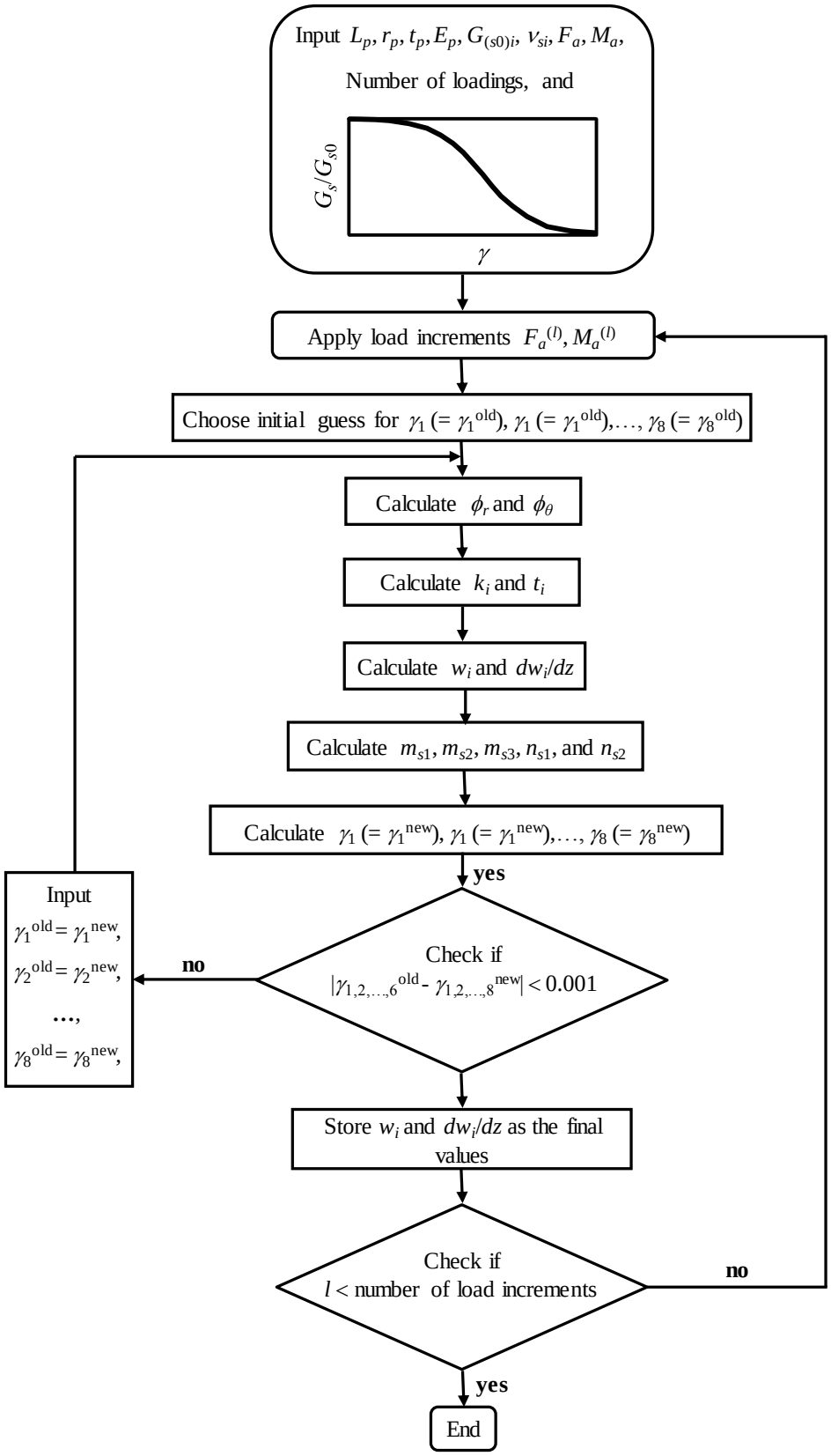

Figure 4.6: Solution algorithm

4.5 Results

In order to verify the mathematical accuracy of the present analysis a comparison of pile response – head displacement and rotation obtained from the present analysis is done with the results of equivalent 3-D FE analysis using nonlinear elastic relationships for the case of small-diameter piles. The analysis is validated with several full-scale field pile-load tests and the *p-y* analysis commonly used to predict laterally loaded pile response, for small-diameter piles embedded in clayey and sandy soil deposit. Further, verification of the present nonlinear elastic approach is done with that of an equivalent 3-D FE analysis using an elastic-plastic constitutive soil model following the Tresca yield criterion for the case of large-diameter monopiles. A comparison of the computational time required to obtain results between the present and equivalent 3-D FE analysis is also shown to demonstrate the computational efficiency of the present analysis.

4.5.1 Verification of present analysis with 3-D FE analysis using nonlinear elastic soil constitutive relationships

In order to verify the mathematical accuracy and computational efficiency of the present formulation, a comparison of the pile response obtained from the present analysis is done with the results of equivalent 3-D FE analyses using the nonlinear elastic soil constitutive relationships described by equation (4.1) and (4.2).

In the 3-D FE analysis (performed using Abaqus), the pile and soil are modeled as a single cylindrical part with appropriate partitioning to represent the pile and soil separately, which ensures no slippage or separation between the soil and pile. The topsoil surface is flush with the pile head and the bottom soil surface is extended to a finite depth below the pile base. The horizontal radial extent of the soil domain is selected to be approximately 30 times the pile diameter from the pile axis for the problems solved. Different boundary conditions are prescribed at the boundaries of the model – all components of displacements are assumed to be zero along the bottom (horizontal) surface and two horizontal components are assumed to be zero along the outer curved (vertical) surface of the soil domain. Eight-noded reduced integration (C3D8R) brick elements are used to model both the soil and pile domain. Concentrated force or moment is applied to a reference point at the pile head, to which all the

nodes of the pile head are connected. These loads (force/moment) are applied in several fixed increments.

The pile in the FE analysis is modeled as an elastic element whereas the soil is modeled using the nonlinear constitutive relationships (given by equation (4.1) or (4.2)). In order to implement the nonlinear equations i.e., the variation of secant shear modulus of soil with the strain the ‘‘field variable (FV)” and the ‘‘user defined field” options, for the material definition in Abaqus is used. In the simulations, the field variable is assigned as the Young’s modulus and the user-defined field (USDFLD) FORTRAN subroutine is written in Microsoft Visual Studio where Young’s modulus is made to vary with the evaluated value of the strain following equation (4.1) or (4.2) within the integration points of each element in the soil domain for each load increment. In the FORTRAN code, the arrays of the strain components in each direction at each integration point within the soil elements are obtained using the GETVRM subroutine at the end of each increment. Then, the strain corresponding to equation (4.1) or (4.2) is calculated. Further, it is checked that if the strain is less than the minimum specified strain ($\varepsilon_{q0} < 10^{-5}$ for equation (4.1) and $\gamma_{oct} < 10^{-6}$ for equation (4.2)) within each element, then the initial Young’s modulus is specified to those elements else for other elements Young’s Modulus is evaluated using equation (4.1) or equation (4.2). The evaluated value of Young’s modulus for each element at the end of each increment is saved as a “solution dependent variable (SDV)” which is then used for the material definition at the integration points of each element of the soil domain in the next load increment. This (USDFLD) subroutine written is linked to the model developed in the Abaqus Create job option and the analysis is performed in an Intel Fortran environment to get the outputs. Note, that for an accurate implementation of the variation of Young’s modulus, it is necessary that the size of the load increments and the size of the elements should be adequately chosen, based on convergence checks. For the problems solved, the pile-soil domain is discretized using a global seed of 1.0 and the applied load is divided into 40 increments.

Figures 4.7(a)-4.7(b) and 4.7(c)-4.7(d) show the comparison of the pile responses (head displacement w_h and rotation ψ_h) obtained from the present and FE analysis, for an applied force and moment, respectively. The nonlinear elastic relationships given by Osman et al. (2007) (equation (4.1)), is used for modeling the soil in the present and FE analysis. The details of the pile-soil inputs are given in the figure itself. For the problems analyzed, the initial shear

modulus G_{s0} of soil is specified to be 10 MPa in the present analysis; the results are obtained for two different values of Poisson's ratio ν_s = 0.2 and 0.49. In the 3-D FE analysis, Young's modulus of soil is varied with the deviatoric strain, therefore, the initial Young's modulus E_{s0} {= $G_{s0} \times 2 \times (1 + \nu_s)$} is given as input for the two cases of Poisson's ratio which are 24 MPa (corresponding to ν_s = 0.2) and 29.8 MPa (corresponding to ν_s = 0.49), respectively. For convergence, the pile-soil domain is discretized using a global seed of 1.0 and the applied load is divided into 40 increments. From the comparisons (4.7(a)-4.7(b) and 4.7(c)-4.7(d)), it is evident that the match between the pile response obtained from the present and FE analyses are in good agreement. Further, an illustration of the degraded value of Young's modulus (FV1) at the end of the 40th increment (final load increment) from the FE analysis, is also shown in Figures 4.8(a)-4.8(b) (for the problems shown in Figures 4.7(a)-4.7(b) corresponding to ν_s = 0.2 and 0.49) and 4.9(a)-4.9(b) (for the problems shown in Figures 4.7(c)-4.7(d) corresponding to ν_s = 0.2 and 0.49) to confirm the implementation of the nonlinear elastic constitutive relationship in Abaqus. It is evident from the figures that the degradation of Young's modulus is predominant around the pile head and near the pile-soil interface. At a greater distance from the pile head, Young's modulus is equal to the initial (small-strain) modulus.

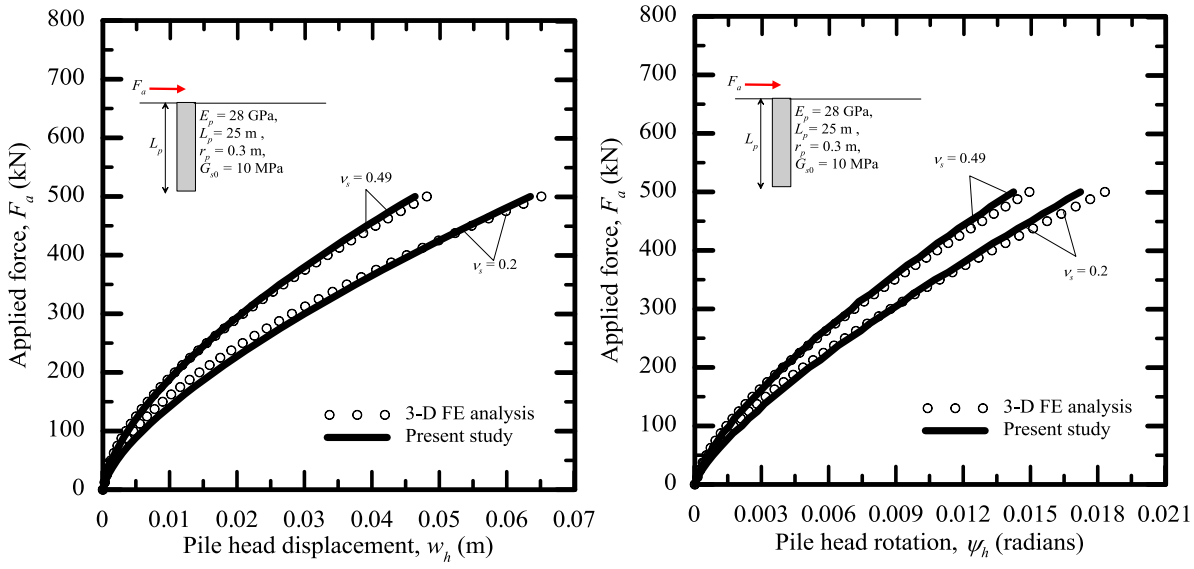

(a) (b)

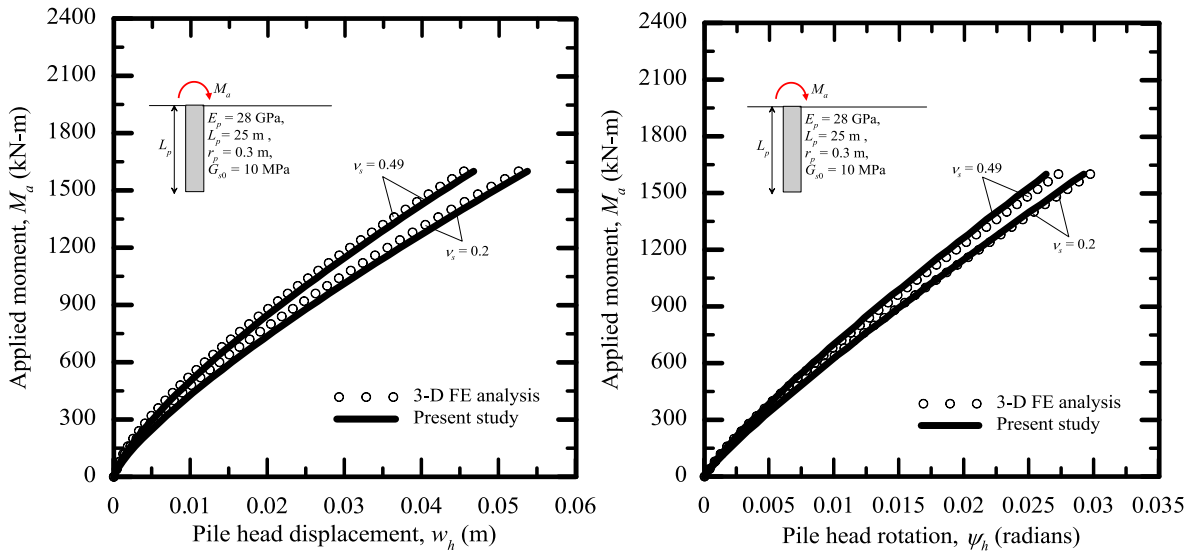

(c) (d)

Figure 4.7: Comparison of (a) pile head displacement, (b) pile head rotation, for an applied force, and (c) pile head displacement, (d) pile head rotation, for an applied moment, using the nonlinear elastic relationship by Osman et al. (2007) for two different values of Poisson's ratio

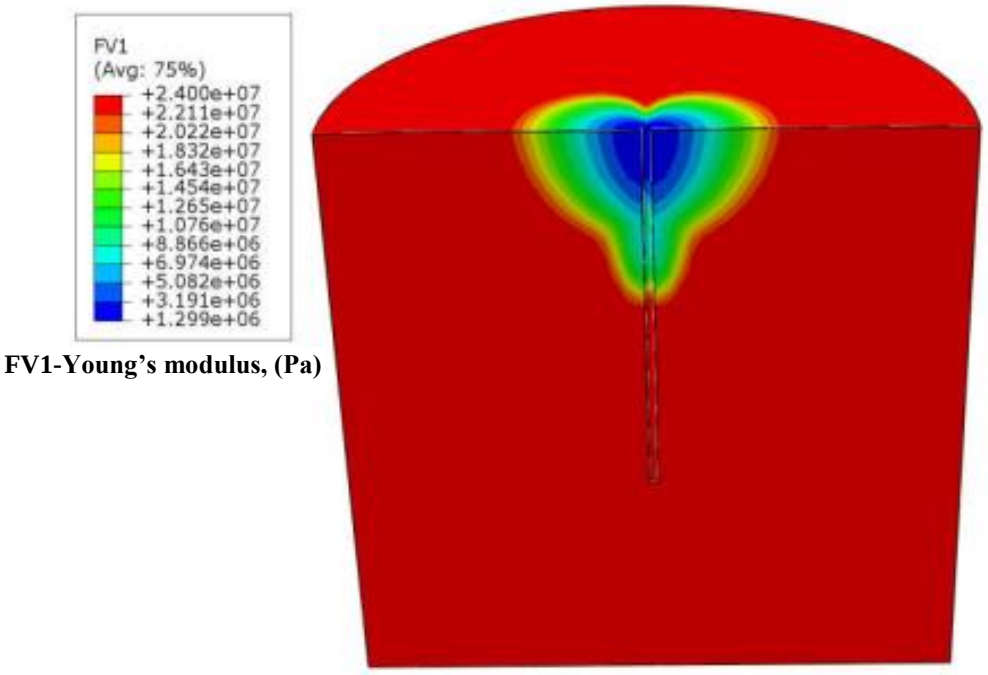

(a)

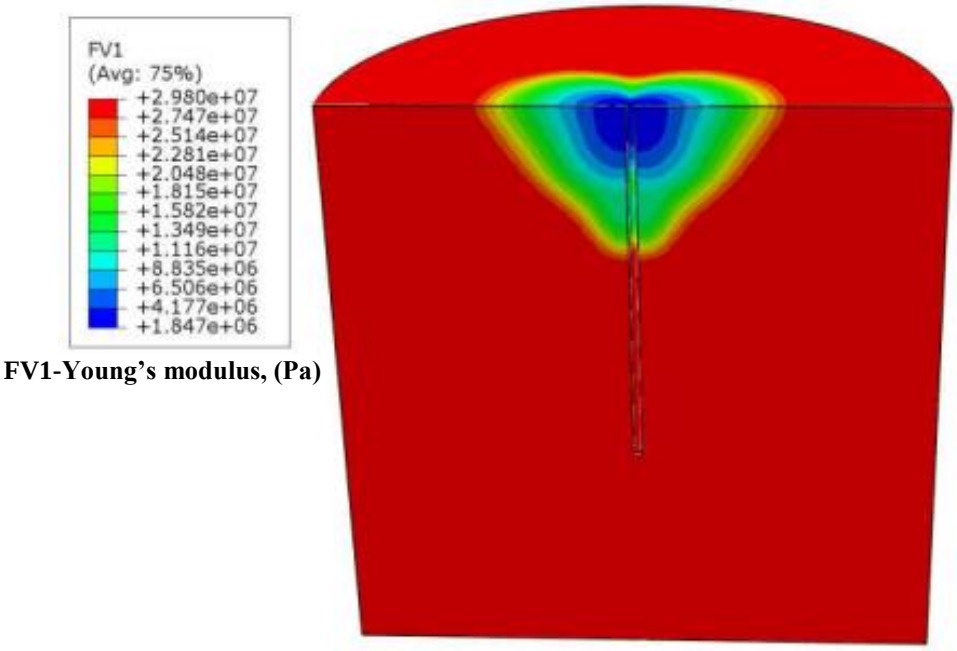

FV1-Young's modulus, (Pa)

(b)

Figure 4.8: Variation of Young's modulus in the soil domain (a) with Poisson's ratio of 0.2, and (b) with Poisson's ratio of 0.49, for an applied force from the 3-D FE analysis in ABAQUS using the nonlinear elastic relationship by Osman et al. (2007), at the end of the 40th increment

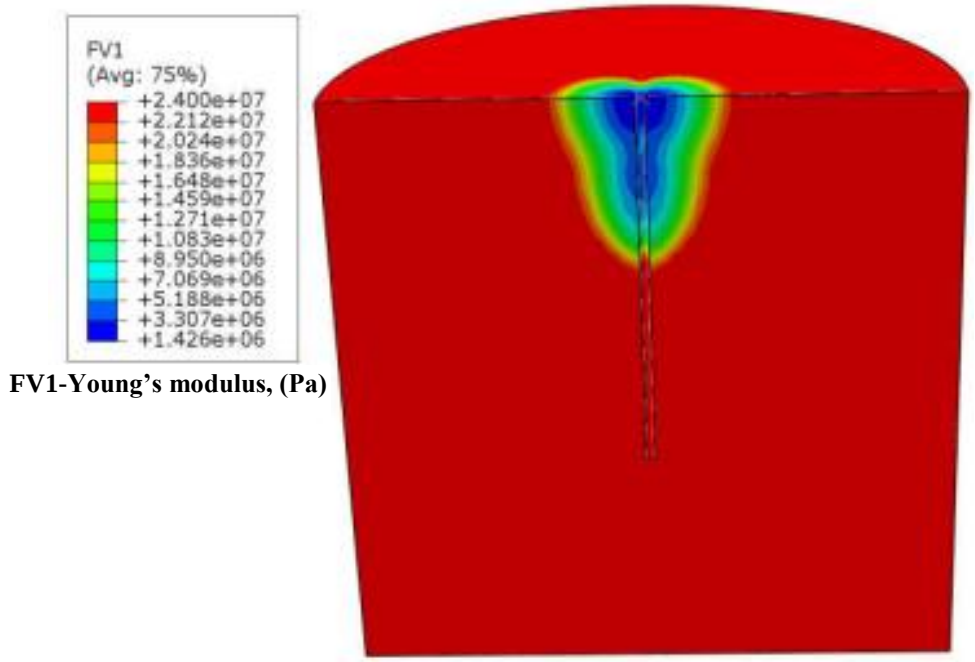

FV1-Young's modulus, (Pa)

(a)

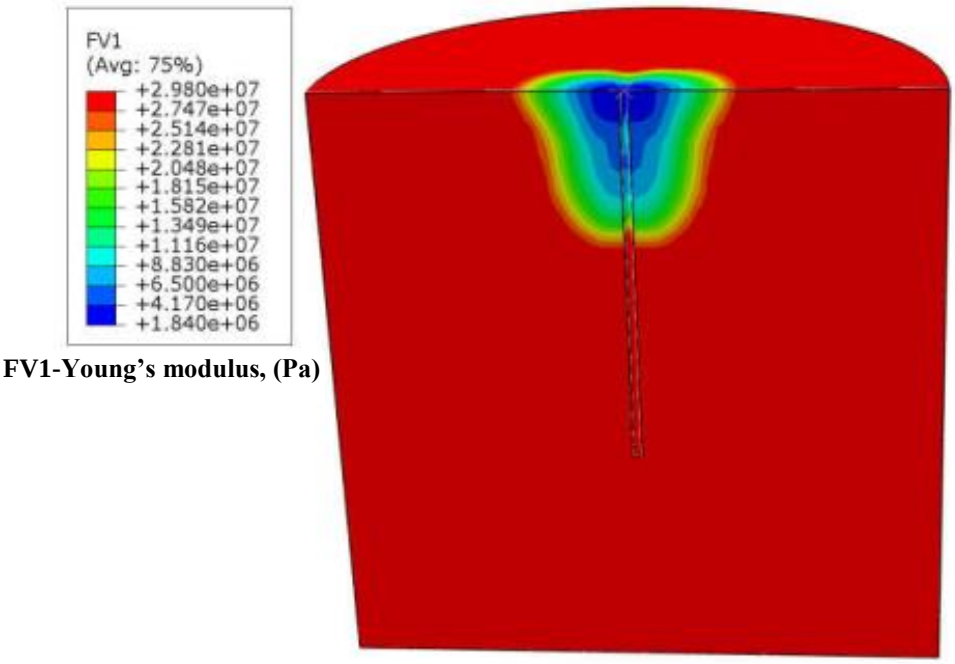

(b)

Figure 4.9: Variation of Young's modulus in the soil domain (a) with Poisson's ratio of 0.2, and (b) with Poisson's ratio of 0.49, for an applied moment from the 3-D FE analysis in Abaqus using the nonlinear elastic relationship by Osman et al. (2007), at the end of the 40th increment

Figures 4.10(a)-4.10(b) and Figures 4.10(c)-4.10(d) show the comparison of pile responses obtained from the present and FE analysis, for an applied force and moment, respectively, following the nonlinear elastic constitutive relationship given by Vardanega and Bolton (2013) (equation (4.2)) where $\gamma_{ref} = 0.002$ is assumed. The details of the pile-soil inputs are given in the figure itself. For the problems analyzed, the initial (small-strain) shear modulus G_{s0} = 20 MPa with ν_s = 0.49 is given as input, in the present analysis. In the 3-D FE analysis, Young's modulus of soil is made to vary with the octahedral shear strain, therefore, the initial Young's modulus E_{s0} {= $G_{s0} \times 2 \times (1 + \nu_s)$} = 59.6 MPa, is given as input. Further, an illustration of the degraded value of Young's modulus (FV1) at the end of the 40th increment from the FE analysis, is also shown in Figures 4.11(a) (for the problems shown in Figures 4.10(a)-4.10(b)) and 4.11(b) (for the problems shown in Figures 4.10(c)-4.10(d)) to confirm the implementation of the nonlinear elastic constitutive relationship in Abaqus.

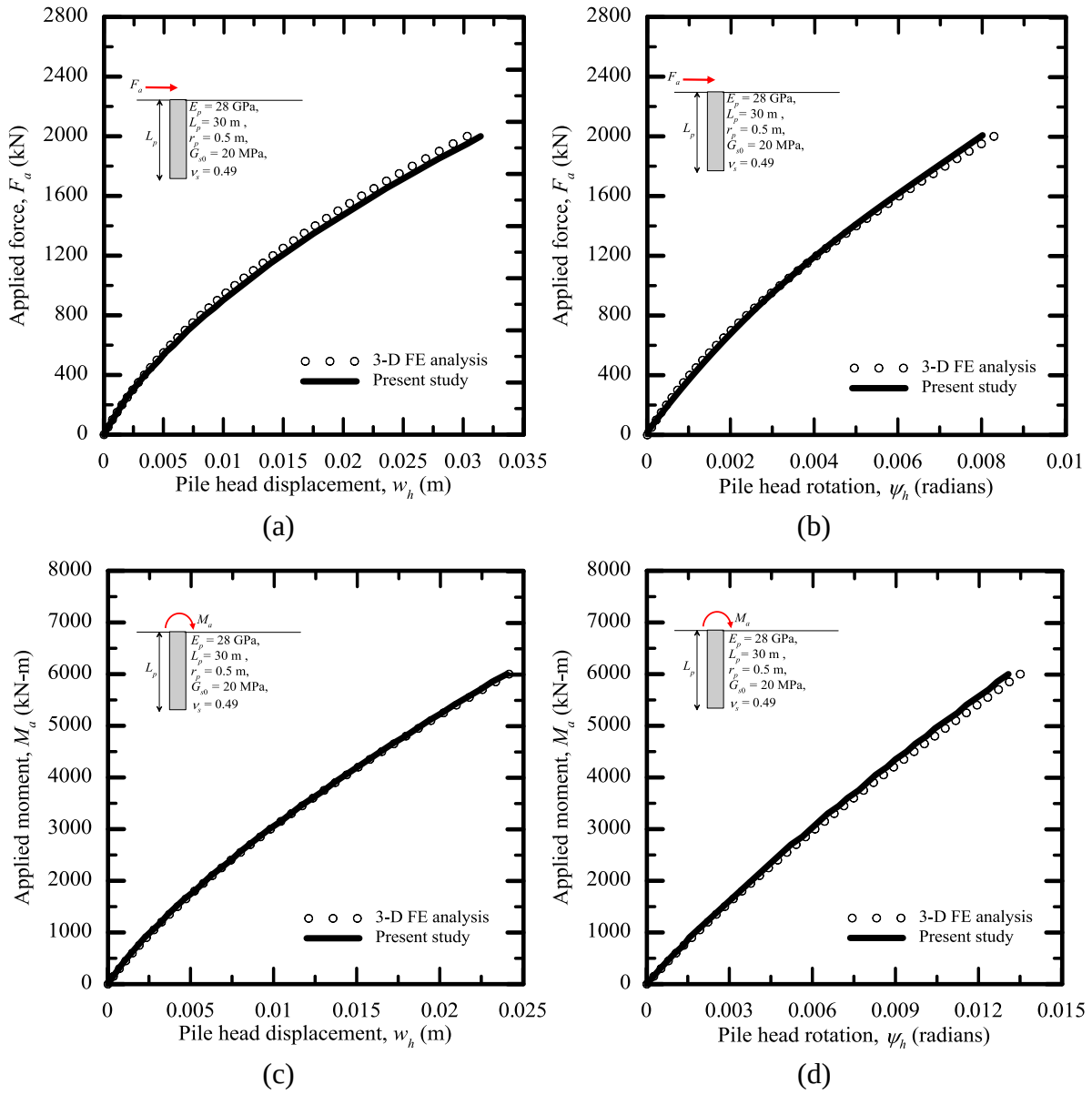

Figure 4.10: Comparison of (a) pile head displacement, (b) pile head rotation, for an applied force, and (c) pile head displacement, (d) pile head rotation, for an applied moment, using the nonlinear elastic relationship by Vardanega and Bolton (2013)

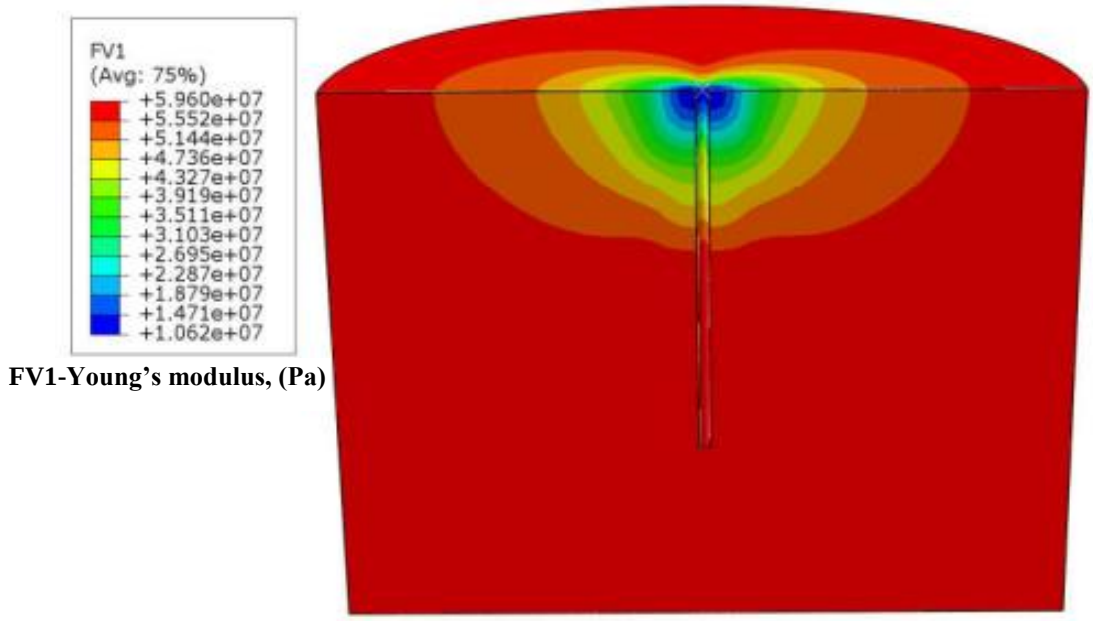

(a)

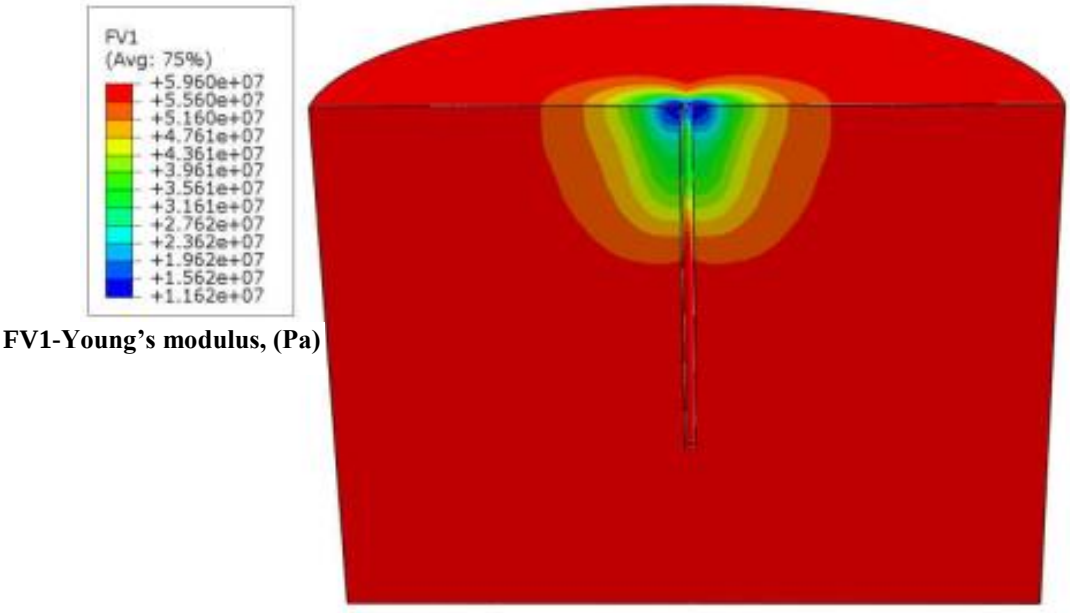

(b)

Figure 4.11: Variation of Young's modulus in the soil domain (a) with Poisson's ratio of 0.49 for an applied force, and (b) with Poisson's ratio of 0.49, for an applied moment from the 3-D FE analysis in Abaqus using the nonlinear elastic relationship by Vardanega and Bolton (2013), at the end of the 40th increment

From the comparisons shown in Figures 4.7 and 4.10, it is evident that the present analysis is mathematically accurate and can be used to predict pile response with a reasonable

degree of accuracy. The difference in the pile responses is approximately less than 8% for the problems demonstrated in Figures 4.7 and less than 4% for the problems demonstrated in Figures 4.10, for the range of applied load. This difference in the prediction may be a result of the assumption of the soil displacement functions in the analysis (equations (4.4)); the assumption of zero vertical displacement does not have a significant influence on the prediction of pile response. A comparison of the computational time (CPU processing time) for the problems solved (Figure 4.7 and 4.10) in a computer with Intel® Core™ i5-3210M CPU @ 2.50 GHz and 8 GB RAM between the present and FE analysis is also depicted in Table 4.2. It is evident from Table 4.2 that the present analysis is computationally efficient compared to the 3-D FE analysis; this is because of the reduction in computational effort to obtain the solutions of the differential equations describing soil displacement (equations 4.25(a) and 4.25(b)) which are 1-D in nature; although, the actual problem is 3-D.

Table 4.2: Computational time required for 3-D FE analysis and present analysis using nonlinear elastic constitutive relationships

Solved problems	3-D FE analysis, (secs)	Present analysis, (secs)
Figures 4.7(a) and (b)	8685	337
Figures 4.7(c) and (d)	8777	356
Figures 4.10(a) and (b)	8918	380
Figures 4.10(c) and (d)	9279	380

4.5.2 Comparison of the present nonlinear elastic analysis with full-scale field pile-load tests and p-y analysis for small-diameter piles in clay soil deposit

To validate the accuracy and reliability of the present analysis, the nonlinear response obtained from the present analysis is compared with the response obtained from full-scale field pile-load tests and the semi-empirical *p-y* method. The comparison is done for five different case studies of field pile-load tests in undrained clayey soil deposit, available in the literature. The prediction of the response from the present analysis is done following the recently developed nonlinear elastic relationship by Vardanega and Bolton (2013) (equation (4.2)) where the initial shear modulus G_{s0} of soil for the undrained clay is estimated following equation (4.3) if elementary parameters describing clay behaviour – s_u, *PI*, and *OCR* are known or can be judiciously estimated based on the soil description in a geotechnical site investigation

report. An illustration of a typical geotechnical site investigation report from the site Manor, Texas is demonstrated in Figures 4.12(a)-4.12(c) from which the description of the soil profile along with necessary inputs for the computational models (*p-y* method or the present analysis) to describe soil behavior can be obtained. Figure 4.12(a) provides a description of the soil profile with depth; the soil is primarily a heavily overconsolidated highly plastic stiff clay. Figure 4.12(b) shows the water content, plastic limit, and liquid limit at different depths; the water content is used to locate the ground water table at the time of the field pile-load test and also to estimate the unit weight of clay while the Plastic limit (PL) and Liquid limit (LL) are used to evaluate the Plasticity index *PI* (= LL – PL) of the soil. Figure 4.12(c) shows the undrained shear strength s_u of the clay deposit with depth from the in-situ penetrometer test.

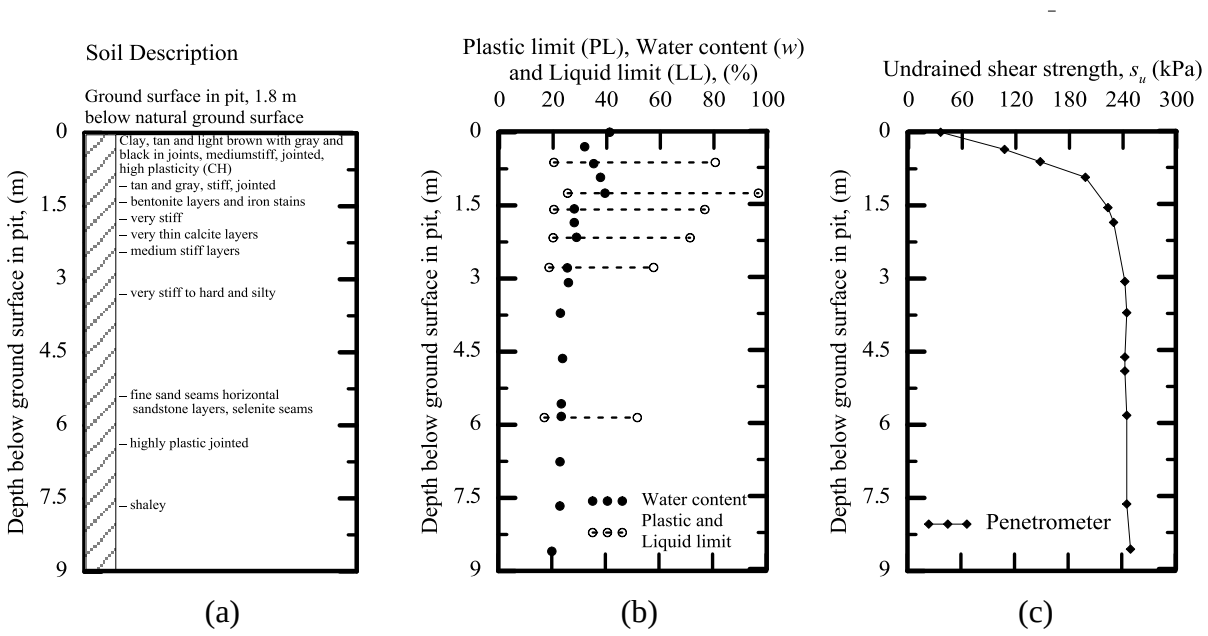

Figure 4.12: Details of the soil profile at the site Manor, Texas (regenerated from Reese et al. 1975)

A comparison of pile head displacement obtained from the present analysis with those of the *p-y* analysis (reported by Reese and Impe (2011) which is also included in the design code API (2011) – Load deflection (*p-y*) curves for stiff clay (Reese et al. 1975)) and the measured data from the field pile-load test, conducted at the Manor, Texas test site (Figure 4.12(a)) by Reese et al. (1975) on a steel pipe pile, is shown in Figure 4.13. To predict the pile response from the present analysis – an average value of s_u = 153 kPa at five pile diameters

(Reese et al. 1975) and PI = 60 (Guo 2012) is computed from Figure 4.12(c) and Figure 4.12(b), respectively, OCR = 6 (since the soil is heavily overconsolidated (Wu et al. 1998)) is assumed, the correlation factor K_c = 260 is obtained from Figure 4.2 to evaluate $E_{s0} = K_c \times s_u$ = 220 × 153/1000 = 48.6 MPa such that G_{s0} = 13.3 MPa for the undrained clay deposit with ν_s = 0.49, and equation (4.3) with $\gamma_{ref} = J \times (PI/1000)$ = 2.2 × (0.6/1000) = 0.00132, are used as inputs. The pile properties and applied loading used in the analysis are – modulus of rigidity E_pI_p = 493.7 MPa, L_p = 15.2 m, r_p = 0.321 m, and the load being applied at an eccentricity e = 0.305 m (Guo 2013). The maximum difference in the pile head displacement for the range of applied load is approximately 16% between the measured data and the predicted response from the present analysis and 7% between the measured data and the predicted response from the *p-y* analysis.

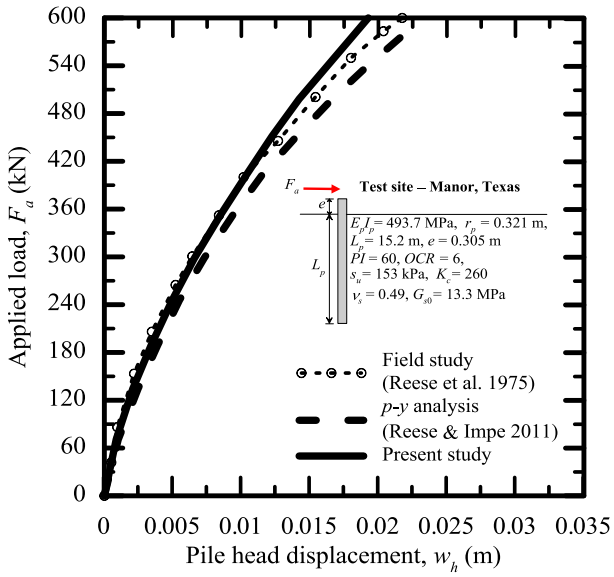

Figure 4.13: Comparison of pile head displacement with measured data from a field test, *p-y* analysis, and the present study at Manor, Texas test site

Figure 4.14 show the comparison of the pile head displacement for the lateral load tests conducted at the Houston, Texas test site (Reese and Welch 1975) on a bored pile with those of the measured data, *p-y* analysis (reported by Reese and Impe (2011) which is also included in the design code API (2011) – Load deflection (*p-y*) curves for stiff clay (Reese et al. 1975)), and the present analysis. To obtain the pile response from the present analysis – G_{s0} = 8.1 MPa is estimated for K_c = 230 (from Figure 4.2) and ν_s = 0.49 for an average value of s_u = 105 kPa

(measured from unconsolidated undrained triaxial compression test), *OCR* = 4.5 (since the soil is reported to be overconsolidated (Wu et al. 1998)), and *PI* = 51 (Reese and Impe 2011, Heidari et al. 2013) and equation (4.3) with γ_{ref} = 2.2 × (0.51/1000) = 0.001122, are used as inputs. The pile properties and applied loading reported are – modulus of rigidity E_pI_p = 400 MPa, length L_p = 15.2 m, r_p = 0.321 m, and the load applied at an eccentricity e = 0.305 m. The maximum difference in the pile head displacement for the range of applied load is approximately 26% between the measured data and the predicted response from the present analysis and 21% between the measured data and the predicted response from the *p-y* analysis.

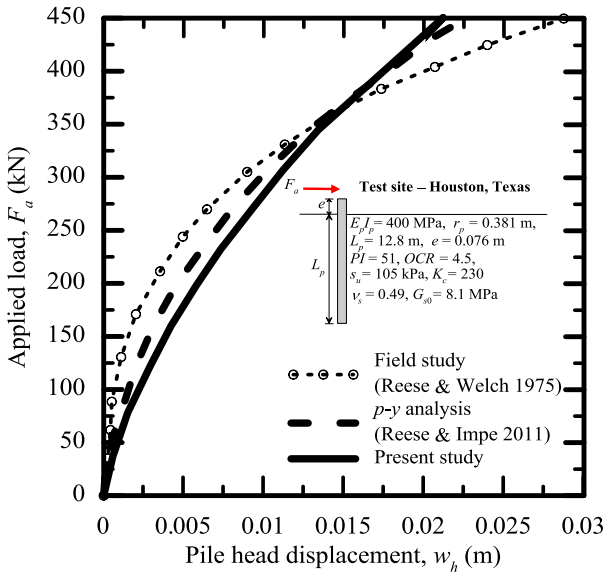

Figure 4.14: Comparison of pile head displacement with measured data from a field test, *p-y* analysis and the present study at Houston, Texas test site

Further, a comparison of the prediction of pile head displacement (Figure 4.15) from the present analysis is also done with the *p-y* analysis (reported by Reese and Impe (2011) which is also included in the design code API (2011) – Load deflection (*p-y*) curves for soft clay (Matlock 1970)) and lateral load tests on steel pipe piles, performed at Sabine, Texas test site (Matlock 1970). The soil was reported to be lightly overconsolidated soft clay with an average s_u = 14.4 kPa measured from in-situ vane shear test and *PI* = 68 (Guo 2013) such that γ_{ref} = 2.2 × (0.68/1000) = 0.001496. G_{s0} = 1.02 MPa is evaluated for K_c = 210 assuming *OCR* = 1.5 for the slightly overconsolidated clay (Wu et al. 1998). The details of the pile and loading properties are provided in the figure itself. The maximum difference in the pile-head

displacement for the range of applied load is approximately 6% between the measured data and the predicted response from the present analysis and 77% between the measured data and the predicted response from the *p-y* analysis.

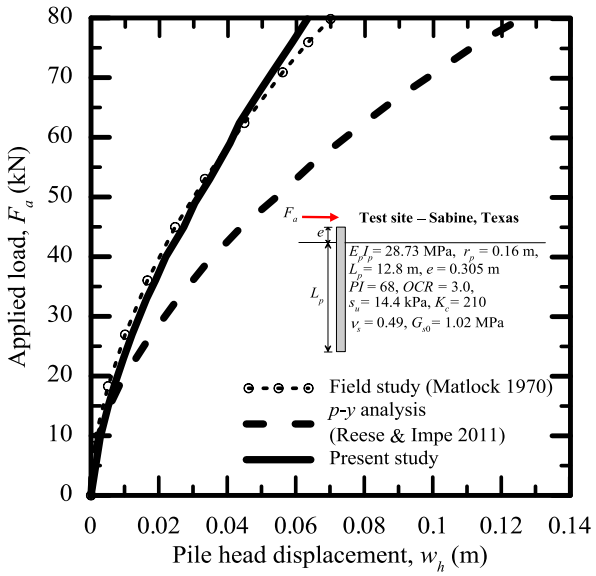

Figure 4.15: Comparison of pile head displacement with measured data from a field test, *p-y* analysis and the present study at Sabine, Texas test site

A comparison of the prediction of pile head displacement (Figure 4.16) from the present analysis is also done with the lateral load tests performed on reinforced concrete short piles (Pile no. 4, Tests site B) at Los Angeles (Bhusan et al. 1979), and the *p-y* analysis formulated by Zhang and Ahmari (2013) for the nonlinear analysis of short piles in cohesive soils. The soil at the site consisted of overconsolidated sandy clay of medium to high plasticity. An average value of s_u = 143.7 kPa (Vallahavan and Alikhanlou 1982) with K_c = 347 (Zhang and Ahmari 2013), and PI = 30 (Bhusan et al. 1979) such that γ_{ref} = 2.2 × (0.30/1000) = 0.00066 are used as input in the analysis for computations. The details of the pile and loading properties are reported in the figure itself. The maximum difference in the prediction of pile head displacement for the range of applied load is approximately 13% between the measured data and the predicted response from the present analysis and 24% between the measured data and the predicted response from the *p-y* analysis.

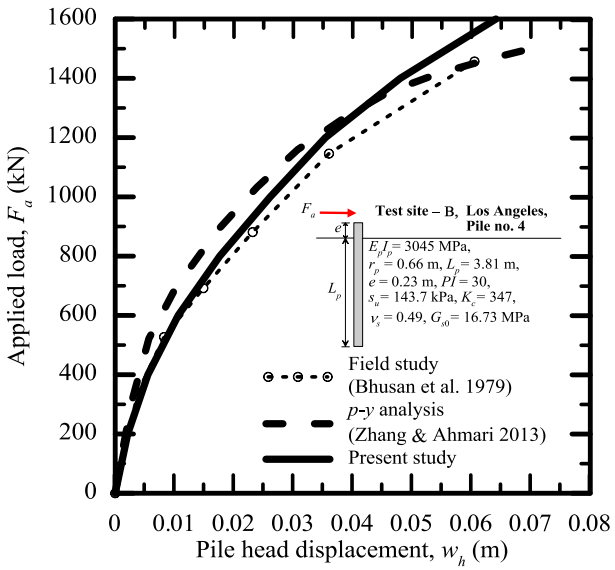

Figure 4.16: Comparison of pile head displacement with measured data from a field test, *p-y* analysis, and the present study at a Los Angeles test site

Pile head displacement (Figure 4.17) from the present analysis is also compared with the lateral load tests performed on reinforced concrete short piles at College Station, Texas (Bierschwale et al. 1970), and the *p-y* analysis developed by Zhang and Ahmari (2013). The soil at the site consisted of medium stiff to stiff sandy clay with an underlying stiff to very stiff fissured clay of high plasticity. An average value of s_u = 100 kPa such with K_c = 250 (Zhang and Ahmari 2013), and PI = 30 % (Bierschwale et al. 1970) such that γ_{ref} = 2.2 × (0.30/1000) = 0.00066 are used as inputs. The maximum difference in the pile head displacement for the range of applied load is approximately 7% between the measured data and the predicted response from the present analysis and 8% between the measured data and the predicted response from the *p-y* analysis.

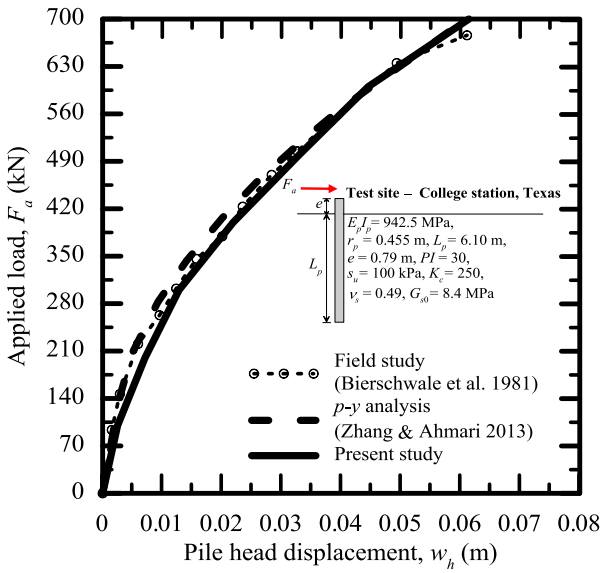

Figure 4.17: Comparison of pile head displacement with measured data from a field test, *p-y* analysis and the present study at College Station, Texas test site

From the comparisons demonstrated in Figures 4.13-4.17, it is evident that the present nonlinear elastic analysis can be used predict pile response with an acceptable degree of accuracy. For the predictions demonstrated in Figures 4.13-4.15, the initial shear modulus which is an input in the present analysis is estimated based on the recommendations of Duncan and Buchignani (1976) (also included in USACE 1990) where the numerical data for *PI* and *OCR* are judiciously chosen which are either reported or recommended by several researchers in the literature. For the problems demonstrated in Figures 4.16 and 4.17, the initial shear modulus reported by Zhang and Ahmari (2013) is used in the present analysis. The difference in the pile response between the present analysis and the measured data may be a result of the pile-soil slippage and separation. Further, the *p-y* analysis predicts reasonably accurate results in comparison to the field tests (see Figure 4.13 and Figures 4.16-4.17); this is because the *p-y* curves for these analyses are generated based on the pile-soil data of the specific site, however, their applicability to obtain pile response at other sites is questionable (e.g., see Figure 4.14). Thus, the *p-y* curves are site-specific and not applicable universally; in fact, *p-y* curves constructed from the pile-soil data of a specific site have failed to produce accurate results when compared to the measured response of that site (e.g., see Figure 4.15).

4.5.3 Comparison of present analysis using nonlinear elastic relationship with field pile-load tests and p-y analysis for small-diameter piles in a sandy soil deposit

To further assess the reliability of the present analysis in predicting the nonlinear response of laterally loaded piles, pile head response obtained from the present analysis is compared with the response obtained from full-scale field pile-load tests and the semi-empirical *p-y* method in sandy soil deposit for three different case studies, available in the literature. The prediction of the response from the present analysis is done following nonlinear elastic relationship given by Oztoprak and Bolton (2013) (equation (4.4)) where the initial shear modulus G_{s0} of the sandy soil deposit is evaluated using equation (4.5).

Figure 4.18 shows a comparison of pile head displacement obtained from the present analysis with those of the *p-y* analysis (reported by Reese and Impe 2011), *p-y* analysis according to API (2011) (recommended by O' Neil and Murchinson 1983), and the measured data from field pile-load test, conducted at the Arkansas river test site (Alizadeh and Davission 1970) on a reinforced pipe pile (Pile 2) and embedded in a sandy soil deposit. For the comparison – an effective internal friction angle $\phi' = 45°$, effective unit of soil $\gamma' = 10.9$ kN/m^3 (Reese and Van Impe 2011, Guo 2010) and $\nu_s = 0.25$ are used as inputs to characterize the sandy soil and $E_pI_p = 69.02$ MPa, $L_p = 16.10$ m, $r_p = 0.480$ m, and $e = 0.031$ m (Guo 2010) are used as inputs for the pile properties and applied loading. To predict the pile response from the present analysis, the initial shear modulus G_{s0} is evaluated at each node along the pile length following equation (4.5) for which the initial void ratio $e_0 = 0.485$ is estimated from $e_0 = [\{(g_s - 1) \times \gamma_w\}/\gamma' - 1]$ where $\gamma_w = 9.81$ kN/m^3 is the unit weight of water and $g_s = 2.65$ is the specific gravity of sand; $C_g = 612.0$, $e_g = 2.17$, and $n_g = 0.44$ corresponding to Ottawa sand are used, since no specific data is available; the initial mean effective stress $\sigma'_{m0} = (\sigma'_{zz} + 2 \times \sigma'_{rr})/3 = \sigma'_{zz} \times (1 + 2 \times K_0)/3 = \gamma' \times z \times (1 + 2 \times K_0)/3$ (where $\sigma'_{zz} = \gamma' \times z$ is effective vertical stress at any depth in the soil and $\sigma'_{rr} = K_0 \times \sigma'_{zz}$ is the effective horizontal stress at any depth z in which $K_0 = 1 - \sin\phi' = 0.3$ (Jaky 1948) is the coefficient of earth pressure at rest for a normally consolidated soil) is evaluated (note that G_{s0} is linearly varying with depth). The nonlinear variation of soil modulus with strain is captured following equation (4.4); the fitted parameters γ_{ref}, γ_e, and α corresponding to the upper bound curve (see Figure 4.3 and Table 4.1) are used since the friction angle of the sandy soil deposit corresponds to that of dense sand (Mayerhoff 1956, Budhu 2010) and it is expected that the rate of degradation of soil modulus for dense

sand would be slower than that of medium (mean curve) and loose (lower bound curve) sand. The response from the *p-y* analysis (API 2011) where *p-y* curves are generated (using LPILE) for an initial modulus of subgrade reaction k_h = 62.43 MN/m^3 corresponding to ϕ' = 45° and sand below the water table is also shown. The maximum difference in the pile head displacement for the range of applied load is approximately 36% between the measured data and predicted response from the present analysis, 17% between the measured data and *p-y* analyses reported by Reese and Impe (2011), and 53% between the measured data and the *p-y* analysis.

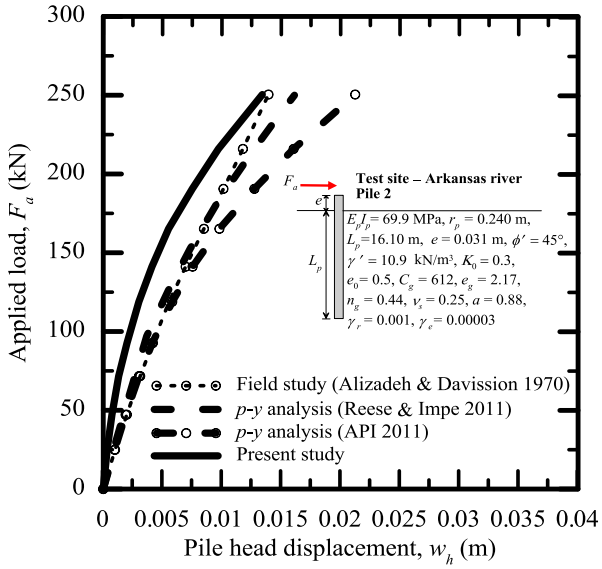

Figure 4.18: Comparison of pile head displacement with measured data from a field test, *p-y* analyses (following Reese and Impe 2011 and API 2011), and the present study, for the test site at Arkansas river (Pile 2)

A comparison of pile head displacement obtained from the present analysis with those of the *p-y* analysis (API 2011) and the measured data from the field pile-load test conducted at the Arkansas river test site (Alizadeh and Davission 1970) on an open-ended pipe pile (Pile 16), is also shown in Figure 4.19. For the comparison – an effective internal friction angle ϕ' = 43°, effective unit of soil γ' = 9.87 kN/m^3 (Guo 2010), and ν_s = 0.15 are used as inputs for the sandy soil deposit; the pile properties and applied loading reported by Guo (2010) are given in the figure itself (Figure 4.18). The initial shear modulus G_{s0} is evaluated at each node along the pile length following equation (4.5) for which the initial void ratio e_0 = 0.64 is estimated using the same procedure as described in the previous problem; C_g, e_g, and n_g corresponding

to Ottawa sand are used; the initial mean effective stress σ'_{m0} at any depth z along the pile length is evaluated for K_0 = 0.32 (as demonstrated in the previous problem). The nonlinear variation of soil modulus with strain is captured following equation (4.4) and the fitted parameters γ_{ref}, γ_e, and α corresponding to the upper bound curve (see Table 4.1 and Figure 4.3) are used. The results for the *p-y* analysis is obtained using the software LPILE where the *p-y* curves are obtained following API (2011) recommendations where k_h = 46.15 MN/m^3 is given as input corresponding to ϕ' = 43° and sand below the water table. The maximum difference in the pile head displacement for the range of applied load is approximately 37% between the measured data and the predicted response from the present analysis and 20% between the measured data and the predicted response from the *p-y* analysis.

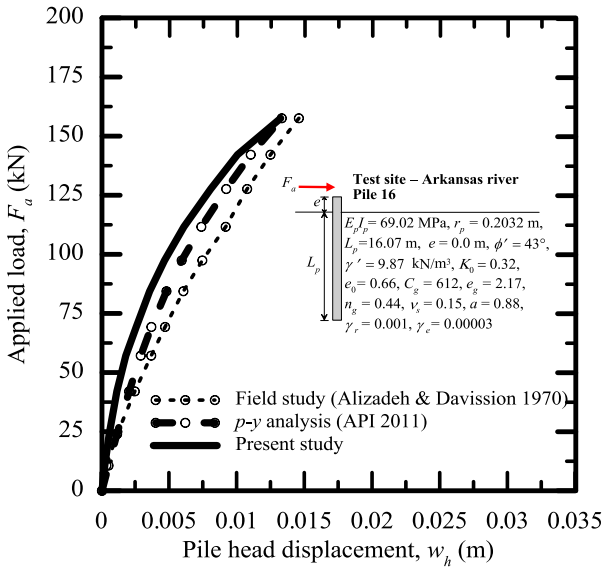

Figure 4.19: Comparison of pile head displacement with measured data from a field test, *p-y* analysis (API 2011) and the present study, for a test site in Arkansas river (Pile 16)

Further, comparison of pile head displacement obtained from the present analysis with those of the *p-y* analysis (Reese and Impe 2011), *p-y* analysis (API 2011) and the measured data from the field pile-load test conducted at the Mustang Island, Texas test site (Cox et al. 1974) on an open-ended pipe pile, is demonstrated in Figure 4.20. For the comparison – an effective internal friction angle ϕ' = 39°, effective unit of soil γ' = 10.4 kN/m^3 (Cox et al. 1974), and ν_s = 0.15 are used as inputs for the sandy soil deposit; the pile properties and applied loading are given in the figure itself (Figure 4.20). The initial shear modulus G_{s0} is evaluated

for e_0 = 0.56 is estimated; C_g, e_g, and n_g corresponding to Ottawa sand are used; the initial mean effective stress σ'_{m0} at any depth z along the pile length is evaluated for K_0 = 0.37. The nonlinear variation of soil modulus with strain is captured following equation (4.4) and the fitted parameters γ_{ref}, γ_e, and α corresponding to the mean curve (see Table 4.1 and Figure 4.3) since the friction angle corresponds to that of a medium dense sand (Mayerhoff 1956, Budhu 2010). The results for the *p-y* analysis is obtained using the software LPILE where the *p-y* curves are obtained following API (2011) recommendations where k_h = 40.72 MN/m^3 is given as input corresponding to ϕ' = 39° and sand below the water table. The maximum difference in the pile head displacement for the range of applied load is approximately 34% between the measured data and the predicted response from the present analysis, 0% between the *p-y* analyses reported by Reese and Impe (2011) and the measured data, and 30% between the measured data and the *p-y* analyses following API (2011) recommendations.

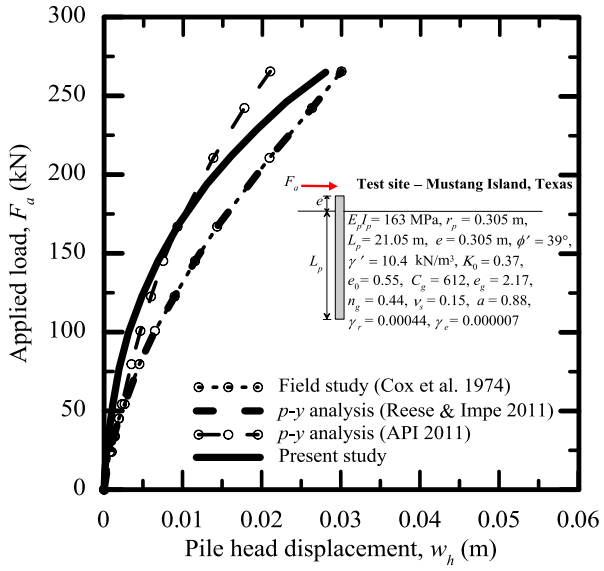

Figure 4.20: Comparison of pile head displacement with measured data from a field test, *p-y* analysis and the present study for a test site in Mustang Island, Texas

From the comparisons demonstrated in Figures 4.18-4.20, the difference between the predicted response from the present analysis and the measured data from field tests is typically greater than the acceptable range of 10-20% in the geotechnical foundation engineering practice. Besides, for all the three case studies, the curvature (i.e., the change in slope) of the plot obtained from the present analysis is appreciably different from those obtained from the field tests. The possible reasons for such differences in the predictions may be because of (i)

pile-soil slippage and separation, (ii) the uncertainty associated in the estimation of G_{s0} (see equation (4.5)) where the parameters corresponding to Ottawa sand are used for calculation in the present analysis, (iii) the nonlinear elastic relationship used might not be completely applicable to the test sites investigated, and (iv) soil yielding with increasing load that can be captured using the theory of plasticity is not included in the present analysis. Nevertheless, it is important to note that the present analysis can be used to predict the nonlinear response of laterally loaded piles in sandy soil deposit, however, further extension of the present nonlinear elastic framework including the plasticity theory which can capture soil yielding within this framework (especially for piles installed in sandy soil deposits) is necessary.

Further, the comparison of the response obtained from measured data with those of the *p-y* analysis where the *p-y* curves are obtained following the API (2011) recommendations also shows that the API recommendations might not always be suitable for predicting laterally loaded pile response (see Figures 4.18 and 4.20) unless calibrations are done to construct the *p-y* curves based on the specific site data (*p-y* analysis performed by Reese and Impe 2011 see Figures 4.18 and 4.20).

4.5.4 Comparison of present nonlinear elastic analysis with elastic-plastic 3-D FE analysis and p-y analysis for large-diameter monopiles in undrained clay soil deposit

Often commercial FE programs are used to obtain the nonlinear response of laterally loaded monopiles because they have several inbuilt elastic-plastic constitutive models which require simple inputs to describe the soil behavior. It will be interesting to check how the monopile response obtained from the present nonlinear elastic framework compares with those of 3-D FE analysis (performed using Abaqus) where the soil is modeled by an elastic-plastic constitutive model. The monopile response obtained from the present and 3-D FE analyses are also compared with the results of the *p-y* analysis to check the applicability of the *p-y* curves recommended in API (2011) to design monopiles.

In the 3-D FE analysis, steel monopiles with hollow circular cross-section and soil are modeled separately as single cylindrical parts within the part module. Three different monopile radius 2, 3, and 3.75 m are modeled where the wall thickness of each monopile is calculated by $t_p = 6.35 + (2 \times r_p)/100$ (mm). The embedment length of each monopile is 35 m with a length of 1 m above the ground surface. The soil domain extends to a finite depth below the

monopile base and the horizontal radial extent is selected to be 9 times the monopile diameter. Eight-noded reduced integration (C3D8R) brick elements are used to model both the soil and monopile with a global seed of 1.4 and 0.8, respectively, in the mesh module. In the property module, appropriate material and sectional definitions are created for the soil and monopile. The monopile is assumed to be linear elastic with E_p = 210 GPa, ν_p = 0.3, and density of 7850 kg/m^3. The soil is considered to be a heavily oversonsolidated stiff undrained clay with undrained shear strength s_u = 100 kPa, OCR = 2.5, and PI = 38 % (typical type of clay available in the UK North Sea where monopiles are being installed (Thomas (1989), Haiderali et al. (2013)) with E_{s0} = 47.9 MPa and ν_s = 0.49 MPa given as input for the clay deposit. The plastic characteristics of the clay are modeled using the Tresca yield criterion where s_u = 100 kPa is given as input. The density of the soil is input as 1800 kg/m^3. The monopile and the soil part instances are then positioned together in the assembly module to introduce a global coordinate system to the model. The analysis is then performed in a sequence of four steps – (i) Initial step – all components of displacements are assumed to be zero along the bottom (horizontal) surface and two horizontal components are assumed to be zero along the outer curved (vertical) surface of the soil domain, (ii) Geostatic step – initial stresses are generated within the soil elements by introducing a gravity load to the soil elements in the load module and simultaneously deactivating the monopile elements in the interaction module, (iii) General static step – the monopile elements are reactivated to model the interaction between the pile and the adjoining soil; the monopile-soil interaction is modelled using the finite sliding, surface-to-surface master slave contact formulation (monopile is the master surface and the soil is the slave surface) where the normal (hard contact – both allowing no separation and separation after contact) and tangential (friction coefficient of 0.25 is given as input, typical for a clay-steel interface (Lemos and Vaughan 2000)) constraints are generated using the penalty method, and (iv) General static step – a gravity load is applied to the monopile elements to simulate the self-weight of the monopile along with the application of static horizontal concentrated load and overturning moment that simulates the loading behaviour of waves, current, and wind at a reference point to which all the nodes of the monopile are connected on the head.

In the *p-y* analysis, the *p-y* curves for the soil at different depths along the monopile are generated using the "Stiff clay without free water (Reese)" criteria with zero base shear available in LPILE which requires inputs of the unit weight of soil γ, s_u, and the strain factor ε_{50} corresponding to a stress of 50% of the ultimate stress. An input of $\gamma = 18$ kN/m^3, $s_u = 100$ kPa, and $\varepsilon_{50} = 0.005$ (recommended by Reese et al. 1975 for clayey soil deposit with s_u ranging from 100-200 kPa) is given as input in the LPILE analysis to generate the *p-y* curves. The soil layer below the monopile base extends to a finite depth below the monopile base. Further, in the analysis, each monopile is modeled as a circular solid pile with equivalent elastic properties.

Figure 4.21(a)-(b) show the comparison of the monopile response (head displacement w_h and rotation ψ_h) obtained from the present 3-D FE analysis (both with and without monopile-soil separation), *p-y* analysis, and the present analysis. The initial shear modulus G_{s0} = 16.1 MPa is given as input to obtain the results from the present analysis using equation (4.3) applicable to undrained clays. The details of the other monopile-soil properties and applied loading are reported in the figures itself. From the comparison shown in Figure 4.21(a) (head displacement w_h), it is evident that the *p-y* analysis (the *p-y* curves for stiff clays were developed from field pile-load tests on pile diameters ranging from 0.254-0.641m) in comparison to the FE analysis and present analysis overpredicts the response for all the cases of monopile diameters considered, therefore, the *p-y* analysis is unsuitable to design monopiles.

Further, the present analysis overestimates the monopile head displacement w_h in comparison to the FE analysis ((Figure 4.21(a))), whereas, a reasonable match of the predictions of the monopile head rotation ψ_h from the present analysis with those of the FE analysis, is obtained (Figure 4.21(b)). This difference in the prediction of monopile response between the present and FE analysis may be because of (i) mismatch in the modeling techniques and (ii) the inputs used to describe the constitutive behavior of soil. Nevertheless, the present analysis using nonlinear elastic relationship is capable of predicting reasonable monopile response in undrained clays, without resorting to elastic-plastic soil models. Although the present analysis does not include monopile-soil separation (an important phenomenon observed in a laterally loaded pile problems), the present analysis is capable of predicting monopile head response accurately, besides, this effect might not be of much importance for monopiles which are typically designed to undergo a maximum head rotation

of ψ_h = 0.5°. A closer examination of the monopile head rotation (see Figure 4.22) in Figure 4.21(b) shows that for ψ_h = 0.5°, the difference between the present and FE analysis is not significant and the phenomenon of gap formation in the analysis can be neglected for monopiles in stiff undrained clays.

An illustration of the CPU processing time is also depicted in Table 4.3. It is evident that the present analysis is far more computationally efficient compared to the 3-D FE analysis framework. Although, the *p-y* analysis is computationally efficient than the present analysis it produces inaccurate results, which is unacceptable.

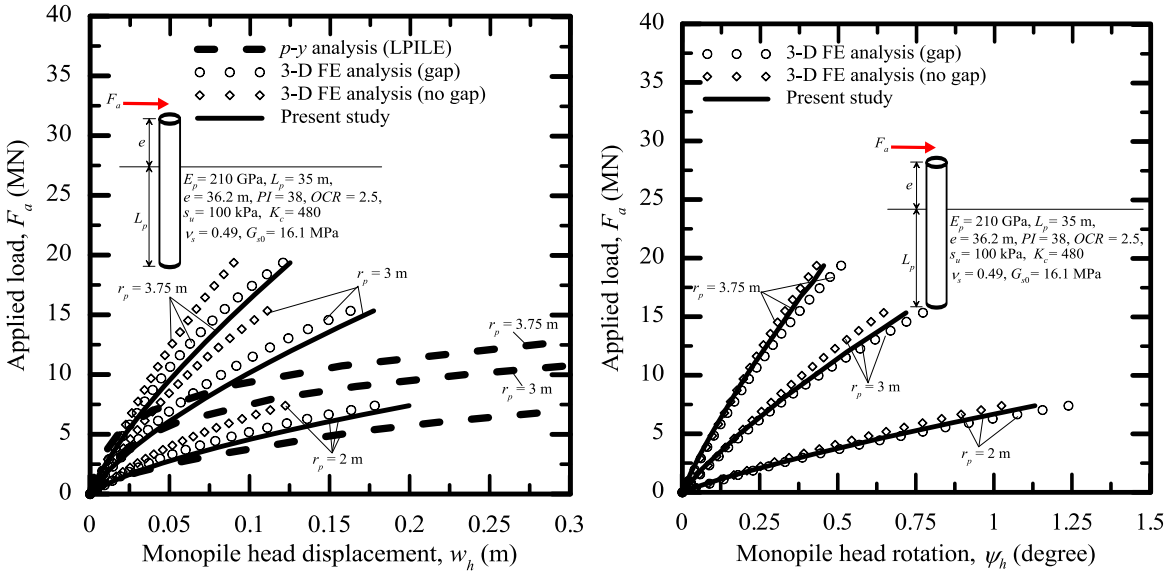

Figure 4.21: Comparison of monopile response obtained from present analysis (using non-linear elastic constitutive relationship (equation (4.3)), 3-D FE analysis (using elastic-plastic constitutive models), and the *p-y* analysis

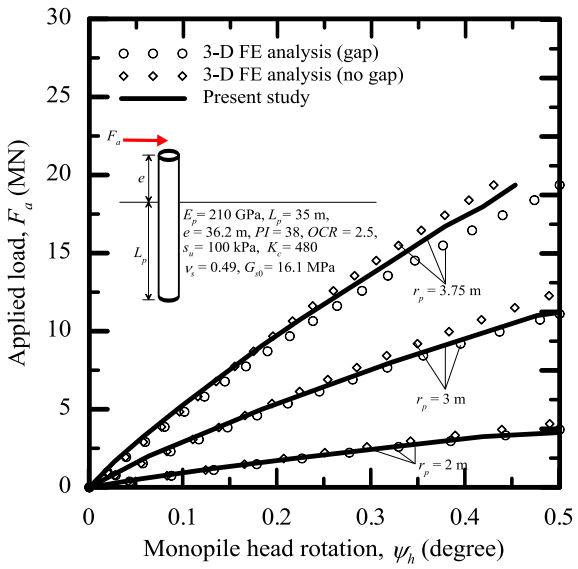

Figure 4.22: Monopile head rotation obtained from the present and 3-D FE analysis up to ψ_h = 0.5°

Table 4.3: Computational time required for 3-D FE analysis, *p-y* analysis and present analysis

Pile radius (m)	**3-D FE analysis, (secs)**	***p-y* analysis, (secs)**	**Present analysis, (secs)**
2	10791	22	512
3	11568	22	533
3.75	12180	22	546

4.6 Summary

A new continuum-based computational method is developed to obtain the response of laterally loaded monopile foundations embedded in a nonlinear elastic soil, subjected to a static force and/or moment at the monopile head. In the analysis, the displacement in the soil is considered to be a product of separable functions and the principle of virtual work is applied to obtain the governing differential equations describing the monopile and soil displacements. An iterative algorithm is followed to solve for the monopile and soil displacements and obtain the monopile response using a 1-D FD numerical scheme.

In the analysis, the soil nonlinearity is taken into account using nonlinear constitutive relationships expressed in the form of a power law and a hyperbolic equation applicable to undrained clay and sandy soil deposits where the degradation of secant shear modulus is expressed as a function of the induced strain in soil. Several example problems are solved to demonstrate the use of the analysis. The results obtained from the analysis are verified with

the results of an equivalent 3-D FE analysis using the same rule of modulus degradation as the present analysis. The present analysis predicts accurate and computationally faster nonlinear pile response in comparison to 3-D FE analysis. The results obtained from the present analysis are validated with the results of measured data from full-scale field pile-load tests and *p-y* analysis in clay and sandy soil deposit, for a few case studies. Further, monopile response in undrained clay obtained from the present nonlinear elastic approach is compared with elastic-plastic 3-D FE analysis. From the comparison, the *p-y* analysis is found to predict unrealistic results for large-diameter monopiles while the present analysis predicts reasonably accurate and computationally efficient results in comparison to the 3-D FE analysis.

CHAPTER 5

Design of Monopiles in Nonlinear Elastic Soil

5.1 Introduction

In this chapter, the step-by-step procedure for the design of monopiles embedded in a nonlinear elastic soil and subjected to extreme lateral loading conditions is demonstrated through two example problems. In the solved example problems, the design considerations are outlined, the procedures recommended in offshore design codes for the calculation of the extreme lateral loads from wind and wave action on the wind turbine structure is demonstrated, the analysis developed in Chapter 4 is performed for the evaluated wind and wave loading on monopiles embedded in undrained clay deposit, and finally, appropriate monopile dimensions satisfying the design requirements for monopiles recommended in offshore design codes are chosen.

5.2 Design Problem 1

From a geotechnical foundation engineering perspective, monopiles supporting offshore wind turbines should satisfy two design criteria (i) Ultimate limit state (ULS) criterion because of applied lateral and axial loads and (ii) Serviceability limit state (SLS) criterion where the maximum allowable limit for monopile head rotation ψ_h at the seabed is 0.5° (DNV 2014) under extreme loading conditions. In this design, it is assumed that (i) the monopile is safe against axial capacity besides, it is also reported in the literature that the effect of the axial loads (static loading from self-weight of the wind turbine tower, turbine, and the substructure assembly) on the lateral response of monopiles supporting offshore wind turbines is negligible (Haiderali et al. 2013, Arany et al. 2015) and (ii) the design of laterally loaded monopiles is typically governed by the serviceability limit state criterion (Arany et al. 2015, 2017) instead of the ultimate limit state criterion, in fact, for most laterally loaded pile problems the allowable head displacement and rotation are often the criteria for design. Therefore, the present design of monopiles is performed satisfying the SLS criterion.

The present design consists of the following steps (i) calculation of the maximum lateral loads from wind and wave action acting on the wind turbine structure which are ultimately transferred to the monopile head, (ii) evaluation of the geotechnical properties of the site, and

(iii) selection of appropriate monopile dimensions that satisfies the serviceability limit state criterion of $\psi_h = 0.5°$ under extreme loading conditions by performing the analysis developed in Chapter 4.

5.2.1 Calculation of maximum lateral loads acting on the wind turbine structure

The wind turbine structure is subjected to dynamic lateral loads from wind, waves, water currents, and vibrations from the rotor and blades with frequencies less than 1 Hz (see Chapter 1, subsection 1.2.1). The effect of the dynamic loadings on the wind turbine structure from water currents, rotor, and blades can be neglected since, they are very small compared the wind and wave loading (Lombardi 2010, Arany et al. 2015). Further, it is shown in this research that the static analysis is sufficient to obtain monopile response because the inertial effect of the monopile and soil, hysteretic and radiation of soil included in the dynamic analysis is insignificant for loading frequencies less than 1 Hz (see Chapter 3). Therefore, in this design, the loading encountered by the wind turbine structure from winds and waves (see Figure 1.1) are modeled as a static horizontal force and the overturning moment at the monopile head (see Figure 4.1).

Calculation of maximum lateral loads from wind

According to the DNV (2014) code, there are numerous wind load scenarios that need to be analyzed for the design of OWT monopile foundation. In this design, the force because of the wind which is expected to be highest when an extreme gust hits the rotor at the hub level at a rated wind speed U_R (DNV 2014, Arany et al. 2015, 2017) is evaluated; the DNV (2014) codes gives the following expression for the calculation of the extreme gust u_{ext} (equation 5.1)

$$u_{ext} = \min\left\{1.35\left(U_{10,1-year} - U_R\right); \frac{3.3\sigma_{U,c}}{1+\frac{0.1D}{\Lambda_1}}\right\} \tag{5.1}$$

where D is the rotor diameter, $\Lambda_1 = L_k/8.1$ is the longitudinal turbulence scale parameter with L_k = 340.2 m (obtained from DNV (2014), also reported by Arany et al. (2015) in their calculations) being the longitudinal integral length scale of turbulence, $\sigma_{U,c} = 0.11U_{10,1\text{-year}}$ is the characteristic standard deviation of wind speed, and $U_{10,1\text{-year}} = 0.8U_{10,50\text{-year}}$ is the 10

minutes wind speed with 1-year return period. The 10 minutes mean wind speed with a 50-year return period $U_{10,50\text{-year}}$ (= $w_k\left[-\ln\left(1-0.98^{\frac{1}{52596}}\right)\right]^{\frac{1}{w_s}}$, where w_k and w_s are the wind speed Weibull distribution scale and shape parameter, respectively) is determined by taking the 98% quantile of the probability distribution of 1-year return period (Table 4-2 in DNV (2014)).

Using equation (5.1), the total wind load F_{wind} at the hub (see Figure 5.1) is estimated by the following equation

$$F_{wind} = \frac{1}{2}\rho_a A_R C_T \left(U_R + u_{ext}\right)^2 \tag{5.2}$$

where ρ_a is the density of air, $C_T = \{3.5 \times (2 \times U_R - 3.5)\}/U_R^2$ is the thrust coefficient following Frohboese and Schmuck (2010), and A_R is the rotor swept area.

The overturning moment M_{wind} at the monopile head is obtained using the following expression

$$M_{wind} = F_{wind}\left(z_{hub} + z_{sur}\right) \tag{5.3}$$

where z_{hub} is the hub height from the sea level and z_{sur} is the mean water depth.

Calculation of maximum lateral loads from wave

According to the DNV (2014) code, the maximum wave force F_{wave} at a height z_w from the seabed and overturning moment M_{wave} at the head of a large-diameter vertical cylindrical monopile can be evaluated following the linear Airy wave theory which is given by the following equations

$$F_{wave} = \frac{4\rho_w g H_m}{2K^2}\frac{\sinh\left\{K\left(z_{sur} + \frac{H_m \sin\alpha}{2}\right)\right\}}{\cosh\left(Kz_{sur}\right)}\xi \tag{5.4}$$

$$z_w = z_{sur}\frac{K\sinh\left(Kz_{sur}\right) - \cos\left(Kz_{sur}\right) + 1}{Kz_{sur}\sinh\left(Kz_{sur}\right)} \tag{5.5}$$

where ρ_w is the density of water, g (= 9.81 m/sec^2) is the gravitational constant, H_m (= 1.87 H_s, such that H_s is the significant wave height (DNV 2014)) is the maximum wave height, K is the wave number, α and ξ are functions of Kr_p (obtained from Table E2 of DNV (2014) code of practice) i.e., the product of the wave number and monopile radius.

The overturning moment M_{wind} at the monopile head is obtained by

$$M_{wave} = F_{wave} z_w \tag{5.6}$$

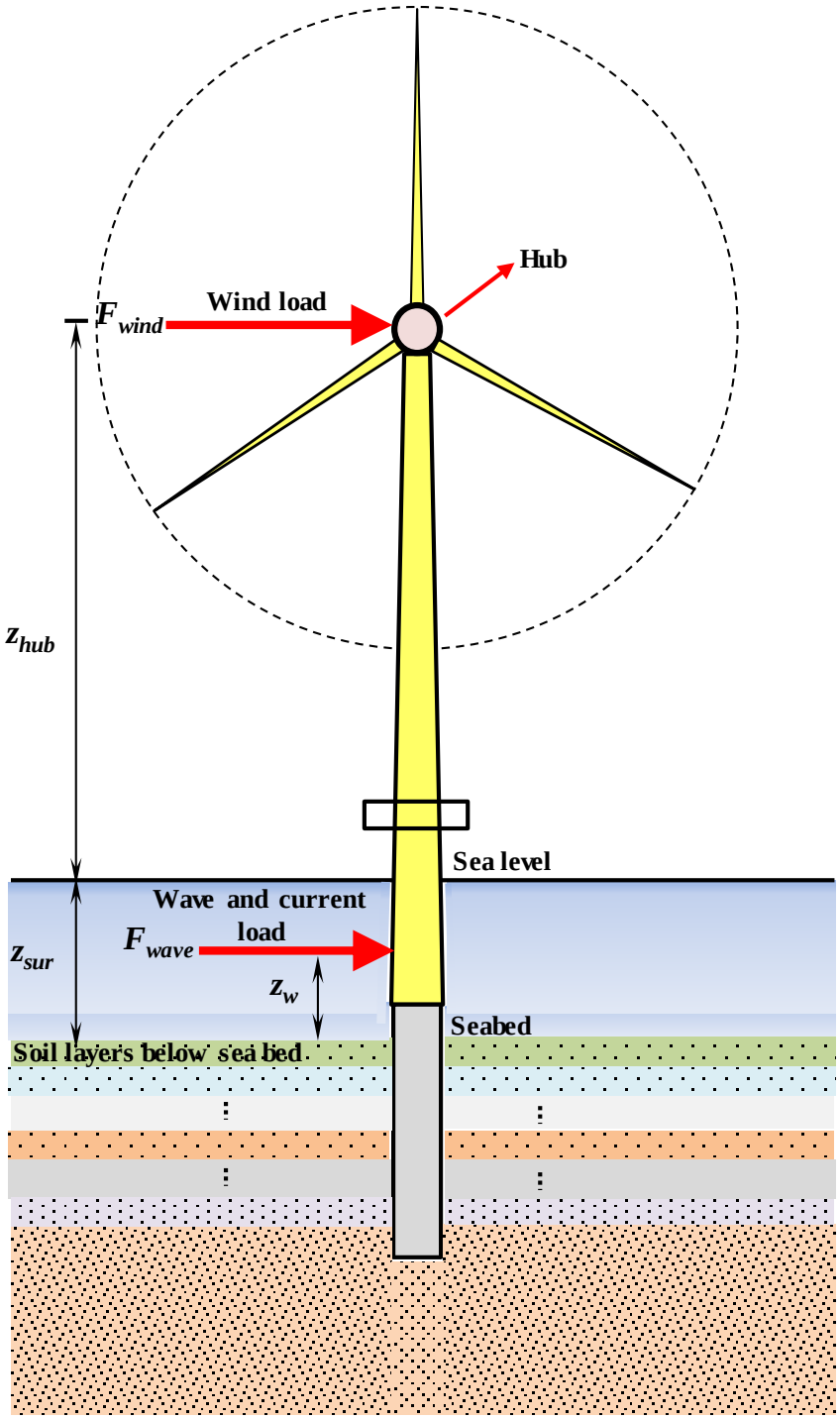

Figure 5.1: OWT-monopile system with imposed wind and wave loads and their point of application

To obtain the maximum force and overturning moments (using equations (5.1)-(5.6)) because of wind and wave action a monopile radius of 2.5 m is assumed (the calculation of wave load is a function of monopile radius). The inputs adopted for the wind turbine dimensions and wind and wave parameters are reported in Table 5.1 and Table 5.2, respectively. The output parameters for the calculation of the maximum force, overturning moments, and the point of application on the wind turbine structure because of wind and wave action are reported in Table 5.3. In the present design, the wind and wave loads on the wind turbine structure are considered to be collinear (based on are DNV (2014) recommendations). Table 5.2 also depicts the total applied force F_a (= F_{wind} + F_{wave}) and moment M_a (= M_{wind} + M_{wave}) at the monopile head because of wind and wave action which is required for performing the analysis developed in Chapter 4 and subsequently, designing the monopile.

Table 5.1: Input parameters of a Siemens SWT-3.6-120 type 3.6 MW wind turbine (Arany et al. 2015)

D	120 m
z_{hub}	87 m

Table 5.2: Input parameters for calculation of wind and wave loading on SWT-3.6-120

U_R	12 m/sec
w_k	8 m/sec
w_s	1.8
ρ_a	1.225 kg/m3
ρ_w	1030 kg/m3
H_s	8.2 m
z_{sur}	25 m
α^*	1.162°
ξ^*	0.04095

* α and ξ are selected from Table E2 of DNV (2014)

Table 5.3: Output parameters for wind and wave loading for OWT supported on a 2.5 m radius monopile

Λ_1	42 m
$U_{10,50\text{-year}}$	18.64 m/sec
$U_{10,1\text{-year}}$	14.92 m/sec
$\sigma_{U,c}$	1.64
u_{ext}	3.942 m/sec
C_T	0.5
A_R	11304 m^2
H_m	15.334 m
K^*	0.064
F_{wind}	0.88 MN
M_{wind}	98.56 MNm
z_w	7.75 m
F_{wave}	2.9 MN
M_{wave}	22.4 MNm
F_a	3.8 MN
M_a	120.96 Nm

* *K is* back-calculated from the selected values of α and ξ for a 2.5 m radius monopile

5.2.2 Evaluation of geotechnical properties of soil

The monopile shown in Figure 5.1 is considered to be embedded in a homogeneous deposit of normally consolidated undrained soft clay. The nonlinear stress-strain behavior of the undrained clay is described by the hyperbolic expression given by Vardanega and Bolton (2013) (equation (4.2); see Chapter 4, subsection 4.3.1). For performing the analysis and obtaining the monopile head response using equation (4.2), G_{s0} [= $E_{s0}/\{2 \times (1 + \nu_s)\}$] is evaluated where $E_{s0} = K_c s_u$ following the correlation is given by Duncan and Buchignani (1976) is used and K_c is obtained from Figure 4.2. Table 5.4 depicts the geotechnical properties of the normally consolidated soft undrained clay.

Table 5.4: Geotechnical properties of normally consolidated soft undrained clay deposit

OCR	*PI* %	s_u (kPa)	K_c	E_{s0} (MPa)	ν_s	G_{s0} (MPa)	J	γ_{ref}
1.0	44	50	390	19.5	0.49	6.54	2.2	0.000968

5.2.3 Selection of monopile dimensions

A radius of r_p = 2.5 m is already chosen for the steel monopile with Young's modulus E_p = 210 GPa in the calculation of wave loads (see subsection 5.2.1). The other dimensions that needs to be evaluated to resist the lateral loads F_a and M_a (see Table 5.2) on the monopile embedded in the homogeneous undrained soft clay deposit are the monopile wall thickness t_p, second moment if inertia I_p, and the embedment length L_p such that the maximum allowable monopile head rotation ψ_h is ≤ 0.5°.

Calculation of monopile wall thickness and second moment of inertia

The monopile wall thickness t_p (unit is mm) and I_p are evaluated from the following equations

$$t_p = 6.35 + \frac{2r_p}{100} \tag{5.7}$$

$$I_p = \frac{\pi}{4}\left\{r_p^4 - \left(r_p - t_p\right)^4\right\} \tag{5.8}$$

For r_p = 2.5 m, t_p = 56.35 mm and I_p = 2.67 m^4.

Calculation of monopile embedment length

For estimating the monopile embedment length L_p, there are several recommendations proposed in the literature, for example, GL (2005) proposes that for offshore piles under extreme static loading conditions the following set of criteria can be followed to determine the pile embedment length (also discussed by Achmus et al. (2008) and Kuo et al. (2012)) (i) vertical tangent criterion i.e., the displacement profile of the pile has vertical tangent at the toe, (ii) zero toe-kick criterion i.e., no or negative pile toe displacement, and (iii) critical pile length criterion i.e., the pile length is so chosen that any further increase in pile length has no or little effect on the pile head response. Achmus et al. (2008) and Kuo et al. (2012) in their analysis on monopiles found that the criterion (i) and (ii) are very conservative i.e., resulting in very

large embedment lengths, hence, unsuitable for monopile design. In the present design, L_p is selected following criterion (iii).

For the selection of the appropriate monopile embedment length, several guesses of L_p are made which satisfies the SLS criterion of $\psi_h \leq 0.5°$. The monopile response for each guess from the present analysis is reported in Table 5.5. It is evident from Table 5.5 that for an applied loading of F_a = 3.8 MN, M_a = 120.96 MNm at the monopile head, and r_p = 2.5 m, a design L_p = 30 m can be used (since $\psi_h < 0.5°$; see Table 5.5). However, following criterion (iii) (as discussed in the previous paragraph), L_p = 40 m should be used since an increase in L_p beyond 40 m has little or no effect on ψ_h. Further, monopile head response (head displacement) from the *p-y* analysis (performed using LPILE software) where the *p-y* curves are developed following "Matlock (1970) soft clay criteria" with zero base shear, γ = 18 kN/m^3, and ε_{50} = 0.02 (applicable to normally consolidated soft undrained clay, Matlock (1970)) as input is also reported in Table 5.5. It is obvious from the table, that the *p-y* analysis significantly overestimates the head displacement for the range of monopile length considered and hence, it is unsuitable for designing large-diameter monopiles. Note, the rotation values from the *p-y* analysis are not obtained as an output in the LPILE software, hence, they are not reported in Table 5.5.

Table 5.5: Monopile embedment length obtained from present and *p-y* analysis in a soft undrained clay deposit

Guess no.	L_p	***Present analysis***		***p-y analysis***	
		w_h (m)	ψ_h (°)	w_h (m)	ψ_h (°)
1	25	0.2059	0.81	1.3516	-
2	30	0.1287	0.49	0.5	-
3	40	0.0840	0.34	0.13	-
4	50	0.0764	0.32	0.092	-
5	60	0.0757	0.32	0.0916	-

5.3 Design Problem 2

In this section, the design of the monopile foundation with r_p = 3.75 m embedded in a heavily overconsolidated medium stiff undrained clay deposit and supporting a Siemens SWT-

6.0-154 type 6 MW wind turbine is discussed. In the design, the same assumptions as the problem 1 are made, the wind and wave loads acting on the turbine structure are evaluated following the same procedures discussed in the design problem 1, the evaluation of the initial elastic modulus and the modulus degradation rule for the heavily overconsolidated medium stiff clay are also the same.

5.3.1 Calculation of maximum lateral loads acting on the wind turbine structure

Table 5.6 and 5.7 depicts the input parameters for the wind turbine structure and the wind and wave loading, respectively, and Table 5.8 depicts the output parameters for a 3.75 m monopile radius.

Table 5.6: Input parameters for a Siemens SWT-6.0-154 type 6.0 MW wind turbine

D	154 m
z_{hub}	87 m

Table 5.7: Input parameters for calculation of wind and wave loading on SWT-6.0-154

U_R	12 m/sec
w_k	8 m/sec
w_s	1.8
ρ_a	1.225 kg/m3
ρ_w	1030 kg/m3
H_s	8.2 m
z_{sur}	25 m
α^*	1.471°
ξ^*	0.05197

[*] α and ξ are selected from Table E2 of DNV (2014)

Table 5.8: Output parameters for wind and wave loading for OWT supported on a 3.75 m radius monopile

Λ_1	42 m
$U_{10,50\text{-year}}$	18.64 m/sec
$U_{10,1\text{-year}}$	14.92 m/sec
$\sigma_{U,c}$	1.64
u_{ext}	3.942 m/sec
C_T	0.5
A_R	18617.06 m^2
H_m	15.334 m
K^*	0.048
F_{wind}	1.45 MN
M_{wind}	162.29 MNm
z_w	9.83 m
F_{wave}	5.92 MN
M_{wave}	58.2 MNm
F_a	7.37 MN
M_a	220.49 MNm

$^*K$ *is* back-calculated from the selected values of α and ξ for a 3.75 m radius monopile

5.3.2 Evaluation of geotechnical properties of soil

Table 5.9 depicts the elastic properties and other the input parameters for the modulus degradation relationship following Vardanega and Bolton (2013) for the heavily overconsolidated medium stiff undrained clay deposit.

Table 5.9: Geotechnical properties of heavily overconsolidated medium stiff undrained clay deposit

OCR	*PI* %	s_u (kPa)	K_c	E_{s0} (MPa)	ν_s	G_{s0} (MPa)	*J*	γ_{ref}
2.5	41	75	455	34.125	0.49	11.45	2.2	0.000902

5.3.3 Selection of monopile dimensions

A radius r_p = 3.75 m is chosen for the steel monopile in the calculation of wave loads (see subsection 5.3.1). For r_p = 3.75 m, t_p = 81.35 mm and I_p = 13.04 m^4 are evaluated. The

calculation of the monopile embedment length L_p such that $\psi_h \leq 0.5°$ for F_a = 7.37 MN and M_a = 220.49 MNm at the head for monopile embedded in medium stiff undrained clay is demonstrated below.

Calculation of monopile embedment length

Several guesses are made to obtain the design L_p which satisfies $\psi_h \leq 0.5°$ (see Table 5.10). For F_a = 7.37 MN and M_a = 220.49 MNm at the monopile head and r_p = 3.75 m, a design L_p = 25 m can be used. However, to satisfy the critical pile length criterion (as discussed in the design problem 1), L_p = 42.5 m should be used since for L_p > 42.5 m the change in ψ_h is negligible. Further, the comparison of the head displacement between the *p-y* analysis (*p-y* curves developed following the "Stiff clay without free water (Reese)" criteria with zero base shear, γ = 18 kN/m^3, and ε_{50} = 0.01 (applicable to medium stiff normally consolidated clay (Matlock 1970) as input)) and the present analysis (see Table 5.10), the *p-y* analysis is found to predict unacceptable results.

Table 5.10: Monopile embedment length for design obtained from present and *p-y* analysis in medium stiff clay

Guess no.	L_p	***Present analysis***		***p-y analysis***	
		w_h (m)	ψ_h (°)	w_h (m)	ψ_h (°)
1	25	0.1200	0.44	1.03	-
2	30	0.0783	0.26	0.27	-
3	35	0.0593	0.19	0.09	-
4	40	0.0498	0.16	0.047	-
5	42.5	0.0449	0.15	0.039	-
6	45	0.0449	0.15	0.035	-

5.4 Summary

A step-by-step design procedure for monopiles embedded in a normally consolidated soft and heavily overconsolidated medium stiff undrained clay deposit is shown through two example problems. In the solved problems, extreme lateral loads from wind and wave action on the wind turbine structure is calculated following the procedures outlined in the DNV code of practice, the soil is characterized by a nonlinear stress-strain relationship that describes the

variation of shear modulus with shear strain, and finally, the design monopile dimensions that satisfy the recommended head response and embedment length criterion outlined in offshore codes of practice are selected through a series of iterations.

It is important to note that the purpose of this chapter is to outline a preliminary procedure for the design of monopile foundations supporting offshore wind turbines, embedded in nonlinear soil deposit. For a complete design, numerous other load case scenarios from wind, waves, currents, rotor, and blades outlined in the DNV code of practice should be considered and the effects of fatigue on monopile dimensions (both embedment length and wall thickness) because of cyclic loading should also be taken into account.

.

CHAPTER 6

Conclusions and Recommendations

The thesis presents a mathematical formulation for the analysis and design of laterally loaded monopiles supporting OWTs. In the formulation, the soil is modeled as a 3-D continuum and the monopile is modeled using various beam theories based on strength of material concepts. In the analysis, the displacements within the soil mass in various directions because of monopile displacement are rationally considered to be a product of separable functions and the calculus of variation is utilized to obtain the differential equations governing soil and monopile displacements. The differential equations governing the soil and monopile displacements are solved analytically/numerically following an iterative algorithm. The formulation outlined in the thesis is developed in stages and includes several aspects of constitutive soil behavior – linear elasticity and linear viscoelasticity with hysteretic material damping (low strain) and nonlinearity (high strain) and loading conditions – static and dynamic. The accuracy and reliability of the developed framework at various stage of the formulation is ensured by comparing pile/monopile response with either 3-D FE framework (performed using Abaqus), existing formulations available in the literature, *p-y* analysis (performed using LPILE or results available in literature), or measured data from full-scale field pile-load tests. This chapter highlights the major contributions, key conclusions, and recommendations for future work.

6.1 Major contributions

The major contribution resulting from this work are as follows:

(i) In various analytical, semi-analytical, and numerical studies on laterally loaded piles, the pile is conventionally modeled as a Euler–Bernoulli beam. Modeling large-diameter monopiles using the Euler–Bernoulli beam theory may not be appropriate, because the Euler–Bernoulli beam theory is strictly valid for long slender piles and does not account for shear deformations, which may have a significant effect on the lateral response of large-diameter monopiles. Therefore, in the mathematical formulation developed in Chapter 2 of the thesis – the analysis of monopiles in linear elastic soil deposit subjected to static loading, a novel

analytical technique to solve the differential equation describing monopile displacement following the Timoshenko beam theory is developed (see equations (2.12)-(2.17)). Further, it is shown that the analysis framework can be progressively simplified to incorporate the Euler-Bernoulli (see section 2.4) and rigid beam (see section 2.4) theory to model monopiles. Hence, a unified framework is developed that can account for different beam theories.

(ii) The analysis developed in Chapter 3 demonstrates a novel analytical technique following the Timoshenko beam theory (includes the effect of rotatory inertia of the monopile cross-section along with the shear deformation; see equations (3.16)-(3.17)) for the dynamic analysis of laterally loaded monopiles in linear viscoelastic soil deposit with hysteretic material damping. It is demonstrated that the analysis can be progressively simplified to incorporate the Rayleigh (includes rotatory inertia of the monopile cross-section and no shear deformation), Euler-Bernoulli (includes translational inertia of the monopile cross-section and no rotatory inertia and shear deformation; see section 3.4), and rigid beam (includes translational and rotatory inertia of the monopile cross-section; see section 3.5) theory. Hence, a unified framework including various beam theories for the analysis of dynamically loaded monopiles/piles is developed. The other advantage of this framework is that unlike the 3-D FE analysis, this solution process does not require the modeling of non-reflecting viscous boundary conditions and takes into account the effect of material and radiation damping within the formulation and solution process.

(iii) Often, 3-D FE software packages with inbuilt constitutive soil models (based on the theory of elasticity and plasticity) are used to predict the nonlinear response of laterally loaded piles/monopiles in the geotechnical foundation engineering practice. However, such constitutive models based on plasticity theory are useful when the design interest is the estimation of ultimate load capacity. For most laterally loaded pile problems, the primary interest in design is the estimation of head displacement and rotation under working load conditions and the use of such sophisticated constitutive soil models based on plasticity theory might not be necessary and nonlinear elastic soil models may be sufficient to predict a reasonably accurate and computationally faster pile response. Therefore, in

Chapter 4 a novel analysis framework is developed to predict the load-deformation response of monopiles (modeled as a Euler-Bernoulli beam) in which the soil is modeled using nonlinear elastic constitutive relationships (describes the variation of secant shear modulus with strain) applicable to undrained clays and sandy soils, available in the literature.

(iv) The analysis framework developed in Chapter 4 has been successfully applied to develop a step-by-step procedure for the design of monopiles in undrained clay soil deposit (Chapter 5).

(v) Several peer-reviewed journals and conference papers (published, accepted, and under review and preparation) have resulted from this work which are reported in the Appendix.

6.2 Conclusions

The major conclusions from the current research work can be summarized as follows:

(i) The Euler-Bernoulli beam theory is sufficient to model monopiles and the Timoshenko or rigid beam theory may not be required because (a) the error in the prediction of monopile head rotation following the Euler-Bernoulli beam theory in comparison to the Timoshenko beam theory is minor and can be neglected, (b) the Euler-Bernoulli beam theory can be used to model monopiles which accounts for both bending and rigid body rotation and is capable of producing accurate results irrespective of the monopile-soil stiffness and slenderness ratio unlike the rigid beam theory which requires a careful consideration of the monopile-soil stiffness and slenderness ratio to produce accurate results, and (c) the difference in the computational time in the present analysis among the different beam theories is not significant.

(ii) The effect of the monopile and soil inertia, hysteretic material damping, and radiation damping of soil included in the dynamic analysis of monopile foundation which is subjected to frequencies less than 1 Hz is not significant, hence, the static analysis is sufficient to obtain the monopile response.

(iii) The nonlinear elastic analysis can be used to predict of pile/monopile response in undrained clay deposit, however, to predict better results for piles/monopiles embedded in sandy soil deposit an elastic-plastic framework would be apt.

(iv) The effect of monopile-soil separation and slippage (an important phenomenon in laterally loaded pile problems) is found to be insignificant for monopiles embedded in stiff undrained clay deposit for $\psi_h \leq 0.5°$ (the design criterion for monopiles supporting OWTs).

(v) The present analysis framework is computationally efficient than 3-D FE analysis framework. The *p-y* analysis is computationally efficient than the present formulation, however, it produces inaccurate results and should not be used for the analysis and design of monopiles.

(vi) The design methodology demonstrated in Chapter 5 should only be used to obtain a first-hand estimate of the monopile dimension.

6.3 Recommendations for future work

Based on the limitations of the current research work, the possible extensions of the present research work are as follows:

(i) The present analysis can be used to obtain the response of piles for other civil engineering structures where the effect of pile-soil separation and slippage may have a significant effect on the nonlinear pile response. Hence, the current nonlinear analysis framework can be extended to include the effect of pile-soil separation and slippage.

(ii) The nonlinear analysis framework should be extended to include elastic-plastic constitutive soil models especially for piles/monopiles in sandy soil deposit.

(iii) Monopiles are subjected to cyclic loading during their lifetime. It has been observed in geotechnical engineering literature that the nature of nonlinearity changes with the number of cycles; the general trend is the degradation of soil modulus with the number of load cycles. This degradation of soil modulus with a cyclic strain may result in a change of the monopile-soil stiffness (K_{rr}, $K_{r\psi}$, and $K_{\psi\psi}$; also see Figure 1.4) which is an input in the calculation of the natural frequency of the OWT structure. Hence, the effect of degradation of

soil modulus with load cycles should be included in the analysis and design of OWT structure monopile system.

REFERENCES

Aasen, S., Page, A. M., Skjolden Skau, K., & Nygaard, T. A. (2017). Effect of foundation modelling on the fatigue lifetime of a monopile-based offshore wind turbine. *Wind Energy Science*, *2*(2), 361-376.

Abadie, C. N. (2015). *Cyclic lateral loading of monopile foundations in cohesionless soils*. (Doctoral dissertation, University of Oxford).

Abadie, C. N., & Byrne, B. W. (2014). Cyclic loading response of monopile foundations in cohesionless soils. In *Physical Modelling in Geotechnics-Proceedings of the 8th International Conference on Physical Modelling in Geotechnics 2014, ICPMG 2014* (Vol. 2, pp. 779-784).

Abdel-Rahman, K., & Achmus, M. (2005). Finite element modelling of horizontally loaded monopile foundations for offshore wind energy converters in Germany. In *Proceedings of the International Symposium on Frontiers in Off-shore Geotechnics (ISFOG). Edited by S. Gourvenec and M. Cassidy. Taylor and Francis, Perth* (pp. 391-396).

Achmus, M., Albiker, J., Peralta, P., & tom Wörden, F. (2011). Scale effects in the design of large diameter monopiles. *EWEA, Brussels, Belgium*: *Europe's Premier Wind Energy Event*.

Achmus, M., Kuo, Y. S., & Abdel-Rahman, K. (2009). Behavior of monopile foundations under cyclic lateral load. *Computers and Geotechnics*, *36*(5), 725-735.

Adhikari, S., & Bhattacharya, S. (2011). Vibrations of wind-turbines considering soil-structure interaction. *Wind and Structures*, *14*(2), 85.

Adhikari, S., & Bhattacharya, S. (2012). Dynamic analysis of wind turbine towers on flexible foundations. *Shock and vibration*, *19*(1), 37-56.

Ahmed, S. S., & Hawlader, B. (2016). Numerical analysis of large-diameter monopiles in dense sand supporting offshore wind turbines. *International Journal of Geomechanics*, *16*(5), 04016018.

Ai, Z. Y., & Li, Z. X. (2015). Dynamic analysis of a laterally loaded pile in a transversely isotropic multilayered half-space. *Engineering Analysis with Boundary Elements*, *54*, 68-75.

Ai, Z. Y., Chen, Y. F., & Jiang, X. B. (2017). Behavior of laterally and vertically loaded piles in multi-layered transversely isotropic soils. *Applied Mathematical Modelling*, *51*, 561-573.

Alderlieste, E. A. (2011). *Experimental modelling of lateral loads on large diameter mono-pile foundations in sand*. (Master of Science thesis in Civil Engineering, Delft University of Technology).

Alizadeh, M., & Davisson, M. T. (1970). Lateral Load Tests on Piles—Arkansas River Project. *Journal of the Soil Mechanics and Foundations Division, ASCE, 96*(5), 1583-1604.

American Petroleum Institute (API). (2011). Petroleum and natural gas industries—specific requirements for offshore structures. Part 4 – geotechnical and foundation design considerations.

Anderson, J. B., Townsend, F. C., & Grajales, B. (2003). Case history evaluation of laterally loaded piles. *Journal of Geotechnical and Geoenvironmental Engineering, ASCE*, *129*(3), 187-196.

Anoyatis, G., & Lemnitzer, A. (2017). Dynamic pile impedances for laterally–loaded piles using improved Tajimi and Winkler formulations. *Soil Dynamics and Earthquake Engineering*, *92*, 279-297.

Anoyatis, G., Mylonakis, G., & Lemnitzer, A. (2016). Soil reaction to lateral harmonic pile motion. *Soil Dynamics and Earthquake Engineering*, *87*, 164-179.

Arany, L., Bhattacharya, S., Adhikari, S., Hogan, S. J., & Macdonald, J. H. G. (2015). An analytical model to predict the natural frequency of offshore wind turbines on three-spring flexible foundations using two different beam models. *Soil Dynamics and Earthquake Engineering*, *74*, 40-45.

Arany, L., Bhattacharya, S., Macdonald, J. H., & Hogan, S. J. (2015). A critical review of serviceability limit state requirements for monopile foundations of offshore wind turbines. In *Offshore Technology Conference*. Offshore Technology Conference.

Arany, L., Bhattacharya, S., Macdonald, J., & Hogan, S. J. (2017). Design of monopiles for offshore wind turbines in 10 steps. *Soil Dynamics and Earthquake Engineering, 92*, 126-152.

Ashford, S. A., & Juirnarongrit, T. (2003). Evaluation of pile diameter effect on initial modulus of subgrade reaction. *Journal of Geotechnical and Geoenvironmental Engineering, ASCE*, *129*(3), 234-242.

Ashour, M., & Norris, G. (2000). Modeling lateral soil-pile response based on soil-pile interaction. *Journal of Geotechnical and Geoenvironmental Engineering, ASCE, 126*(5), 420-428.

Ashour, M., Norris, G., & Pilling, P. (1998). Lateral loading of a pile in layered soil using the strain wedge model. *Journal of Geotechnical and Geoenvironmental Engineering, ASCE*, *124*(4), 303-315.

Ashour, M., Norris, G., & Pilling, P. (2002). Strain wedge model capability of analyzing behavior of laterally loaded isolated piles, drilled shafts, and pile groups. *Journal of Bridge Engineering*, *7*(4), 245-254.

Atkinson, J.H. (2000). Non-linear soil stiffness in routine design. *Géotechnique*, *50*(5), 487-508.

Banerjee, P. K., & Davies, T. G. (1978). The behaviour of axially and laterally loaded single piles embedded in nonhomogeneous soils. *Geotechnique, 28*(3), 309-326.

Barari, A., Bagheri, M., Rouainia, M., & Ibsen, L. B. (2017). Deformation mechanisms for offshore monopile foundations accounting for cyclic mobility effects. *Soil Dynamics and Earthquake Engineering*, *97*, 439-453.

Basu, D., Salgado, R., & Prezzi, M. (2009). A continuum-based model for analysis of laterally loaded piles in layered soils. *Géotechnique, 59*(2), 127-140.

Bekken, L. (2009). *Lateral behavior of large diameter offshore monopile foundations for wind turbines*. (Master of Science thesis in Civil Engineering, Delft University of Technology and Ballast Nedam Engineering).

Bhattacharya, S., & Adhikari, S. (2011). Experimental validation of soil–structure interaction of offshore wind turbines. *Soil Dynamics and Earthquake Engineering*, *31*(5-6), 805-816.

Bhattacharya, S., Cox, J. A., Lombardi, D., & Muir Wood, D. (2013). Dynamics of offshore wind turbines supported on two foundations. *Proceedings of the Institution of Civil Engineers-Geotechnical Engineering*, *166*(2), 159-169.

Bhattacharya, S., Lombardi, D., & Wood, D. M. (2011). Similitude relationships for physical modelling of monopile-supported offshore wind turbines. *International Journal of Physical Modelling in Geotechnics*, *11*(2), 58-68.

Bhowmik, S. K. (1992). *Three-dimensional non-linear finite element analysis of laterally loaded piles in clay*. (Doctoral dissertation, University of Illinois at Urbana-Champaign).

Bhushan, K., Fong, P. T., & Haley, S. C. (1979). Lateral load tests on drilled piers in stiff clays. *Journal of the Geotechnical Engineering Division, ASCE*, *105*(8), 969-985.

Bierschwale MW, Coyle HM, Bartoskewitz RE. (1981). Lateral load test on drilled shafts founded in clay. Drilled Piers and Caissons, *Proceedings of a Session Sponsored by the Geotechnical Engineering Division at the ASCE National Convention, St. Louis, Missouri*, 98–112.

Bisoi, S., & Haldar, S. (2014). Dynamic analysis of offshore wind turbine in clay considering soil–monopile–tower interaction. *Soil Dynamics and Earthquake Engineering*, *63*, 19-35.

Bisoi, S., & Haldar, S. (2015). Design of monopile supported offshore wind turbine in clay considering dynamic soil–structure-interaction. *Soil Dynamics and Earthquake Engineering*, *73*, 103-117.

Blaney, G.W. Kausel. E. & Roesset, J.M. (1976). Dynamic stiffness of piles. *In: Proceedings of the 2nd International Conference on Numerical Methods in Geomechanics, Blacksburg,Virginia*.

Bowles, J.E. (1996). *Foundation Analysis and Design*, 5th edn. McGraw-Hill, New York.

Budhu, M. (2010). *Soil mechanics and foundations*. 3rd edition, John Wiley & Sons, Inc., New York.

Byrne, BW, McAdam, R, Burd, HJ, Houlsby, GT, Martin, CM, Gavin, K, Doherty, P., Igoe, D., Zdravkovic, L., Taborda, D.M.G., Potts, D.M., Jardine, R.J., Sideri, M., Schroeder, F.C., Muir Wood, A., Kallehave, D. and Skov Gretlund, J. (2015a). Field testing of large diameter piles under lateral loading for offshore wind applications. *Edinburgh, UK*: *Proc 16 European Conference on Soil Mechanics and Geotechnical Engineering* (*ECSMGE*), pp 1255–1260.

Byrne, BW, McAdam, R, Burd, HJ, Houlsby, GT, Martin, CM, Zdravkovic, L, Taborda, DMG, Potts, DM, Jardine, RJ, Sideri, M, Schroeder, FC, Gavin, K, Doherty, P, Igoe, D, Muir Wood, A, Kallehave, D and Skov Gretlund, J. (2015b). New design methods for large diameter piles under lateral loading for offshore wind applications. *Oslo*, *Norway*: *Proc 3rd International Symposium on Frontiers in Offshore Geotechnics* (*ISFOG*).

Carswell, W., Arwade, S. R., DeGroot, D. J., & Myers, A. T. (2016). Natural frequency degradation and permanent accumulated rotation for offshore wind turbine monopiles in clay. *Renewable Energy*, *97*, 319-330.

Carter, D. P. (1984). *A non-linear soil model for predicting lateral pile response*. (Doctoral dissertation, ResearchSpace@ Auckland).

Carter, J. P., & Kulhawy, F. H. (1992). Analysis of laterally loaded shafts in rock. *Journal of Geotechnical Engineering, ASCE*, *118*(6), 839-855.

Chong, S. H., & Pasten, C. (2018). Numerical study on long-term monopile foundation response. *Marine Georesources & Geotechnology*, *36*(2), 190-196.

Chow, Y. K. (1987). Axial and lateral response of pile groups embedded in nonhomogeneous soils. *International Journal for Numerical and Analytical Methods in Geomechanics*, *11*(6), 621-638.

Cowper, G. R. (1966). The shear coefficient in Timoshenko's beam theory. *Journal of Applied Mechanics*, *33*(2), 335-340.

Craig, R. R., & Kurdila, A. J. (2006). *Fundamentals of structural dynamics*. 2nd Edition, John Wiley & Sons.

Darendeli, B. M. (2001). *Development of a new family of normalized modulus reduction and material damping curves*. (PhD dissertation, University of Texas at Austin, TX, USA).

Dasari, G. R. (1996). *Modelling the variation of soil stiffness during sequential construction*. (Doctoral dissertation, University of Cambridge)

Davisson, M. T., & Gill, H. L. (1963). Laterally loaded piles in a layered soil system. *Journal of the Soil Mechanics and Foundations Division*, *ASCE*, *89*(3), 63-94.

Depina, I., Le, T. M. H., Eiksund, G., & Benz, T. (2015). Behavior of cyclically loaded monopile foundations for offshore wind turbines in heterogeneous sands. *Computers and Geotechnics*, *65*, 266-277.

Desai, C. S. & Appel, G. C. (1976). 3-D analysis of laterally loaded structures. Num. Meth. Geomech., Am. Soc. Civ. Engrs. Ed. Desai, C.S., 2, 405-418.

Desai, C. S., & Appel, G. C. (1976). 3-D analysis of laterally loaded structures. In *Proceedings of the 2nd International Conference on Numerical Methods in Geomechanics, Blacksburg* (pp. 405-418).

DNV (2014). Design of Offshore Wind Turbine Structures. Offshore Standard DNV-OS-J101.

DNV. (2002). Guidelines for design of wind turbines-DNV/Riso. Code of practice, DNV,USA.

Doherty, P., & Gavin, K. (2012). Laterally loaded monopile design for offshore wind farms. *Proceedings of the Institution of Civil Engineers-Energy*, *165*(1), 7-17.

Duncan, J. M., & Buchigani, A. L. (1976). *An engineering manual for settlement studies.* (Geotechnical report, Civil engineering department, University of California Berkeley, CA).

Duncan, J. M., & Chang, C. Y. (1970). Nonlinear Analysis of Stress and Strain in Soils. *Journal of the Soil Mechanics and Foundations Division, ASCE, 96*(5), 1629-1653.

El-Marsafawi, H., Kaynia, A.M., & Novak, M. (1992). *Interaction factors and the superposition method for pile group dynamic analysis*. (Report GEOT192, Geotechnical Research Center, The University of Western Ontario).

Fahey, M., & Carter, J. P. (1993). A finite element study of the pressuremeter test in sand using a nonlinear elastic plastic model. *Canadian Geotechnical Journal, 30*(2), 348-362.

Faruque, M. O., & Desai, C. S. (1982). 3-D material and geometric nonlinear analysis of piles. In *Proceedings of the Second International Conference on Numerical Methods in Offshore Pilling* (pp. 553-575).

Filonenko-Borodich, M. (1946). On a certain system of functions and its applications in theory of elasticity. Prikl. Mat. Mekh. 10, 193–208 (in Russian).

Frohboese, P., & Schmuck, C. (2010). Thrust coefficients used for estimation of wake effects for fatigue load calculation. In *European Wind Energy Conference* (pp. 1-10).

Gazetas, G. (1995). Simplified Approach for Pile and Foundation Interaction Analysis (Discussion). *Journal of Geotechnical Engineering, ASCE, 121*(2), 228-230.

Gazetas, G., & Dobry, R. (1984). Horizontal response of piles in layered soils. *Journal of Geotechnical Engineering, ASCE, 110*(1), 20-40.

Georgiadis, M. (1983). Development of p-y curves for layered soils. In *Geotechnical practice in offshore engineering* (pp. 536-545). ASCE.

Germanischer Lloyd (GL). (2005). Guideline for the certification of offshore wind turbines. Hamburg, Germany.

Gerolymos, N., & Gazetas, G. (2006). Winkler model for lateral response of rigid caisson foundations in linear soil. *Soil Dynamics and Earthquake Engineering*, *26*(5), 347-361.

Gill, H. (1968). *Soil behavior around laterally loaded piles*. (Technical Report, DTIC Document).

Gowda, P. K. (1992). *Laterally loaded pile analysis for layered soil based on the strain wedge model*. (MS thesis, University of Nevada, Reno, Nevada).

Grajales, F. J., Beemer, R. D., Murali, M., Aubeny, C. P., & Biscontin, G. (2015). Response of short monopiles for offshore wind turbine foundations: virgin and post-cyclic capacity. In *Proceedings of the 68th Canadian Geotechnical Conference, Quebec City, Canada*.

Guo, W. D. (2012). Simple model for nonlinear response of 52 laterally loaded piles. *Journal of Geotechnical and Geoenvironmental Engineering, ASCE*, *139*(2), 234-252.

Guo, W. D., & Lee, F. H. (2001). Load transfer approach for laterally loaded piles. *International Journal for Numerical and Analytical Methods in Geomechanics*, *25*(11), 1101-1129.

Guo, W. D., & Zhu, B. T. (2010). Nonlinear response of 20 laterally loaded piles in sand. *Australian Geomechanics*, *45*(2), 67.

GWEC. (2017). http://www.gwec.net/global-figures/global-offshore/. (accessed May 23, 2017).

Haiderali, A. E., & Madabhushi, G. S. P. (2013, September). Evaluation of the py Method in the Design of Monopiles for Offshore Wind Turbines. In *Proc., Offshore Technology Conf*, (Vol. 3, pp. 1824-1844).

Hansen, M., Wolf, T.K., and Rasmussen, K.L. (2011). *Investigation of the Behaviour of Laterally Loaded Monopiles in Cohesionless Soil*. (Student report, School of Engineering and Science, Aalborg University, Denmark).

Hara, A., Ohta, T., Niwa, M., Tanaka, S., & Banno, T. (1974). Shear modulus and shear strength of cohesive soils. *Soils and Foundations*, *14*(3), 1-12.

Hardin, B. O., & Black, W. L. (1966). Sand Stiffness Under Various Triaxial Stresses. *Journal of the Soil Mechanics and Foundations Division, ASCE*, *92*(2), 27-42.

Hardin, B. O., & Black, W. L. (1968). Vibration Modulus of Normally Consolidated Clay. *Journal of the Soil Mechanics and Foundations Division, ASCE*, *94*(2), 353-370.

Hardin, B. O., & Drnevich, V. P. (1972). Shear Modulus and Damping in Soils. *Journal of the Soil Mechanics and Foundations Division, ASCE, 98*(7), 667-692.

Hearn, E. N., & Edgers, L. (2010). Finite element analysis of an offshore wind turbine monopile. In *GeoFlorida 2010: Advances in Analysis, Modeling & Design* (pp. 1857-1865).

Heidari, M., Jahanandish, M., El Naggar, H., & Ghahramani, A. (2013). Nonlinear cyclic behavior of laterally loaded pile in cohesive soil. *Canadian Geotechnical Journal*, *51*(2), 129-143.

Higgins, W., Vasquez, C., Basu, D., & Griffiths, D. V. (2012). Elastic solutions for laterally loaded piles. *Journal of Geotechnical and Geoenvironmental Engineering, ASCE*, *39*(7), 1096-1103.

Ho, A., Mbistrova, A., & Corbetta G. (2016). The European offshore wind industry-key trends and statistics 2015. *European Wind Energy Association (EWEA), Brussels, Belgium, Technical Report*.

Humar J. (2012). *Dynamics of Structures*, Third Edition. CRC Press.

IRENA (International Renewable Energy Agency). (2012). Wind Power Renewable Energy Technologies: Cost analysis series, (http://www.irena.org/Document).

Ishibashi, I., & Zhang, X. (1993). Unified dynamic shear moduli and damping ratios of sand and clay. *Soils and Foundations*, *33*(1), 182-191.

Jaky, J. (1948). Pressure in Silos. *Proc., 2nd Int. Conf. on Soil Mechanics and Foundation Engineering*, Rotterdam, The Netherland, 1, 103–107.

Kallehave, D., Byrne, B. W., Thilsted, C. L., & Mikkelsen, K. K. (2015). Optimization of monopiles for offshore wind turbines. *Phil. Trans. R. Soc. A*, *373*(2035), 20140100.

Kaynia, A. M., & Kausel, E. (1991). Dynamics of piles and pile groups in layered soil media. *Soil Dynamics and Earthquake Engineering*, *10*(8), 386-401.

Kaynia, A.M., Kausel, E. (1982). *Dynamic stiffness and seismic response of pile groups*. (Research Report R82-03, Cambridge, MA: Massachusetts Institute of Technology).

Kim, B. T., Kim, N. K., Lee, W. J., & Kim, Y. S. (2004). Experimental load-transfer curves of laterally loaded piles in Nak-Dong River sand. *Journal of Geotechnical and Geoenvironmental Engineering, ASCE*, *130*(4), 416-425.

Kim, Y., & Jeong, S. (2011). Analysis of soil resistance on laterally loaded piles based on 3D soil–pile interaction. *Computers and Geotechnics*, *38*(2), 248-257.

Klinkvort, R. T., & Hededal, O. (2013). Lateral response of monopile supporting an offshore wind turbine. *Proceedings of the Institution of Civil Engineers-Geotechnical Engineering*, *166*(2), 147-158.

Klinkvort, R. T., & Hededal, O. (2014). Effect of load eccentricity and stress level on monopile support for offshore wind turbines. *Canadian Geotechnical Journal*, *51*(9), 966-974.

Kondner, R. L. (1963). Hyperbolic stress-strain response: cohesive soils. *Journal of the Soil Mechanics and Foundations Division, ASCE*, *89*(1), 115-144.

Kooijman, A. P. (1989). Comparison of an elastoplastic quasi three-dimensional model for laterally loaded piles with field tests. *Numerical models in geomechanics-NUMOG III*, 675-682.

Kramer, S. L. (1996). Geotechnical earthquake engineering prentice hall. *Upper Saddle River, NJ*.

Kuhlemeyer, R. L. Static and Dynamic Laterally Loaded Floating Piles. *Journal of the Geotechnical Engineering Division, ASCE, 105*(2), 289-304.

Kuo, Y. S., Achmus, M., & Abdel-Rahman, K. (2011). Minimum embedded length of cyclic horizontally loaded monopiles. *Journal of Geotechnical and Geoenvironmental Engineering, ASCE, 138*(3), 357-363.

Leblanc, C., Byrne, B. W., & Houlsby, G. T. (2010b). Response of stiff piles to random two-way lateral loading. *Géotechnique, 60*(9), 715-721.

Leblanc, C., Houlsby, G. T., & Byrne, B. W. (2010a). Response of stiff piles in sand to long-term cyclic lateral loading. *Géotechnique, 60*(2), 79-90.

Lee, J., & Salgado, R. (2000). Analysis of calibration chamber plate load tests. *Canadian Geotechnical Journal, 37*(1), 14-25.

Lemos, L. J. L., & Vaughan, P. R. (2000). Clay-interface shear resistance. *Géotechnique, 50*(1), 55-64.

Lesny, K., & Hinz, P. (2007). Investigation of monopile behaviour under cyclic lateral loading. London UK: *Proceedings of the 6th International Offshore Site Investigtion and geotechnics Conference: Confronting New Challenges and Sharing Knowledge*, 383-390.

Lesny, K., & Wiemann, J. (2005). Design aspects of monopiles in German offshore wind farms. In *Proceedings of the International Symposium on Frontiers in Offshore Geotechnics* (pp. 383-389). AA Balkema Publishing.

Lesny, K., & Wiemann, J. (2006). Finite-element-modelling of large diameter monopiles for offshore wind energy converters. In *GeoCongress 2006: Geotechnical Engineering in the Information Technology Age* (pp. 1-6).

Lesny, K., Paikowsky, S. G., & Gurbuz, A. (2007). Scale effects in lateral load response of large diameter monopiles. In *Contemporary Issues In Deep Foundations* (pp. 1-10).

Li, W., Zhu, B., & Yang, M. (2017). Static response of monopile to lateral load in overconsolidated dense sand. *Journal of Geotechnical and Geoenvironmental Engineering, ASCE*, *143*(7), 04017026.

Liao, W., Zhang, J., Wu, J., & Yan, K. (2018). Response of flexible monopile in marine clay under cyclic lateral load. *Ocean Engineering*, *147*, 89-106.

Liu, H., Zheng, C., Ding, X., Kouretzis, G. P., & Sloan, S. W. (2016). A revised solution for the horizontal vibration of an end-bearing pile in viscoelastic soil. *International Journal for Numerical and Analytical Methods in Geomechanics*, *40*(13), 1890-1900.

Lombardi, D. (2010). *Dynamics of offshore wind turbines.* (Doctoral dissertation, University of Bristol).

Lombardi, D., Bhattacharya, S., & Wood, D. M. (2013). Dynamic soil–structure interaction of monopile supported wind turbines in cohesive soil. *Soil Dynamics and Earthquake Engineering*, *49*, 165-180.

Makris, N., & Gazetas, G. (1992). Dynamic pile-soil-pile interaction. Part II: Lateral and seismic response. *Earthquake Engineering & Structural Dynamics*, *21*(2), 145-162.

Matlock, H. (1970). Correlations for design of laterally loaded piles in soft clay. In *Proc. 2nd Annual Offshore Technology Conference, Houston, Texas, 1970* (Vol. 1, pp. 577-594).

Matlock, H., & Reese, L. C. (1960). Generalized solutions for laterally loaded piles. *Journal of the Soil Mechanics and Foundations Division, ASCE*, *86*(5), 63-94.

McClelland, B., & Focht, J. A. (1958). Soil modulus for laterally loaded piles. *Transactions of the American Society of Civil Engineers*, *123*(1), 1049-1063.

Menq, F. Y. (2003). *Dynamic properties of sandy and gravelly soils*. (Doctoral dissertation, University of Texas at Austin, TX, USA).

Meyerhof, G. G. (1956). Penetration tests and bearing capacity of cohesionless soils. *Journal of the Soil Mechanics and Foundations Division, ASCE*, *82*(1), 1-19.

Mindlin, R. D. (1936). Force at a Point in the Interior of a Semi-Infinite Solid. *Journal of Applied Physics*, *7*, 195-202.

Møller, I. F., & Christiansen, T. H. (2011). *Laterally loaded monopile in dry and saturated sand-static and cyclic loading: experimental and numerical studies*. (Masters Project, Aalborg University Esbjerg).

Murphy, G., Igoe, D., Doherty, P., & Gavin, K. (2018). 3D FEM approach for laterally loaded monopile design. *Computers and Geotechnics*, *100*, 76-83.

Mylonakis, G. (2001). Elastodynamic model for large-diameter end-bearing shafts. *Soils and Foundations*, *41*(3), 31-44.

Nicolai, G., & Ibsen, L. B. (2015). Response of monopiles under cyclic lateral loading in sand. In *EWEA Offshore 2015*. The European Wind Energy Association.

Nogami, T., & Novak, M. (1977). Resistance of soil to a horizontally vibrating pile. *Earthquake Engineering & Structural Dynamics*, *5*(3), 249-261.

Norris, G. M. (1986). Theoretically based BEF laterally loaded pile analysis. In *Proc. 3rd Int. Conf. on Numerical Methods in Offshore Piling* (pp. 361-386).

Novak, M. (1974). Dynamic stiffness and damping of piles. *Canadian Geotechnical Journal*, *11*(4), 574-598.

Novak, M., & Nogami, T. (1977). Soil-pile interaction in horizontal vibration. *Earthquake Engineering & Structural Dynamics*, *5*(3), 263-281.

Novak, M., Aboul-Ella, F., & Nogami, T. (1978). Dynamic soil reactions for plane strain case. *Journal of the Engineering Mechanics Division, ASCE*, *104*(4), 953-959.

Nozoe, H., Gyōten, Y., & Fukusumi, T. (1985). Dynamic analysis of a soil-pile system by the finite Fourier-Henkel transformation method–Case of a floating pile in horizontal vibration. *Theoretical and applied mechanics*, *33*, 377-392.

O'Neill, M. W., & Murchison, J. M. (1983). *An evaluation of py relationships in sands*. (Report GT-DF02-83, Departemnt of Civil Engineering, University of Houston).

O'Neill, M. W., Reese, L. C., & Cox, W. R. (1990). Soil behavior for piles under lateral loading. In *Offshore Technology Conference*. Offshore Technology Conference.

Osman, A. S., White, D. J., Britto, A. M., & Bolton, M. D. (2007). Simple prediction of the undrained displacement of a circular surface foundation on non-linear soil. *Géotechnique*, *57*(9), 729-737.

Oztoprak, S., & Bolton, M. D. (2013). Stiffness of sands through a laboratory test database. *Géotechnique*, *63*(1), 54-70.

Padrón, L. A., Aznárez, J. J., & Maeso, O. (2008). Dynamic analysis of piled foundations in stratified soils by a BEM–FEM model. *Soil Dynamics and Earthquake Engineering*, *28*(5), 333-346.

Page, A. M., Skau, K. S., Jostad, H. P., & Eiksund, G. R. (2017). A New Foundation Model for Integrated Analyses of Monopile-based Offshore Wind Turbines. *Energy Procedia*, *137*, 100-107.

Pak, R. Y., & Jennings, P. C. (1987). Elastodynamic response of pile under transverse excitations. *Journal of Engineering Mechanics, ASCE*, *113*(7), 1101-1116.

Pasternak, P. L. (1954). On a new method of analysis of an elastic foundation by means of 487 two foundation constants (in Russian). Gosudarstuennogo Izdatelstvo Literaturipo 488 Stroitelstvui Arkhitekture, Moscow, USSR.

Poulos, H. G. (1971). Behavior of Laterally Loaded Piles: I-Single Piles. *Journal of the Soil Mechanics and Foundations Division, ASCE*, *97*(5), 711-731.

Pradhan, D. L. (2012). *Development of p-y curves for monopiles in clay using finite element model Plaxis 3D Foundation* (Master's thesis, Norwegian University of Science and Technology).

Pressley, J. S., & Poulos, H. G. (1986). Finite element analysis of mechanisms of pile group behaviour. *International Journal for Numerical and Analytical Methods in Geomechanics*, *10*(2), 213-221.

Rajapakse, R. K. N. D., & Shah, A. H. (1987). On the lateral harmonic motion of an elastic bar embedded in an elastic half-space. *International Journal of Solids and Structures*, *23*(2), 287-303.

Rajapakse, R. K. N. D., & Shah, A. H. (1989). Impedance curves for an elastic pile. *Soil Dynamics and Earthquake Engineering*, *8*(3), 145-152.

Randolph, M.F. (1981). The response of flexible piles to lateral loading. *Geotechnique*, 31(2), 247-259.

Reese, L. C. (1956). Non-dimensional solutions for laterally loaded piles with soil modulus assumed proportional to depth. In *Proc. 8th Texas Conf. SMFE, The Univ. of Texas*.

Reese, L. C. (1997). Analysis of laterally loaded piles in weak rock. *Journal of Geotechnical and Geoenvironmental Engineering, ASCE*, *123*(11), 1010-1017.

Reese, L. C., & Wang, S. T. (1997). LPILE Plus 3.0 Technical manual of documentation of computer program. *Ensoft, Inc., Austin, Texas*.

Reese, L. C., & Welch, R. C. (1975). Lateral Loading of Deep Foundations in Stiff Clay. *Journal of the Geotechnical Engineering Division, ASCE*, *101*(7), 633-649.

Reese, L. C., Cox, W. R., & Koop, F. D. (1975). Field testing and analysis of laterally loaded piles in stiff clay. In *Proc. 7th Offshore Technology Conference, Houston, Texas,* (pp. 672-690).

Reese, Lymon C., and William F. Van Impe. (2011). *Single Piles and Pile Groups Under Lateral Loading*. 2nd Edition, CRC Press, Taylor and Francis Group, London, UK.

Roesset, J. M. (1980). The use of simple models in soil structure interaction. In *Civil engineering and nuclear power* (pp. 1-25). ASCE.

Roesset, J. M., & Angelides, D. (1980). Dynamic stiffness of piles. In *Numerical methods in offshore piling* (pp. 75-81). Thomas Telford Publishing.

Salgado, R. (2008). *The engineering of foundations*. The McGraw-Hill Companies, Inc.

Seed, H. B. & Idriss, I. M. (1970). *Soil moduli and damping factors for dynamic response analyses*. (Report EERC, University of California, Berkeley, CA, USA).

Sen, R., Davies, T. G., & Banerjee, P. K. (1985). Dynamic analysis of piles and pile groups embedded in homogeneous soils. *Earthquake engineering & structural dynamics*, *13*(1), 53-65.

Shadlou, M., & Bhattacharya, S. (2014). Dynamic stiffness of pile in a layered elastic continuum. *Geotechnique*, *64*(4), 303-319.

Shadlou, M., & Bhattacharya, S. (2016). Dynamic stiffness of monopiles supporting offshore wind turbine generators. *Soil Dynamics and Earthquake Engineering*, *88*, 15-32.

Shames, I. H. & Dym, C. L. (1985). *Energy and Finite Element Methods in Structural Mechanics*. CRC Press.

Shen, W. Y., & Teh, C. I. (2004). Analysis of laterally loaded piles in soil with stiffness increasing with depth. *Journal of Geotechnical and Geoenvironmental Engineering*, ASCE, *130*(8), 878-882.

Shibuya, S., Mitachi, T., Yamashita, S., & Tanaka, H. (1996). Recent Japanese practice for investigating elastic stiffness of ground. In *Advances in site investigation practice* (pp. 875-886). Thomas Telford Publishing.

Siemens, A.G. (2016). Wind Turbine SWT-3.6-120-Technical specifications.

Sørensen, S. P. H., Ibsen, L. B., & Augustesen, A. H. (2010). Effects of diameter on initial stiffness of py curves for large-diameter piles in sand. *In The European Conference on Numerical Methods in Geotechnical Engineering* (pp. 907-912). CRC Press LLC.

Strutt J. W. (1877). Theory of Sound. London: Macmillan Publications Co., Inc

Sun, K. (1994). Laterally loaded piles in elastic media. *Journal of Geotechnical Engineering*, ASCE, *120*(8), 1324-1344.

Sun, K., & Pires, J. A. (1993). Simplified approach for pile and foundation interaction analysis. *Journal of Geotechnical Engineering*, ASCE, *119*(9), 1462-1479.

Sun, K., & Pires, J. A. (1995). Closure to "Simplified Approach for Pile and Foundation Interaction Analysis" by Kerning Sun and Jose A. Pires. *Journal of Geotechnical Engineering*, *121*(2), 229-230.

Tajimi, H. (1969). Dynamic analysis of a structure embedded in an elastic stratum. In *Proc. 4th World Conf. on Earthq. Engng,* Santiago,Chile; (pp. 53-69).

Thammarak, P. (2009). *Dynamic response of laterally-loaded piles*. (Ph.D. thesis, University of Texas at Austin.

Thomas, S. (1989). Geotechnical investigation of UK test sites for the foundations of offshore structures, Department of energy offshore technology report OTH 89 294.

Trochanis, A. M., Bielak, J., & Christiano, P. (1991). Three-dimensional nonlinear study of piles. *Journal of Geotechnical Engineering, ASCE*, *117*(3), 429-447.

USACE. (1990). *Engineering and design: settlement analysis*. (Engineer manual 1110–1–1904, US Army Corps of Engineers).

Vallabhan, C. G., & Das, Y. C. (1991). Modified Vlasov model for beams on elastic foundations. *Journal of geotechnical engineering, ASCE*, *117*(6), 956-966.

Vallahban CVG, Alikhanlou F. (1982). Short rigid piles in clay. *Journal of Geotechnical Engineering, ASCE*, 108 (10):1255–1271.

Vardanega, P. J., & Bolton, M. D. (2013). Stiffness of clays and silts: Normalizing shear modulus and shear strain. *Journal of Geotechnical and Geoenvironmental Engineering, ASCE*, *139*(9), 1575-1589.

Varun, Assimaki, D., & Gazetas, G. (2009). A simplified model for lateral response of large diameter caisson foundations—Linear elastic formulation. *Soil Dynamics and Earthquake Engineering*, *29*(2), 268-291.

Vesic, A. B. (1961). Beams on elastic subgrade and the Winkler's hypothesis. In *Proceedings, 5th International Conference on Soil Mechanics and Foundation Engineering* (Vol. 1, pp. 845-850).

Viggiani, G., & Atkinson, J. H. (1995). Stiffness of fine-grained soil at very small strains. *Géotechnique*, *45*(2), 249-265.

Vlasov, V. Z. & Leont'ev, N. N. (1966). Beams, plates and shells on elastic foundations. Jerusalem, Israel: Israel Program for Scientific Translations.

Wakai, A., Gose, S., & Ugai, K. (1999). 3-D elasto-plastic finite element analyses of pile foundations subjected to lateral loading. *Soils and Foundations*, *39*(1), 97-111.

Wiemann, J., Lesny, K., & Richwien, W. (2004). Evaluation of the pile diameter effects on soil-pile stiffness. In *Proceedings of the 7th German Wind Energy Conference (DEWEK), Wilhelmshaven*.

Wu, G., & Finn, W. L. (1997). Dynamic elastic analysis of pile foundations using finite element method in the frequency domain. *Canadian Geotechnical Journal*, *34*(1), 34-43.

Xu, L. Y., Cai, F., Wang, G. X., & Ugai, K. (2013). Nonlinear analysis of laterally loaded single piles in sand using modified strain wedge model. *Computers and Geotechnics*, *51*, 60-71.

Yan, L. I., & Byrne, P. M. (1992). Lateral pile response to monotonie pile head loading. *Canadian Geotechnical Journal*, *29*(6), 955-970.

Yang, M., Luo, R., & Li, W. (2017). Numerical study on accumulated deformation of laterally loaded monopiles used by offshore wind turbine. *Bulletin of Engineering Geology and the Environment*, 1-11.

Yang, X., Zhang, C., Huang, M., & Yuan, J. (2017). Lateral loading of a pile using strain wedge model and its application under scouring. *Marine Georesources & Geotechnology*, 1-11.

Yang, Z., & Jeremić, B. (2005). Study of soil layering effects on lateral loading behavior of piles. *Journal of Geotechnical and Geoenvironmental Engineering*, *ASCE*, *131*(6), 762-770.

Zaaijer, M. B. (2006). Foundation modelling to assess dynamic behaviour of offshore wind turbines. *Applied Ocean Research*, *28*(1), 45-57.

Zdravkovic, L, Taborda, DMG, Potts, DM, Jardine, RJ, Sideri, M, Schroeder, FC, Byrne, BW, McAdam, R, Burd, HJ, Houlsby, G.T, Martin, C.M, Gavin, K, Doherty, P, Igoe, D, Muir Wood, A, Kallehave, D and Skov Gretlund, J. (2015). Numerical modeling of large diameter piles under lateral loading for offshore wind applications. *Oslo*, *Norway*: *Proc 3rd International Symposium on Frontiers in Offshore Geotechnics* (*ISFOG*), pp 759–764.

Zhang, J., Andrus, R. D., & Juang, C. H. (2005). Normalized shear modulus and material damping ratio relationships. *Journal of Geotechnical and Geoenvironmental Engineering*, *ASCE*, *131*(4), 453-464.

Zhang, L., & Ahmari, S. (2013). Nonlinear analysis of laterally loaded rigid piles in cohesive soil. *International Journal for Numerical and Analytical Methods in Geomechanics*, *37*(2), 201-220.

Zheng, C., Liu, H., Ding, X., & Fu, Q. (2013). Horizontal vibration of a large-diameter pipe pile in viscoelastic soil. *Mathematical Problems in Engineering*, *2013*.

Zhong, R., & Huang, M. (2013). Winkler model for dynamic response of composite caisson-piles foundations: Lateral response. *Soil Dynamics and Earthquake Engineering*, *55*, 182-194.

Zhu, B., Sun, Y. X., Chen, R. P., Guo, W. D., & Yang, Y. Y. (2015). Experimental and analytical models of laterally loaded rigid monopiles with hardening p–y curves. *Journal of Waterway, Port, Coastal, and Ocean Engineering*, *141*(6), 04015007.

APPENDIX

List of Publications

***Refereed Journal Publications* (Published or Accepted)**

[1] **Gupta, B. K.**, Basu, D. (2018). Timoshenko Beam Theory based Dynamic Analysis of Laterally Loaded Piles in Multilayered Viscoelastic Soil. ***Journal of Engineering Mechanics, ASCE***, *114*(9):04018091-1-17.

[2] **Gupta, B. K.**, Basu, D. (2018). Applicability of Timoshenko, Euler–Bernoulli and rigid beam theories in analysis of laterally loaded monopiles and piles. ***Géotechnique***, (Available online, Ahead of print).

[3] **Gupta, B. K.**, Basu, D. (2017). Analysis of Laterally Loaded Short and Long Piles in Multilayered Heterogeneous Elastic Soil. ***Soils and Foundations***, *57*: 92–110.

[4] **Gupta, B. K.**, Basu, D. (2016). Response of laterally loaded rigid monopiles and poles in multi-layered elastic soil. ***Canadian Geotechnical Journal***, *53*(8): 1281-1292.

[5] **Gupta, B. K.**, Basu, D. (2016). Analysis of laterally loaded rigid monopiles and poles in multilayered linearly varying soil. ***Computers and Geotechnics***, *72*: 114–125.

***Refereed Journal Publications* (Under review and Preparation)**

[6] **Gupta, B. K.**, Basu, D. Design of laterally loaded monopiles in undrained clay deposits. (*Manuscript under preparation*).

[7] **Gupta, B. K.**, Basu, D. (2018). A Computationally Efficient 3-D Continuum-Based Model for Nonlinear Analysis of Laterally Loaded Piles. ***Géotechnique***. (*Manuscript under the first review*).

[8] **Gupta, B. K.**, Basu, D. (2018). Soil Resistances for Laterally Loaded Rigid Piles in Multilayered Elastic Soil. ***Geomechanics and Geoengineering, An International Journal*** (*Manuscript under the first review*).

***Refereed Conference Publications* (Published or Accepted)**

[1] **Gupta, B. K.**, Basu, D. (2018). Nonlinear elastic analysis of laterally loaded piles. ***GeoEdmonton, 71st Canadian Geotechnical Conference*, Edmonton, Canada** (Accepted).

[2] **Gupta, B. K.**, Basu, D. (2018). Dynamic Analysis of Laterally Loaded End-Bearing Piles in Homogeneous Viscoelastic Soil using Timoshenko Beam Theory**.** ***IFCEE Florida, ASCE*, USA**.

[3] **Gupta, B. K.**, Basu, D. (2017). Dynamic analysis of rigid monopiles in multi-layered viscoelastic soil. *GeoOttawa*, ***70th Canadian Geotechnical Conference*, Ottawa, Canada**.

[4] **Gupta, B. K.**, Basu, D. (2017). Analysis investigating the applicability of Timoshenko, Euler-Bernoulli, and rigid beam theories in modeling laterally loaded monopiles. ***Proceedings of the 19th International Conference on Soil Mechanics and Geotechnical Engineering,* Seoul, Korea**, 2763-2766.

[5] **Gupta, B. K.**, Basu, D. (2016). Design charts for laterally loaded rigid monopiles in multi-layered elastic soil. ***Geo-Chicago*, ASCE, USA**, 393-406.

[6] **Gupta, B. K.**, Basu, D. (2015). Analysis of Offshore Wind Turbine Rigid Monopile Foundation. ***15th Pan-American conference on soil mechanics and geotechnical engineering-From fundamentals to application in geotechnics,* Buenos Aires**, 822-829.

[7] **Gupta, B. K.**, Basu, D. (2015). Analysis of rigid monopiles in multilayered elastic soil. ***GeoQuebec, 68th Canadian Geotechnical Conference*, Quebec City, Canada**.

***Refereed Conference Publications* (Under review)**

[8] **Gupta, B. K.**, Basu, D. (2019). A Continuum Based Formulation for Nonlinear Analysis for Laterally Loaded Piles. ***GeoCongress, Philadelphia, Pennsylvania*, USA, *ASCE***.